AFIT/GE/ENG/97D-13

Scattering From Dielectric Bodies

THESIS

Presented to the Faculty of the School of Engineering

of the Air Force Institute of Technology

Air University

In Partial Fulfillment of the

Requirements for the Degree of

Master of Science in Electrical Engineering

Jeffery M. Parks, BSEE

Captain, USAF

December, 1997

AFIT/GE/ENG/97D-13

Scattering From Dielectric Bodies

THESIS

Jeffery M. Parks
Captain, USAF

AFIT/GE/ENG/97D-13

The views expressed in this thesis are those of the author and do not reflect the official policy or position of the Department of Defense or the United States Government.

AFIT/GE/ENG/97D-13

Scattering From Dielectric Bodies

Jeffery M. Parks, BSEE

Captain, USAF

Approved:

Maj. Peter J. Collins (PhD) Thesis Advisor	26 NOV 97 Date
Maj. Paul Skinner (PhD) Committee Member	20 NOV 97 Date
Dr. Kueichien Hill Committee Member	26 NOV 97 Date
Maj. Mike Temple (PhD) Committee Member	26 Nov 97 Date

Acknowledgements

I wish to express my sincere appreciation to the people who have contributed to my thesis. My special thanks to my thesis advisor Major Pete Collins for his guidance and help throughout this research, my sponsor Major Paul Skinner, and committee members Dr. Kueichien Hill and Major Mike Temple.

Others helpful in completing this research include Russ Hastings and Mike Suggs from the AFIT Fabrication Shop who spent countless hours fabricating the targets. Bill Forester of Mission Research Corporation (MRC) was vital in the process of material characterization. Running 3D-RCIE was only achieved through numerous conversations with Andrew Seidl of Lockheed Martin Missiles And Space Co., Inc. RCS measurements at WL/XPN were accomplished through the coordination efforts of Captain Andy Gillespie and Butch Porter. I am very thankful to Alan Buterbaugh of MRC for measuring the targets and spending hours and hours processing the data. Thanks also to Dr. Brian Kent of WL/XPN and Dr. Byron Welsh of MRC for their help and insight into RCS uncertainty.

I am eternally grateful to my wife, Katrina, for her love, understanding and encouragement during this challenging program. I thank her for not only being there for me, but for her unselfish understanding for the many times I could not be there for her.

Jeffery M. Parks

Table of Contents

List of Figures

List of Tables

List of Symbols

Symbol	Page
ϵ_r Relative Permittivity	3-8
μ_r Relative Permeability	3-8
N_p Number of Patches	3-17
N_a Number of Illumination Angles	3-17
ϵ' Real Part of the Permittivity	4-8
ϵ'' Imaginary Part of the Permittivity	4-11
μ' Real Part of the Permeability	4-12
μ'' Imaginary Part of the Permeability	4-12
HH Horizontal Polarization	4-20
VV Vertical Polarization	4-20

List of Abbreviations

Abstract

The purpose of this study was to develop an RCS measured database of non-PEC targets and provide an example of its use to validate a code, 3D-RCIE. RCS prediction codes that handle penetrable materials require measured data to determine their accuracy.

The materials used for this research include polyethylene and polyurethane with dielectric constants around 2.3 and 1.03, respectively. The polyethylene targets include a mini-arrow, ogive, conesphere, conesphere with a gap, sphere, and a large and small cube. The cubes were the only targets made from the polyurethane foam. Additionally, r-card was applied to the cubes and mini-arrow.

The material properties of the two materials were measured using an X-band waveguide reflectometer. The RCS measurements were accomplished for each target at the Wright Laboratory Signature Technology Office's Multispectral Measurement Facility (WL/XPN). For each measurement, an uncertainty analysis was completed. RCS predictions of each target were accomplished using 3D-RCIE, a method of moments electromagnetic scattering code based on the radiation condition integral equations.

The comparison of measured and predicted RCS data indicated that the linear mesh rate had a large impact on the results. Use of the appropriate mesh sizes generally produced good comparisons. For targets that were electrically large, mesh sizes were limited by the computer resources which in turn greatly deteriorated the predicted results. Furthermore, 3D-RCIE provided the most accurate predictions on the polyethylene targets, less the sphere and r-card application.

Scattering From Dielectric Bodies

I. Introduction

1.1 Background

One important parameter of the modern military aircraft is its Radar Cross Section (RCS). The RCS is one of several variables a radar system uses to detect and track a target. The RCS of a target is the amount of power in the incident field that is intercepted by the target and scattered back to the source [15]. It is a fictitious area that can be thought of as the geometrical area required to produce the target's return if the energy intercepted by this geometric area were re-radiated isotropically. RCS is used for a variety of purposes including target identification and stealth technology.

RCS prediction techniques for Perfect Electric Conductors (PEC) have become realizable with the advent of the modern computer. RCS computer prediction codes have several advantages over experimental RCS measurements. A key advantage is the ability to produce RCS predictions of inaccessible targets at a much reduced cost. Prediction codes have also attained accurate results for simple targets but tend to breakdown for realistically sized complex targets. The accuracy of the codes is determined by comparing the RCS computer prediction of a known simple target to experimental RCS measurements of the same target.

The Electromagnetic Code Consortium (EMCC) has collected a large database of measured and predicted RCS data on simple PEC (metal) and Radar Absorbing Material (RAM) coated shapes. Such geometries include flat plates, cylinders, ogives, and cone-spheres. This reference data is used to determine a computer code's ability to accurately predict the RCS of a target. However, one must be aware that the measured data does contain some degree of uncertainty. For example, Figure 1.1 is a model depicting the RCS as determined by a code. The input parameters for the code allow the target dimensions and material properties to be precise values. Furthermore, the target is suspended in free space and is located an infinite distance from the radar allowing the incident field to be

planar as required by the definition of RCS. In reality, the measured RCS of a target, depicted in Figure 1.2, cannot achieve this perfection. The target's dimensions and material properties, although close, will not be exact. A compact range, used to measure the RCS, will only approximate an incident plane wave due to the finite distance between the target and radar. Additionally, the target must be physically mounted on a pylon in the range eliminating the possibility of achieving free space.

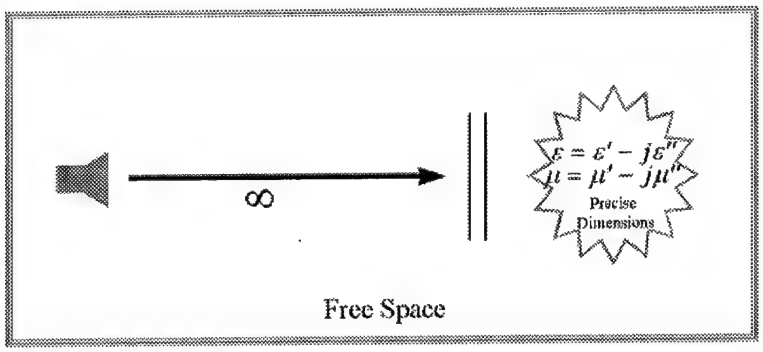

Figure 1.1 A graphical computer prediction code model for determining the RCS of a target.

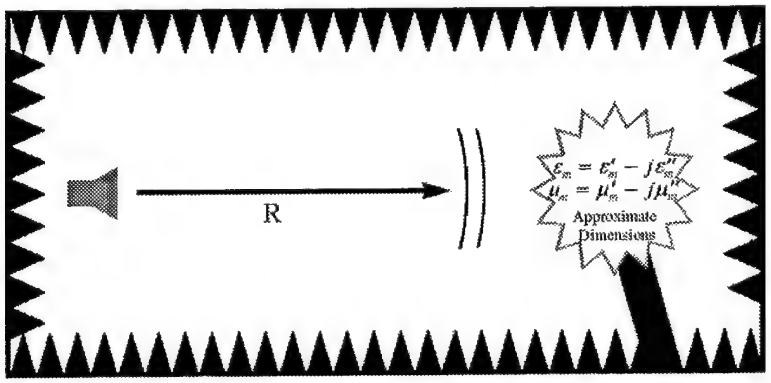

Figure 1.2 A model for experimentally measuring the RCS of a target.

The majority of research in this area has been accomplished for PECs only even though RCS applies to any target, regardless of composition. The RCS prediction of a low dielectric body is a different and more challenging problem than a PEC for two reasons. First, the energy of the incident wave penetrates a low dielectric material. Second, low dielectric materials generally do not conduct well resulting in low RCS values.

1.2 Problem Definition

Many systems being designed today include low dielectric (non-PEC) features. In response, several new non-validated RCS codes have been developed. In order to verify the accuracy of the codes a measured RCS database of non-PEC targets needs to be developed. My research will develop this database with emphasis on characterizing the measurement uncertainties and provide an example of its use to validate a new dielectric computer code.

1.3 Scope

My research has three goals: to measure the RCS of a group of dielectric targets accurately, to use a computer code to predict the RCS of the targets, and then to compare both sets of data to validate the code. The measured RCS database will be created from five different target shapes. Each shape will be machined from two different, lossless dielectric material samples of different permittivities. The RCS of the targets will be measured at one facility, Wright Laboratory's Multispectral Measurement Facility (WL/XPN), from 2 to 18 GHz. Finally, an RCS prediction code based on a new integral equation formulation called the Three Dimensional Radiation Condition Integral Equations (3D-RCIE), will be used to demonstrate the code validation process.

1.4 Assumptions

To accomplish this research, several assumptions were made. The materials used in this study are assumed to be homogeneous. An error budget will account for all significant measured RCS data uncertainty. The computer predictions are fully converged, thus representing the best possible solution. And, any numerical errors from calculations of the RCS predictions are negligible.

1.5 Sequence of Presentation

This thesis document is divided into five chapters. Each chapter has a parallel structure mirroring the steps involved in creating the RCS database and using it to validate an RCS code. Specifically, each chapter organizes the information into sections related

to validation target choice, target measurement, and code validation. Chapter II is an overview of the knowledge required to understand the basics of this research. The following chapter addresses the methodology and approach to complete the RCS database and use it for code validation. Chapter IV contains the results and analysis of the measured and simulated data collected in this research, and Chapter V provides the conclusion.

II. Background Theory

This chapter provides an overview of the knowledge required to understand the basics of this research. It is divided into three sections. First is an introduction into the shapes and compositions of the targets used to create the RCS database. The second section discusses the measurement theory for determining the material properties and RCS of these targets. Finally, the last section describes the code and code validation process based on this RCS database.

2.1 Targets

RCS benchmark targets used for code validation generally are dependent on shape only. The shape of a PEC target dictates the scattering phenomena. Thus, by shaping the target appropriately, one can test a code's ability to model a particular scattering mechanism. A non-PEC target allows energy to propagate into and through it. Therefore, the low dielectric targets used in this research are dependent upon material composition, as well as shape.

2.1.1 Target Shapes. The EMCC is an organization formed by representatives from NASA and three US DOD services with the purpose of integrating efforts on the development of electromagnetic codes [22]. The EMCC has established a set of geometries to be used for RCS code validation. The RCS of five metallic Bodies of Revolution (BOR) from the set were measured by Woo for code validation purposes [22]. The shapes include the ogive, double ogive, conesphere, conesphere with a gap, and the NASA almond. These geometries, and others, were chosen because some of the shapes are well documented and understood both analytically and from range measurement aspects; others may provide problematic surface features. All-in-all, the variety of shapes were picked to determine strengths and weaknesses of the test codes.

For example, two of the samples measured are the conesphere and the conesphere with a gap. The conesphere has geometry similar to an ice cream cone. This target provides an excellent baseline because it is well documented. Additionally, it has a relatively low cross section at some aspects which provides for a very sensitive test. The conesphere

with a gap is the same shape as the conesphere, except there is a small gap between the hemisphere and the cone. The small gap tests a program's ability to separate small features on a large target. The analysis of both large and small features on a target is a complex and difficult problem [7]. These features make the conesphere and conesphere with a gap excellent target shapes to measure the fidelity of an RCS code.

2.1.2 Target Materials. The targets used to create the RCS database for this research are made of homogeneous material with a low dielectric constant. Dielectrics are generally considered nonconductors (typically they are non-metallic). The following is the developement of the dielectric constant from Balanis [2].

Consider a slab of dielectric material. When an electric field, (E_a), is applied to the material, the charges are aligned. The net effect is that between the upper and lower surfaces of the dielectric material there is a net electric polarization vector (P) directed from the upper toward the lower surfaces, in the same direction as the applied electric field E_a, whose amplitude is given by

$$P = q_{sp} \tag{2.1}$$

where q_{sp} is the surface charge density. The electric flux density (D) is related to that of free space D_o by

$$D = D_o + P = \epsilon_o E_a + P \tag{2.2}$$

where ϵ_o is the permittivity of free space and the magnitude of P is given by Equation (2.1). The electric flux density D of (2.2) can also be related to the applied electric field intensity E_a by a parameter which is designated as ϵ_s (farads/meter). Therefore,

$$D = \epsilon_s E_a \tag{2.3}$$

Comparing (2.2) and (2.3), P is also related to E_a by

$$P = \epsilon_o \chi_e E_a \tag{2.4}$$

or

$$\chi_e = \frac{1}{\epsilon_o}\frac{P}{E_a} \tag{2.5}$$

where χ_e is the electric susceptibility. Substituting (2.4) into (2.2) and equating the result to (2.3), it can be writen

$$D = \epsilon_o E_a + \epsilon_o \chi_e E_a = \epsilon_o(1+\chi_e)E_z = \epsilon_s E_a \tag{2.6}$$

or that

$$\epsilon_s = \epsilon_o(1+\chi_e) \tag{2.7}$$

ϵ_s is the static permittivity of a medium whose relative value ϵ_{sr} is given by

$$\epsilon_{sr} = \frac{\epsilon_r}{\epsilon_o} = 1+\chi_e \tag{2.8}$$

which is referred to as the relative permittivity, or better known as the dielectric constant.

The dielectric constant or relative permittivity indicates the relative energy storage capabilities of a dielectric material; the larger its value, the greater its ability to store energy [2]. This value has a wide range – including 96 for Titania and only 2.16 for Vaseline [5]. For this thesis, low dielectric constants are defined as having a value of 3 and below.

One commonly used low dielectric material is Styrofoam. Styrofoam 103.7 (99.75% polystyrene and 0.25% filler), as calculated by Von Hippel, has an effective dielectric constant of 1.03 [20]. Styrofoam is made of small air pockets surrounded by polystyrene. Plonus models this material as "randomly arranged and closely spaced dielectric shells (ping-pong balls)" [18]. This characteristic can cause problems for codes because each of the cells (or balls) will scatter the incident wave. Plonus was the first to note that Styrofoam and other polystyrene materials have two scattering mechanisms:

> The total back scatter from an aggregate of N particles will in general be composed of a coherent and an incoherent contribution. Coherent scattering results when a systematic relation between the phases of scatters exists, or when the particle density changes within a distance of a wavelength. This type of scattering is proportional to N^2 since amplitudes rather than intensities (power)

> add. Incoherent scattering is the usual contribution from an aggregate of randomly distributed particles which act independently of each other, implying that no systematic relation between the phases of the scatterer exists; hence it is proportional to N. This type of scattering will then be strictly a consequence of the random arrangements of the particles. This is due either to the random motion or fluctuation in time about some average distribution when the aggregate is illuminated with a steady signal, or to the random fluctuations about some average when many samples of a material consisting of a random distribution of particles are examined. [18]

Thus, coherent scattering comes from the overall shape of the target while incoherent scattering is due to the nature of the material composition which consists of tightly packed individual scatterers.

To model the RCS of Styrofoam mathematically, Plonus developes the following Equation (2.9). The total scattering cross section is given by

$$\sigma = \sigma_i \mid \int_0^\infty \overline{n}(r) e^{-2ikr} dr|^2 + \sigma_i \int_0^\infty \overline{n}(r) dr \tag{2.9}$$

where $\overline{n}(r)$ is the time average of the distribution function (which represents the time average particle density at location r), r is the distance from the center to the observer, and σ_i is the RCS of one scatterer [18]. The first term of Equation (2.9) is the coherent RCS. Changes in the material density of Styrofoam are small so $\overline{n}(r)$ is nearly constant and the coherent scattering remains small. The largest change in material properties occurs at the Styrofoam / air boundary (the surface of the target). At this point, $\overline{n}(r)$ jumps from zero to its normal value, making the integral non-zero. Therefore, the largest contribution to coherent scattering for a Styrofoam target is the surface of the target [4].

The second term in Equation (2.9) is the incoherent RCS. Incoherent scattering represents the sum of the scattering from each of the cells within the target. The total number of scattering cells is directly proportional to the volume of the target. Additionally, the size of the cells greatly affect the RCS. Smaller cells produce lower incoherent scattering [4]. Since most RCS codes don't account for this incoherent scattering term, Styrofoam was discarded as a candidate material in favor of polyethylene which is a homogeneous material with no internal structure.

Having discussed some of the considerations involved with choosing proper benchmark targets, we now turn to the measurement theory involved in measuring these targets.

2.2 Measurement Theory

To properly benchmark non-PEC targets, the target's material properties must be accurately measured in addition to its RCS. The following sections discuss the theory behind these two measurements.

2.2.1 Material Property Characterization. A major source of error found in predicting the RCS of non-metallic objects is the failure to accurately characterize the material properties of that object. According to Barnhart, material specifications given by the manufacturer may vary five to twenty percent or more [3]. Because of this, RCS code predictions have performed poorly due to inaccurate material characteristics. Fortunately there are many ways to measure material characteristics.

Afsar described many methods for material characterization, but the most accurate technique for higher frequencies uses transmission line theory [1]. Transmission line theory measurements are well suited for material measurements for several reasons. First, the field is well known and understood. Second, the energy used in the measurements is confined within the system allowing for any measured losses to be attributed to the material and not to the measurement equipment [1].

Two properties used to characterize a material include permittivity (ϵ) and permeability (μ) [3]. Permittivity is the ability of a material to store electrical energy and permeability is its ability to store magnetic energy. From these parameters, the characteristic impedance and the refractive index of the material can be found. Pozar defines characteristic impedance as the ratio of voltage to current for a traveling wave [19]. The index of refraction of a medium is the ratio of the speed of light in free space to that in the medium [5]. Detailed experimental procedures and background theory for measuring material properties are described by Von Hippel [20]. Even though his book is over forty years old, it is still a standard today.

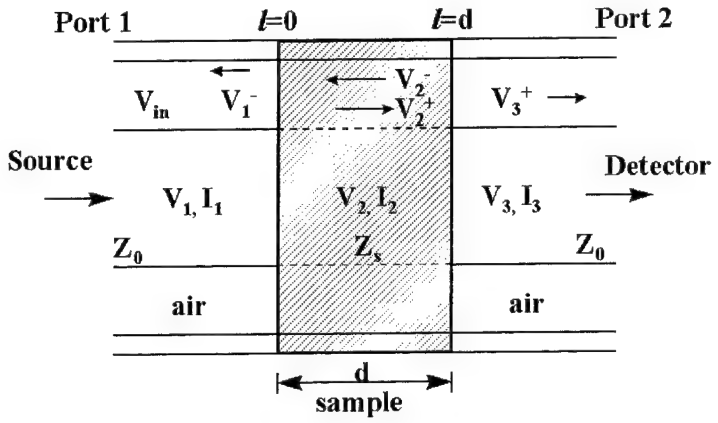

Figure 2.1 Airline Filled with Material.

Transmission line measurements make use of small material samples fitted inside a transmission line holder. The samples must fit snugly into the holder and are small compared to the wavelength. Also, the samples must accurately represent the material being characterized. A signal generator is used to apply an electromagnetic wave to the sample. The amplitude and phase of the reflected and transmitted wave are measured and used to calculate the required material properties.

Two of the methods described by Von Hippel to characterize materials use rectangular waveguides or coaxial transmission lines [20]. Both methods are relatively easy to accomplish. The advantage of using the rectangular waveguide is that the shapes of the samples are easy to fabricate because they are rectangular blocks. However, the rectangular waveguide can only support the Transverse Electric (TE) and Transverse Magnetic (TM) modes, but not the Transverse Electromagnetic (TEM) mode. Limiting the number of modes limits the frequency band for which the materials can be sampled. On the other hand, the coaxial line can measure all three modes, TE, TM and TEM. Although, the washer-shaped samples required for the transmission line holder can be difficult to fabricate.

Using this methodology, a technique for computing the complex permittivity and permeability using S-parameter data has been developed. Consider a sample of material installed in an air line as shown in Figure 2.1. Assuming no mismatches and solving the boundary conditions at $l = 0$ and $l = d$, $S_{11}(\omega)$ and $S_{21}(\omega)$ can be related to the reflection

coefficient (Γ) and the transmission coefficient (T) by the following equations [12]:

$$S_{11}(\omega) = \frac{(1-T^2)\Gamma}{1-T^2\Gamma^2} \tag{2.10}$$

$$S_{21}(\omega) = \frac{(1-\Gamma^2)T}{1-T^2\Gamma^2} \tag{2.11}$$

Furthermore,

$$\Gamma = \frac{Z_s - Z_o}{Z_s + Z_o} = \frac{\sqrt{\frac{\mu_r}{\epsilon_r}} - 1}{\sqrt{\frac{\mu_r}{\epsilon_r}} + 1} \tag{2.12}$$

$$T = exp(-j\omega\sqrt{\mu\epsilon}d) = exp[-j(\frac{\omega}{c})\sqrt{\mu_r\epsilon_r}d] \tag{2.13}$$

Equations (2.10) and (2.11) allow Γ and T to be derived by measuring $S_{11}(\omega)$ and $S_{21}(\omega)$. These quantities can then be used to calculate ϵ_r and μ_r [12].

When measuring $S_{11}(\omega)$ and $S_{21}(\omega)$, a sample length of $\lambda_g/4$ should be chosen to minimize uncertainties with ϵ_r and μ_r, where λ_g is the wavelength in the waveguide [12]. Additionally, the sample should not be larger than $\lambda_g/2$. Using the following equation, where λ_o is the wavelength in free space and λ_c is the cutoff wavelength of the guide, the sample length can be determined [12].

$$\lambda_g = Re\left(\frac{1}{\sqrt{(\frac{\epsilon_r\mu_r}{\lambda_o^2} - \frac{1}{\lambda_c^2})}}\right) \tag{2.14}$$

In determining the sample length it is assumed that a good estimate of ϵ_r and μ_r is available, which is not always the case. One such situation arises with foam. Foam is manufactured in many different weights, and the permittivity is a function of its weight. For expanded foam Jasik provides the following equation, Equation (2.15), to determine the permittivity where ρ is the density of the foam, ρ_o is the density of the unexpanded foam, and ϵ^o/ϵ_o is the relative dielectric constant of the unexpanded foam [13].

$$log\frac{\epsilon_r}{\epsilon_o} = \frac{\rho}{\rho_o} log\frac{\epsilon^o}{\epsilon_o} \tag{2.15}$$

2.2.2 Radar Cross Section. The Radar Cross Section, as defined by Knott, is a measure of power scattered in a given direction when a target is illuminated by an incident wave [15]. RCS is normalized to the power density of the incident wave at the target so that it does not depend on the distance of the target from the illumination source. The mathematical definition for RCS (σ) is given by:

$$\sigma = \lim_{r \to \infty} 4\pi r^2 \frac{|\ E^{scat}|^2}{|\ E^{inc}|^2} \tag{2.16}$$

where r is the distance from the radar to the object and E^{scat} and E^{inc} are the scattered and incident electric fields at the target [15].

An RCS compact range is a facility in which RCS measurements are accomplished to characterize the radar signature of an object. To achieve accurate results, three conditions must be met. First, the object must be in the far field to eliminate any distance dependencies. Second, the target is considered to be in free space so that the scattering phenomena comes solely from that target. Finally, the incident field is assumed to be planar [9]. To achieve this criteria, six methods are used: 1) the walls, floor, and ceiling are covered with a combination of pyramidal and wedge type absorber to reduce backscatter as well as proper shaping of the pedestal with appropriate absorber added; 2) vector background subtraction is used to reduce clutter; 3) hardware gating is used to isolate the scattered field to the area around the target; 4) software gating can sometimes be used to process out interactions between the target and target support; 5) pulse integration is used to reduce noise; 6) a large antenna/target separation is maintained or a reflector is used to simulate large distances [9].

In practice none of these conditions are met perfectly. Thus one must try and determine the impact of not meeting these conditions on the accuracy of the RCS measurements.

2.2.3 RCS Measurement Accuracy. The known accuracy of measured RCS data is mandatory for computer code validation. The definition of RCS assumes that the target is in the far-field, in free-space, and illuminated by a plane wave. These conditions are

approximated in a compact range. However, to the extent that these conditions are not met, the RCS measurement is in error.

In recent years a general methodology for characterizing this error using an RCS range error budget has been in work in a joint effort between the Department of Defense (DoD) Radar Cross Section Measurement Working Group (RCSMWG) and the Metrology Division of the National Institute of Standards and Technology (NIST) [6]. As part of the effort, Wittmann, Francis, Muth, and Lewis, have composed a list of sources of uncertainty in RCS measurements [21]. Additionally, they discussed methods for estimating their impact on RCS measurement errors.

The measurement of RCS, σ, can be quantified by a statement of uncertainty

$$\sigma = \sigma_0 \pm \Delta\sigma, \tag{2.17}$$

where $\Delta\sigma$ is the uncertainty. In error bound terms,

$$\sigma_0 + \Delta\sigma_+ > \sigma > \sigma_0 - \Delta\sigma_-, \tag{2.18}$$

where $\Delta\sigma_+$ and $\Delta\sigma_-$ may or may not be equal. When uncertainties are stated logarithmically,

$$\Delta\sigma_\pm(dB) = \pm 10log\left(1 \pm \frac{\Delta\sigma}{\sigma_0}\right), \tag{2.19}$$

the resulting uncertainties, $\Delta\sigma_\pm(dB)$, will not present symmetric bounds if they are symmetric in natural units. The nonlinear nature of Equation (2.19) must be considered when reporting uncertainties. For example, if $\Delta\sigma/\sigma_0 = 1$, then $\Delta\sigma_+(dB) \approx 3$, while $\Delta\sigma_-(dB) = -\infty$. Therefore, as $\Delta\sigma \to 0$, the following equation,

$$\Delta\sigma(dB) \approx 4.34\frac{\Delta\sigma}{\sigma_0} \tag{2.20}$$

linearly relates logarithmic uncertainty to relative uncertainty [21].

The following is a list of the uncertainties and their causes for monostatic target and calibration measurements [21].

2.2.3.1 Average Illumination. Average illumination refers to the non-uniformity of the plane wave over the target. A non-uniform plane wave is typically a result of a pointing error or deformities in the plane wave. For compact ranges, boresighting is not a problem. Deformities in the plane wave can result from imperfect antennas and/or reflectors. This uncertainty can be characterized by probing the plane wave or be removed in the calibraton process if the target zone is the size of the calibration target, or smaller.

2.2.3.2 Background-Target Interactions. Energy scattered from the target and then rescattered by the background, or vice versa, is a result of target/background interactions. To minimize this uncertainty gating is utilized. However, some error, mainly target/pylon interaction, remains and cannot be removed. This error is difficult to characterize because it is target/pylon dependent, but it can be minimized if proper consideration is taken in choosing a pylon.

2.2.3.3 Cross-Polarization. Cross-polarization error is a result of an antenna that is not perfectly polarized due to alignment errors or physical defects. Furthermore, cross-polarization uncertainties can occur if the target's cross-polarization response is large compared to the main polarization response, even if the antenna does not have any alignment or physical imperfections.

2.2.3.4 Drift. Drift uncertainty is a result of the instability in the radar over time. This uncertainty can be quantified by repeating measurements of the same target over an extended time period.

2.2.3.5 Frequency. This error source is the uncertainty in the RCS due to uncertainty in the frequency. Frequency uncertainty is a function of the quality of the equipment and the environmental conditions, thus making it fairly easy to control.

2.2.3.6 Integration. Uncertainty due to target motion during the measurement results in integration error. This error is generally an issue for large targets and can be controlled by slowing or stopping the target rotation rate.

2.2.3.7 I-Q Imbalance. An I-Q imbalance results when the measured amplitude is a function of input phase for the in-phase and quadrature responses of the receiving system. The uncertainty can be estimated by measuring the power as the input phase of the test signal is varied from 0 to 360 degrees [21].

2.2.3.8 Near Field. This source of uncertainty is due to ripple or taper in the incident plane wave. By definition, the RCS assumes that the target is illuminated by a plane wave. For compact ranges the plane wave is approximated due to the short range. This uncertainty can be characterized by probing the quiet zone, the region where the incident field is assumed planer.

2.2.3.9 Noise-Background. This error is a grouping of the uncertainty sources which contribute to the received signal whether or not the target is present. Basically, it is the sensitivity of the radar. Background subtraction and averaging can mitigate this uncertainty. According to [21], the observed residual noise-background is bounded by the worst-case estimate,

$$\Delta\sigma(dB) = -20log\left(1 - 10^{-log(S/N)}\right), \tag{2.21}$$

where S is the signal and N is the noise in relative units, not logarithmic units.

2.2.3.10 Nonlinearity. A nonlinear relationship between the receiver output and input causes this error. Nonlinearity uncertainty can be estimated by noting the deviation from linearity while using an attenuator to vary the test signal from a given reference level [21].

2.2.3.11 Range. Range uncertainty is caused by uncertainty in the distance from the antenna to the target. This error does not exist in compact ranges.

2.2.3.12 Target Orientation. Uncertainty in orientation or alignment of the target can produce the largest source of uncertainty, especially for large targets. This error can be minimized by properly aligning the target on the mount.

2.2.3.13 Overall Uncertainty of Calibration. Calibration error is error in the calibration process due to the previously listed error sources, plus the uncertainty in the calibration target geometry and the RCS prediction of that target. The potential for a large source of error which is difficult to quantify is the calibration process. According to [6], this uncertainty can be greatly reduced and quantified by using the double calibration method and choosing a squat cylinder as a calibration target.

The double calibration method, as the name implies, utilizes two separate and distinct calibration targets. The idea behind this method is that the second calibration target measurement is used to monitor the quality of the primary calibration measurement. The "exact" calculated primary calibration data can be compared with the "measured" primary calibration data using the following equation [6]:

$$\sigma(\omega,\theta) = 4\pi \mid \frac{E_{cal,primary}(\omega,\theta) - E_{cal,primary,bkg}(\omega,\theta)}{E_{cal,sec,meas}(\omega,\theta) - E_{cal,sec,bkg}(\omega,\theta)} \mid \cdot E_{cal,sec,exact}(\omega,\theta) \tag{2.22}$$

The most common calibration target is the sphere because it has an exact Mie series solution, is relatively easy to make, and its RCS is independent of orientation. However, there are some disadvantages to using a sphere. The scattering characteristics of a sphere can cause significant target-mount interaction errors, it is sensitive to manufacturing tolerances, and a sphere does not interface well with "rotator-pylon" RCS measurement supports [6]. A better choice for a calibration target is a squat cylinder. A squat cylinder is easier to manufacture to a given tolerance and greatly reduces the interaction between the target and support. However, it should be noted that "exact" solutions are more difficult to produce and the cylinder must be accurately aligned in the elevation plane [6].

2.2.3.14 Overall Uncertainty. The components of uncertainties, $\Delta\sigma_i$, can be combined using the root sum of squares (RSS) to determine the overall uncertainty, $\Delta\sigma$,

$$\frac{\Delta\sigma}{\sigma_o} = \sqrt{\sum_i \left(\frac{\Delta\sigma_i}{\Delta\sigma_o}\right)^2}. \tag{2.23}$$

Equation (2.23) uses relative, not logarithmic, uncertainty. To determine the relative uncertainty use Equation (2.19). Once $\left(\frac{\Delta\sigma}{\sigma_o}\right)$ has been determined, the bounds for logarithmic

Target Uncertainty	dB
Average Illumination	0.4
Background-Target Interactions	0.5
Cross Polarization	neg
Drift	neg
Frequency	neg
Integration	neg
IQ Imbalance	neg
Near Field	0.4
Noise-Background	0.7
Nonlinearity	0.2
Range	neg
Target Orientation	n.a.
Calibration Target	1.2
Overall Uncertainty (RSS)	1.5
	-2.3

Table 2.1 A sample summary of RCS uncertainties.

uncertainty can again be found from Equation (2.19). An example of overall uncertainty for a fictional RCS measurement is depicted in Table 2.1. An entry of "neg" indicates a negligible impact and "n.a." indicates that this source is not considered a factor.

2.3 Code Validation

The main purpose behind benchmarking targets is to validate computer programs. The following sections discuss RCS comparisons and introduce the code used in this research.

2.3.1 RCS Measurement Comparisons. RCS code predicted data can easily be validated by comparing the results to mathematical models, experimental data, and even well validated RCS programs. Comparing the results to experimental data is an excellent opportunity if the data already exists. Unfortunately, there has not been a high demand for the RCS of dielectrics in the past so very little experimental data exists. One of the few published papers measuring the RCS of dielectrics was accomplished by Gupta on dielectric straps [11]. He determined a strap size and material composition that minimized the RCS so the straps could be used to suspend other targets and not add appreciably

to their overall RCS. Gupta has provided a large amount of data in this area including RCS measurements for different strap lengths and widths, changes in polarization, various dielectric materials, and different angles of incidence.

2.3.2 Three Dimensional Radiation Condition Integral Equations (3D-RCIE). Accurate prediction of the RCS of targets by computation is a complex problem. While many methods have been developed, the most accurate software uses integral equations. The main approach to solve these equations has been the Method of Moment (MoM). This method converts the integral equations into a finite NxN matrix. The value of N is a function of the complexity of the target. The value of N for PEC targets is given by

$$N \approx 2\eta^2 \frac{A}{\lambda^2} \tag{2.24}$$

where A is the surface area of the target, λ is the wavelength, and η is the "meshing rate" or number of samples per linear wavelength [7]. As seen in equation (2.24), the size of N can quickly become very large. For this research the targets are not PECs making them penetrable by the incident field. Thus, the MoM formulation is often based upon volumetric, not surface integral equations, resulting in even larger values of N. Depending on the case, the solution may be out of reach for most computers and too time consuming for even the supercomputers.

3D-RCIE was developed to tackle this and other integral equation problems. 3D-RCIE is a system of integral equations which can be applied to the solution of electromagnetic boundary value problems. The following is a summary of the developement by Colby of the Radiation Condition Integral Equations (RCIE) [7].

To describe the electromagnetic scattering from a target and solve the resulting boundary value problem using integral equations, one must use a Green's function to express the scattered fields in terms of unspecified surface currents. The incident and scattered fields are combined in an equation representing the surface boundary conditions on the scatterer. The resulting integral equations are then solved for the unspecified

current. Basically, the resulting equations express the boundary conditions on the surface of the scatterer while satisfying the radiation condition using a Green's function.

The current formulation of the RCIE differs from the standard integral equations in several ways. First, a separation of field variables based on chiral field combinations is employed. Next, the RCIE are developed as a weak equivalent of the radiation condition. Finally, the explicit nature of the scatterer is incorporated by applying the local surface boundary conditions on the body.

The region exterior to the body consists of free space in which the E and H fields obey Maxwell equations.

$$\begin{aligned} \nabla \times \overline{H} &= ik\overline{E} \\ \nabla \times \overline{E} &= -ik\overline{H} \end{aligned} \tag{2.25}$$

Given one of the fields within a volume, one may construct the other from the curl of the given field. Equation (2.25) may be separated by introducing chiral or handed fields which are linear combinations of E and H. The chiral fields are defined by

$$\begin{aligned} \overline{F}^R &= \overline{H} + i\overline{E} \\ \overline{F}^L &= \overline{H} - i\overline{E} \end{aligned} \tag{2.26}$$

where R and L refer to the right and left-hand fields, respectively. To reduce the number of equations, α is introduced to denote either R or L. From (2.25) and (2.26) the F-fields are seen to obey

$$\nabla \times \overline{F}^\alpha = \pm k\overline{F}^\alpha \tag{2.27}$$

Equation (2.27) implies that the right and left-hand chiral fields are dynamically decoupled in free space and propagate independently. This separation has important implications concerning the independence and completeness of the derived relations which are obscured if developed in terms of the usual coupled E and H-fields.

Consider the scattering body surrounded by a large spherical surface centered on the body, Figure 2.2, where S_b is the surface of the scatterer, S_o is the surface of a large sphere

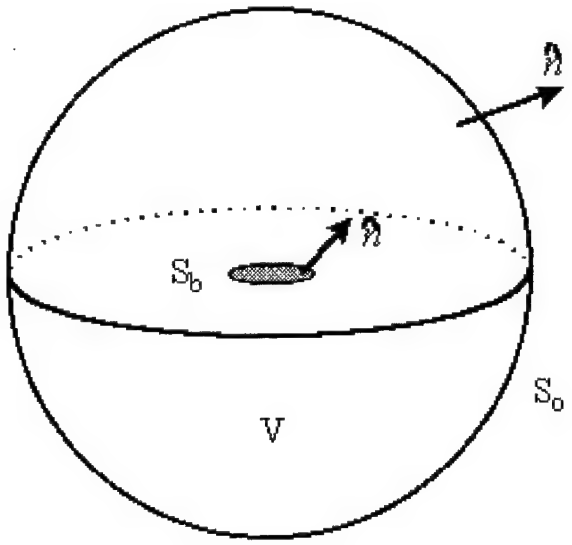

Figure 2.2 The volume exterior to the scattering body is bounded by the surface of the scatterer, S_b, and a large sphere, S_o, centered on the scatterer.

surrounding the scattering body, and V is the volume of the sphere. At each point on the surface the scattered wave is approximated by a planar wave front and the outward going radiation condition takes the form

$$\begin{aligned} \hat{n} \times \overline{E} &= \overline{H} \\ \hat{n} \times \overline{H} &= -\overline{E} \end{aligned} \tag{2.28}$$

where $\hat{n}$ is the outward directed normal. Like Equation (2.25), the radiation condition couples the E and H-fields. Using the chiral fields the above conditions separate into independent constraints for each chiral field

$$\hat{n} \times \overline{F}^{\alpha} = \pm i\overline{F}^{\alpha} \tag{2.29}$$

One consequence of Equation (2.29) is that all outward going right or left-hand fields share the same vector direction on the surface. Therefore, any two outward going fields of the same handedness will obey

$$(\overline{F}_1^{\alpha} \times \overline{F}_2^{\alpha}) \cdot \hat{n} = 0 = (\hat{n} \times \overline{F}_1^{\alpha}) \cdot \overline{F}_2^{\alpha} = \pm i\overline{F}_1^{\alpha} \cdot \overline{F}_2^{\alpha} \tag{2.30}$$

Equation (2.30) provides an alternative to Equation (2.29) in that if $\overline{F}_1^\alpha$ is known to be outward going at a point then Equation (2.30) holds only if the $\overline{F}_2^\alpha$ is also outward going. For any two solutions of Equation (2.27) we have from the standard vector identities that

$$\nabla \cdot (\overline{F}_1^\alpha \times \overline{F}_2^\alpha) = 0 \tag{2.31}$$

therefore, the cross product of any two F-fields of the same handedness yields a vector field with zero divergence. Using the divergence theorem and understanding from Equation (2.31) that the volume integral vanishes and the surface of the volume, V, is the union of S_b and S_o, it follows that

$$\int\int_{S_b} (\overline{F}_1^\alpha \times \overline{F}_2^\alpha) \cdot \hat{n} dA = \int\int_{S_o} (\overline{F}_1^\alpha \times \overline{F}_2^\alpha) \cdot \hat{n} dA \tag{2.32}$$

This expression, Equation (2.32), is the relation sought which connects the left-hand sides of Equation (2.30) to the integrals over the tangent fields on S_b.

The prevalence of the above surface integrals motivates the use of an inner product notation as defined by

$$\langle F_1 | F_2 \rangle = \int\int_{S_b} (\overline{F}_1 \times \overline{F}_2) \cdot \hat{n} dA \tag{2.33}$$

Unlike the usual inner products, $\langle | \rangle$ is skew-symmetric. That is, a matrix $((a_{ij}))$ is skew-symmetric if $a_{ij} = -a_{ij}$ [17].

From Equations (2.30) and (2.32) we obtain the result; given any two chiral fields, F_1^α and F_2^α, which are solutions of the field Equation (2.27) in the volume and obey the radiation condition will satisfy

$$\langle F_1^\alpha | F_2^\alpha \rangle = 0 \tag{2.34}$$

Equation (2.34) provides a weak or integrated form of the radiation condition expressed by Equation (2.30). Consider two sets, Λ^α, of testing fields (one right-handed and one left-handed) as those solutions of Equation (2.27) on V which obey the radiation condition. These sets each form linear spaces in that the sum of any two members is also a member. By construction the inner product of any two members of Λ^α vanishes by the above argument. One then arrives at the following definition for a weak radiation condition: A field

distribution, $\overline{F}$, on the surface, S_b, is said to obey the weak α-handed radiation condition if $\langle T^\alpha | F \rangle = 0$ for all $T^\alpha \in \Lambda^\alpha$.

If the total chiral fields exterior to the scattering body as the sum of incident and scattered fields are considered, a more useful form of this weak radiation condition is

$$\overline{F}^\alpha = \overline{F}^\alpha_{Incident} + \overline{F}^\alpha_{Scattered} \tag{2.35}$$

Since the scattered chiral fields are members of the testing field sets, Λ^α, the inner product with any testing field T^α must vanish

$$\langle T^\alpha | F^\alpha_{Scattered} \rangle = 0 \tag{2.36}$$

Taking the inner product of a testing field T^α with both sides of Equation (2.35) results in the desired form

$$\begin{aligned} \langle T^R | F^R \rangle &= \langle T^R | F^R_{Incident} \rangle \\ \langle T^L | F^L \rangle &= \langle T^L | F^L_{Incident} \rangle \end{aligned} \tag{2.37}$$

Equation (2.37) is the Radiation Condition Integral Equations. The RCIE refer only to the radiation condition and are independent of the boundary conditions on the surface of the scatterer. Also, Equation (2.37) each refer to dynamically independent fields and are completely independent requirements on the tangent fields. Much more detail on this development can be found in [7].

This simplified approach using the RCIE is discussed by Colby:

> The RCIE approach simplifies many aspects in numerical treatment of electromagnetic scattering problems. For example, the scattering equations obtained for perfect conductors, Equation (2.38), involve only integrals of the total tangent H-field times the testing fields with no derivatives of unspecified H-field distribution appearing. The absence of derivative terms implies that H-field (current) continuity is not required in the selection of the H-field basis functions. This is counter to the usual situation with the Electric Field Integral Equations (EFIE) or dyadic Green's functions for which continuity of the longitudinal current components is employed. Relaxing the current continuity requirement permits basis function meshes with elements that need not

share common nodes with neighboring elements. This essentially eliminates the "meshing" problem associated with overlapping basis functions such as roof-tops, which even for just surface modeling remains nontrivial [7].

$$\begin{aligned} \langle T^R | H \rangle &= \langle T^R | F^R_{Incident} \rangle \\ \langle T^L | H \rangle &= \langle T^L | F^L_{Incident} \rangle \end{aligned} \tag{2.38}$$

Benefits of RCIE are that it is numerically more stable than other integral equations used to date. 3D-RCIE also uses a pulse basis to reduce the meshing, η, of a complex target. Meshing is the way in which a geometry is described for a computer algorithm. As seen in Equation (2.24), λ is squared so any reduction in this area can greatly decrease the size of N. Additionally, 3D-RCIE uses the Block Generalized Minimal Residual (BGMR) algorithm to solve the system matrix. BGMR has reduced the solution time over other algorithms by ten to twenty percent [7].

Several problems have been noted using 3D-RCIE. The pulse basis function slows down for large meshing rates leading to larger system matrices. Also, the pulse basis has trouble modeling traveling wave contributions. This can be a serious problem for certain geometries. Work is continuing to improve in these areas.

III. Methodology

The previous chapter provided the knowledge to understand the importance of composition and shape of benchmark targets, the theory behind RCS and material property characterization, and the mathematical description of electromagnetic scattering. Chapter 3 now applies that theory to create an RCS database and use it to validate an RCS prediction code. The first section discusses the targets and materials chosen for the database. The following section describes the measurement of the materials and the RCS along with the accuracy of the RCS measurements. The final section describes the use of the validation code.

3.1 Targets

The following section describes the benchmark targets and materials chosen for this research. A brief description of each target and target material is included along with the motivation behind its choice as a benchmark target. Also, a brief description of the target fabrication process is provided.

3.1.1 Target Shapes. The targets selected were chosen to test program performance on a variety of problematic scattering mechanisms. Additionally, some of the shapes were chosen and scaled to exact dimensions of already published targets for comparison purposes. It should be noted, however, that the geometries were chosen as PEC scatters, thus, a low dielectric penetrable material may or may not exhibit the same scattering phenomena. The test objects fabricated for this research include two cubes, a sphere, an ogive, a mini-arrow, a conesphere, and a conesphere with a gap. Note that all dimensions are given in inches.

3.1.1.1 Small Cube. The cube is a good example of a non-BOR target. It provides 6 flat surface areas to test edge scattering for a flat faceted body. The cube is also composed of eight corners which act as corner reflectors for a penetrable body. The flat surfaces provide the opportunity to easily apply r-card. The cube is designed to be 1.181 inches per side (Figure 3.1 (a)). This length was selected to match one (1) wavelength

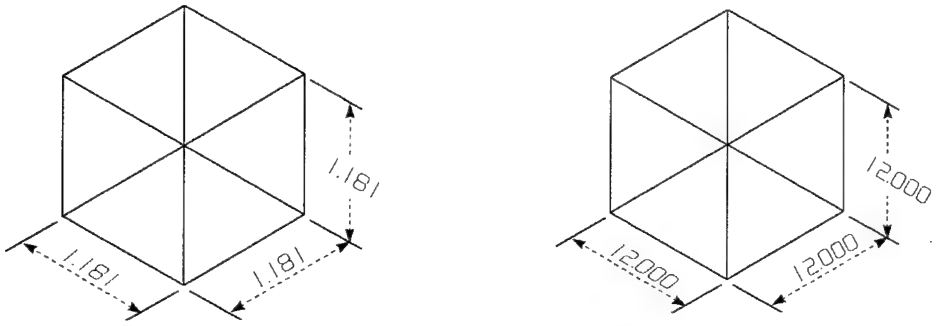

(a). (b).

Figure 3.1 The desired dimensions for the small cubes (a) and the large cubes (b).

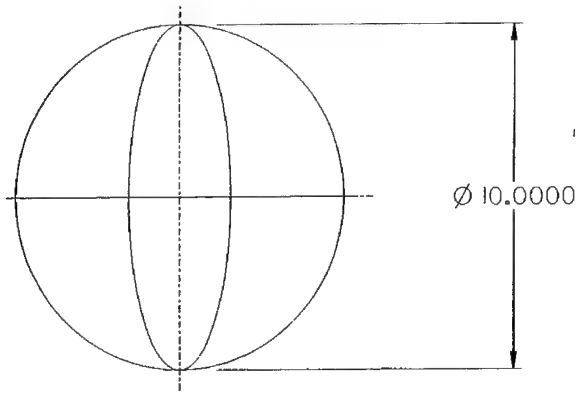

Figure 3.2 The desired dimensions of the sphere.

at the middle frequency, 10 GHz. This will allow the code to be tested below and in the resonant region for the same target.

3.1.1.2 Large Cube. This target exhibits the same properties as the small cube, except it is 12 inches on a side (Figure 3.1 (b)). This length is the largest the available materials would allow.

3.1.1.3 Sphere. The sphere is a sound target because of its traveling and creeping wave phenomena. Additionally, the Mie series also provides an exact solution. Finally, the low dielectric material will induce internally reflected energy testing spherical cavity effects. The sphere, as seen in Figure 3.2, is 10 inches in diameter.

3.1.1.4 Ogive. The ogive provides a geometry that has a large dynamic range dependent upon looking broadside or down the axis of rotation. Also, a large dynamic

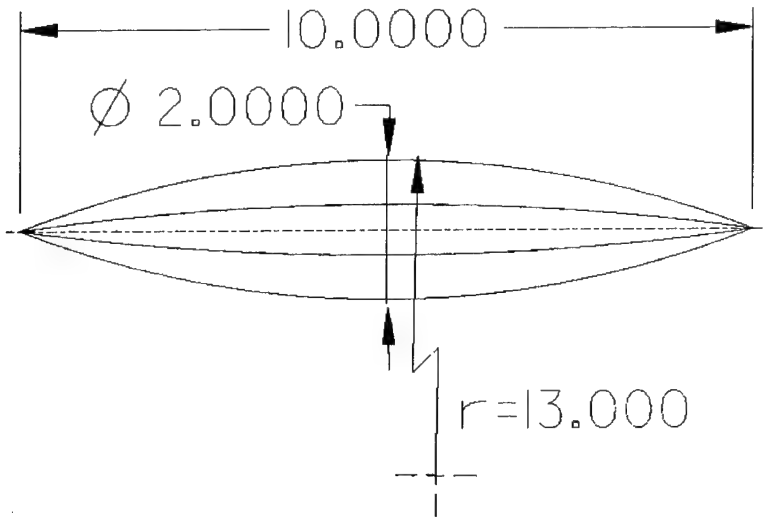

Figure 3.3 The desired dimensions of the ogive.

range exists between the two polarizations. The two sharp points at each end of the target have posed difficulty for some codes. The ogive used in this research is modeled after the PEC ogive measured by Woo [22] which has a 1 inch diameter, 10 inch length, and a half angle of 22.62 degrees. See Figure 3.3.

3.1.1.5 Mini-arrow. The flat faceted design of the mini-arrow has proven to be a very low RCS target nose on. The penetrable material will provide the opportunity for the incident energy to be internally reflected off one or more of the five flat surfaces or corners. The mini-arrow, as seen in Figure 3.4 is almost 10 inches long, 1.5 inches high, and 2.5 inches wide.

3.1.1.6 Cone-sphere. The cone-sphere is a classical RCS target and is well documented. This target provides a sensitive test for the program to model low RCS objects. The tip has also proven to be problematic for some codes to model. The dimensions of the cone-sphere are also modeled after Woo [22] and are found in Figure 3.5.

3.1.1.7 Cone-sphere with a gap. This target incorporates the same features as the cone-sphere, except the added small gap provides a sensitive test of the code's ability

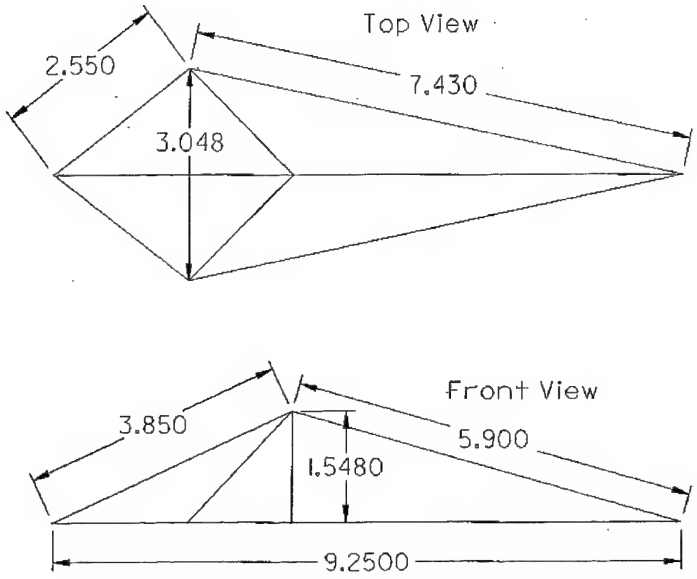

Figure 3.4 The desired dimensions of the mini-arrow.

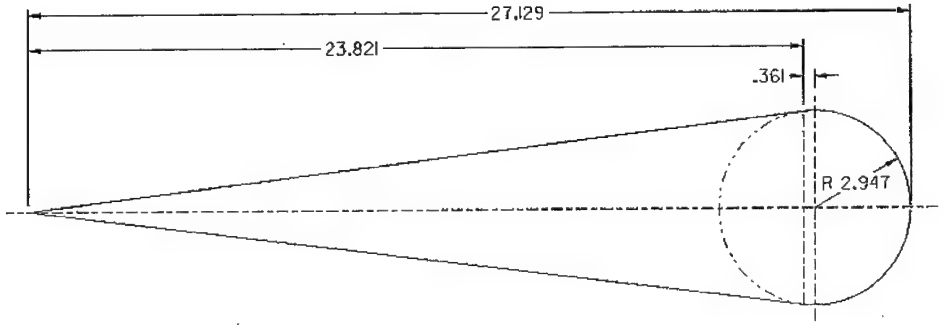

Figure 3.5 The desired dimensions of the conesphere.

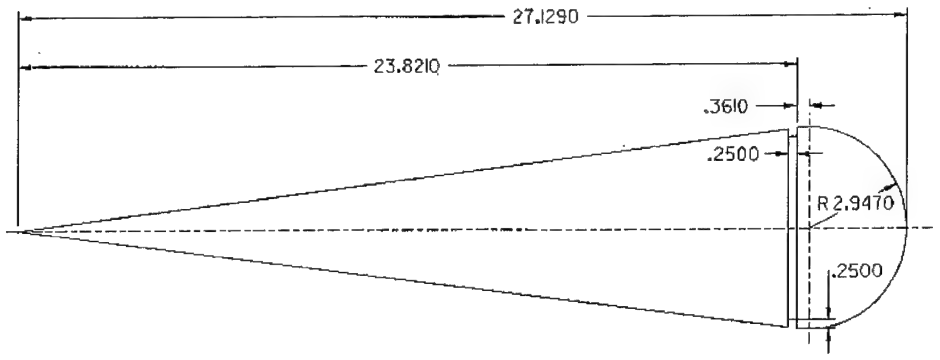

Figure 3.6 The desired dimensions of the conesphere with a gap.

to model small features on a larger target. The 0.25 inch wide and 0.25 inch deep gap is added between the intersection of the cone and sphere, as seen in Figure 3.6.

3.1.2 Materials. The two low dielectric materials chosen for this research were polyethylene and polyurethane.

3.1.2.1 Polyethylene. Polyethylene is a low dielectric polymer with a dielectric constant around 2.3 [20]. The material is fairly easy to work with, as far as polymers go. The material proved to be rather soft and is very susceptible to temperature changes. A big advantage of this material compared to others of similar composition and material properties, e.g. Teflon, was the ability to purchase it in large blocks which allowed the appropriate size of the targets to be fabricated. However, some manufacturing deformities in the form of air bubbles were found due to the large size of material required. For this research the materials are assumed to be homogeneous. If the test data is perturbed due to an inhomogeneity in the material, it will be noted.

3.1.2.2 Polyurethane. Polyurethane is a very low dielectric foam with a dielectric constant close to one. The material acquired for this research was a large sheet, 4x8x1 feet, of 3 lbs/ft^3 polyurethane foam. The dielectric constant, determined in Section 3.2.1, is about 1.03. Unfortunately, the foam acquired was not rigid so the goemetries manufactured were limited to the cubes.

3.1.3 Target Fabrication. The targets were fabricated by the AFIT Model Shop. The fabrication process involved the use of saws, milling machines, and lathes.

3.1.3.1 Small Cube. The polyethylene cube was fabricated with a saw and milling machine. The saw cut the material to the approximate size and the milling machine completed the process with a smooth, flat surface. The polyurethane was cut using a band saw because it was not a rigid material, thus reducing the accuracy of its dimensions.

3.1.3.2 Large Cube. The large cubes were fabricated in the same manner as the small cubes.

3.1.3.3 Sphere. The polyethylene sphere was made using the lathe. The lathe attached to two knobs at opposite ends of the material. As the material was rotated, the blade cut the material as it followed a template of the appropriate radius of curvature. To achieve a very fine finish, the depth and width of the cuts were reduced. After the sphere was complete less the protruding knobs, an aluminum collar was devised to hold the sphere so the lathe could rotate the sphere on the other axis to remove the knobs. A sphere from the polyurethane could not be fabricated.

3.1.3.4 Ogive. The ogive was produced using the lathe. The material was first secured by the lathe at opposite ends and rotated. The blade followed a template to produce the required shape of the body. As the ogive started to take shape, one of the ends was released so the material could be cut to a point. After the desired shape and finish was complete, an aluminum collar was fabricated to hold the ogive. The lathe attached to the collar and the other point was cut. An ogive from the polyurethane could not be fabricated.

3.1.3.5 Mini-arrow. The mini-arrow was completed using the milling machine. A block of material slightly larger in length and width and quite a bit larger in height was cut with a saw. The extra material at the base was secured so the mill could cut the top, or faceted face, of the mini-arrow. Additionally, a larger block of material had the top face of the mini-arrow cut out of it. The mini-arrow was then bonded into

the larger block, which was secured so the flat bottom of the shape could be milled. A mini-arrow from the polyurethane could not be fabricated.

3.1.3.6 Conesphere. The conesphere was fabricated using the lathe. The material was held at opposite ends and a taper attachment was utilized as the lathe cut the cone portion. As the desired shape was approached, the cone end of the material was released to allow the point to be cut. After the cone section was complete, an aluminum collar was fabricated so the lathe could hold the shape. The sphere segment was then cut as the blade followed a template. A polyurethane cone-sphere could not be fabricated.

3.1.3.7 Conesphere with a gap. The conesphere with a gap was fabricated in the same manner as the cone-sphere. The gap was cut using the lathe after the shape was complete. A polyurethane geometry could not be made.

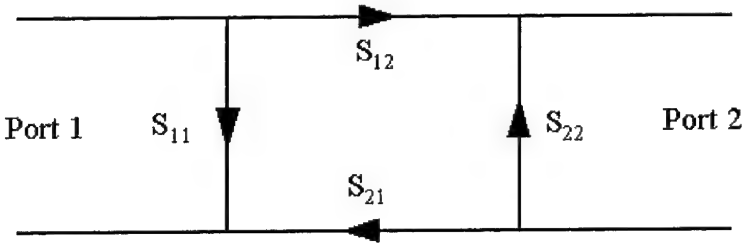

Figure 3.7 S-Parameter Definition for a Two-Port Network.

3.2 Measurements

3.2.1 Material Measurements. The material characteristics of the polyethylene and polyurethane were measured using rectangular waveguides. The waveguide method simplified the fabrication of material test samples. The measurements were performed using separate specimens of each material and an X-band waveguide. Because of the X-band limitations, measurements were accomplished for an 8-12 GHz range in steps of 10 MHz.

The primary piece of equipment for the measurement set-up was the network analyzer. The analyzer measures the parameters of a network consisting of a length of waveguide containing the material sample by comparing the incident wave with the reflected wave. The network analyzer displays the measured data in the form of the complex scattering matrix parameters S_{11} and S_{21} which are defined in Figure 3.7 for a two-port device. From the S-parameter data, the material complex relative permittivity (ϵ_r) and relative permeability (μ_r) can be calculated.

The rectangular waveguide set-up utilized was available from WL/XPN, Wright Laboratories, Signature Technology Directorate, Wright-Patterson AFB, OH. This set-up was a full two-port configuration capable of measuring S_{11} and S_{21}. This set-up consisted of an HP 8510C network analyzer, an HP 8515A S-Parameter Test Set, waveguide sections and waveguide adapters. The HP 8510C measures 401 discrete frequencies between 8 and 12 GHz, averaging 128 measurements at each step. To determine the permeability and permittivity, the data was transferred from the HP 8510C to an external computer and calculated from the Equations (2.1) through (2.4) using a Matlab program.

For the polyethylene sample the guide wavelength can be determined from Equation (2.14) using ϵ_r and μ_r given by Von Hippel [20] to be 2.3 and 1.0, respectively, and allowing the cutoff wavelength to be twice the waveguide width, or 1.8 inches. At 12 GHz, or the smallest wavelength, the maximum sample length, $\lambda_g/2$, is 0.352 inches. At the middle frequency, 10 GHz, $\lambda_g/4$ is 0.219 inches. A sample size of 0.200 inches was chosen.

In determining the sample length of the polyurethane, an estimate of the permittivity first had to be found. From Knott, the dielectric constant for 70.0 lbs/ft^3 polyurethane is 2.06 [15]. Therefore, from Equation (2.15) the relative dielectric constant for the 3 lbs/ft^3 expanded foam is 1.03. At 12 GHz the maximum sample length of $\lambda_g/2$ is 0.582 inches. At the middle frequency, 10 GHz, $\lambda_g/4$ is 0.381 inches. A sample size of 0.300 inches was chosen.

To insure accurate and representative data for the materials, several procedures were followed. Each specimen was measured five times to preclude a poor measurement from biasing data. To insure that the samples were representative, two polyethylene samples and three polyurethane samples were extracted from the bulk material and measured. Three polyurethane samples were chosen to provide additional data due to the difficulty in fabricating precise sample sizes for this material. Additionally, the samples were removed from the waveguide between each measurement set and a new calibration set was run to allow a certain randomness in each measurement as would be expected from slight misalignment errors.

3.2.2 RCS Measurements. To evaluate the accuracy of the RCS code predictions, the error sources in the RCS measurement data must be minimal and well characterized. The RCS measurements were accomplished at Wright Laboratory's Multispectral Measurement Facility (WL/XPN), Wright-Patterson AFB, OH. This advanced compact RCS/antenna measurement range is one of the premier facilities of its kind in the world.

The WL/XPN Compact RCS/Antenna Range was designed to develop the technology of advanced RCS measurements and to perform one-of-a-kind RCS and antenna measurements. The compact range is a Gregorian dual reflector/dual chamber design. The main reflector is a full blended, rolled edge parabolic design. Its focus is also one of

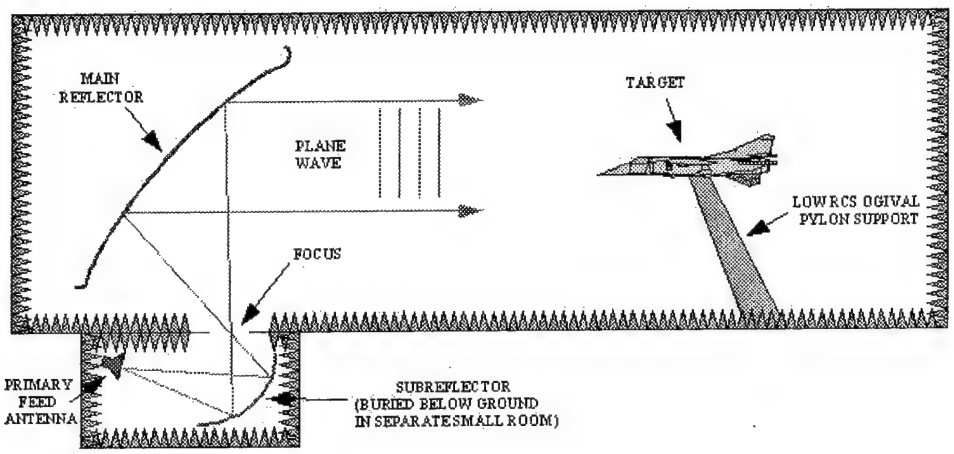

Figure 3.8 The WL/XPN compact RCS/Antenna range design.

the foci of the serrated edge, elliptical subreflector located in a separate anechoic chamber beneath the main chamber floor. With its large focal length and low stray signal level, this dual reflector design prevents blockage of the main collimated beam and achieves extremely pure plane wave properties over a large target zone. The WL/XPN compact RCS/Antenna range design is depicted in Figure 3.8.

The WL/XPN Advanced Compact Range operates a Lintek 5000 radar system with continuous frequency coverage from 0.8-18.0 GHz and 26.0-36.0 GHz, each using a single antenna. The radar system's capabilities include a pulsed IF or pulsed CW mode, dual receive channels, and variable integrations, which allows a trade off of speed versus sensitivity. A typical 0.8-18.0GHz scan with 10 MHz increments at 1024 integrations takes approximately 1 second.

Additional information for the WL/XPN Compact RCS/Antenna Range is listed below and can be found at their web site, *http://www.wl.wpafb.af.mil/mmf/*:

- Room Size: 96 (length) $\times$ 59 (width) $\times$ 45 (height) feet
- Main Reflector: 38 $\times$ 38 feet, parabolic
- Sub-Reflector: 19 $\times$ 10 feet, ellipsoidal
- Quiet Zone Size: 20 (wide) $\times$ 15 (height) $\times$ 25 (length) feet
- Amplitude Ripple: $<$ 0.2 dB

- Amplitude Taper: < 0.25 dB
- Cross Polarization Level: < -35 to -40 dB
- Temperature: 70 degrees ± 1.5 degree Fahrenheit
- Polarizations: H, VV, HV, VH and combinations (RCP, LCP).

For this research, the targets were measured from 2 to 18 GHz, in 20 MHz increments, in both polarizations, and from 0 to 360 degrees, in 0.5 degree increments, in azimuth.

3.2.3 RCS Measurement Uncertainty. As discussed in Chapter 2, there are numerous uncertainties that can cause error in an RCS measurement. The WL/XPN Compact RCS/Antenna Range has accomplished detailed analysis to characterize the range and utilizes various techniques to minimize error. The following addresses each uncertainty component as it concerns the measurements for this thesis accomplished at WL/XPN. A large majority of these areas were addressed in an extensive range characterization effort [14].

3.2.3.1 Average Illumination. This compact range uses a Gregorian dual reflector/dual chamber design where the main reflector is a full blended, rolled edge parabolic design. This design achieves extremely pure plane wave properties over a large zone (15 by 20 feet). However, very slight deformities are present in the vertical axis. The calibration cylinder utilized for these measurements is approximately 9 inches in diameter and 4 inches in height. Any deformities in this target zone are removed in the calibration process, which includes all but the sphere and two large cubes for this target set. Any uncertainty for the two large cubes and sphere due to average illumination uncertainty is assumed minimal.

3.2.3.2 Background-Target Interactions. This area is extremely difficult to quantify because it is target/pylon dependent. One method used to determine this uncertainty is to transform the data from the frequency to the time domain. By studying the transformed data, the returns caused by interactions between the target and mount may be identified. Once the unwanted returns are identified, each return can be transformed

back to the frequency domain and used as uncertainty. For the target set used in this research, this method could not be used because the interactions could not be identified. The targets are made of penetrable material causing numerous returns to be delayed in time, thus masking the returns caused by interactions. Therefore, an error contribution due to target-background interactions of 0.1 dB will be carried for each target. This is a very general error contribution that the range carries [14].

3.2.3.3 Cross-Polarization. Cross polarization response is approximately 35 dB down from the main polarization. For this target set, it is assumed that cross polarization response is negligible.

3.2.3.4 Drift. Studies of radar drift for the WL/XPN range radar over several days have shown that the drift is very small. This is due in part to the quality of the Lintek 5000 radar system and the temperature control, 70 degrees F $\pm$1.5 degrees F, of the range and control room. The longest measurement for this thesis is only two hours reducing this error to very low values. The drift for a measurement less than one hour is 0.08 dB [14].

3.2.3.5 Frequency. For this radar system the long term frequency stability is less than 1×10^{-10} Hz. Furthermore, the radar acquisition code measures and calibrates the radar to the specific operating frequencies. Frequency uncertainty is very small and is calibrated out, if present at all [14].

3.2.3.6 Integration. Because of the small size of the targets and the slow rotation rate, an hour or more per 360 degree rotation, the movement of the target in relation to the radar is very slow. More specifically, the largest target for this research in length is the conesphere. At its furthest point from the center of rotation, the conesphere will move only 1.53×10^{-4} inches per frequency step! Thus, uncertainty due to target motion is negligible.

3.2.3.7 I-Q Imbalance. Any error caused by an I-Q imbalance is included in the calibration data.

3.2.3.8 Near Field. This compact range uses a Gregorian dual reflector/dual chamber design where the main reflector is a full blended, rolled edge parabolic design. This design achieves extremely pure plane wave properties over a large zone (15 by 20 feet). Moreover, the calibration cylinder utilized for these measurements is approximately 9 inches in diameter and 4 inches in height. Any deformities in this target zone are removed in the calibration process, which includes all but the sphere, two large cubes, and conespheres for this target set. Any uncertainty for these targets due to near field uncertainty is assumed minimal and not a concern.

3.2.3.9 Noise-Background. The uncertainty due to noise-background can be determined by Equation (2.21). For this range, the noise, N, is measured as a function of frequency. Furthermore, the signal, S, is measured as a function of frequency and azimuth angle per target. Therefore, it would be inappropriate to assign one value of uncertainty for each target, frequency, and azimuth angle. The noise-background uncertainty is provided in Chapter 4, along with the other measured results.

3.2.3.10 Nonlinearity. For this radar system, the radar output and input are linear to the noise floor over the dynamic range. The dynamic range of the system is approximately 80 dB. For targets above this range, attenuation is added raising the noise floor and maintaining the dynamic range. Uncertainty due to nonlinearity is not a concern.

3.2.3.11 Range. During the calibration process, the range is referenced to the calibration standard eliminating this uncertainty.

3.2.3.12 Target Orientation. Vertical alignment is accomplished with high precision using a digital meter. Alignment in the azmuthal plane can be done, if needed, after the measurement is completed by shifting the data. Target orientation is not a significant contribution of uncertainty for this target set.

3.2.3.13 Overall Uncertainty of Calibration. The overall uncertainty for the calibration is calculated as a function of frequency. The data is a comparison of the resulting RCS from the double calibration procedure with the "exact" calibration target

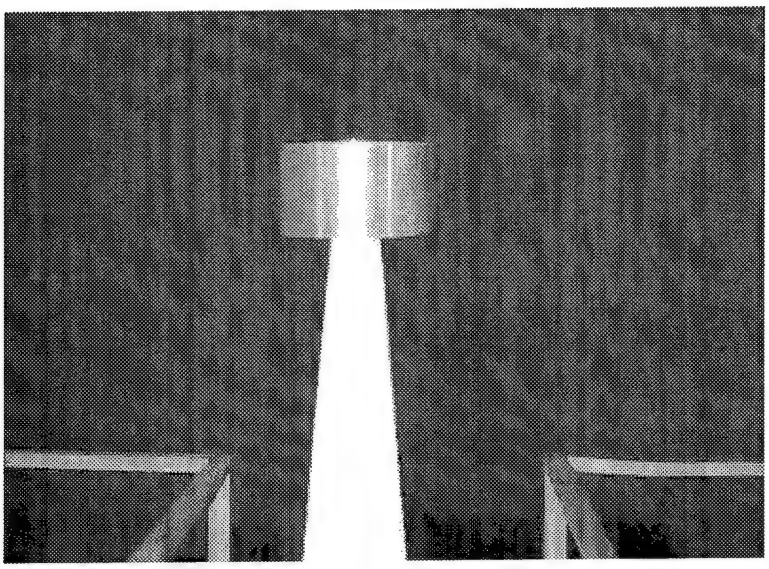

Figure 3.9 The 7.5 inch diameter and 3.5 inch tall squat cylinder is mounted for a calibration measurement.

solution. The "exact" solutions for the calibration targets, squat cylinders, were calculated at each frequency step using the CICERO Moment Method body of revolution (BOR) code. A squat cylinder mounted for a calibration measurement is pictured in Figure 3.9. After the double calibration is complete, a comparison of the "exact" vs. the "measured" data is produced. From this data the minimum uncertainty at each frequency step can be determined. The uncertainty for the calibration is provided in Chapter 4.

3.2.3.14 Overall Uncertainty. The overall uncertainty for this target set can be calculated using Equation (2.23). Table 3.1 is a listing of uncertainty components and their values as it applies to this research. Two uncertainty components, noise-background and calibration, will be calculated in the following chapter.

Target Uncertainty	dB
Average Illumination	neg
Background-Target Interactions	0.1
Cross Polarization	neg
Drift	0.08
Frequency	neg
Integration	neg
IQ Imbalance	neg
Near Field	neg
Noise-Background	chap 4
Nonlinearity	neg
Range	neg
Target Orientation	neg
Calibration Target	chap 4

Table 3.1 A summary of RCS uncertainties.

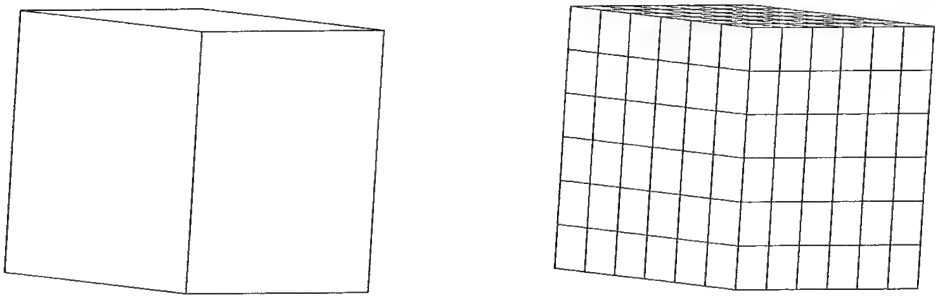

(a). (b).

Figure 3.10 The PostScript output from Mesh for a Small Cube of a coarse mesh (a) and a fine mesh (b).

3.3 Code Validation

3.3.1 3D-RCIE. 3D-RCIE is composed of the programs MESH, PULSE2, LUFACTOR, and BLGMRP. These four programs collectively implement a numerical matrix solution to the RCIE for scattering of a plane wave from a body, as discussed in Chapter 2. MESH provides the ability to program the target surface into the desired PULSE2 geometry input file. PULSE2 produces the matrix form of the RCIE. This system of equations is then solved by either LUFACTOR or BLGMRP. PULSE2 is then used again to produce the RCS from this solution [8]. More detail on the RCIE theory and the code operation can be found in the Final Report [7] and the User's Manual [8].

3.3.1.1 MESH. To calculate the RCS of a target using PULSE2 requires the target geometry to be described in terms of bicubic patches. A bicubic patch is specified by a list of 16 points or x, y, z values smoothly interpolated to form a patch surface. Encompassed in a patch is data not only providing geometry coordinates, but also boundary conditions. To efficiently produce patch data in the appropriate form, the MESH utility was devised. MESH combines several geometry generation, mesh refinement, and plotting utilities into one package [8].

There are three steps to produce a MESH output. First, a coarse mesh is developed in the MESH language (Figure 3.10(a)). This provides a model of the target geometry in terms of a relatively small number of patches. The second step is to visually check the

uniformity of the coarse mesh in the PostScript output. This can also be augmented by using the command "check". "Check" will provide in the output file the total surface area and the volume of the target looking in the x, y, and z axes. The volumes should all be positive, equal numbers. The final step is to subdivide the coarse mesh into a fine mesh, Figure 3.10(b), which is then used by PULSE2. The size of the fine mesh depends on the number of points per wavelength desired.

3.3.1.2 PULSE2. The PULSE2 program computes both the matrix form of the RCIE from the MESH output and the RCS of the target from the matrix solution. Two files containing the system matrix and the excitation vectors for each target are first calculated by PULSE2. The system matrix is comprised of complex numbers which correspond to the moment method impedance matrix elements. The size of the matrix file is given in terms of the number of patches, N_p, by $2N_p(2N_p + 1)$. The right-hand-side vector file size contains $2N_aN_p$ complex number, where N_a is the number of illumination angles.

After the solution vectors are computed, PULSE2 is then utilized to calculate the RCS. The RCS is calculated at each view angle in terms of magnitude and phase. PULSE2 also calculates both horizontal and vertical polarizations.

3.3.1.3 LUFACTOR. LUFACTOR computes the solutions to the standard problem

$$Ax = b \tag{3.1}$$

where A is a general square matrix of complex numbers of rank N, b is a right-hand-side excitation vector, and x is a solution vector from which the surface H-fields are computed. LUFACTOR is based on the LINPACK routines CGECO and CGESL which LU factors the matrix A and then back solves for each x given the corresponding b [8]. The main advantage of this program is that it does not make any approximations, thus providing the exact solution to Equation (3.1) if one exists. The disadvantages of LUFACTOR are the run time and storage capacity of the computer. Complete LU factorization takes time

of order N^3 to complete and order N^2 to solve [8]. This program also stores the entire matrix in the main memory which can also be a problem.

3.3.1.4 BLGMRP. Block Generalized Minimal Residual (BLGMRP) provides an iterative solution for Equation (3.1). Iterative solvers are not "exact" like the LU factoring solvers. This provides the potential for faster run times. However, BLGMRP can have problems solving some matrices. BLGMRP also has trouble converging when basis function patch sizes on the feature were 5 to 10 times smaller than neighboring basis function patches. Thus, users are cautioned by Colby [8] when using BLGMRP.

IV. Results and Analysis

This chapter presents the measured and simulated data collected in this research. It consists of three sections. The first section presents the targets and their precise dimensions. The second section is comprised of the measured material parameters, the RCS measurement error, and the measured RCS data. The final section presents the simulated RCS data and draws comparisons to the measured values. Complete sets of data not presented in this chapter are located in the appendices due to the large volume of data acquired during this research.

4.1 Targets

The fabrication of the targets was a nontrivial task. Difficulties were encountered with both the shaping of the targets and their material compositions resulting in limited precision. The polyethylene is a fairly good material to machine, but it was quite susceptible to temperature changes and compression. The polyurethane is not a rigid material so its uses were limited to the cubes. The following sections present the actual dimensions of the targets along with their tolerances. Each of the targets was measured numerous times using a micrometer. The dimensions were determined by averaging the measurements. The tolerances were then found by calculating the largest difference between each measurement and the averaged measurement.

4.1.1 Target Shapes.

4.1.1.1 Small Cube - Polyethylene. The polyethylene cube was the easiest target to make as is reflected in its accuracy. The cube's measurements are shown in Figure 4.1 (a) and a picture of the cube is located in Figure 4.2. The error is ± 0.002 inches.

4.1.1.2 Small Cube - Polyurethane. The small polyurethane cube shape could only be made using a band saw and not a milling machine due to the material. This is reflected in the large error ± 0.04 inches. The dimensions of the cube are given in Figure 4.1 (b).

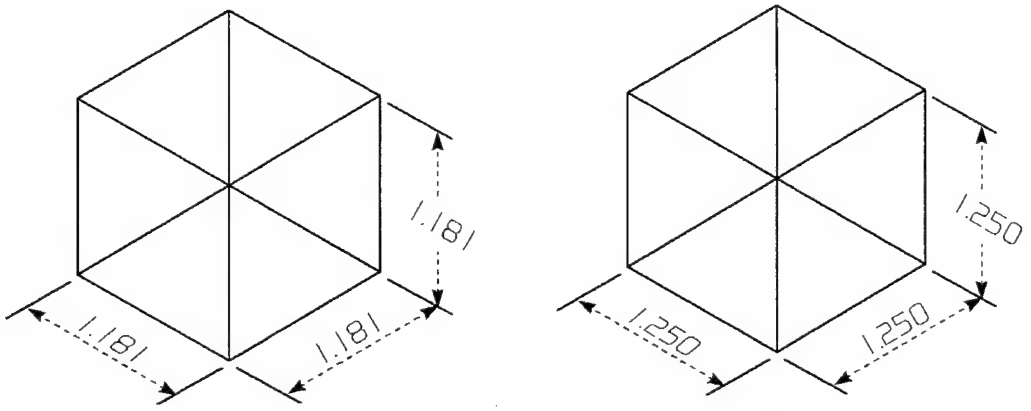

(a). (b).

Figure 4.1 The dimensions for the small cubes composed of polyethylene (a) and polyurethane (b).

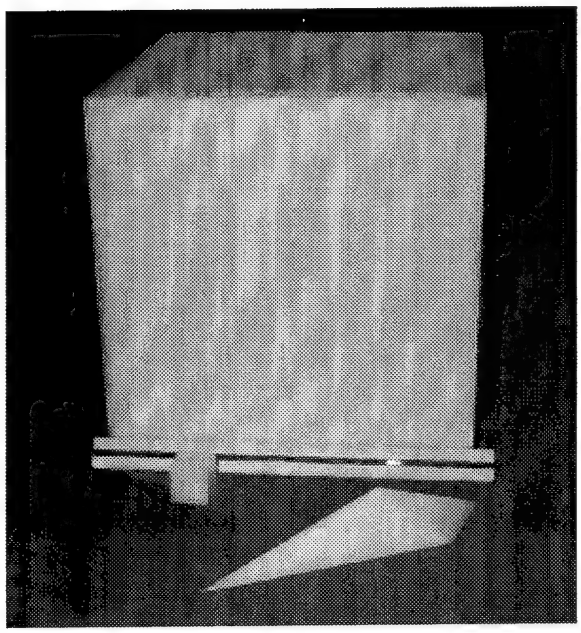

Figure 4.2 The small cube, large cube and mini-arrow made from polyethylene.

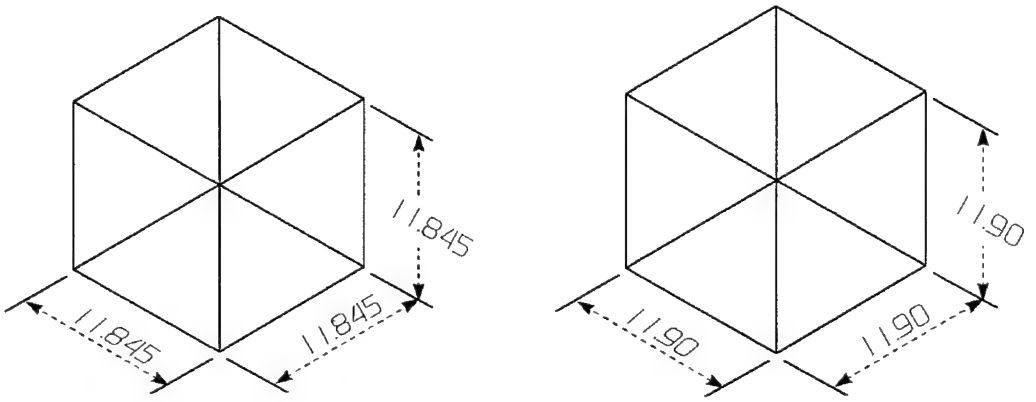

(a). (b).

Figure 4.3 The dimensions for the large cubes composed of polyethylene (a) and polyurethane (b).

4.1.1.3 Large Cube - Polyethylene. The large polyethylene cube was also relatively easy to manufacture because it was milled. The desired length of each side was 12 inches because this was the largest dimension for which the material could be acquired. However, in the fabrication process the sides were slightly milled to insure a cube with smooth, flat sides. The dimensions are given in Figure 4.3 (a) and a picture is provided in Figure 4.2. The error is ± 0.005 inches.

4.1.1.4 Large Cube - Polyurethane. Similar to the small polyurethane cube, the large polyurethane cube shape was made using a band saw resulting in a large error of ± 0.2 inches! The dimensions are found in Figure 4.3 (b).

4.1.1.5 Sphere. The sphere was a difficult target to fabricate. During the fabrication process, the sphere, as discussed in Section 3.1.1.3, was first secured on the lathe by knobs at opposite ends. Because of the large weight of the sphere, the material was "squeezed" together from opposite ends to properly secure it. During the removal of the knobs, a collar was tightened on the sphere as to allow the lathe to hold it. Again, the collar also compressed the material. The resulting target acquired a lot of error. The dimensions of the sphere are given in Figure 4.4 and a picture is provided in Figure 4.5. The two dimensions given in Figure 4.4 are averages of several measurements in that particular

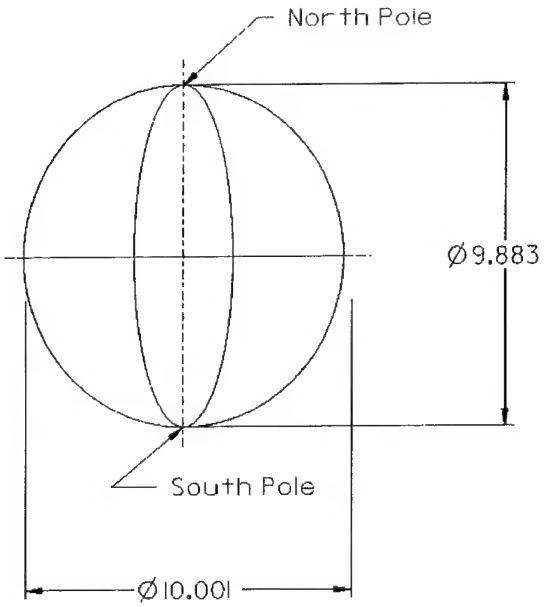

Figure 4.4 The dimensions of the sphere.

area. Depending on the location of the measurement, relatively significant differences in the diameter are noted. The error carried with the sphere is ± 0.1 inches.

4.1.1.6 Ogive. The ogive was the easist BOR target to fabricate due to its symmetry and smaller size. The resulting dimensions are slightly less than desired and are given in Figure 4.6. A pictrue of the ogive is found in Figure 4.7. The error is ± 0.005 inches.

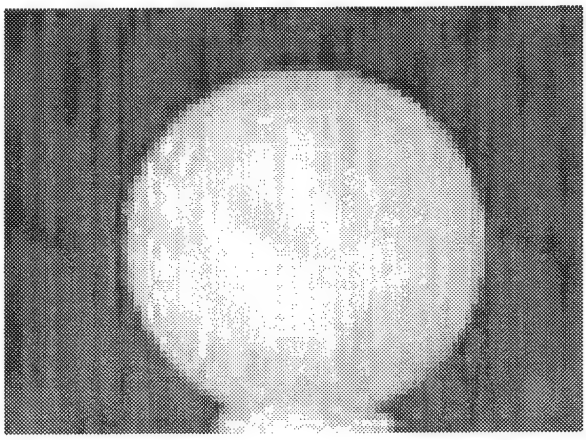

Figure 4.5 The polyethylene sphere.

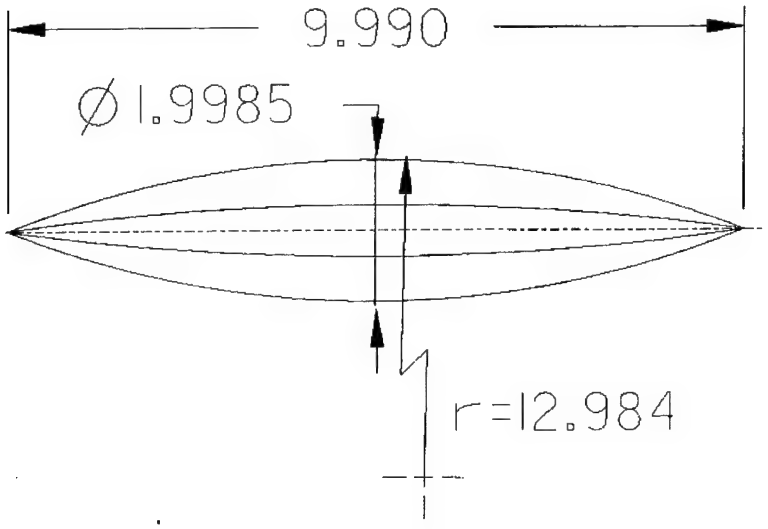

Figure 4.6 The dimensions of the ogive.

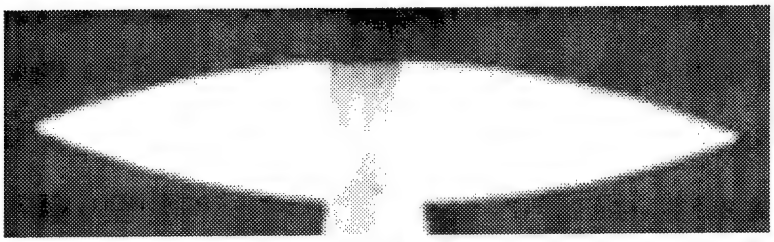

Figure 4.7 The ogive fabricated from polyethylene.

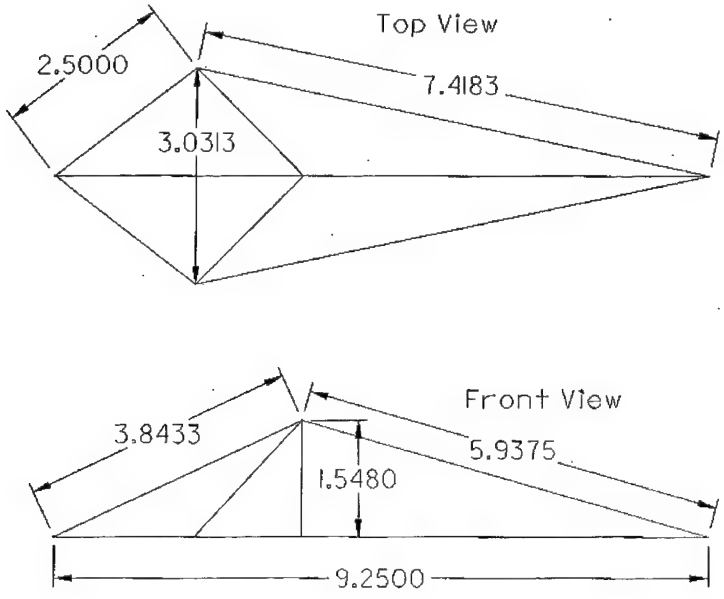

Figure 4.8 The dimensions of the mini-arrow.

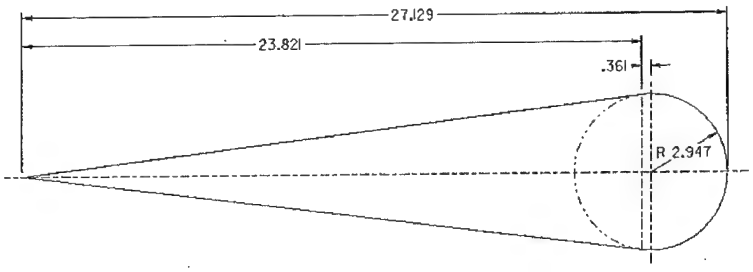

Figure 4.9 The dimensions of the conesphere.

Figure 4.10 The polyethylene conesphere.

4.1.1.7 Mini-arrow. The mini-arrow was also machined allowing precision in the dimensions of the target. The resulting dimensions are located in Figure 4.8 and a picture is provided in Figure 4.2. The error for the measurements is ± 0.0025 inches.

4.1.1.8 Cone-sphere. The cone-sphere was a very difficult and time-consuming target to make. During the fabrication process, the target was secured to the lathe, in a horizontal position, for days at a time. In addition to dimension changes due to temperature changes, the target also "sagged" due to its own weigth when the lathe was not in operation. These problems coupled with the difficulty of the manufacturing process resulted in relatively modest changes from the desired dimensions, as seen in Figure 4.9. The conesphere is shown in Figure 4.10. The error for these measurements is ± 0.005 inches.

4.1.1.9 Cone-sphere with a gap. The cone-sphere with a gap had the same difficulties as the conesphere. Additionally, a slight deformity in the material was found during the fabrication process. A small hairline void about $\frac{1}{4}$ inch deep and $\frac{1}{2}$ inch in length is located on the sphere end of the cone-sphere. The dimensions of the cone-sphere with a gap are found in Figure 4.11. The error in the measurements is also ± 0.005 inches.

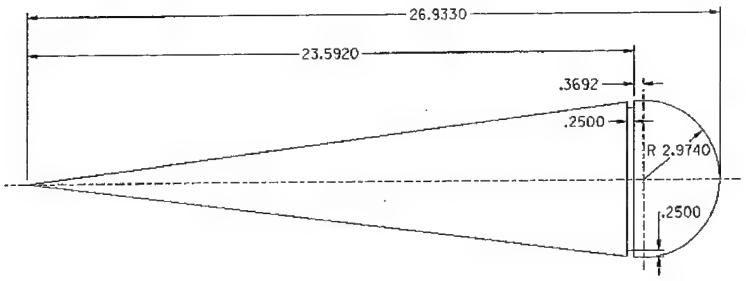

Figure 4.11 The dimensions of the conesphere with a gap.

Target	Tolerance (inches)
Small Polyethylene Cube	±0.002
Small Polyurethane Cube	±0.04
Large Polyethylene Cube	±0.005
Large Polyurethane Cube	±0.2
Sphere	±0.1
Ogive	±0.005
Mini-Arrow	±0.0025
Conesphere	±0.005
Conesphere with a Gap	±0.005

Table 4.1 Summary of the tolerances for each target.

4.1.1.10 Summary of Tolerance. Table 4.1 is a summary of the tolerances for each target.

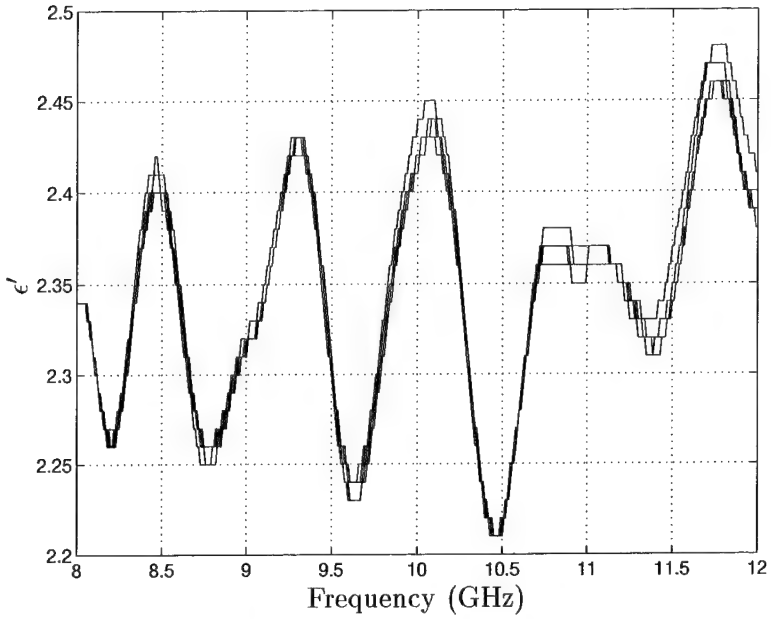

Figure 4.12 Permittivity of the real part (ϵ') of Polyethylene Sample A.

4.2 Measurements

4.2.1 Material Measurements. This section presents the results obtained from measuring the properties of the material samples using the X-band waveguide transmission line set-up. Because of the large amount of data, only the permittivity (ϵ') real value of the polyethylene samples are presented in a step-by-step fashion. The equivalent permittivity and permeability data for the polyurethane samples and remaining polyethylene samples are located in Appendix A.

4.2.1.1 Polyethylene. As discussed in Section 3.2.1, two samples of polyethelyene, length 0.2008 and 0.1986 inches, were measured five times from 8 to 12 GHz in steps of 10 MHz, averaging 128 measurements per step. The data was then transfered to an external computer and the permittivity and permeability were calculated using a Matlab routine. The raw data for the real part of the polyethylene permittivity (ϵ'), Sample A, is presented in Figure 4.12. Next, the average of the five measurements for this sample was calculated in Figure 4.13. Along with the average, the standard deviation, normalized to $n-1$, was also determined in Figure 4.13.

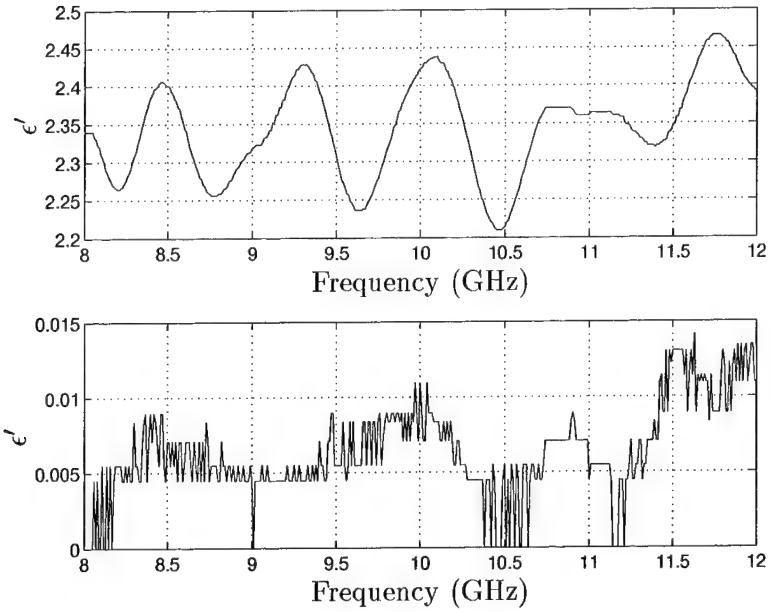

Figure 4.13 The Average Permittivity and Standard Deviation of the real part (ϵ') of Polyethylene Sample A.

Several items are rather apparent from Figures 4.12 and 4.13. First, the permittivity has an undesired oscillation. Second, all five measurements are very close to each other. The closeness of the measurements to each other indicates that a poor measurement did not cause the oscillation. Another contribution to this behavior could be unwanted reflections within the waveguide set-up or propagating modes. However, a calibration was accomplished before each measurement reducing this possibility. The peaks of the oscillations are approximately 900 MHz apart resulting in reflection location of 13.13 inches. This distance is approximately the distance between the two adapters for the set-up. Thus, a mismatch at the adapter probably is the major cause of the oscillations. When the material sample is inserted into the waveguide, the phase of the reflected energy is altered not allowing it to be "calibrated out".

The same procedure was followed for Sample B. The real part of the permittivity for the five measurements of Sample B is located in Figure 4.14. Figure 4.15 is the average and standard deviation of the same measurements. Again, oscillations in the data matching that of Sample A can be observed.

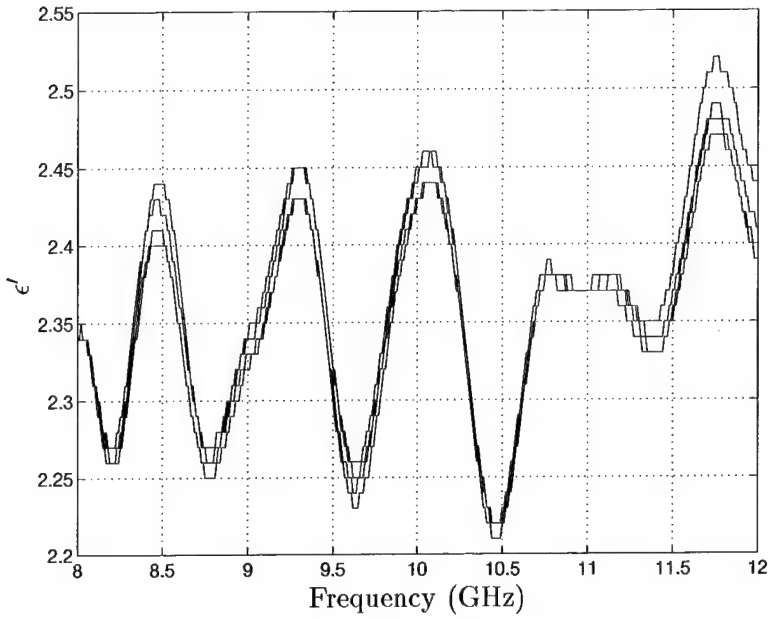

Figure 4.14 Permittivity of the real part (ϵ') of Polyethylene Sample B.

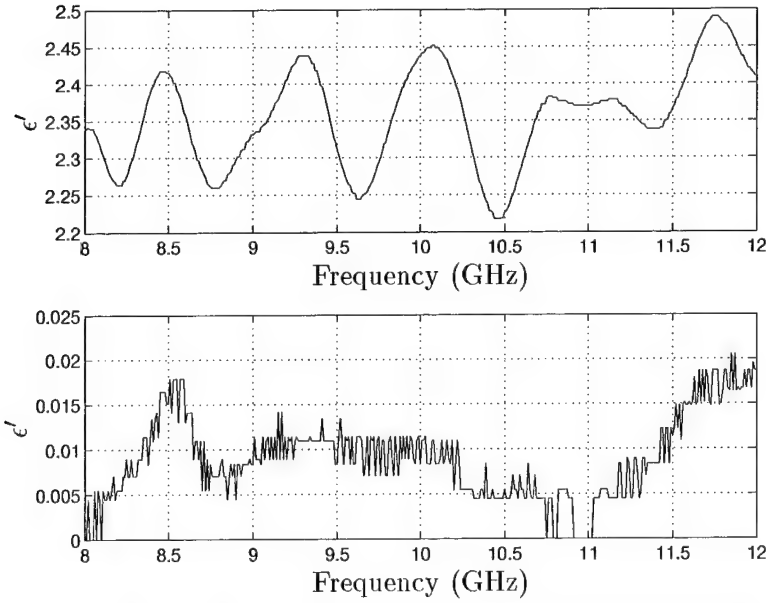

Figure 4.15 The Average Permittivity and Standard Deviation of the real part (ϵ') of Polyethylene Sample B.

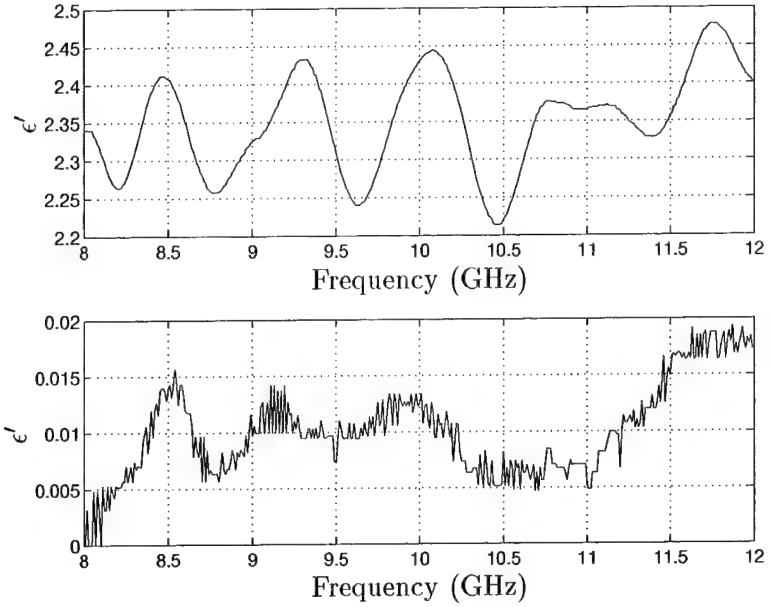

Figure 4.16 The Average Permittivity and Standard Deviation of the real part (ϵ') of the Polyethylene Samples.

The average and standard deviation of both samples is compiled in Figure 4.16. Friederich [10], Von Hippel [20], and Parker [16] provide data on the dielectric constant of polyethylene versus frequency. They agree that the dielectric constant is essentially constant over a wide range of frequencies, including the X-band. Therefore, it is reasonable to determine the dielectric constant for the polyethylene by averaging the data for as many complete periods as possible. Averaging will mitigate the error caused by the mismatch. In fact, Friederich states that when a matierial is known to have a relatively constant dielectric constant over a small frequency band, he will average the rectangular waveguide data for that frequency band, even if only one frequency is desired [10]. For these measurements there are nearly five periods between 8 and 12 GHz. The mean for the real portion of the permittivity is 2.3498 and the standard deviation is 0.01. Von Hippel presents a dielectric constant of 2.25 [20], Parker states that it is 2.30 [16], and Friederich uses 2.35 [10]. Thus, 2.3498 agrees well.

The imaginary part of the permittivity, ϵ'', for the polyethylene was found using the same method as describe above. The average permittivity and standard deviation for all measurements of both samples is located in Figure 4.17 (the full data set is presented

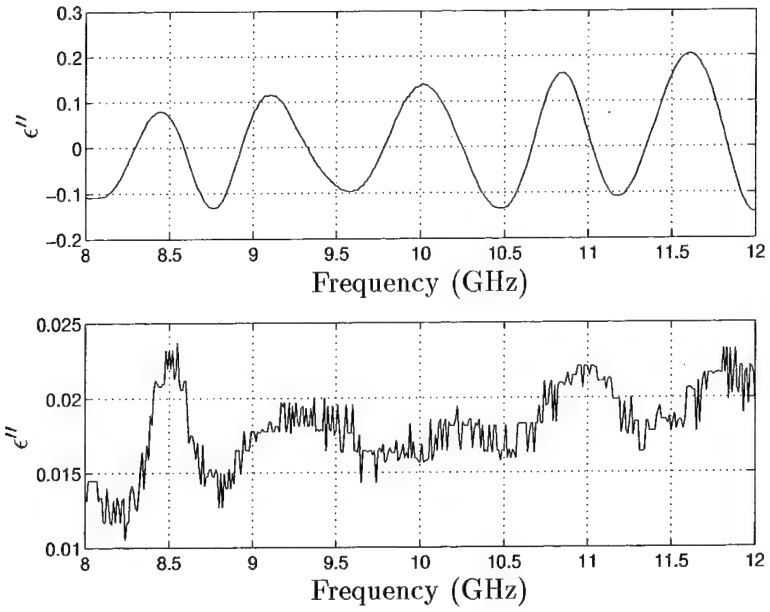

Figure 4.17 The Average Permittivity and Standard Deviation of the imaginary part (ϵ'') of the Polyethylene Samples.

in Figures A.6 through A.10 in Appendix A). It is evident that this data has the same oscillatory nature as that of ϵ'. Similarly, the mean was calculated over the entire frequency. The mean for ϵ'' is 0.0059 with a standard deviation of 0.018.

The average permeability and standard deviations for the real and imaginary parts, μ' and μ'', for both samples can be found in Figures 4.18 and 4.19, respectively. Again, the repeating oscillations are present in both sets of data. The average μ' is 1.0002 with a standard deviation of 0.0049 while the average μ'' is 0.0 with a standard deviation of 0.0073.

4.2.1.2 Polyurethane. The permittivity and permeability for the three polyurethane samples were calculated using the same procedure as the polyethylene samples. Each sample was measured independently five times from 8 to 12 GHz in increments of 10 MHz with an average of 128 measurements per increment. Only a summary is presented here in the text with the complete data set located in Appendix A.

Due to the compositon of the polyurethane and its foam-like qualities, the samples were very difficult to fabricate resulting in a relatively large tolerance. The desired length

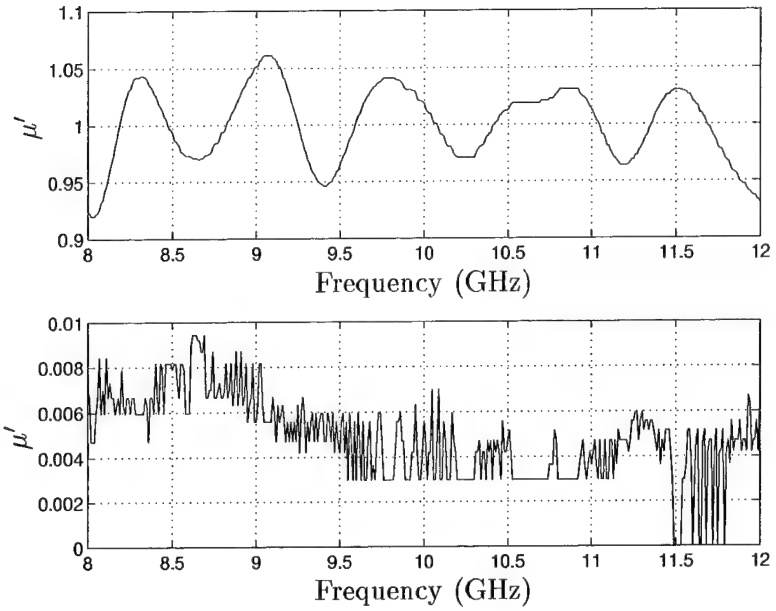

Figure 4.18 The Average Permeability and Standard Deviation of the real part (μ') of the Polyethylene Samples.

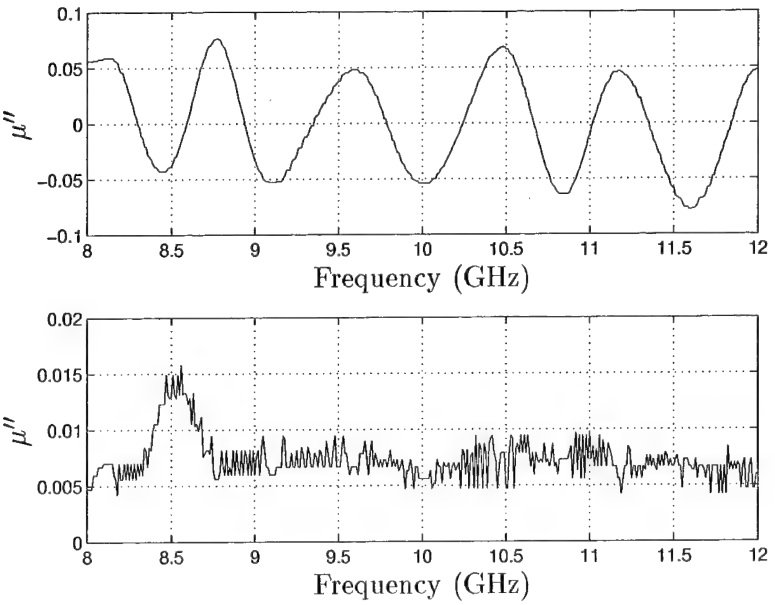

Figure 4.19 The Average Permeability and Standard Deviation of the imaginary part (μ'') of the Polyethylene Samples.

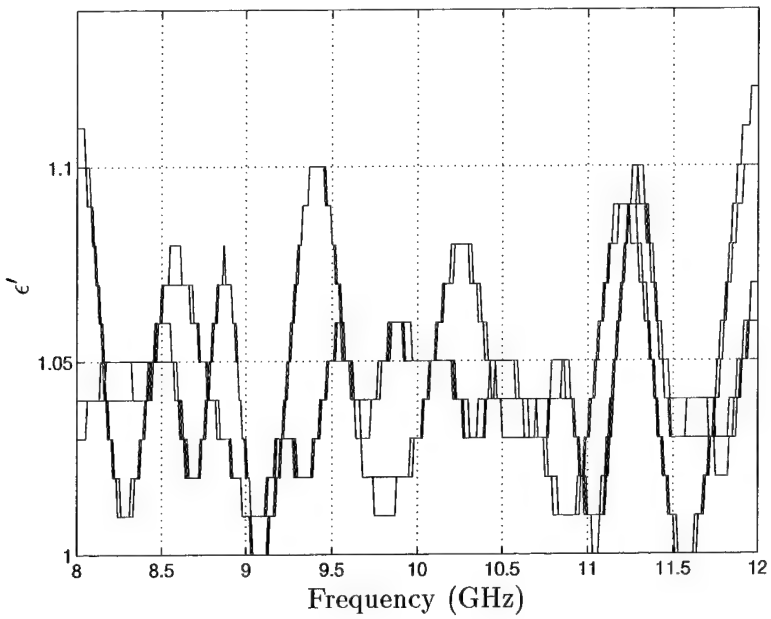

Figure 4.20 Permittivity of the real part (ϵ') of Polyurethane Sample A.

of the samples as discussed in Section 3.2.1 was 0.300 inches but the true lengths for samples A, B, and C resulted in 0.323, 0.322, and 0.331 inches, respectively. The difficult fabrication process coupled with the very low dielectric constant resulted in out-of-family measurements. The five measurements of ϵ' for Sample A are located in Figure 4.20 and the average ϵ' with standard deviation for all three samples are located in Figure 4.21.

The oscillations that are present in the polyethylene data are also present in the polyurethane data. However, Figure 4.20 shows the measurements for the polyurethane Sample A do not map each other as was the case with the polyethylene samples. Additionally, Samples B and C follow this trend as is apparent in Figure 4.21 with the large standard deviation, thus greatly reducing the confidence in the measurements. The mean for the real portion of the permittivity is 1.0436 and the standard deviation is 0.0147.

The average of all three samples versus frequency and their associated standard deviations for ϵ'', μ', and μ'' are graphed in Figures 4.22, 4.23, and 4.24 respectively. All three polyurethane data sets follow the same trend as ϵ'. The five measurements from each sample are out-of-family and include oscillations. The mean for ϵ'', μ', and μ'' and the

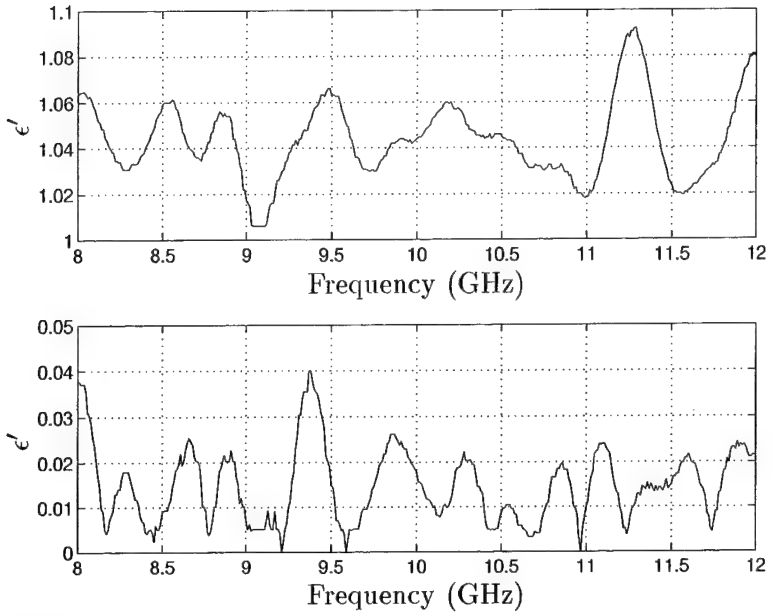

Figure 4.21 The Average Permittivity and Standard Deviation of the real part (ϵ') of the Polyurethane Samples.

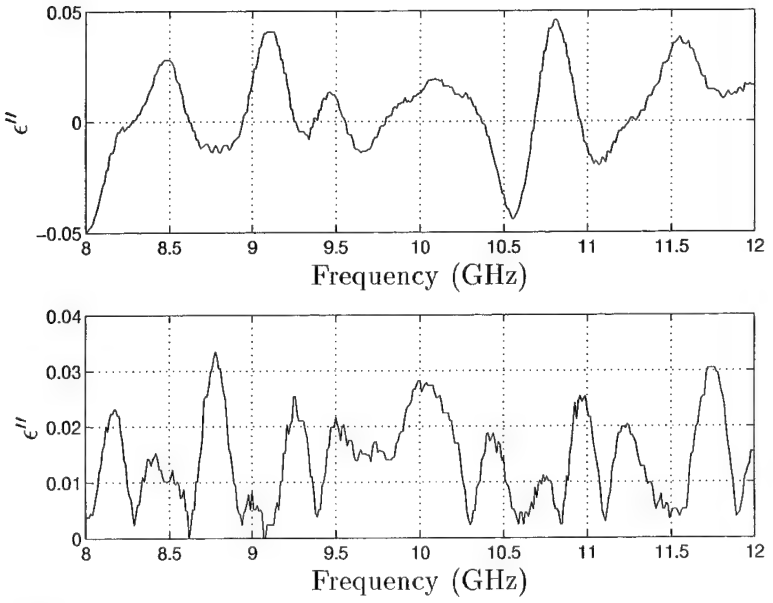

Figure 4.22 The Average Permittivity and Standard Deviation of the imaginary part (ϵ'') of the Polyurethane Samples.

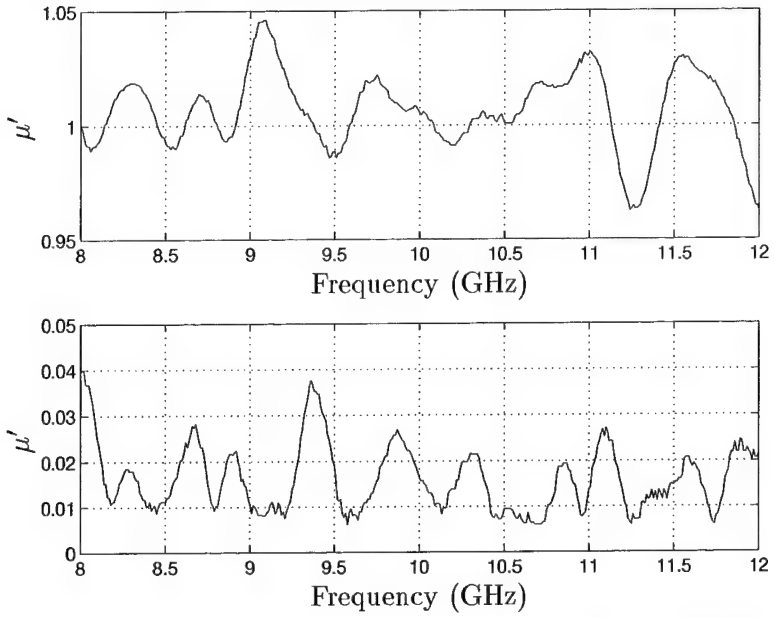

Figure 4.23 The Average Permeability and Standard Deviation of the real part (μ') of the Polyurethane Samples.

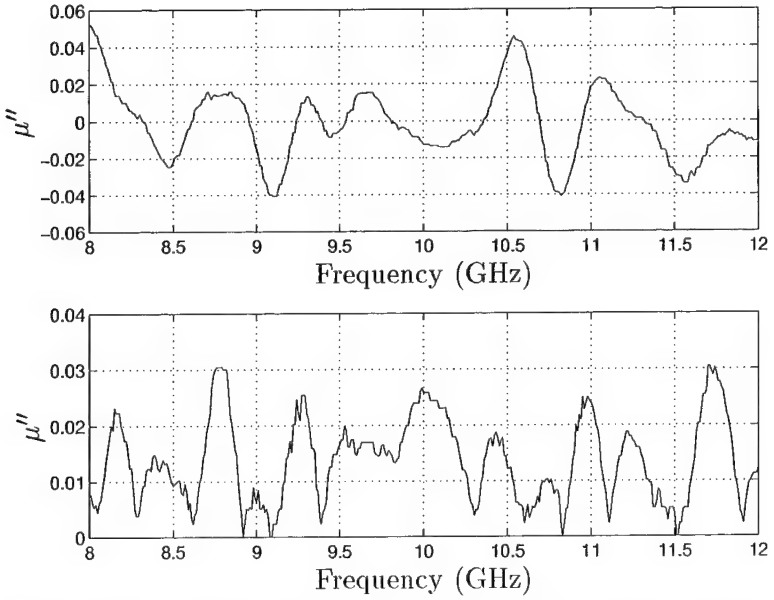

Figure 4.24 The Average Permeability and Standard Deviation of the imaginary part (μ'') of the Polyurethane Samples.

associated standard deviations are 0.0048 and 0.014, 1.0065 and 0.0161, and -0.0015 and 0.0136, respectively.

4.2.1.3 Summary of Material Measurements. A summary of the material parameters for both polyethylene and polyurethane at specific frequencies is provided in Tables 4.2 and 4.3. Note that the mean was calculated using all data points, not the 5 data points listed per parameter in the tables.

Polyethylene						
Parameter	8 GHz	9 GHz	10 GHz	11 GHz	12 GHz	Mean
ϵ'	2.340	2.325	2.430	2.366	2.401	2.3498
ϵ''	-0.107	0.074	0.137	0.028	-0.144	0.0059
μ'	0.924	1.051	1.019	1.013	0.931	1.0002
μ''	0.056	-0.033	-0.054	-0.011	0.047	0.0000

Table 4.2 Summary of material properties for the polyethylene.

Polyurethane						
Parameter	8 GHz	9 GHz	10 GHz	11 GHz	12 GHz	Mean
ϵ'	1.064	1.017	1.044	1.019	1.081	1.0436
ϵ''	-0.050	0.018	0.013	-0.012	0.016	0.0048
μ'	1.000	1.030	1.005	1.031	0.963	1.0065
μ''	0.052	-0.015	-0.013	0.018	-0.011	0.0000

Table 4.3 Summary of material properties for the polyurethane.

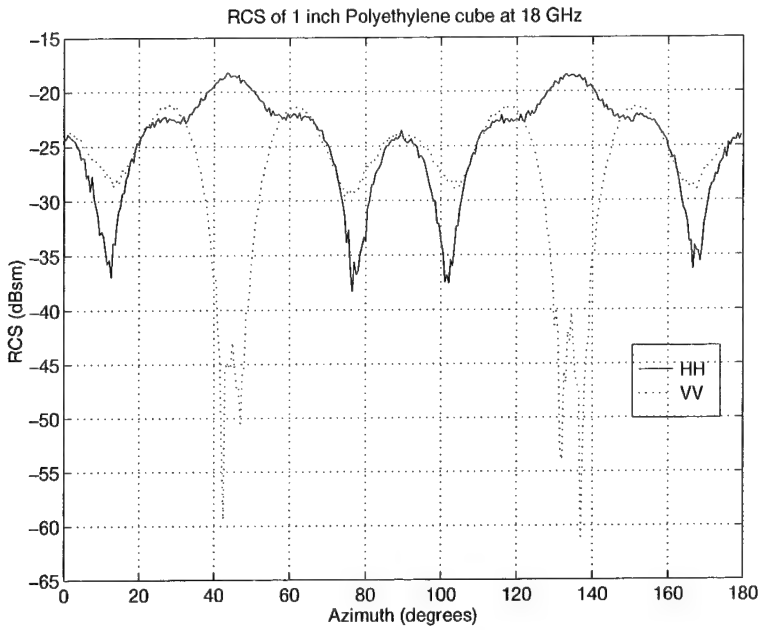

Figure 4.25 The RCS vs. azimuth of the small polyethylene cube at 18 GHz.

4.2.2 RCS Measurements. This section presents a representative sample of the measured RCS database. For each target a brief description is given noting outstanding features and any anomalies in the measurement. This data set will provide the reference used for the code validation in Section 4.3.

The RCS measurements for this research were accomplished at Wright Laboratory's Multispectral Measurement Facility (WL/XPN), Wright-Patterson AFB, OH. Each of the targets were measured for both polarizations from 2 to 18 GHz, in 20 MHz increments, and from 0 to 360 degrees, in 0.5 degree increments, in azimuth. With these parameters, the data lends itself to many detailed uses including magnitude versus azimuth as well as magnitude versus frequency plots. For example, the small polyethylene cube RCS versus azimuth for 18 GHz is presented in Figure 4.25 and the RCS versus frequency at 45 degrees of the same target is in Figure 4.26.

The data for each measurement was provided in three columns. The first column is the azimuth angle. The next two columns are the I (real part) and Q (imaginary part) channel data, respectively. The frequency is folded into the azimuth angle starting with 2 GHz and then incrementing by 20 MHz until 18 GHz is reached. Thus, there are 801 rows

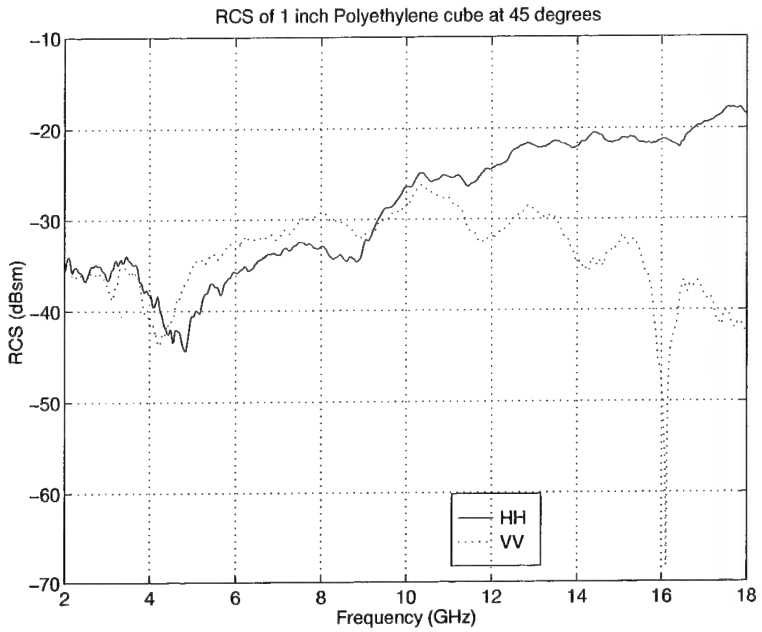

Figure 4.26 The RCS vs. frequency of the small polyethylene cube at 45 degrees.

of I and Q channel data corresponding to a particular frequency for each angle. Overall, each data set has 576,720 rows of data. The RCS in dB per square meter (dBsm) was calculated using a Matlab routine solving the following equation:

$$\sigma = 10 \cdot log_{10}(I^2 + Q^2) \tag{4.1}$$

The RCS of all the targets listed in Section 4.1.1 were measured and are presented here. Global RCS plots in color for each target and both polarizations are located in Appendix B. Additionally, Global Time Domain color plots of several of the targets are also located in Appendix B. Note that the scales for each plot are not the same.

In addition to the targets listed in Section 4.1.1, three of the targets, both the small polyethylene and polyurethane cubes and the mini-arrow, were measured with r-card applied. The r-card was not characterized but the manufacturer data states that it has a surface impedance of 1500 $\Omega/square$. The r-card was applied to each face of the target without any overlap. It should also be noted that the r-card was secured to each target with mylar tape on the outside. Adhesive was not used between each target face and

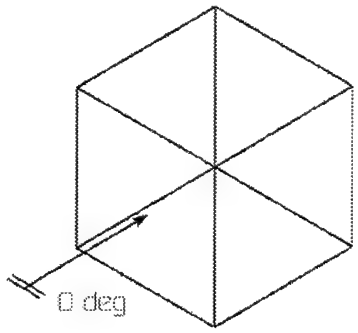

Figure 4.27 The orientation of all cubes for RCS measurements.

the r-card. Although the r-card appeared flush against each target face upon inspection, it is possible that there may have been a small air gap(s) between the faces and r-card.

4.2.2.1 Small Cube - Polyethylene. The orientation of all the cubes during the RCS measurement process is pictured in Figure 4.27. Each of the four faces were aligned at 0, 90, 180, and 270 degrees. The small cubes were mounted on a foam tapered pylon, pictured in Figure 4.28, to reduce target/mount interactions. The small polyethylene cube was measured using 4096 integrations and the global plots are located in Appendix B as seen in Figures B.1 and B.2. The penetrable material is readily apparent in several aspects. Because the energy is coupled inside the cube and reflected off of the inner walls, the face of the cube does not provide the largest return as would be expected with a PEC. Also, at 45 degrees the larger return tends to be at horizontal polarization (HH) instead of vertical polarization (VV). For a PEC, the vertical corner would provide a larger return at VV, but due to the material, the back walls act as a corner reflector for HH making its return larger.

4.2.2.2 Small Cube - Polyurethane. The three most noticeable aspects of the RCS for the small polyurethane cube are the low returns, the lack of uniformity, and the similarity between HH and VV. The strongest returns are located at the faces as a result of reflections from the front and back faces. The low dielectric constant of the material does not couple the energy nearly as well as the polyethylene resulting in low returns, especially at the corners. The non-uniformity of the return is a result of fabrication of the target.

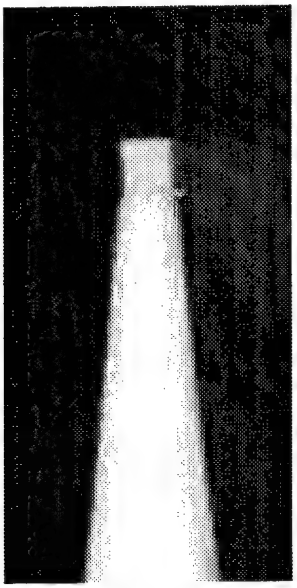

Figure 4.28 The small polyurethane cube mounted for RCS measurements.

As discussed in Section 4.1.1.2, the cube was cut by hand resulting in less than precision dimensions. Furthermore, the material did not lend itself to a smooth cut. The cube mounted for RCS measurements is pictured in Figure 4.28. The number of integrations used for this measurement are 8192.

4.2.2.3 Small Cube with R-card - Polyethylene. As would be expected, the RCS of the small polyethylene cube with r-card resembles the return of the small polyethylene cube without r-card, but lower in magnitude. The r-card reduces the energy allowed to penetrate the polyethylene reducing the internal reflected energy. The global plots for the small polyethylene cube with r-card are located in Figures B.3 and B.4. This target was measured using 4096 integrations.

4.2.2.4 Small Cube with R-card - Polyurethane. Use of the r-card on the small polyurethane cube produced results opposite than what is typically expected with r-card. The RCS increased rather than decreased, as seen in Figures B.7 and B.8. Similar to the polyurethane cube without r-card, this target produced the highest returns from the faces of the cube. However, the stronger return was from the front face as opposed to the rear face, as is the case with both cubes without the r-card. Also, the r-card

tends to produce returns from the front corners whereas no returns at these locations were measured for the polyurethane cube without r-card. This target was measured using 8192 integrations.

4.2.2.5 Large Cube - Polyethylene. The larger cubes were mouned on a larger cylindrical mount due to their size and weight, as picutured in Figure 4.29. The large polyethylene cube has the largest return of any targets measured in this research at 20 dBsm. The global plots for this target are provided in Figures B.9 and B.10. A large return was produced from each face, as expected. Additionally, large returns nearly 50 degrees wide at the higher frequencies are also present on the corners, espcially for VV. This is mainly a result of the energy allowed to penetrate into the material and reflect back towards the radar. It also interesting to note that the returns at the corners are stronger for VV than HH, which is the opposite for the small polyethylene cube. The large polyethylene cube was measured using 4096 integrations.

4.2.2.6 Large Cube - Polyurethane. The large polyurethane cube has a very similar return to that of the small polyurethane cube, as seen in Figures B.11 and B.12. Both measurements show that the faces produce the largest returns and very little return at the corners. The dynamic range of the cube is fairly large, 0 to below -60 dBsm, and the return is fairly uniform. Although, the global RCS plot for HH is quite a bit more uniform than VV. This may be a result of the fabrication of the target. The polyurethane material was produced in a large sheet measuring 1 ft x 4 ft by 8 ft. The large cube was cut from a corner of that sheet resulting in two faces cut by hand using a band saw and two faces as manufactured. When the cube was measured, the manufactured faces were located at 0 and 90 degrees, while the cut faces were at 180 and 270 degrees. From the range vs. azimuth time domain plot for VV, Figure B.13, it can be seen that the strong non-uniform returns are between 0 and 90, and 270 and 360 degrees, and emanate from the back corner. Thus, it is reasonable to assume that the non-uniformity is due to the fabrication of the cube with a band saw. The large cube was measured using 8192 integrations.

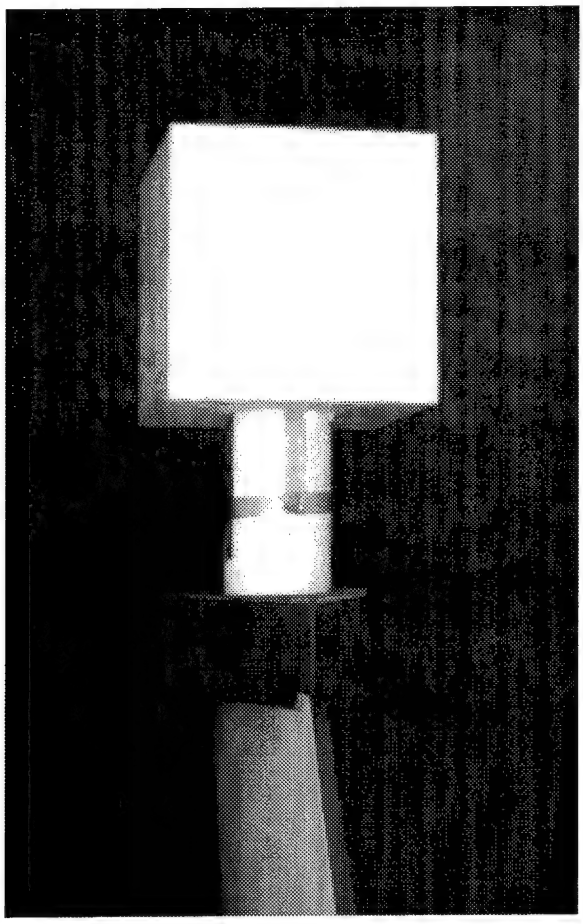

Figure 4.29 The large polyethylene cube mounted for RCS measurements.

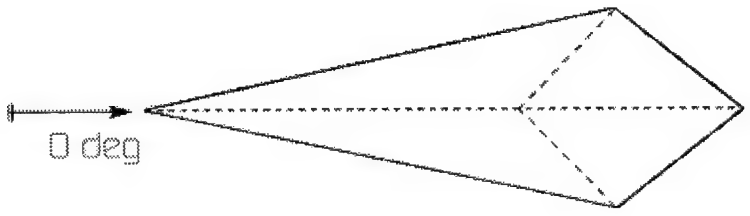

Figure 4.30 The orientation of the mini-arrows for RCS measurements.

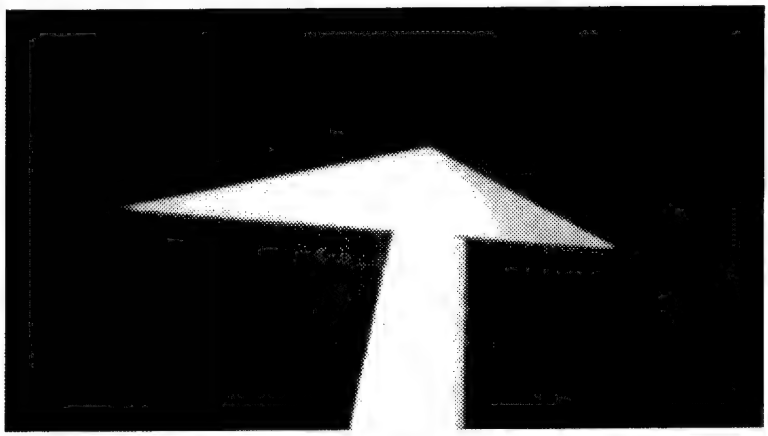

Figure 4.31 The mini-arrow mounted for RCS measurements.

4.2.2.7 Mini-Arrow. During RCS measurements, the nose was aligned with 0 degrees as depicted in Figure 4.30. The same tapered mount used by the small cubes was also used to mount the mini-arrows, as pictured in Figure 4.31. The RCS, located in Figures B.14 and B.15, from the mini-arrow appears to be counter-intuitive. The long gradual slope of the nose, located at 0 degrees, produces a larger return than the tail. The largest returns are present at the side view, or around 90 degrees. At or near this angle, the back two faces and the bottom face may be reflecting energy back towards the receiver. The very strong return at 105 degrees (and 255 degrees) closely matches the angle of the longer back face. Both polarizations tend to have the same features except at and around the nose view, at which point HH produces larger spurious returns. Overall, HH tends to produce larger returns for this target. The mini-arrow was measured using 4096 integrations.

4.2.2.8 Mini-Arrow with R-card. The mini-arrow with the r-card applied produces a very interesting return when compared with the mini-arrow without r-card. The global RCS plots are located in Figures B.16 and B.17. It appears that the orientation of the mini-arrow was reversed, which is not the case. The very strong and polarization independent return at 105 degrees now is located around 75 degrees (or 285 degrees), is reduced in angle width, and is much stronger for HH than VV. As was discussed earlier, the r-card reduces the energy allowed to penetrate the material. Thus, the return at 75 degrees is a reflection from the long front face of the nose, whereas a much weaker return

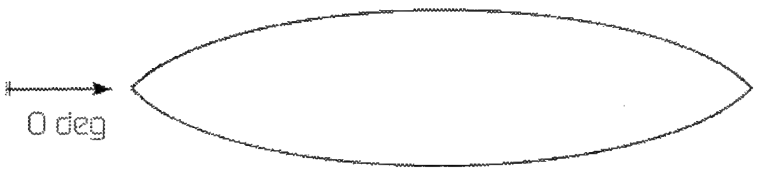

Figure 4.32 The orientation of the ogive for RCS measurements.

was noticed without the r-card at this angle. Additionally, a weaker return is present at 125 degrees matching the front face of the tail end. The r-card also greatly reduced the return at nose view for HH. HH also tends to have larger returns than VV. The number of integrations for this measurement was 4096.

4.2.2.9 Ogive. The ogive was measured using 16384 integrations because of the known low RCS at the nose. The return from the ogive has a large dynamic range depending upon orientation, as seen in Figures B.18 and B.19. Also, the broadside return is dependent upon polarization. At broadside, the main return is not from the specular, but rather from the incident field propagating into the target and returning back. The orientation of the ogive for this measurement is shown in Figure 4.32 and pictures of it mounted for RCS measurements are included in Figures 4.33 (a) and (b).

4.2.2.10 Sphere. The RCS returns from the polyethylene 10 inch diameter sphere are very puzzling. A sphere, if near perfect, should be independent of orientation and polarizations. This is not the case with the results for this sphere, as seen in Figures B.20 and B.21. Both polarizations are very similar from 2 to 6 GHz, but then they both differ with VV maintaing a larger return over the remaining frequency range. The main return for both polarizaitons is a combination of creeping wave and internally reflected energy. The difference in RCS returns may be a result of the creeping wave. The sphere was fabricated using a lathe. In the orientation that the sphere was measured, the lathe cut across its equator, or side to side. Although these cuts were relatively fine to the touch, they may have helped propagate a creeping wave in the VV direction and attenuated the HH creeping wave. The sphere is not perfect, but it seems doubtful that the error present

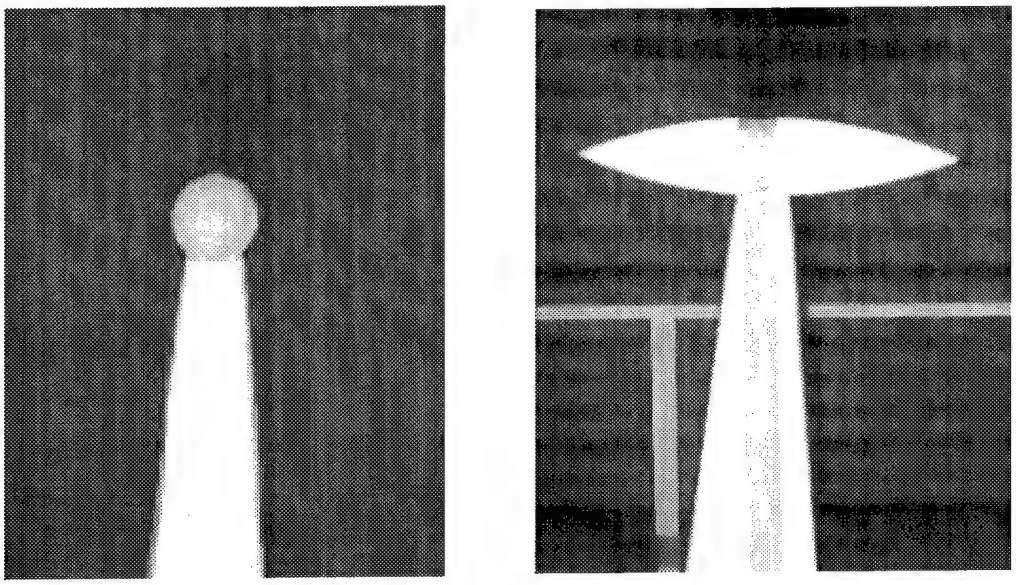

(a). (b).

Figure 4.33 The ogive is mounted for RCS measurements. Nose view (a). Side view (b).

in its dimensions could solely have this much affect on the outcome. A picture of sphere mounted for RCS measurements is provided in Figure 4.34.

The major advantage for using a sphere as a validation target is that it has an exact solution. Using the Mie series, the exact RCS was plotted in Figures 4.35 and 4.36 for a 10 inch diameter sphere with a dielectric constant of 2.35. Additionally, the HH and VV measured data was plotted for comparison purposes. From the plots, it is evident that the measured data has acquired a significant amount of error. For validation purposes, the Mie series data should be used instead of the measured data. The Mie series RCS data for this target is provided in the CD.

4.2.2.11 Conesphere. The hemisphere end of the conespheres was oriented at 0 degrees, as Figure 4.37 shows, for these measurements. The global RCS plots are located in Figures B.22 and B.23. For the first 75 degrees, the specular from the hemisphere provides the main return which is relatively constant around -30 dBsm. At 75 degrees, the largest return is visible. From the time domain plot in Figure B.24, it is apparent that the main return at 75 degrees is due to the back of the cone aligning with the radar. Furthermore, a lesser return that is frequency independent is noticeable from the front of

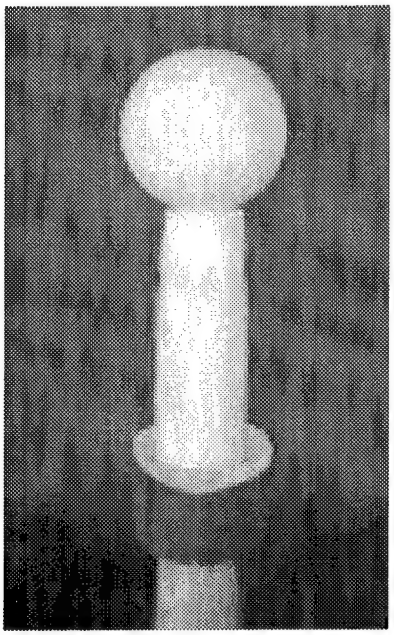

Figure 4.34 The sphere is mounted for RCS measurements.

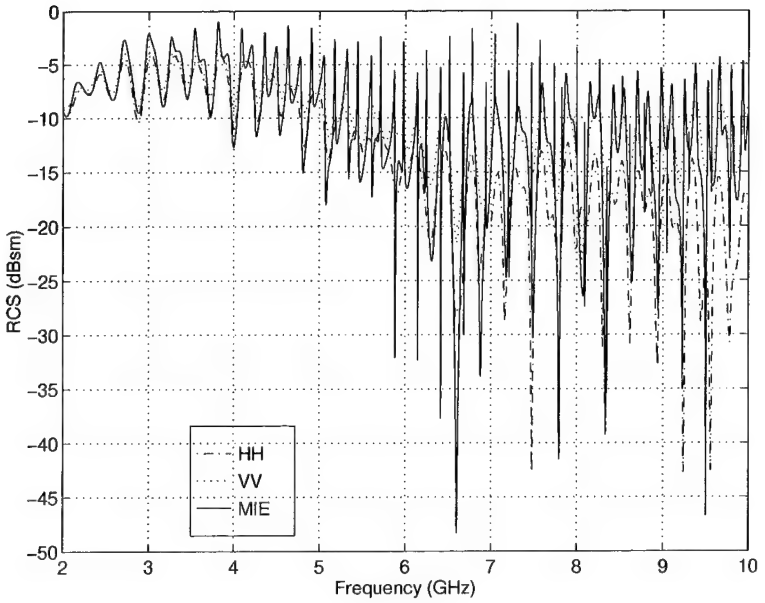

Figure 4.35 The monostatic RCS comparison of measured data and Mie series data for the polyethylene sphere from 2 to 10 GHz.

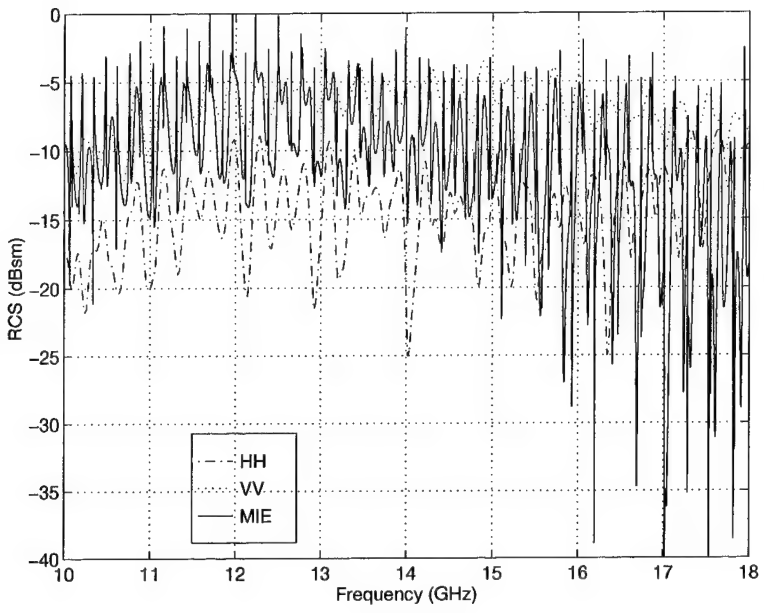

Figure 4.36 The monostatic RCS comparison of measured data and Mie series data for the polyethylene sphere from 10 to 18 GHz.

Figure 4.37 The orientation of the conespheres for RCS measurements.

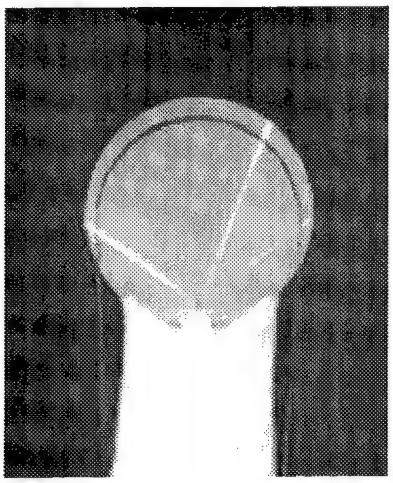

(a).

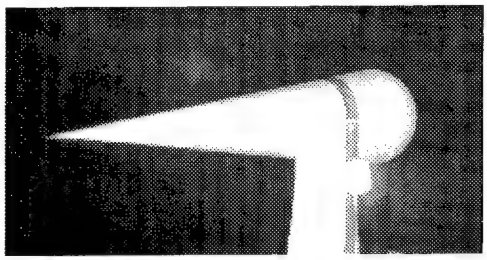

(b).

Figure 4.38 The conesphere is mounted for RCS measurements. Nose view (a). Side view (b).

the cone aligning with the radar. The strong returns between 75 and 285 degrees are due to the hemisphere coupling energy. The tip of the cone does not cause a significant return. Also, both polarizaitons are relatively similar. The conesphere was measured with 8192 integrations and is pictured mounted for RCS measurements in Figures 4.38 (a) and (b). Note that the time domain plot provided for the conesphere in Figure B.24 is very similar to that of the conesphere with a gap, both polarizaitons.

4.2.2.12 Conesphere with a Gap. A PEC conesphere with a gap has a very different RCS than just a conesphere. However, this is not the case with polyethylene, as seen in Figures B.25 and B.26. Both HH and VV for both conespheres are nearly identical. Thus, the gap has very little affect on the overall RCS. This target was also measured with 8192 integrations.

4.2.3 RCS Measurement Uncertainty. As discussed in Chapter 3, the uncertainties for the RCS measurements of the targets were presented, less the calibration and background-noise uncertainties. Both of these uncertainties are presented here. Furthermore, the complete overall uncertainty for the targets is discussed.

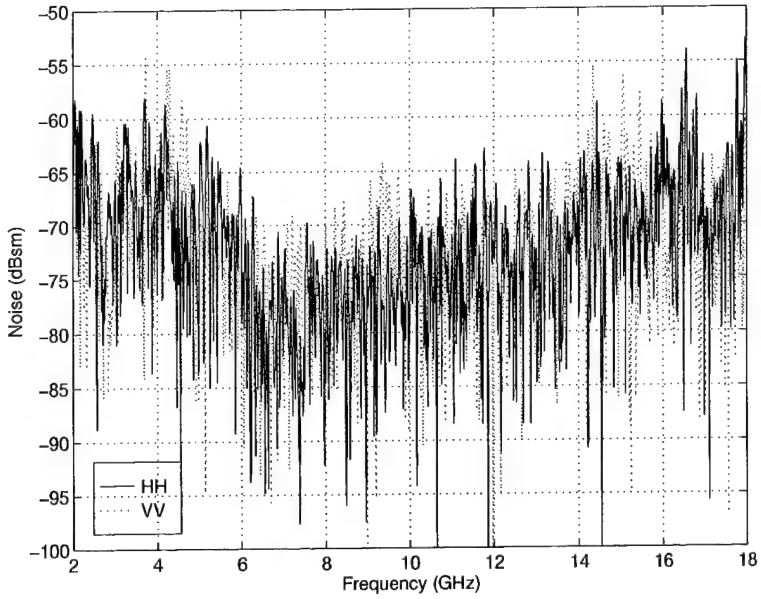

Figure 4.39 The background noise.

4.2.3.1 Noise-Background. To determine the noise-background uncertainty from Equation (2.21), both the signal and noise are required. S is the RCS return from the target. To find N, the background noise of the range is required. The background noise is basically the RCS of the empty chamber. For WL/XPN, the RCS is measured with the target mount on the pedestal, but is then removed through vector subtraction.

Figure 4.39 is the resulting background noise for one measurement. The background noise was measured from 2 to 18 GHz, in 10 MHz increments, for a total of 1601 data points. As is apparent, the data is very "noisy." However, a definite pattern does exist. To mitigate this "noise", three different background noise measurements were averaged. Due to the limited number of background noise samples, 3, the average was still quite "noisy." Because of this, the resulting data was then "smoothed" using a window of 41 points, or approximately 2.5% of the data. The "smoothed" background noise is plotted in Figure 4.40. The large decrease at 6 GHz is a result of a traveling wave tube. The traveling wave tube has a finite bandwidth so it is utilized from 6 to 18 GHz. Note that the three noise plots, averaged noise plot, and "smoothed" noise plot are located in Appendix C.

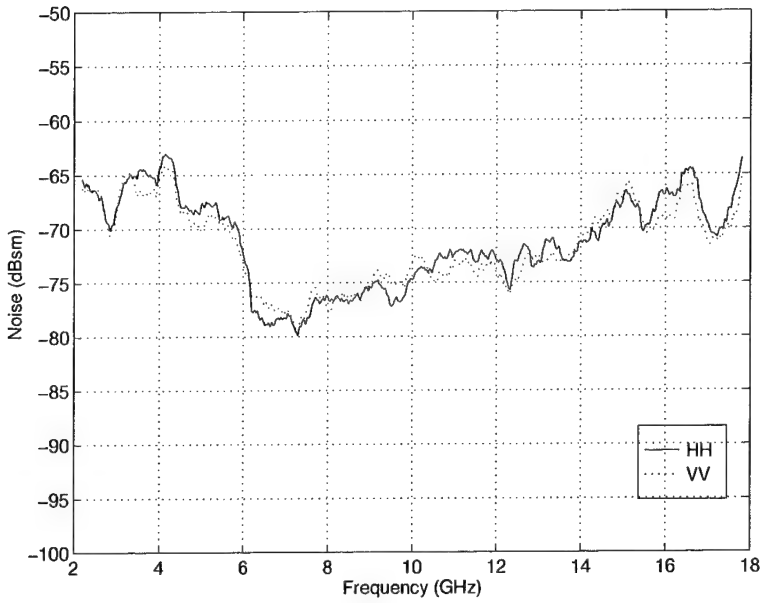

Figure 4.40 The background noise averaged and "smoothed".

Now that the noise, N, is known, the noise-background uncertainty can be determined. As an example, let's use the small polyethylene cube at 18 GHz. The RCS at 18 GHz for the small cube is shown in Figure 4.25. Figure 4.41 is a plot of the noise-background uncertainty per azimuth angle for the small polyethylene cube. The uncertainty was calculated using Equation (2.21) and values of -63 and -65 dBsm for the HH and VV noise, respectively. The uncertainty is relatively small except at the corners of the cube for VV. At those angles, the RCS was very low, resulting in a higher uncertainty level.

A problem with Equation (2.21) is that the $\Delta\sigma$ grows very large as the signal-to-noise ratio (SNR) approaches 0 dB. Even though Equation (2.21) is a worst-case estimate, its validity at low SNR values is debatable. For this research, uncertainty due to noise-background will be limited to a maximum of 5 dB, which is approximately equivalent to a SNR of 7 dB. This should be considered for targets with an RCS that approaches the noise floor.

4.2.3.2 Calibration Uncertainty. As discussed in Chapter 3, the calibration uncertainty is produced by comparing the "exact" calibration target solution to the measured results of the double calibration. This comparison, for the small polyethylene cube,

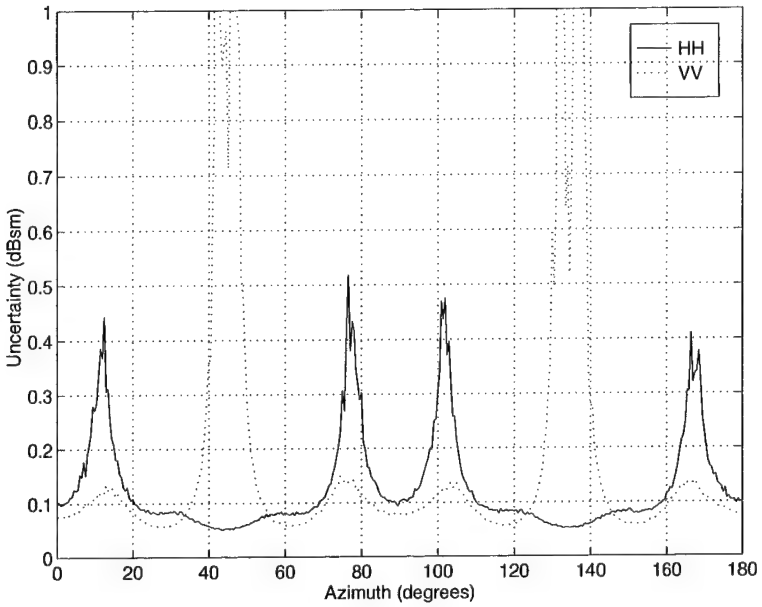

Figure 4.41 The noise-background uncertainty for the small polyethylene cube at 18 GHz.

is plotted in Figure 4.42. The deviation from 0 dB is the calibration uncertainty. Calibration uncertainty for other polyethylene targets including the large cube, mini-arrow, and conespheres, is provided in Appendix C.

4.2.3.3 Overall Uncertainty. Now that the calibration and noise-background uncertainties are known, the overall uncertainty can be determined by the RSS. Determining the uncertainties from Figures 4.40 and 4.42 at 18 GHz, and using the values in Table 3.1, the overall uncertainty for the small polyethylene cube at 18 GHz can be calculated (see Figure 4.43). The calibration uncertainties used were -0.34 and -0.30 dBsm for HH and VV, respectively. The values of -63 and -65 dBsm were used for the noise-background uncertainties. This overall uncertainty can now be used as error bounds when reporting the measured RCS, as is the case with Figure 4.44.

The plots of the measured RCS with error bounds of other targets are located in Appendix C. The targets include the small polyethylene cube at 10 GHz, the large polyethylene cube at 2 GHz, the polyethylene mini-arrow at 6 GHz, the polyethylene ogive at 10 GHz, and both of the polyethylene conespheres at 2 GHz.

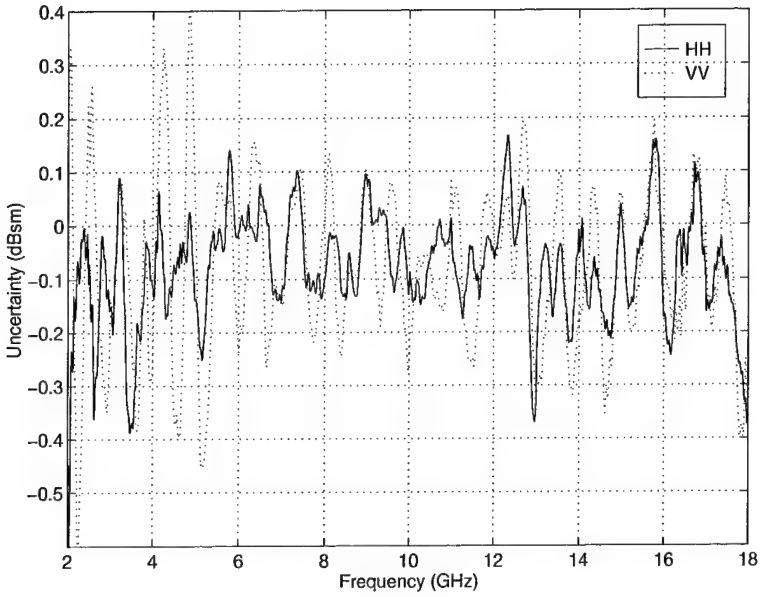

Figure 4.42 The calibration data for the small polyethylene cube.

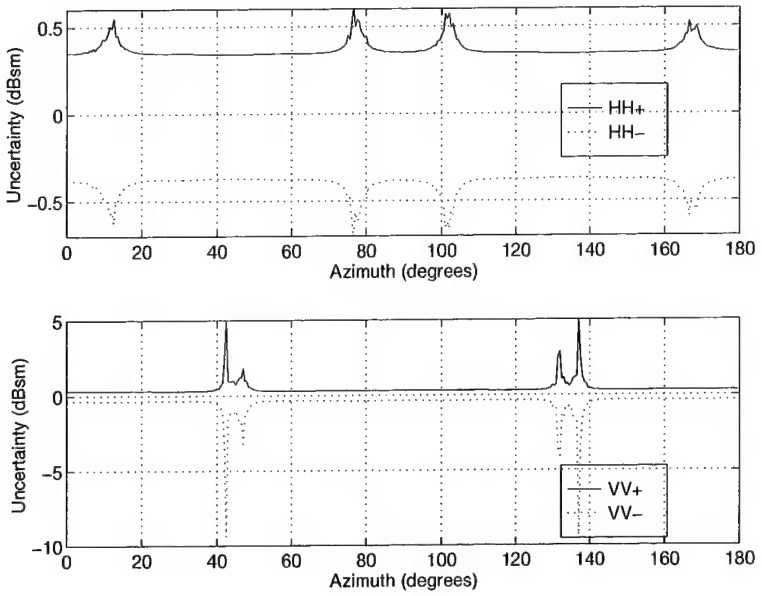

Figure 4.43 The overall uncertainty for the small polyethylene cube at 18 GHz.

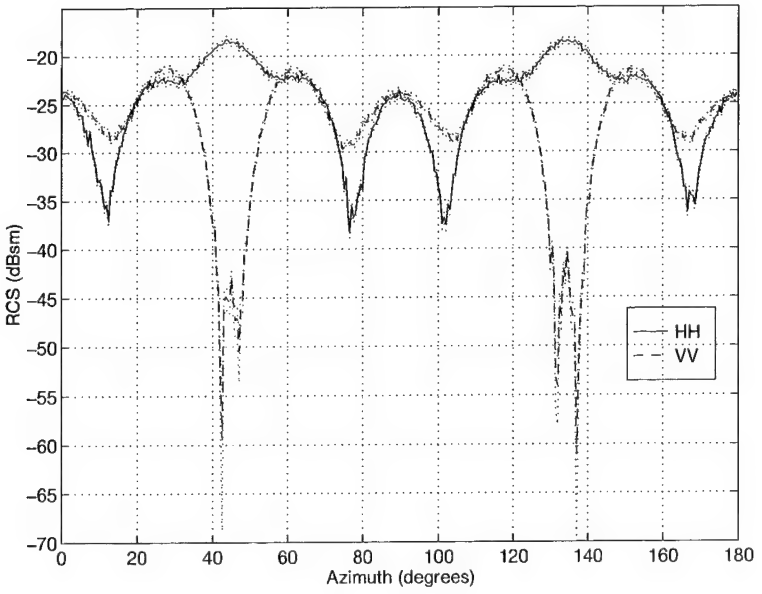

Figure 4.44 The measured RCS of the small polyethylene cube at 18 GHz with error bounds.

4.3 Code Validation

In this section the results of the RCS target measurements, material characterization, and uncertainty analysis are used to validate a computer program. In this case, the validation is performed by comparing the code results with the measured results of the dielectric targets described in this research.

4.3.1 3D-RCIE. The computer program used for this research is 3D-RCIE. 3D-RCIE, as described in Section 3.3, consists of four programs. MESH, the geometry and mesh generating utility, is first used to generate surface patches used PULSE2. PULSE2 then computes the system matrix and excitation vectors. The matrix is then solved by BLGMRP or by LUFACTOR. PULSE2 is then utilized again to compute the RCS from the matrix solution. Note that BLGMRP and LUFACTOR are provided as part of this program. However, any matrix solving routine can be used to solve the matrix. Also, the default values for each program were used unless otherwise specified.

To run the code the Aeronautical Systems Center Major Shared Resource Center (ASC MSRC) was utilized. The ASC MSRC, physically located in Building 676 on Wright-Patterson AFB, is part of the DoD High Performance computing community. The ASC MSRC is comprised of high performance application servers, high availability data servers, a Scientific Visualization facility, and an array of applications supporting five computational technology areas (see Figure 4.45).

To run 3D-RCIE, the IBM SP was chosen because of its many processor elements (PE). The IBM SP system is a parallel computer based on the IBM RS/6000 processor. It has 256 PEs, each of which is an RS/6000 P2SC model 595 processor with a clock speed of 135MHz. Each PE has 1 GB of RAM. One major drawback to the IBM SP is that the user is only allowed two processes running at one time. More details on the IBM and ASC MSRC can be obtained from their homepage at *http://www.asc.hpc.mil.*

To evaluate the program a test plan was formulated. The initial test plan was to first run each of the targets from 2 to 18 GHz, in 2 GHz increments, and from 0 to 180 degrees, in 1 degree increments, for the monostatic RCS using BLGMRP. Because BLGMRP does not produce the exact solution, at least one run per target would also be

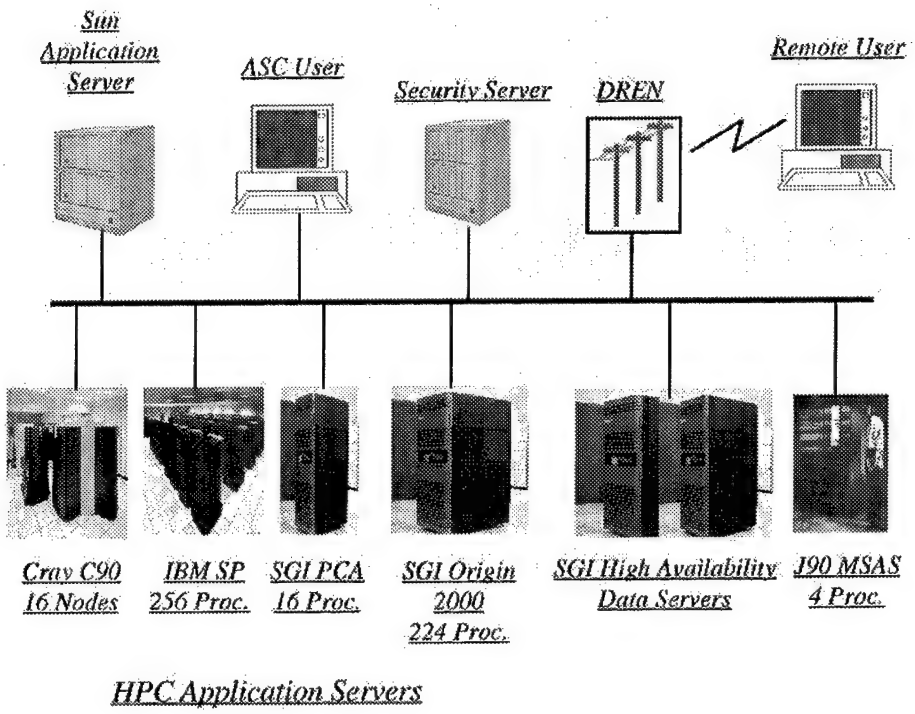

Figure 4.45 Stylized View of the ASC MSRC.

done using LUFACTOR for comparison purposes. Next, one run per target would use the dimension tolerances determined in Section 4.1.1. Finally, two runs per target would be accomplished for material measurement uncertainty. It should be noted that each target was not limited to the runs described above. Additionally, all the runs previously listed were not accomplished for some of the targets for various reasons that will be presented. The following subsections detail the runs for each target.

For this research it was assumed that the materials are lossless ($\epsilon'' = 0$) and that they are non-ferromagnetic, resulting in a permeability of free space ($\mu' - j\mu'' = 1 - j0$). Thus, the materials are characterized by the dielectric constant or relative permittivity (ϵ'). From Table 4.2, the average ϵ' for the polyethylene is 2.35, which is used for purposes of this validation, independent of frequency. Furthermore, the uncertainty used herein is provided by the standard deviation. For the polyethylene, the maximum standard deviation is nearly 0.02, therefore each target will have at least one run for a relative permittivity of 2.33 and 2.37. Likewise, the average relative permittivity of the polyurethane is 1.04 with a maximum standard deviation of ± 0.04.

While running 3D-RCIE it became apparent that the matrices were quite large and required a lot of memory because of the electrical size of the targets. This became a problem for the larger targets. As a rule of thumb, the linear mesh rate is generally desired to be greater than $10/\lambda$, especially for penetrable bodies. However, errors occurred on certain runs even though the IBM has 1 GB of RAM and access to another 1 GB of memory. Two errors were noted. Both LUFACTOR and BLGMRP would return an error that there was not enough memory available to solve the given problem. Also, an erroneous value error of 22 was noted while reading in the matrix by BLGMRP on certain runs. Consistency in these errors did not seem to occur. For example, The conesphere with a mesh rate of $16.7/\lambda$ had a matrix rank of 17328 and a matrix size of 2.4 GB, but could not be solved. On the other hand, the large polyethylene cube with a mesh rate of $11.5/\lambda$ and a matrix rank of 12696 could be solved even though the matrix size was 3.7 GB. Although considerable time and effort was spent discussing these errors with authorities on 3D-RCIE and the IBM SP, a complete understanding of the problems was never determined. In the end, the largest meshing rate for each geometry was determined by trial and error.

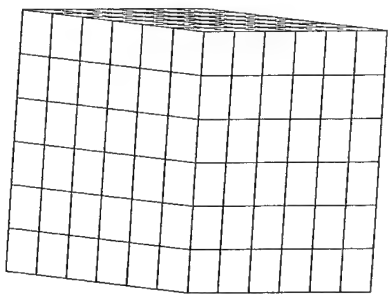

Figure 4.46 Small Cube Mesh (mesh size: 0.01).

The following subsections discuss the results of the code for each target. Provided in each section is a representation of the mesh geometry for each target and a table listing all the runs that were completed. Each table consists of the mesh size, rank of the matrix that was solved, the storage required to store the matrix, the time required to run PULSE2, BLGMRP and LUFACTOR, and the dielectric constant. The time listed for PULSE2 is the time it took, CPU time, to compute the system matrix and excitation vectors, not the RCS from the solved matrix. Computing the RCS by PULSE2 and the generation of the surface patches by MESH were on the order of a few minutes, therefore those times are not included. The large difference in mesh sizes, see Table 4.4, is a result of using the same input file for several frequencies. For example, the same mesh size of 0.003 meters in the input file for the small polyethylene cube results in a mesh size of $50/\lambda$ at 2 GHz and only $12.5/\lambda$ at 8 GHz. A few representative plots are provided, while the complete set is located in Appendix D.

4.3.1.1 Small Cube - Polyethylene. The small polyethylene cube with and without r-card had the most runs completed by 3D-RCIE for several reasons. First, these targets were electrically small resulting in relatively short run times. Second, the small cubes were the first targets that were run for this research so extra runs were accomplished for experimentation purposes. From Table 4.4, the difference in run times is apparent. In general, BLGMRP performed twice as fast as LUFACTOR for the larger matricies. It is also interesting to note the PULSE2 time increases with the matrix size. The code performed very well on the small polyethylene cube with the exception of a few cases. A

Frequency (GHz)	Mesh Size	Matrix Rank	Matrix Size (MB)	PULSE Time (min)	BLGMRP Time (min)	LUFACTOR Time (min)	Dielectric Constant
2	$50/\lambda$	2400	46	3	19	21.6	2.35
4	$25/\lambda$	2400	46	3	19	21.6	2.35
6	$10/\lambda$	864		1	3		2.35
6	$16.7/\lambda$	2400	46	3	19	21.6	2.35
7	$14.3/\lambda$	2400	46	3	19		2.35
8	$12.5/\lambda$	2400	46	3	19		2.35
8	$18.75/\lambda$	5400	233	8.4	105	203	2.35
10	$15/\lambda$	5400	233	8.4	111	203	2.35
10	$15/\lambda$	5400	233	8.4	111		2.33
10	$15/\lambda$	5400	233	8.4	111		2.37
10*	$15/\lambda$	5400	233	8.4	111		2.35
12	$12.5/\lambda$	5400	233	8.4	118	203	2.35
13	$11.5/\lambda$	5400	233	8.4	122		2.35
14	$14.3/\lambda$	9600	737	19	449	1066	2.35
16	$12.5/\lambda$	9600	737	19	472	1066	2.35
18	$11.1/\lambda$	9600	737	19	493	1066	2.35

Table 4.4 RCS matrix for the small polyethylene cube. The * indicates that the cube dimensions were altered by 0.002 inches for this measurement.

good example is Figure 4.47, the RCS at 14 GHz. 3D-RCIE follows the measured data pattern of peaks for HH and valleys for VV at 45 degrees very closely and differs by about 1 dB. A run at 13 GHz was chosen becuase of the very low return at incidence to the face of the cube and the large return from the corner at 45 degrees. From Figure D.8, it can be seen that the code perfomed with very little error at this frequency. At 10 GHz one wavelength matches the length of the cube. From Figure D.6, the code performs well with a maximum of 1 dB separation at the corners for HH and faces for VV. From Figure C.9, the measured uncertainty bounds at 10 GHz for HH is ± 0.2 dBsm and ± 0.3 dBsm for VV. The code performed poorly at 2 and 18 GHz, Figures D.1 and D.11, respectively. At the lower frequencies the measured return was very noisy which may account for some error. A higher meshing rate may have produced better results at 18 GHz. Uncertainty resulting from different sizes of cube lengths were explored for 6 and 8 GHz in Figures D.12 and D.13, respectively. For these two cases, relatively substantial changes in the mesh size, 16.7 and $10/\lambda$ for 6 GHz and 18.75 and $12.5/\lambda$ for 8 GHz, had almost no affect on the RCS.

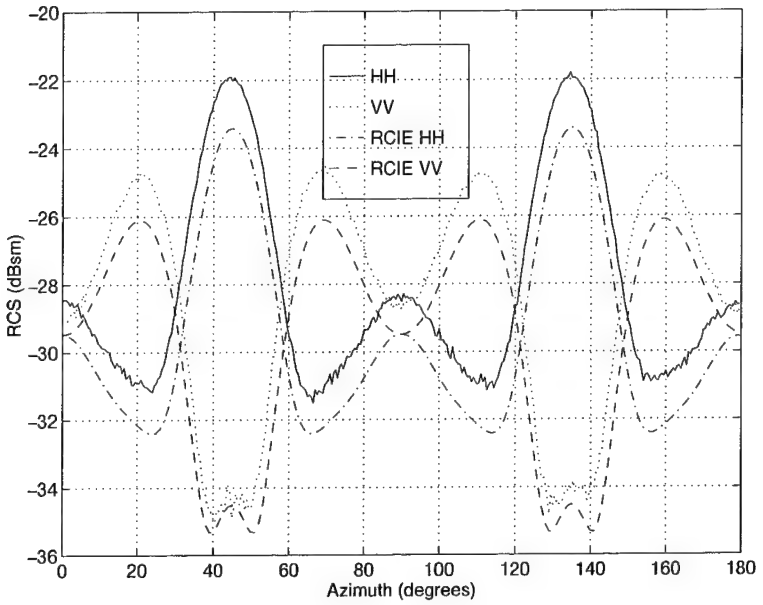

Figure 4.47 The monostatic RCS of the small polyethylene cube using 3D-RCIE and measured data obtained at 14 GHz. The mesh size is $14.3/\lambda$ and BLGMRP was used to solve the matrix.

Figures D.14 and D.15 compare changes in the dielectric constant for both polarizations at 10 GHz. The dimension error is presented in Figure D.16 at 10 GHz. Almost no difference is noted except for HH at the faces of the cube.

BLGMRP and LUFACTOR were compared at each frequency. The results are presented in Figures D.17 through D.25. For this target, BLGMRP matched LUFACTOR exactly.

All-in-all, 3D-RCIE performed very well on this target. The only exceptions noted were at 2 and 18 GHz. Furthermore, very little uncertainty is introduced do to mesh size, target dimension error, material property measurements, and using BLGMRP.

4.3.1.2 Small Cube - Polyethylene With R-card. The same runs completed on the small polyehtylene cube without r-card were also made for the same target with the addition of the $1500\Omega/square$ r-card. Unlike the previous target, the code did not match the measured RCS well. In general, the results from the code tended to follow the RCS measured pattern but they were not equal. A good example is at 7 GHz. In Figure 4.48

Frequency (GHz)	Mesh Size	Matrix Rank	Matrix Size (MB)	PULSE Time (min)	BLGMRP Time (min)	LUFACTOR Time (min)	Dielectric Constant
2	$50/\lambda$	2400	46	3	25	21.6	2.35
4	$25/\lambda$	2400	46	3	26	21.6	2.35
6	$10/\lambda$	864		1	7		2.35
6	$16.7/\lambda$	2400	46	3	28	21.6	2.35
7	$14.3/\lambda$	2400	46	3	29		2.35
8	$12.5/\lambda$	2400	46	3	32		2.35
8	$18.75/\lambda$	5400	233	8.5	145	203	2.35
10	$15/\lambda$	5400	233	8.5	154	203	2.35
10	$15/\lambda$	5400	233	8.5		203	2.33
10	$15/\lambda$	5400	233	8.5		203	2.37
10*	$15/\lambda$	5400	233	8.5		203	2.35
12	$12.5/\lambda$	5400	233	8.5	164	203	2.35
13	$11.5/\lambda$	5400	233	8.5	173		2.35
14	$14.3/\lambda$	9600	737	19	597	1065	2.35
16	$12.5/\lambda$	9600	737	19	626	1065	2.35
18	$11.1/\lambda$	9600	737	19	698	1065	2.35

Table 4.5 RCS matrix for the small polyethylene cube with r-card. The * indicates that the cube dimensions were altered by 0.002 inches for this measurement.

it can be seen that the code follows the measured RCS, but it's off by as much as 5 dB at the peaks and even more at the nulls.

Similar to the small polyethylene cube without the r-card, the uncertainty caused by mesh sizes, material properties, dimension tolerances, and BLGMRP is very small. Figures D.37 and D.38 plot the RCS using different mesh sizes at 6 and 8 GHz, resulting in very little difference. The changes in the dielectric constant, Figures D.39 and D.40, are also fairly small. In Figure D.41, the size of each side was increased by 0.002 inches and virtually no difference in the RCS was noted. Finally, Figures D.42 through D.50 show that BLGMRP and LUFACTOR return the same results for this target.

Concluding that 3D-RCIE does not perform well on dielectrics coated with r-card should not be determined from this one target. First, the r-card surface impedance utilized was not measured but taken from the manufacturer's data. Second, the r-card was secured to the target with mylar tape on the outside and not with adhesive. Thus, gaps between the r-card and material may have existed.

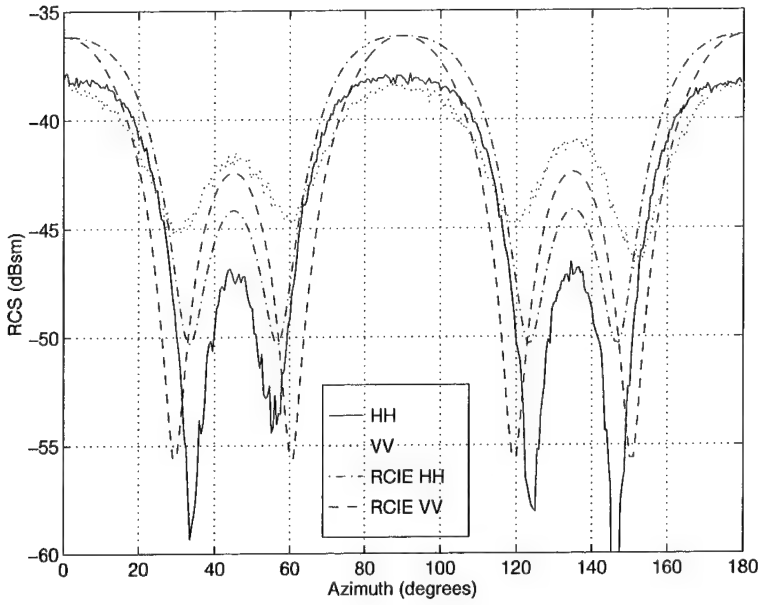

Figure 4.48 The monostatic RCS of the small polyethylene cube with r-card using 3D-RCIE and measured data obtained at 7 GHz. The mesh size is $14.3/\lambda$ and BLGMRP was used to solve the matrix.

4.3.1.3 Small Cube - Polyurethane. The small polyurethane cube had runs completed at each frequency as previously specified and one at 10 GHz using the dimension tolerances, as seen in Table 4.6. Comparisons between BLGMRP and LUFACTOR were not accomplished because the same geometry in the previous sections had resulted in no differences between the two. The comparison results between the measured data and that of 3D-RCIE for this target were very poor. Figure 4.49 contains all the negative features seen throughout the runs. First, it is apparent that 3D-RCIE and the measured data aren't even close. Second, the measured data is very noisy. Finally, the measured data isn't symmetric.

The code predictions of this target may be in error due to the dielectric constant used. The dielectric constant of 1.04 may not be a true representation of the material. The noisy and non-symmetric measured data, as discussed in Seciton 4.2.2.2, is a result of the inability to properly fabricate the target and the low RCS return. Evidence of the dimension uncertainty can be seen in Figure D.60. A change of 0.04 inches per side results in large difference in RCS returns. The largest source of error is probably a result of the

Frequency (GHz)	Mesh Size	Matrix Rank	Matrix Size (MB)	PULSE Time (min)	BLGMRP Time (min)	LUFACTOR Time (min)	Dielectric Constant
2	$50/\lambda$	2400	46	3	19		1.04
4	$25/\lambda$	2400	46	3	18		1.04
6	$16.7/\lambda$	2400	46	3	18		1.04
8	$12.5/\lambda$	2400	46	3	17		1.04
10	$15/\lambda$	5400	233	8	97		1.04
10*	$15/\lambda$	6144	302	10	134		1.04
12	$12.5/\lambda$	5400	233	8	97		1.04
14	$10.7/\lambda$	5400	233	8	98		1.04
16	$9.4/\lambda$	5400	233	8	98		1.04
18	$8.3/\lambda$	5400	233	8	98		1.04

Table 4.6 RCS matrix for the small polyurethane cube. The * indicates that the cube dimensions were altered by 0.04 inches for this measurement.

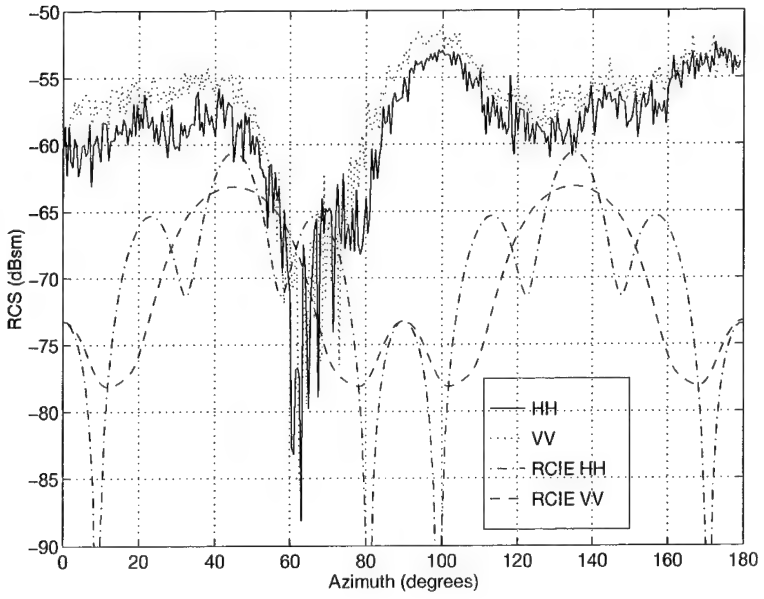

Figure 4.49 The monostatic RCS of the small polyurethane cube using 3D-RCIE and measured data obtained at 10 GHz. The mesh size is $15/\lambda$ and BLGMRP was used to solve the matrix.

Frequency (GHz)	Mesh Size	Matrix Rank	Matrix Size (MB)	PULSE Time (min)	BLGMRP Time (min)	LUFACTOR Time (min)	Dielectric Constant
2	$50/\lambda$	2400	46	3	25		1.04
4	$25/\lambda$	2400	46	3	22		1.04
6	$16.7/\lambda$	2400	46	3	22		1.04
8	$12.5/\lambda$	2400	46	3	23		1.04
10	$15/\lambda$	5400	233	9	120		1.04
10*	$15/\lambda$	6144	302	10	167		1.04
12	$12.5/\lambda$	5400	233	9	125		1.04
14	$10.7/\lambda$	5400	233	9	125		1.04
16	$9.4/\lambda$	5400	233	9	129		1.04
18	$8.3/\lambda$	5400	233	9	133		1.04

Table 4.7 RCS matrix for the small polyurethane cube with r-card. The * indicates that the cube dimensions were altered by 0.04 inches for this measurement.

very low predicted RCS return, which is below the subtracted noise floor of the chamber. Furthermore, the separation between the measured RCS and the noise floor is very small resulting in a large uncertainty. Use of the small polyurethane cube for validation purposes is not acceptable.

4.3.1.4 Small Cube - Polyurethane With R-card. The small polyurethane cube with r-card had similar poor results as the polyurethane cube without r-card. In addition to the uncertainties listed in the previous section, the uncertainty due to the manufacture's value of the r-card and its application process to the target are now factors. The results, Figures D.61 through D.69, show the differences between the measured and calculated results. This target should not be used for validation purposes.

4.3.1.5 Large Cube - Polyethylene. The large polyethylene cube had a limited number of runs accomplished, Table 4.8, for several reasons. First, this target was one of the last ones to be run and time on the IBM was limited. Second, the smallest mesh rate that could run, 0.013 meters, did not allow a favorable linear mesh rate at frequencies above 4 GHz. The runs that were accomplished provided very good results. Figure 4.50 is the large cube at 2 GHz. For VV only two areas, 18 and 45 degrees, show any significant difference, and that is less than 2 dB. HH has a relatively constant difference, also less

Frequency (GHz)	Mesh Size	Matrix Rank	Matrix Size (MB)	PULSE Time (min)	BLGMRP Time (min)	LUFACTOR Time (min)	Dielectric Constant
2	$10/\lambda$	9600	737	20	516		2.35
2	$11.5/\lambda$	12696	3760	31	994		2.35
2	$10/\lambda$	9600	737	20	520		2.33
2	$10/\lambda$	9600	737	20	527		2.37
2*	$10/\lambda$	9600	737	20	516		2.35
4	$5/\lambda$	9600	737	20	780		2.35

Table 4.8 RCS matrix for the large polyethylene cube. The * indicates that the cube dimensions were altered by 0.005 inches for this measurement.

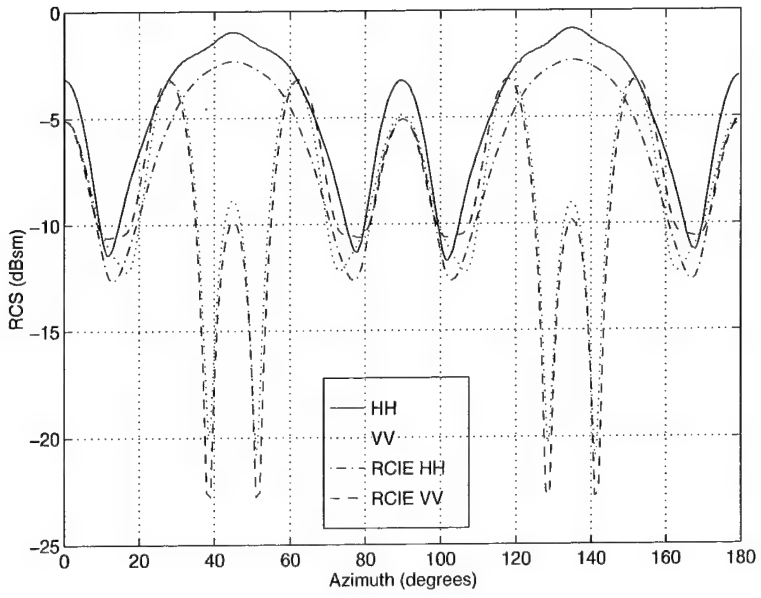

Figure 4.50 The monostatic RCS of the large polyethylene cube using 3D-RCIE and measured data obtained at 2 GHz. The mesh size is $10/\lambda$ and BLGMRP was used to solve the matrix.

Frequency (GHz)	Mesh Size	Matrix Rank	Matrix Size (MB)	PULSE Time (min)	BLGMRP Time (min)	LUFACTOR Time (min)	Dielectric Constant
2	$10/\lambda$	9600	737	19	363	1064	1.04
2*	$10/\lambda$	9600	737	19	368		1.04
4	$5/\lambda$	9600	737	19	363		1.04

Table 4.9 RCS matrix for the large polyurethane cube. The * indicates that the cube dimensions were altered by 0.2 inches for this measurement.

than 2 dB, but the patterns of the measured and calculated data match well. At this frequency, the error bounds from Figure C.11 are only ± 0.4 and 0.3 dBsm for HH and VV, respectively. At 4 GHz, Figure D.71, the RCS has more features but both HH and VV match fairly well. Figures D.72 and D.73 show comparisons of altering the mesh size and utilizing the dimension tolerances. Very little difference is noted. Differences in the dielectric constant at 2 GHz are presented in Figures D.74 and D.75. For HH there is very little difference, but changes in ϵ' are noticeable at 18 and 45 degrees for VV. Note that these are the locations of the differences between the measured and calculated data for VV at 2 GHz.

4.3.1.6 Large Cube - Polyurethane. Like the previous target, the large polyurethane cube had limited runs for the same reasons. At 2 and 4 GHz, Figures D.76 and D.77 respectively, the code and measured results do not compare well. Similarly, poor results were achieved with the other polyurethane targets so a run using LUFACTOR was performed to verify that large error was not due to a specific matrix solving routine. As presented in Figure D.79, both BLGMRP and LUFACTOR returned the same solution.

In Figure D.78, the RCS is compared for an increase of 0.2 inches per side resulting in drastically different returns. Obviously, the dimension error of this target introduces a lot of uncertainty into the RCS. This target should not be used for validation purposes.

4.3.1.7 Sphere - Polyethylene. The polyethylene sphere also had limited runs because of restricted IBM SP time, coarse mesh rate, poor measured RCS data, and poor results. The RCS of a sphere is independent of azimuth angle, but the 3D-RCIE predicted return is not (Figure 4.52). Both polarizations have relatively large fluctuations

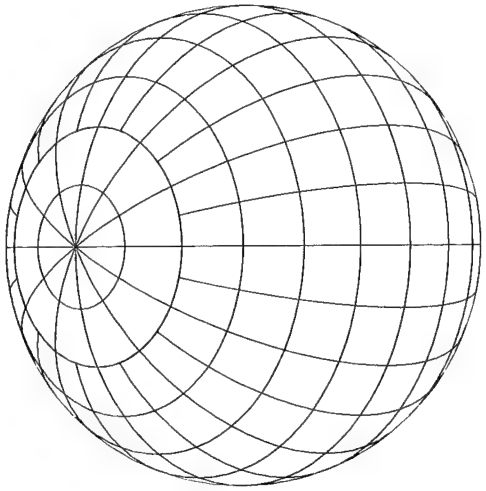

Figure 4.51 Sphere Mesh (mesh size: 0.03).

Frequency (GHz)	Mesh Size	Matrix Rank	Matrix Size (MB)	PULSE Time (min)	BLGMRP Time (min)	LUFACTOR Time (min)	Dielectric Constant
2	$10/\lambda$	4032	130	5	72	89	2.35
2	$16.7/\lambda$	11760	1100	27	735		2.35
2*	$10/\lambda$	4032	130	5	72		2.35

Table 4.10 RCS matrix for the sphere. The * indicates that the sphere dimensions (diameter) were altered by 0.1 inches for this measurement.

with a maximum for HH of nearly 2.5 dB in only 25 degrees! Obviously, this is a result of the way MESH describes the geometry (Figure 4.51). PEC spheres of smaller sizes, which are not presented here, were tested at finer linear mesh rates and similar patterns were observed, although the fluctuations were much smaller in amplitude. A reasonable approach may be to average the data. An average for HH and VV is -10.13 and -10.22 dBsm, respectively, which is only 1 dB lower than the measured data. A run with a finer linear mesh rate was also done at 2 GHz, Figure D.81, and similar fluctuating results were obtained. For this case, HH and VV averaged -9.82 and -10.09 dBsm, respectively, which is even closer to the measured data. The Mie series solution at 2 GHz is -9.4 dBsm.

The uncertainty caused by dimension tolerances is plotted in Figure D.82. Even though the dimension error was large for this target, the RCS only changed by a tenth of a dB. LUFACTOR was also used to solve the matrix for this target, Figure D.83, and no

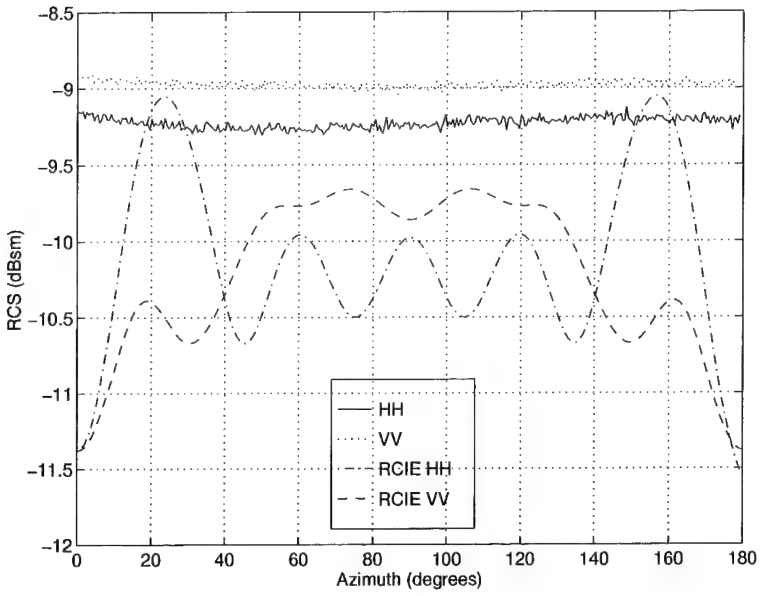

Figure 4.52 The monostatic RCS of the polyethylene sphere using 3D-RCIE and measured data obtained at 2 GHz. The mesh size is $10/\lambda$ and BLGMRP was used to solve the matrix.

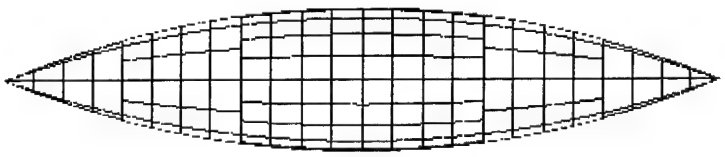

Figure 4.53 Ogive Mesh (mesh size:0.01).

difference was noted. It appears that fluctuations in the RCS are due to this particular geometry, but averaging the data is a good approximation of the true RCS.

4.3.1.8 Ogive. The code performed very well on the ogive for frequencies 10 GHz and below. All the runs, less one at 6 GHz and two at 10 GHz, were all completed with the with the same mesh size of 0.003 meters. This was the smallest size that could be solved without receiving any errors. With this mesh size the ideal $10/\lambda$ is achieved for 10 GHz and below.

For the lower frequencies, the code had trouble around the tips. In Figure 4.54, the RCS at 6 GHz, the main difference between the two results is within the first 20

Frequency (GHz)	Mesh Size	Matrix Rank	Matrix Size (MB)	PULSE Time (min)	BLGMRP Time (min)	LUFACTOR Time (min)	Dielectric Constant
2	$50/\lambda$	14784	1750	40	1081		2.35
4	$25/\lambda$	14784	1750	40	1107		2.35
6	$10/\lambda$	5616	252	9	122	226	2.35
6	$16.7/\lambda$	14784	1750	40	1186		2.35
8	$12.5/\lambda$	14784	1750	40	1263		2.35
10	$10/\lambda$	14784	1750	40	1354		2.35
10	$10/\lambda$	14784	1750	40	1341		2.33
10	$10/\lambda$	14784	1750	40	1354		2.37
10*	$10/\lambda$	14784	1750	40	1354		2.35
10	$7.5/\lambda$	8976	644	17	403	873	2.35
12	$8.33/\lambda$	14784	1750	40	1393		2.35
14	$7.1/\lambda$	14784	1750	40	1432		2.35
16	$6.25/\lambda$	14784	1750	40	1445		2.35
18	$5.6/\lambda$	14784	1750	40	1484		2.35

Table 4.11 RCS matrix for the ogive. The * indicates that the ogive dimensions were altered by 0.005 inches for this measurement.

degrees from the tip. As the frequency increases, this discrepancy also increases. The error bounds, Figure C.15, at this frequency are generally less than ± 0.5 dBsm, even at the tips. Another note is that at 180 degrees, 3D-RCIE should be predicting the same RCS for both polarizations, but it is not. Again, as frequency increases, this difference also increases. This difference is particularly large, 10 dB, at 16 GHz (see Figure D.110). Colby mentioned that a problem with 3D-RCIE is trouble it has with traveling waves [7]. At broadside, 90 degrees, this geometry would be expected to propagate this phenomena for VV in the resonant region. At 6 GHz, the diameter of the ogive is approximately one wavelength, or the start of the resonant region. From Figure 4.54, it can be seen that VV matches very well at and near broadside at 6 GHz. In fact, this is true up to 10 GHz. As the frequency increases the features from the measured data increase. At which point 3D-RCIE tends to vary quite a bit. This is evident in Figure D.110. It is also noted that at 14-18 GHz, VV is not symmetric about 90 degrees, as would be expected.

Uncertainty in the RCS due to uncertainty in the dimensions is nonexistent (Figure D.113). Additionally, changes in the dielectric constant have very little effect on the

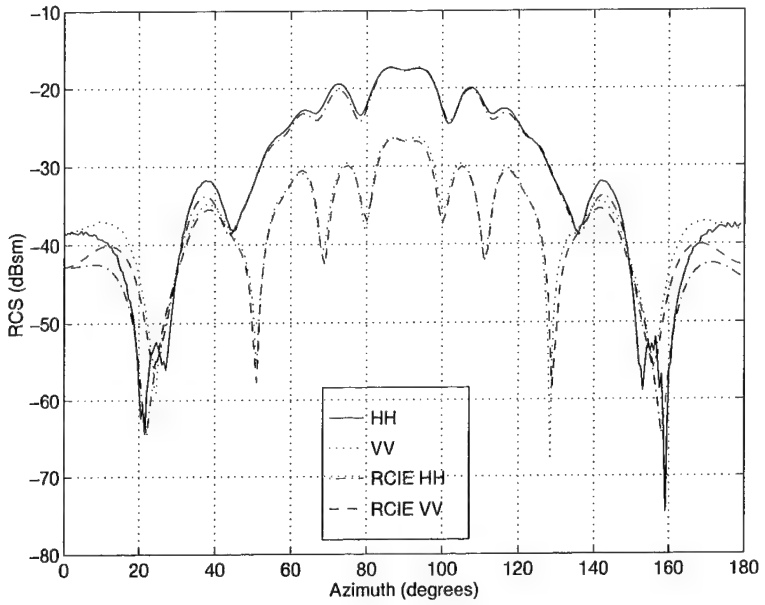

Figure 4.54 The monostatic RCS of the ogive using 3D-RCIE and measured data obtained at 6 GHz. The mesh size is $16.7/\lambda$ and BLGMRP was used to solve the matrix.

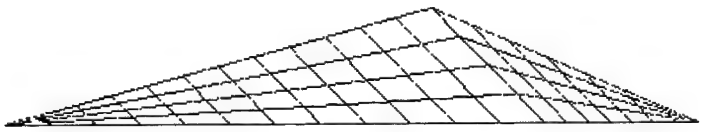

Figure 4.55 Mini-Arrow Mesh (mesh size: 0.015).

RCS (Figure D.114 and D.115). A larger effect on the RCS is the change in mesh sizes. This is evident in Figure D.112. In this case, the RCS from 3D-RCIE is plotted for two mesh sizes at 6 GHz: $16.7/\lambda$ and $10/\lambda$. The main disagreement is around the nose at which point the $16.7/\lambda$ is closer to the actual. However, disagreement between the two are present throughout. Thus, for this geometry a smaller linear mesh rate for the higher frequencies would probably produce more accurate results.

4.3.1.9 Mini-Arrow - Polyethylene. The polyethylene mini-arrow proved to be very challenging for 3D-RCIE to predict. The mini-arrow was only measured up to 10 GHz, Table 4.12, because of the poor performance of the code and the limited linear mesh rate. The smallest mesh rate that could be solved was 0.005 meters. Figure 4.56 is the

Frequency (GHz)	Mesh Size	Matrix Rank	Matrix Size (MB)	PULSE Time (min)	BLGMRP Time (min)	LUFACTOR Time (min)	Dielectric Constant
2	$30/\lambda$	8928	638	19	682		2.35
4	$15/\lambda$	8928	638	19	552		2.35
6	$10/\lambda$	8928	638	19	552	860	2.35
6	$10/\lambda$	8928	638	19	508		2.33
6	$10/\lambda$	8928	638	19	535		2.37
6*	$10/\lambda$	8928	638	19	248		2.35
6	$8.3/\lambda$	6320	320	12	196		2.35
8	$7.5/\lambda$	8928	638	19	587		2.35
10	$6/\lambda$	8928	638	19	572		2.35

Table 4.12 RCS matrix for the mini-arrow. The * indicates that the mini-arrow dimensions were altered by 0.0025 inches for this measurement.

RCS of the mini-arrow at 6 GHz and is representative of each return. The measured RCS for both polarizations showed the strongest frequency independent returns around 110 to 115 degrees, presumably due to internal reflections from the back face. 3D-RCIE didn't match this return but predicted a larger return at broadside, 90 degrees. For 8 and 10 GHz, this return tends to shift to a slightly higher azimuth angle, Figures D.87 and D.88. The uncertainty in the measured data at 6 GHz, Figure C.13, is very large from 0 to 20 and 140 to 180 degrees. However, this does not explain the significant differences from 20 to 140 degrees. In general, the RCS patterns of the measured and predicted data do not match well except at 2 GHz (Figure D.84).

To check the uncertainty of the predictions, runs were accomplished using LUFACTOR, different mesh sizes, dimension tolerances, and varied dielectric constants. Figure D.89 shows that BLGMRP and LUFACTOR produce the same results. Altering the dimensions by 0.0025 inches, Figure D.91, also had very little effect. Additionally, varying the dielectric constant produced almost no difference (Figures D.92 and D.93). However, a rather significant change in the RCS was produced by varying the mesh size, Figure D.90, with the largest difference noted around 0 and 180 degrees. A smaller mesh size might improve the overall 3D-RCIE return for a good portion of the return, but it does not mitigate the strong return at broadside.

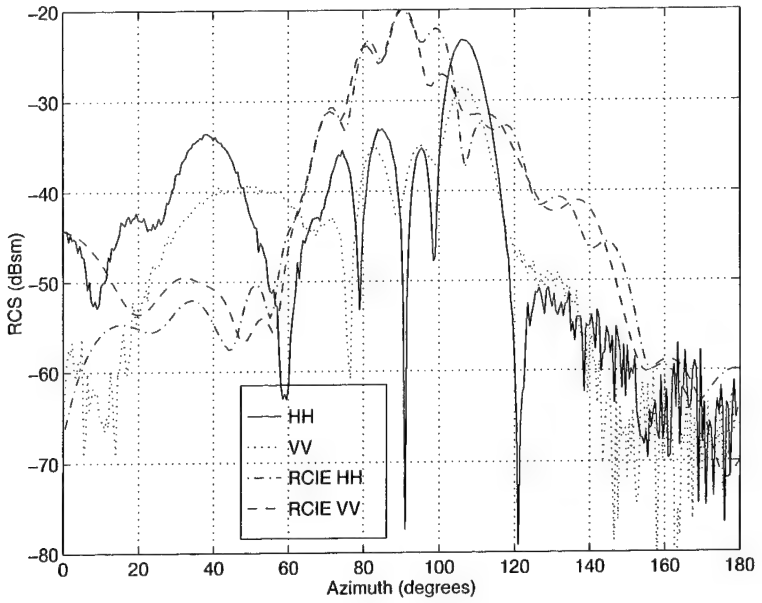

Figure 4.56 The monostatic RCS of the polyethylene mini-arrow using 3D-RCIE and measured data obtained at 6 GHz. The mesh size is $10/\lambda$ and BLGMRP was used to solve the matrix.

4.3.1.10 Mini-Arrow - Polyethylene With R-card. The same runs accomplished for the mini-arrow were also done for the mini-arrow with r-card applied, with one exception; BLGMRP would not converge so LUFACTOR was used. The maximum number of iterations for BLGMRP is defaulted to 30. This value was increased to 100, but convergence was still not achieved. The results to this target are very similar to the mini-arrow without any r-card applied.

The uncertainty due to dimension tolerances and changes in the dielectric constants, Figures D.100, D.101 and D.102, is very little. Changing the mesh size, Figure D.99, resulted in large RCS changes around 0 and 180 degrees. For this target, the largest return was measured at 80 degrees, which was probably due to reflections from the front face of the mini-arrow. For the most part, 3D-RCIE predicted this return fairly well (See Figures D.94 through D.98). However, the code again predicted very large broadside returns which are not present in the measured data. Additionally, relatively strong returns were predicted at 110 degrees, which also is not present in the measured data.

Frequency (GHz)	Mesh Size	Matrix Rank	Matrix Size (MB)	PULSE Time (min)	BLGMRP Time (min)	LUFACTOR Time (min)	Dielectric Constant
2	$30/\lambda$	8928	638	19		860	2.35
4	$15/\lambda$	8928	638	19		860	2.35
6	$10/\lambda$	8928	644	19		860	2.35
6	$10/\lambda$	8928	638	19		860	2.33
6	$10/\lambda$	8928	638	19		860	2.37
6*	$10/\lambda$	8928	638	19		860	2.35
6	$8.3/\lambda$	6320	320	12		317	2.35
8	$7.5/\lambda$	8928	638	19		860	2.35
10	$6/\lambda$	8928	638	19		860	2.35

Table 4.13 RCS matrix for the mini-arrow with r-card. The * indicates that the mini-arrow dimensions were altered by 0.0025 inches for this measurement.

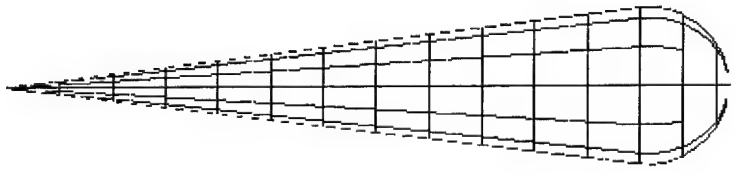

Figure 4.57 Conesphere Mesh (mesh size: 0.05).

Frequency (GHz)	Mesh Size	Matrix Rank	Matrix Size (MB)	PULSE Time (min)	BLGMRP Time (min)	LUFACTOR Time (min)	Dielectric Constant
2	$10/\lambda$	5856		10	140	255	2.35
2	$15/\lambda$	13536	1470	36	957		2.35
2	$15/\lambda$	13536	1470	36	1083		2.33
2	$15/\lambda$	13536	1470	36	957		2.37
2*	$15/\lambda$	13536	1470	36	936		2.35
4	$7.5/\lambda$	13536	1470	36	1072		2.35
6	$5/\lambda$	13536	1470	36	1136		2.35
8	$3.75/\lambda$	13536	1470	36	1320		2.35
10	$3/\lambda$	13536	1470	36	1280		2.35
12	$2.5/\lambda$	13536	1470	36	1188		2.35
14	$2.1/\lambda$	13536	1470	36	1040		2.35
16	$1.9/\lambda$	13536	1470	36	925		2.35
18	$1.7/\lambda$	13536	1470	36	831		2.35

Table 4.14 RCS matrix for the conesphere. The * indicates that the conesphere dimensions were altered by 0.005 inches for this measurement.

4.3.1.11 Cone-Sphere - Polyethylene. The smallest linear mesh rate that could be run for the conesphere was 0.01 meters. This resulted in only the 2 GHz runs achieving mesh rates of $10/\lambda$ or better, as seen in Table 4.14. At this same frequency, the code agreed well with measured data as far as the pattern is concerned (see Figure 4.58). Generally there is a difference of around 2 dB, except towards the tip, where HH has a rather large separation. The measurement uncertainty at 2 GHz from Figure C.17 is only ± 0.3 dBsm for both polarizations. Furthermore, the code prediction at nose on, 180 degrees, is lower by 7 dB for both polarizations. This was also a problem with the ogive at nose on. As the frequency increases, the differences between the measured and predicted values are very large.

Varying the dimensions of the conesphere had very little effect on the RCS, as seen in Figure D.127. In Figure D.126 two different mesh sizes were plotted at 2 GHz resulting in a noticeable difference. Changing the dielectric constant had a relatively small effect on the results except around the tip. At that point, Figures D.128 and D.129, there is quite a discrepancy in both polarizations. This may account for some of the differences seen in

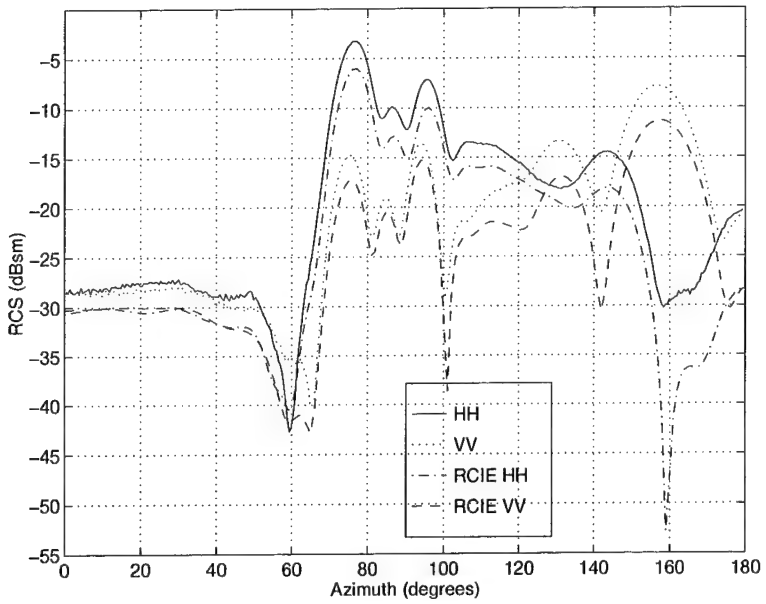

Figure 4.58 The monostatic RCS of the conesphere using 3D-RCIE and measured data obtained at 2 GHz. The mesh size is $15/\lambda$ and BLGMRP was used to solve the matrix.

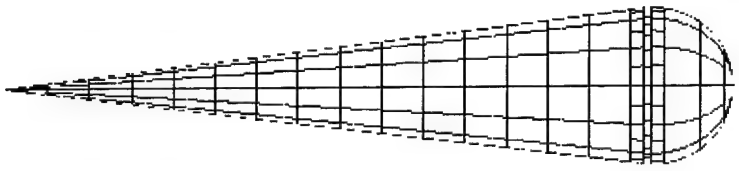

Figure 4.59 Conesphere With a Gap Mesh (mesh size: 0.04).

the same area in Figure 4.58. In Figure D.130, BLGMRP and LUFACTOR showed no differences.

For this target, the code performed fairly well for the correct size linear mesh rate. The importance of choosing this parameter carefully coupled with the ability to solve a matrix of resulting size is apparent when considering the results presented. Similar results obtained at 2 GHz would probably be obtained at all frequencies if the appropriate mesh rate were used to solve the problem. The code did show some difficulties around the tip, as was also noted with the tip of the ogive.

4.3.1.12 Cone-Sphere With a Gap - Polyethylene. The results from the conesphere with a gap are very similar to the conesphere. Due to the addition of the

Frequency (GHz)	Mesh Size	Matrix Rank	Matrix Size (MB)	PULSE Time (min)	BLGMRP Time (min)	LUFACTOR Time (min)	Dielectric Constant
2	$10/\lambda$	7008		13	201	427	2.35
2	$13.6/\lambda$	12552	1260	33	792		2.35
2	$13.6/\lambda$	12552	1260	33	792		2.33
2	$13.6/\lambda$	12552	1260	33	792		2.37
2*	$13.6/\lambda$	12552	1260	33	811		2.35
4	$6.8/\lambda$	12552	1260	33	914		2.35
6	$4.5/\lambda$	12552	1260	33	1062		2.35
8	$3.4/\lambda$	12552	1260	33	1158		2.35
10	$2.7/\lambda$	12552	1260	33	1064		2.35
12	$2.3/\lambda$	12552	1260	33	1035		2.35
14	$1.9/\lambda$	12552	1260	33	970		2.35
16	$1.7/\lambda$	12552	1260	33	876		2.35
18	$1.5/\lambda$	12552	1260	33	783		2.35

Table 4.15 RCS matrix for the conesphere with a gap. The * indicates that the conesphere with a gap dimensions were altered by 0.005 inches for this measurement.

gap, the smallest mesh size that could be run for this target was 0.011 meters. Like the conesphere, the only good comparison between 3D-RCIE and the measured data occurred at 2 GHz, Figure D.131. At this frequency both polarizations match the measured results well, less HH as the tip approaches normal incidence. The difference between the predicted and measured results is generally around 3 dB and a larger difference, around 7 dB, is also present on the tip at 180 degrees, which has been noted for the conesphere and ogive. As the frequency increases, the predicted results deteriorate.

Altering ϵ', Figures D.142 and D.143, did little to change the results as did increasing the overall size of the target by 0.005 inches, Figure D.141. Also, LUFACTOR and BLGMRP returned the same results, Figure D.144. Using different mesh sizes at 2 GHz, Figure D.140, did result in distinguishable differences. Again, if proper mesh sizes were utilized then accurate results would probably be attainable for the other frequencies.

4.3.1.13 Summary of 3D-RCIE Performance. A strong limitation of 3D-RCIE is the time required to produce the RCS. In each table the CPU time required to run PULSE2 and solve the resulting matrix, BLGMRP or LUFACTOR, is listed. Small

changes in the linear mesh rate greatly affect the time it takes to run these programs. For example, in Table 4.11, the ogive was run at 6 GHz for a linear mesh rate of $10/\lambda$ (.005 meters) and $16.7/\lambda$ (.003 meters). From $10/\lambda$ to $16.7/\lambda$, the matrix rank nearly trippled, the PULSE2 time increased by a factor of 4, and the BLGMRP time increased by a factor of 10. Additionally, the resulting RCS, Figure D.112, shows very little difference between the two returns. Overall, solving the matrix easily requires the largest amount of time. LUFACTOR typically required twice as much time as BLGMRP, and may produce the exact results. Proper mesh size and the choice between LUFACTOR and BLGMRP are target dependent.

In all, 147 runs using 3D-RCIE were presented ranging from 20 to 1524 minutes. In general the code performed well when the proper linear mesh rates were used. Very good RCS predictions were noted at certain frequencies with the polyethylene large and small cubes, ogive, and conespheres. However, the tips of the conesphere and ogive did present some difficulties. 3D-RCIE was also challenged by the mini-arrow and sphere. For most of the geometries, small changes in the permittivity and geometry dimensions had relatively little effect on the RCS. Uncertainty with the r-card value and the polyurethane target fabrication and material characterization did not allow satisfactory comparisons between measured and calculated RCS data.

V. Conclusion and Recommendations

5.1 Conclusions

The targets used in this research included a small and large cube, mini-arrow, ogive, conesphere, conesphere with a gap and a sphere. All the targets were made of polyethylene. Additionally, the small and large cubes were fabricated from polyurethane.

The targets were fabricated at the AFIT Fabrication Shop. The polyethylene proved to be a fairly good material to work with. The cubes and mini-arrow were machined with relatively little error. The BOR's were more difficult to fabricate resulting in larger dimension uncertainty. The sphere acquired the most error. The polyurethane had foam-like qualities which made it difficult to work with. The small and large cubes did not attain precise dimensions.

The properties of the the polyethylene and polyurethane were measured using an X-band waveguide. The measurements for both materials had an undesired oscillation throughout the 4 GHz frequency range. It was determined that the oscillations were a result of reflections from a mismatch between the back adapter and the waveguide. To mitigate the reflections, the data was averaged over the frequency band. Unlike the polyethylene, the polyurethane measurements were not repeatable as a result of the very low dielectric properties of the material and the poor manufacturing tolerances of the sample.

The main objective of my research was to develop an RCS database of dielectric targets. The RCS of all targets was measured from 2 to 18 GHz. Additionally, r-card was applied to the small cubes and the mini-arrow. Less the sphere, the polyethylene targets produced good, symmetric RCS data. The RCS of the sphere proved that the target was not spherical. The difficulty in fabricating targets from polyurethane was proven by the target's RCS. Both cube measurements were not symmetric. Finally, due to uncertainty in the application process of the r-card and uncertainty in its surface impedance, the targets with r-card should not be considered in the database.

To determine the accuracy of the RCS measurements, an uncertainty analysis was accomplished. For this target set, the uncertainty contributions were composed of uncertainty due to background-target interactions, drift, noise-background, and calibration.

The background-target interactions could not be determined from the data because of the nature of the dielectric material. Therefore, a default value that the range carries was used. In general the overall uncertainty was very low, typically less than ± 0.5 dBsm. However, as the return signal approached the subtracted noise floor, the noise-background contribution dominated resulting in a relatively larger overall uncertainties.

A secondary objective of this research was to use the database of dielectric targets to validate a RCS computer prediction code. The code utilized was 3D-RCIE. Most of the targets proved to be electrically large for this code. As a result, runs were completed for each target using the ASC MSRC IBM SP. Code runs on the IBM were limited due to limited access by AFIT. Even on the IBM SP, memory problems were encountered limiting the fidelity of RCS predictions for the larger targets at higher frequencies. In general the code performed well when the proper linear mesh rates were used. Very good RCS predictions were noted at certain frequencies with the polyethylene large and small cubes, ogive, and conespheres. The small polyethylene cube performed within 1 dB of the measured data at all frequencies but 2 and 18 GHz. The large polyethylene cube matched the measured data very well at 2 and 4 GHz with only a 2 dB difference for HH and very little variance for VV. For 10 GHz and below, the ogive generally varied 2 dB from the measured RCS. And, both of the conespheres performed well at 2 GHz with less than a 2 dB discrepancy for both polarizations. 3D-RCIE was challenged by the mini-arrow and sphere. The predicted RCS for the sphere fluctuated with respect to azimuth angle. 3D-RCIE did not perform well on the mini-arrow at any frequency. Uncertainty with the r-card value, the polyurethane target fabrication and material characterization did not allow satisfactory comparisons between measured and calculated RCS data.

5.2 Recommendations

Based upon the results of this thesis, it is recommended that future research continue in the following areas.

First, different targets and materials could be utilized. Other useful targets may include variations on the targets used in this research or others, such as cylinders, disks, and wedges. A practical, well-documented low dielectric material is Teflon. Teflon is typically

easy to acquire and work with. If a foam material is desired due to its very low dielectric constant, it is recommended that only foams with a rigid structure be used. Another consideration when choosing materials and targets is the ability to have the targets fabricated to the desired precision. Utilizing R-card or RAM on a target is another variation, but the property characteristics of that material must be precisely known.

Next, a better method of characterizing the material properties of the target material needs to be used. One such method includes the use of a coaxial line. The washer-shaped specimen is more difficult to fabricate than the specimen for the rectangular waveguide, but the propagation modes are limited allowing a larger frequency range to be measured.

For this research, RCS measurements were limited to monostatic. Of course, bistatic measurements would also provide valuable data. Furthermore, the accuracy of the RCS measurements should be explored. The use of a well validated MoM code would provide an excellent way to validate the RCS measurements.

Finally, several areas of 3D-RCIE need to be explored. First, due to the limited nature of this research, code runs on each target were also limited. More detail on each target should be explored for validation purposes. Second, the code should be run in parallel. Running 3D-RCIE serially was not an efficient use of resources and limited the electrical size of the targets. Additionally, another routine could be used to solve the matrix instead of BLGMRP or LUFACTOR. Next, other targets with flat, faceted designs should be explored. 3D-RCIE did not perform well on the mini-arrow. Last, the electrical size of the targets should be reduced. Limited computer resources did not allow runs of the larger targets at the higher frequencies to be accomplished.

Appendix A. Material Measurements

This appendix is a compilation of the material measurements for the polyethylene and polyurethane. Two samples of polyethylene and three samples of polyurethane were measured five times each using an X-band waveguide. The HP 8510C network analyzer measured S_{11} and S_{21} for each sample from 8 to 12 GHz, in 10 MHz steps averaging 128 measurements per step. From the S-parameter data, an external computer calculated the permittivity and permeability using a Matlab routine.

For each sample, the five measurements of the real and imaginary portion of the permittivity and permeability are plotted. The average of the five measurements per sample and the corresponding standard deviation are also plotted. Finally, all the sample measurements of each material are averaged and plotted.

A.1 Polyethylene

Measurement	Sample	Figure
ϵ'	Average A and B	A.1
ϵ'	A	A.2
ϵ'	Average A	A.3
ϵ'	B	A.4
ϵ'	Average B	A.5
ϵ''	Average A and B	A.6
ϵ''	A	A.7
ϵ''	Average A	A.8
ϵ''	B	A.9
ϵ''	Average B	A.10
μ'	Average A and B	A.11
μ'	A	A.12
μ'	Average A	A.13
μ'	B	A.14
μ'	Average B	A.15
μ''	Average A and B	A.16
μ''	A	A.17
μ''	Average A	A.18
μ''	B	A.19
μ''	Average B	A.20

Table A.1 Listing of the material measurements for polyethylene.

Permittivity - Real Part (ϵ')

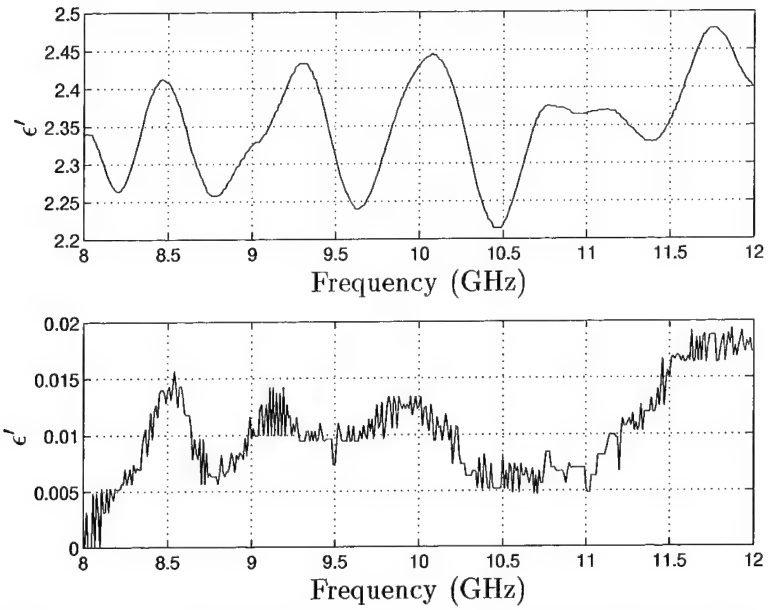

Figure A.1 The Average Permittivity and Standard Deviation of the real part (ϵ') of the Polyethylene Samples.

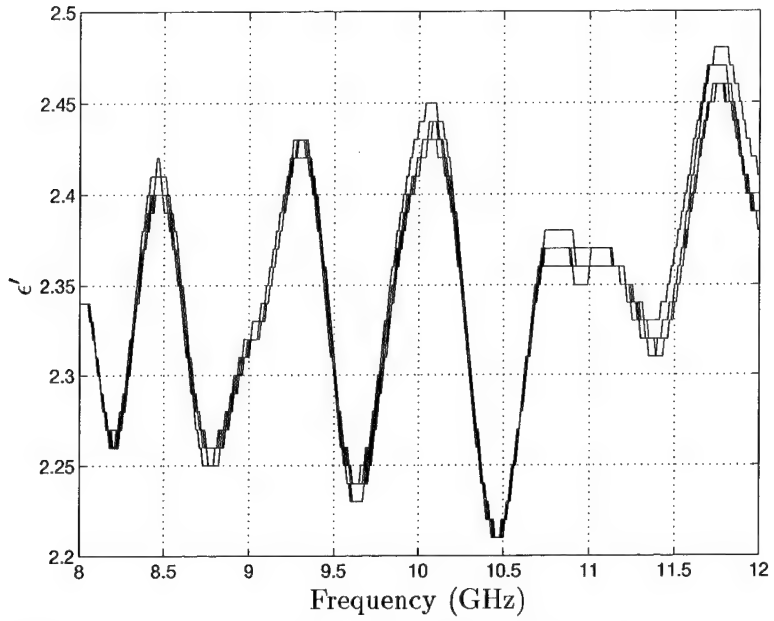

Figure A.2 Permittivity of the real part (ϵ') of Polyethylene Sample A.

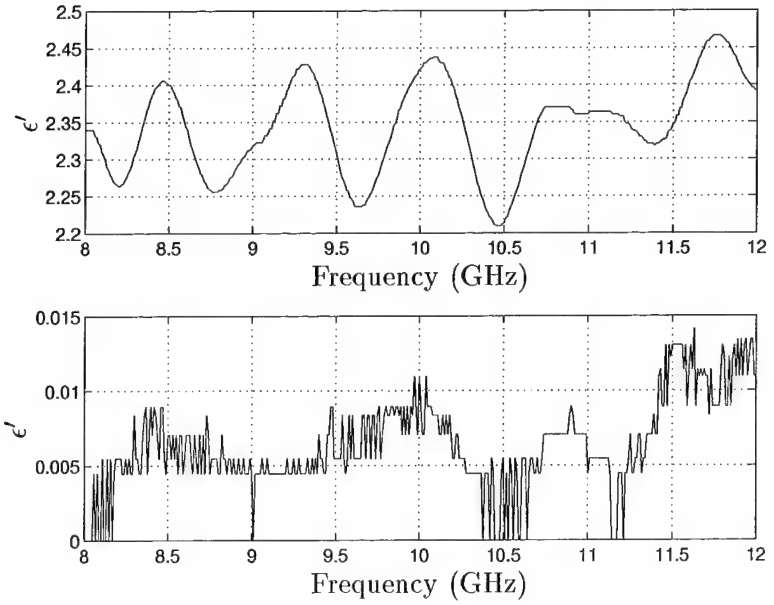

Figure A.3 The Average Permittivity and Standard Deviation of the real part (ϵ') of Polyethylene Sample A.

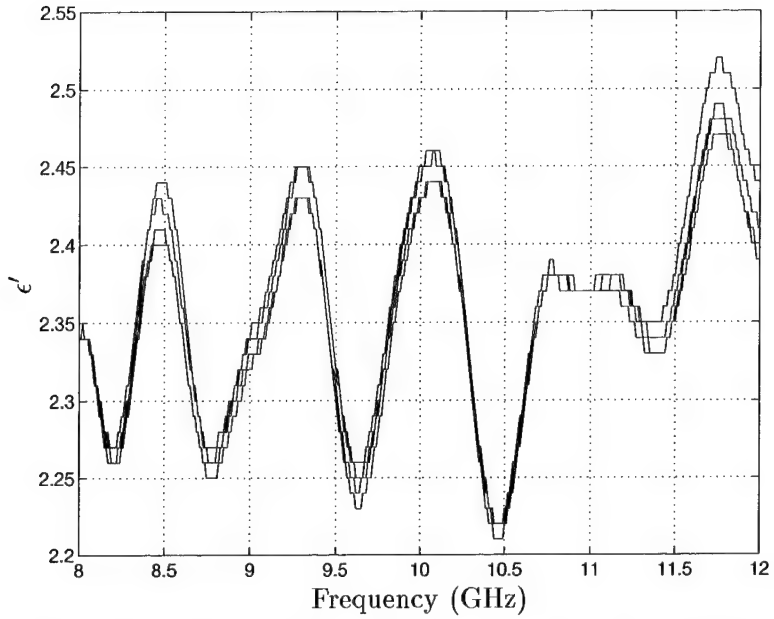

Figure A.4 Permittivity of the real part (ϵ') of Polyethylene Sample B.

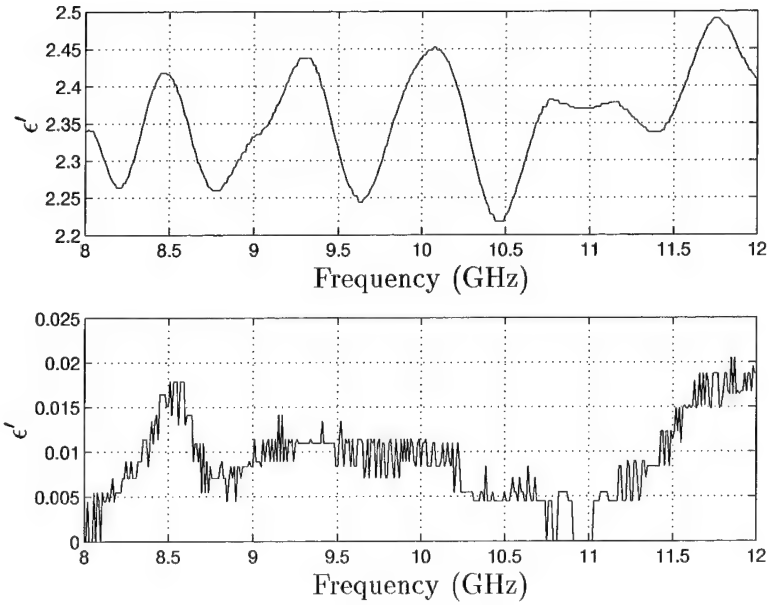

Figure A.5 The Average Permittivity and Standard Deviation of the real part (ϵ') of Polyethylene Sample B.

Permittivity - Imaginary Part (ϵ'')

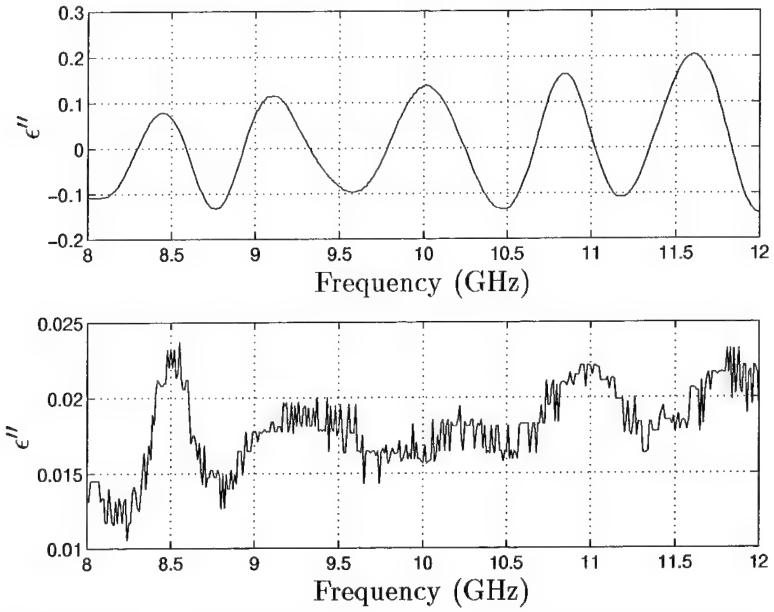

Figure A.6 The Average Permittivity and Standard Deviation of the imaginary part (ϵ'') of the Polyethylene Samples.

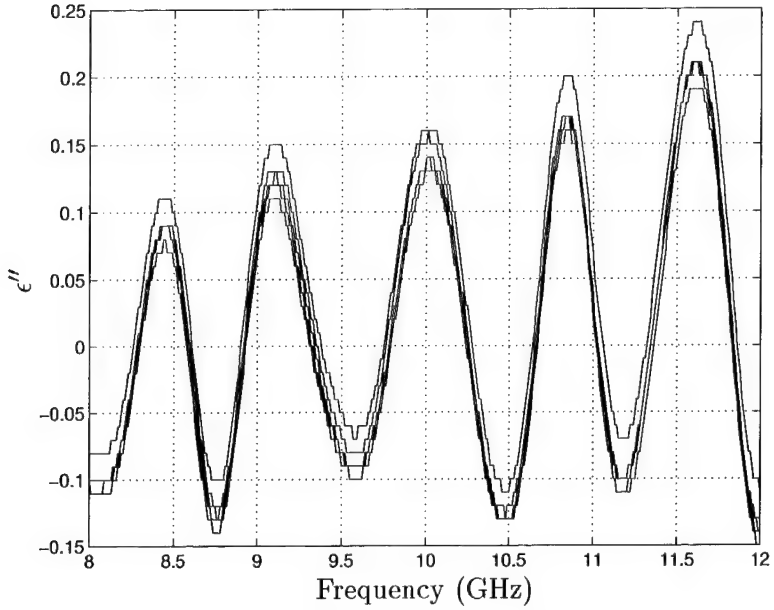

Figure A.7 Permittivity of the imaginary part (ϵ'') of Polyethylene Sample A.

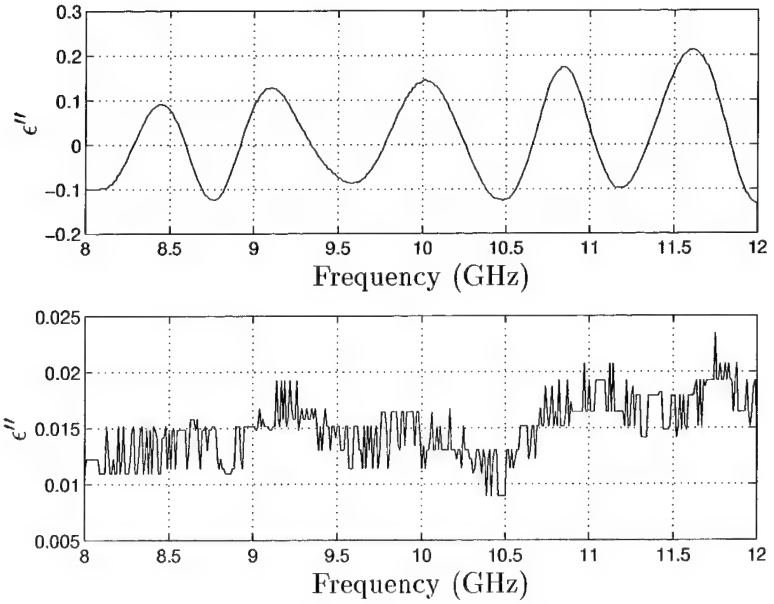

Figure A.8 The Average Permittivity and Standard Deviation of the imaginary part (ϵ'') of Polyethylene Sample A.

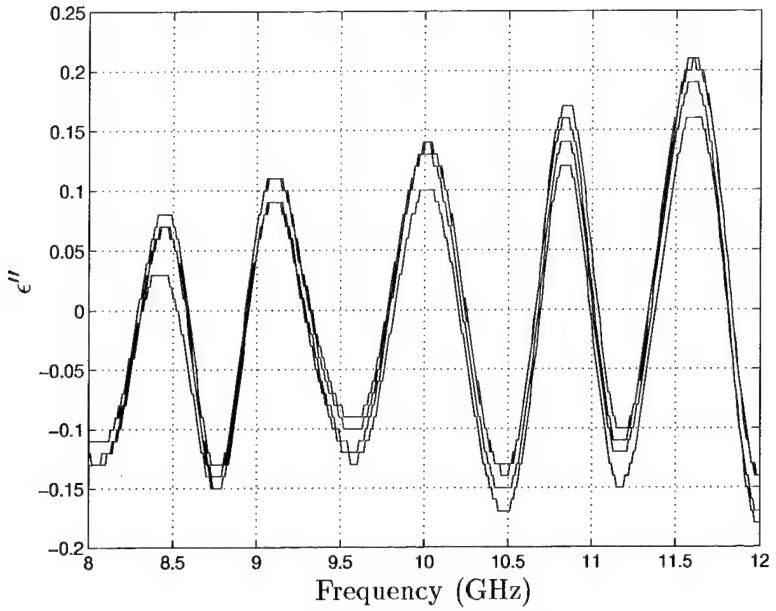

Figure A.9 Permittivity of the imaginary part (ϵ'') of Polyethylene Sample B.

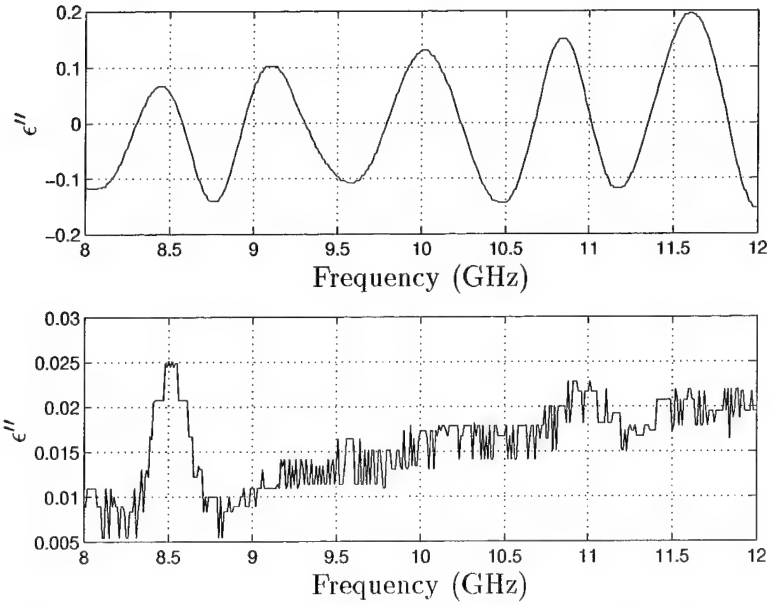

Figure A.10 The Average Permittivity and Standard Deviation of the imaginary part (ϵ'') of Polyethylene Sample B.

Permeability - Real Part (μ')

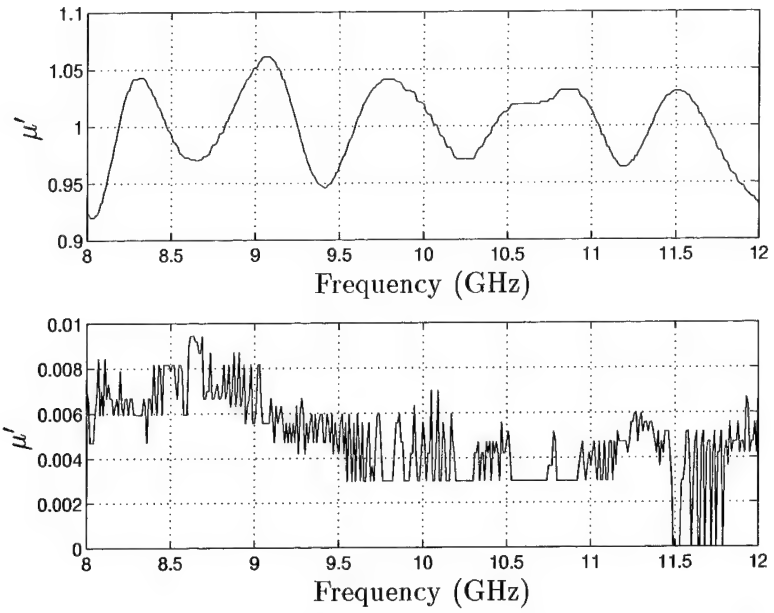

Figure A.11 The Average Permeability and Standard Deviation of the real part (μ') of the Polyethylene Samples.

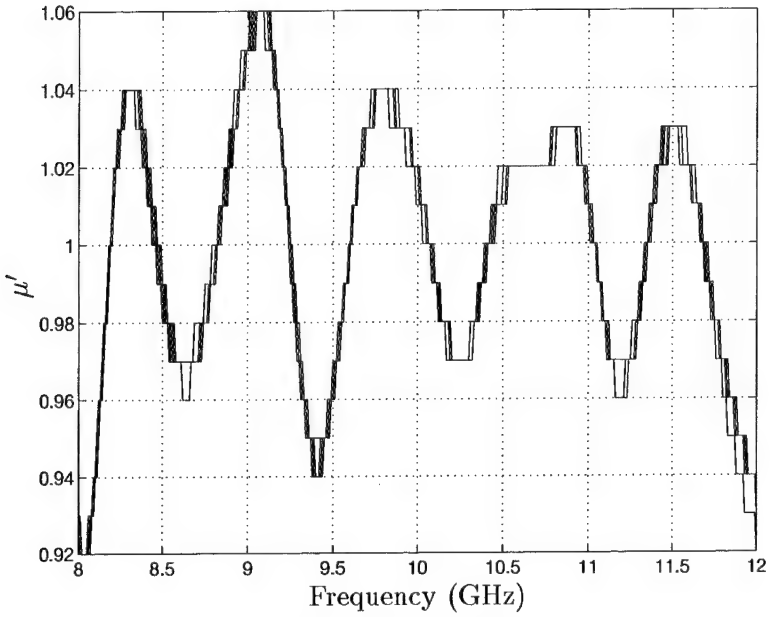

Figure A.12 Permeability of the real part (μ') of Polyethylene Sample A.

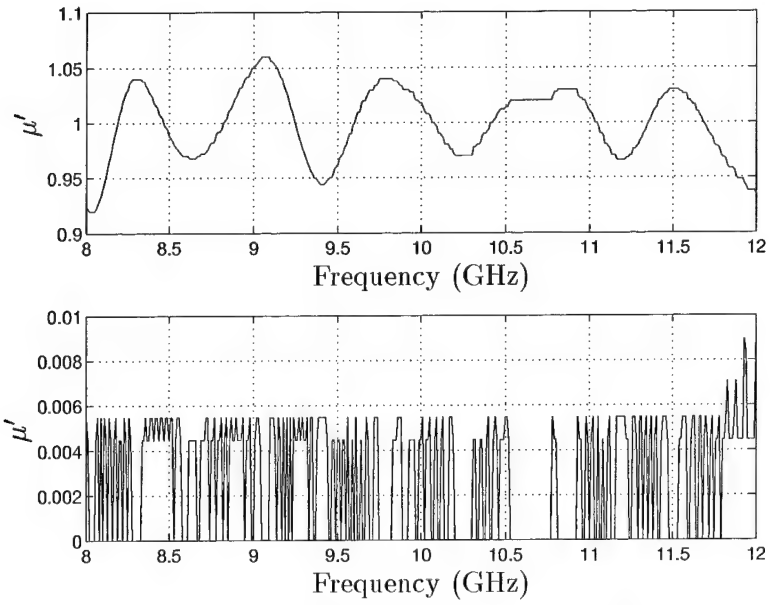

Figure A.13 The Average Permeability and Standard Deviation of the real part (μ') of Polyethylene Sample A.

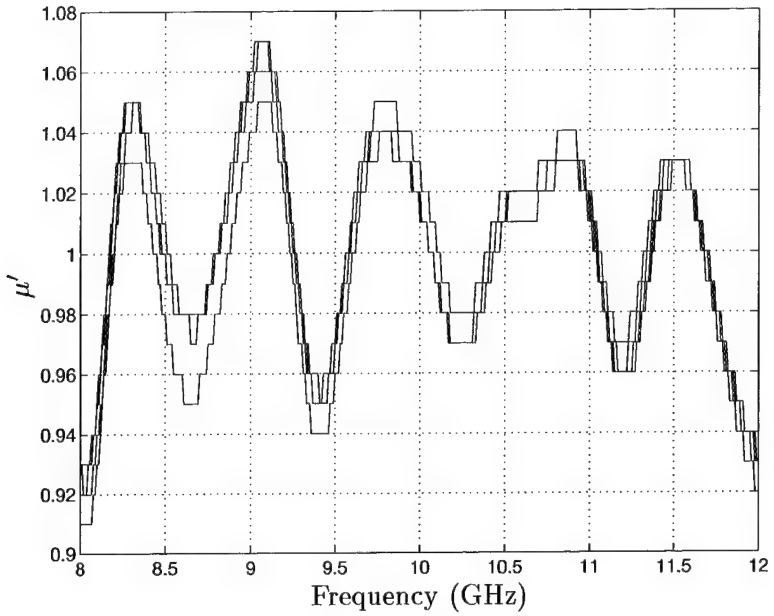

Figure A.14 Permeability of the real part (μ') of Polyethylene Sample B.

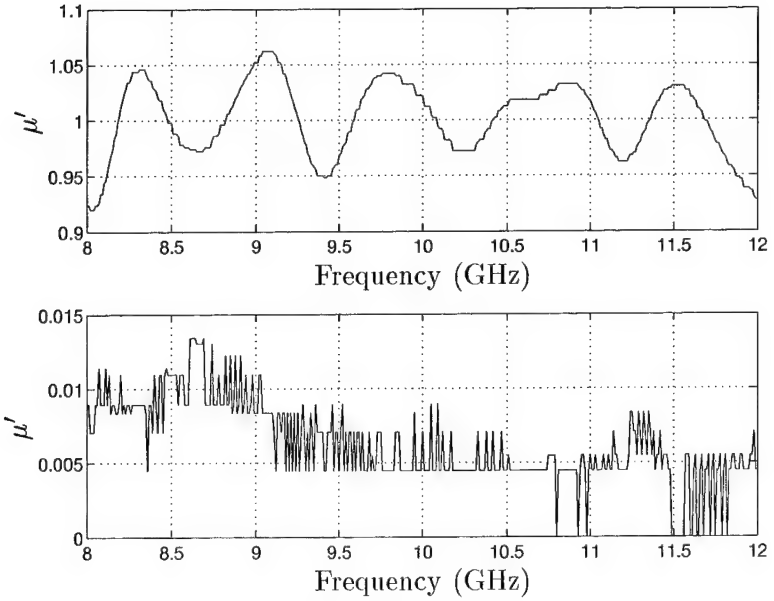

Figure A.15 The Average Permeability and Standard Deviation of the real part (μ') of Polyethylene Sample B.

Permeability - Imaginary Part (μ'')

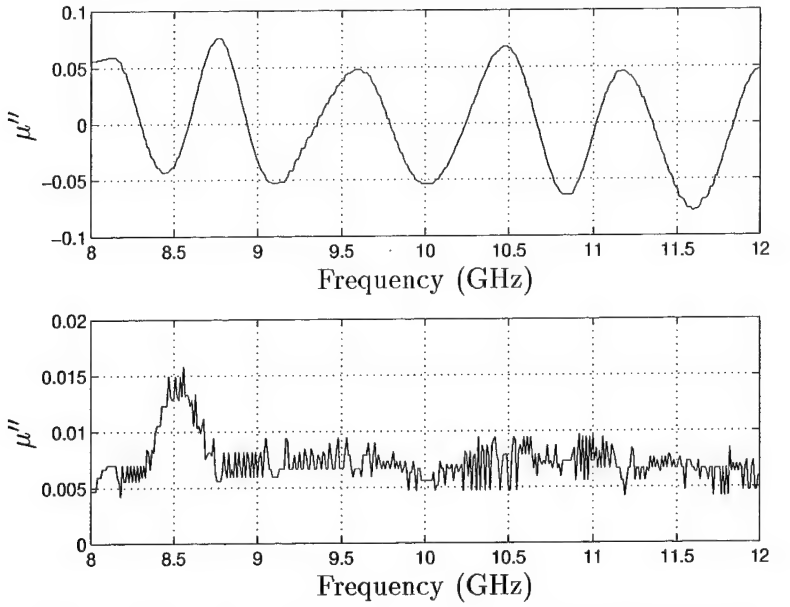

Figure A.16 The Average Permeability and Standard Deviation of the imaginary part (μ'') of the Polyethylene Samples.

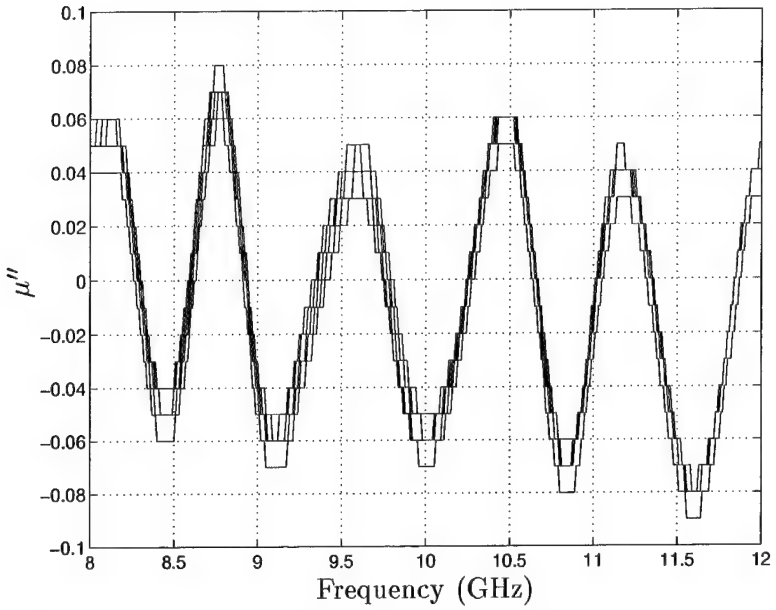

Figure A.17 Permeability of the imaginary part (μ'') of Polyethylene Sample A.

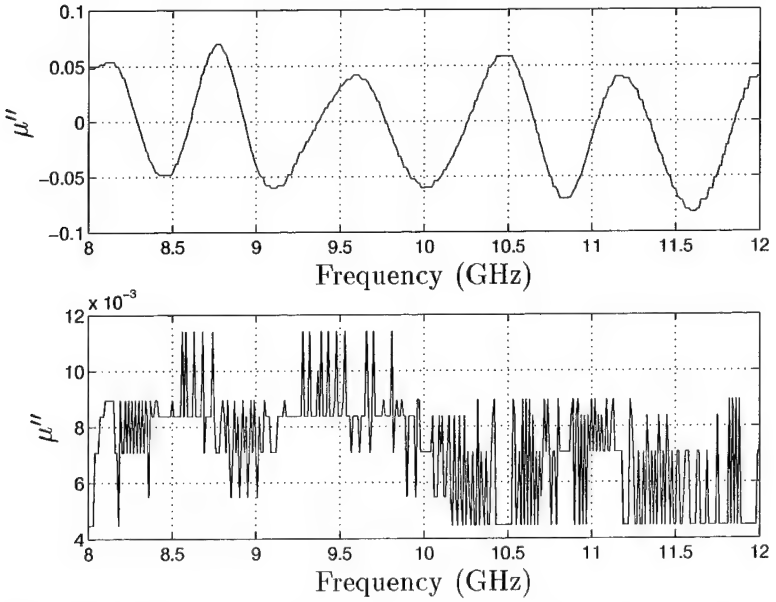

Figure A.18 The Average Permeability and Standard Deviation of the imaginary part (μ'') of Polyethylene Sample A.

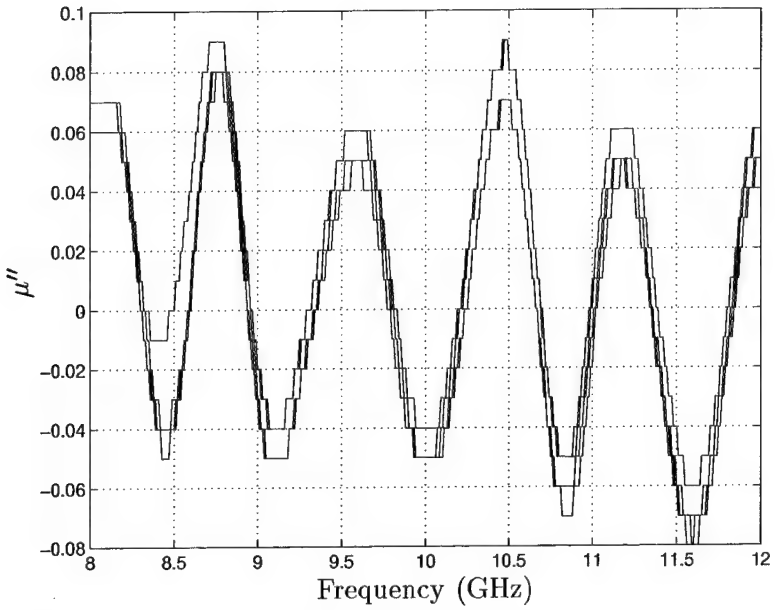

Figure A.19 Permeability of the imaginary part (μ'') of Polyethylene Sample B.

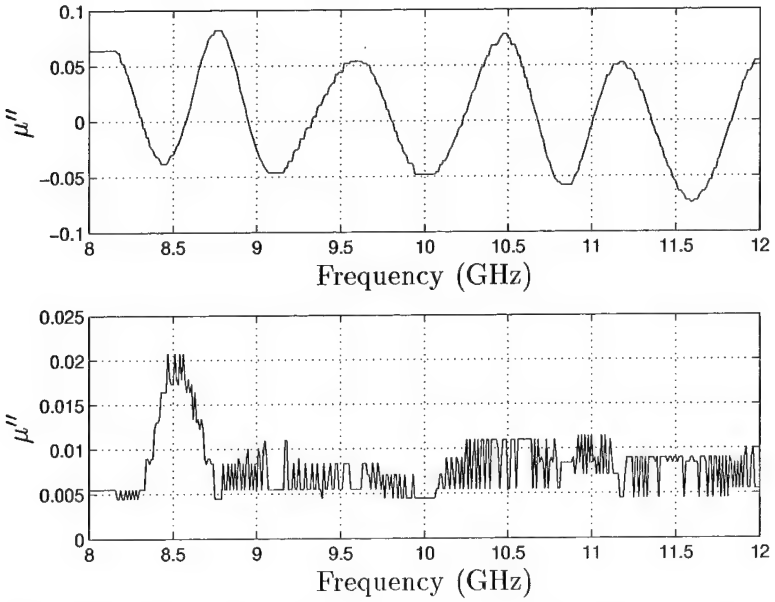

Figure A.20 The Average Permeability and Standard Deviation of the imaginary part (μ'') of Polyethylene Sample B.

Measurement	Sample	Figure
ϵ'	Average A, B, and C	A.21
ϵ'	A	A.29
ϵ'	Average A	A.23
ϵ'	B	A.24
ϵ'	Average B	A.25
ϵ'	C	A.26
ϵ'	Average C	A.27
ϵ''	Average A, B and C	A.28
ϵ''	A	A.29
ϵ''	Average A	A.23
ϵ''	B	A.24
ϵ''	Average B	A.25
ϵ''	C	A.26
ϵ''	Average C	A.27
μ'	Average A, B and C	A.35
μ'	A	A.36
μ'	Average A	A.37
μ'	B	A.38
μ'	Average B	A.39
μ'	C	A.40
μ'	Average C	A.41
μ''	Average A, B and C	A.42
μ''	A	A.43
μ''	Average A	A.44
μ''	B	A.45
μ''	Average B	A.46
μ''	C	A.47
μ''	Average C	A.48

Table A.2 Listing of the material measurements for polyurethane.

Permittivity - Real Part (ϵ')

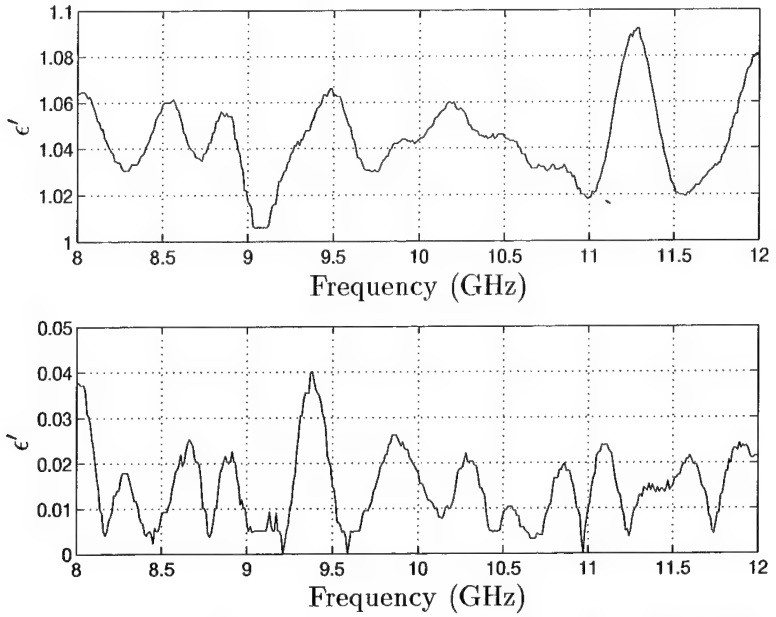

Figure A.21 The Average Permittivity and Standard Deviation of the real part (ϵ') of the Polyurethane Samples.

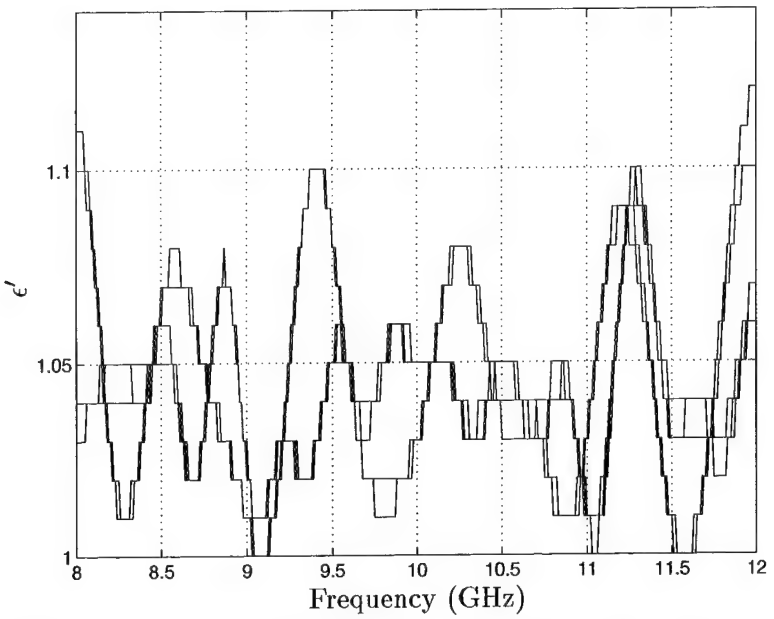

Figure A.22 Permittivity of the real part (ϵ') of Polyurethane Sample A.

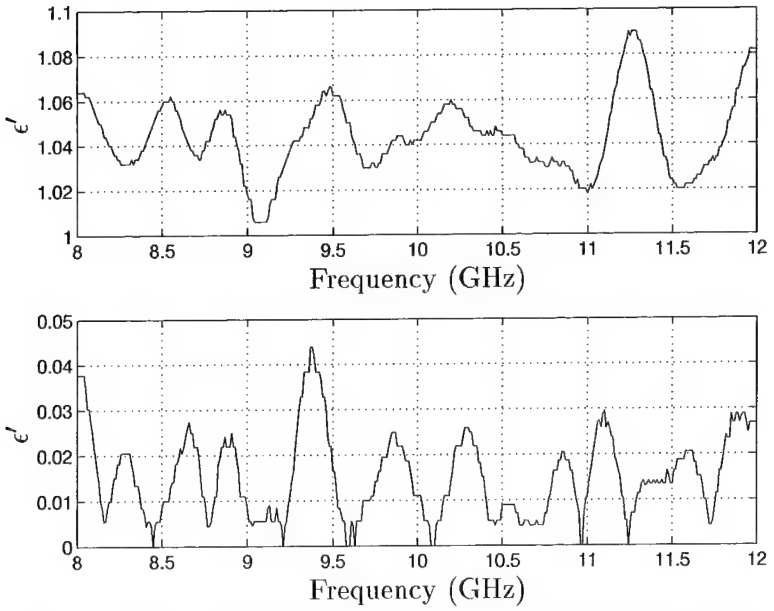

Figure A.23 The Average Permittivity and Standard Deviation of the real part (ϵ') of Polyurethane Sample A.

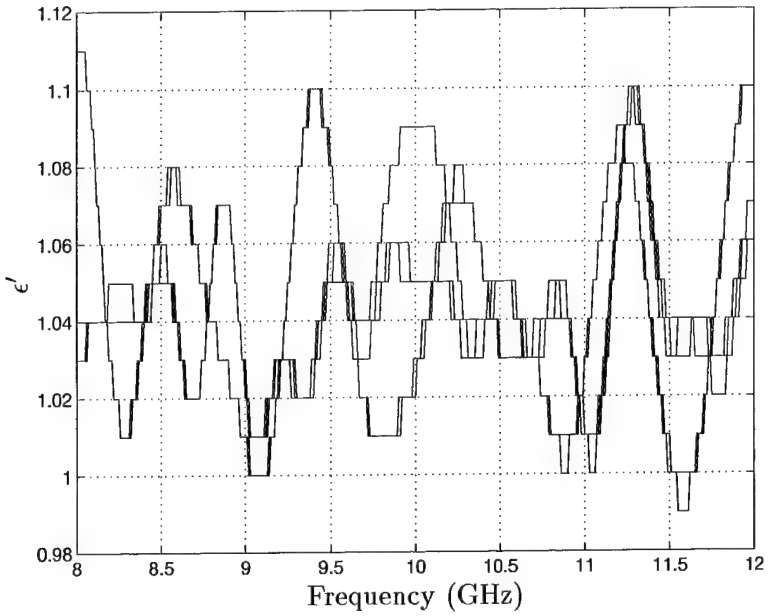

Figure A.24 Permittivity of the real part (ϵ') of Polyurethane Sample B.

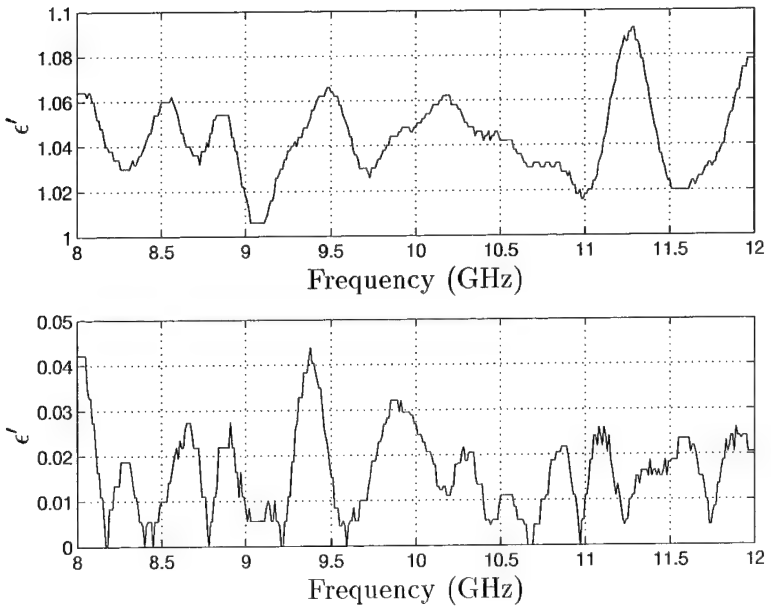

Figure A.25 The Average Permittivity and Standard Deviation of the real part (ϵ') of Polyurethane Sample B.

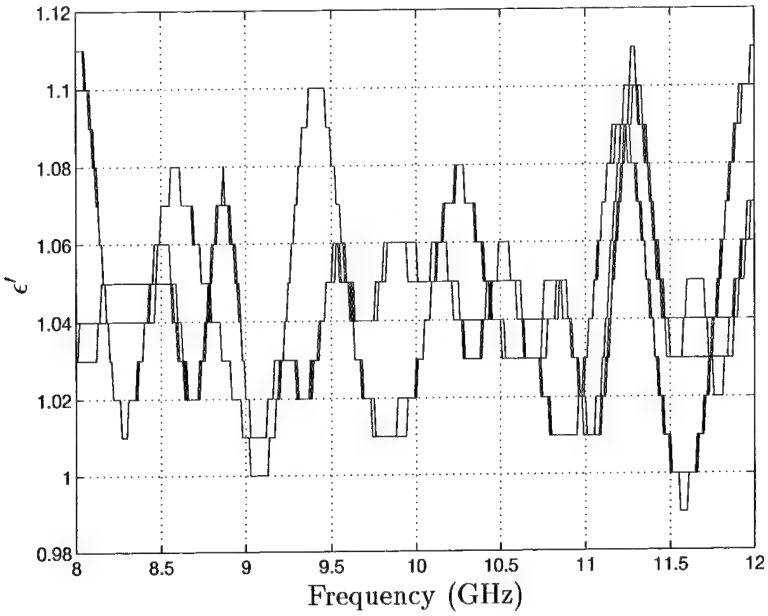

Figure A.26 Permittivity of the real part (ϵ') of Polyurethane Sample C.

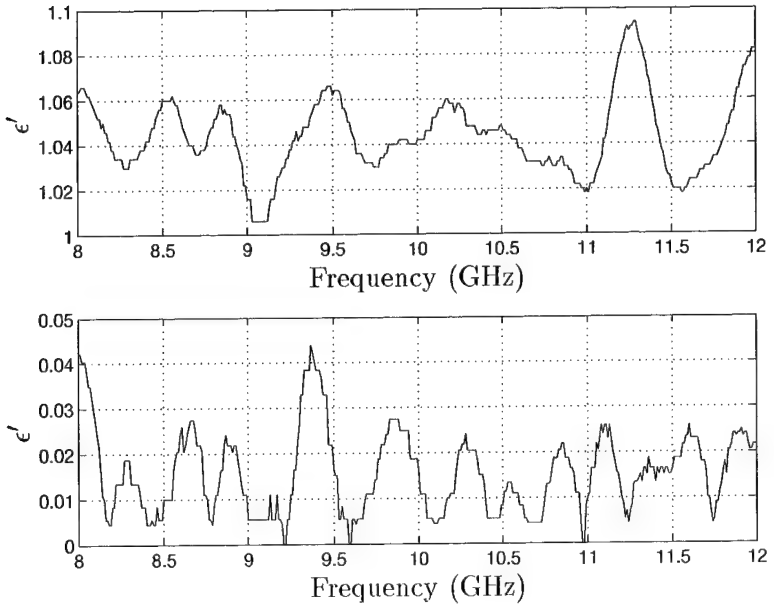

Figure A.27 The Average Permittivity and Standard Deviation of the real part (ϵ') of Polyurethane Sample C.

Permittivity - Imaginary Part (ϵ'')

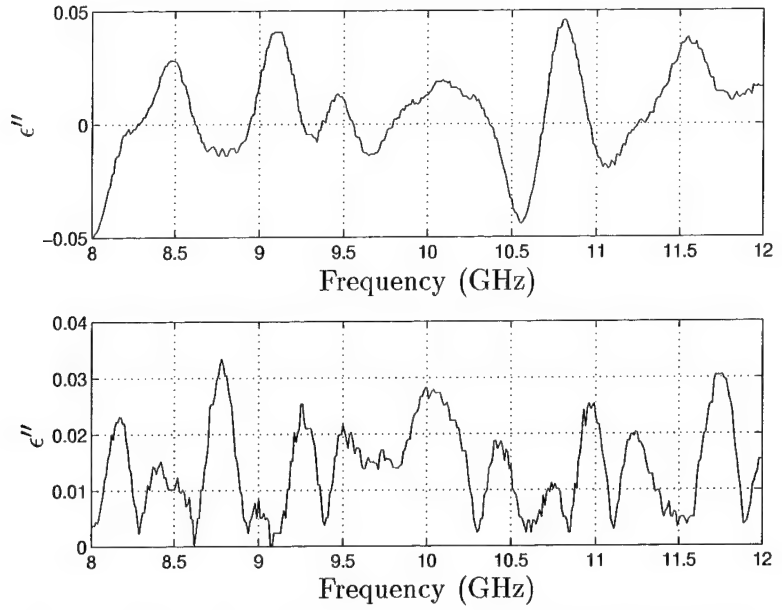

Figure A.28 The Average Permittivity and Standard Deviation of the imaginary part (ϵ'') of the Polyurethane Samples.

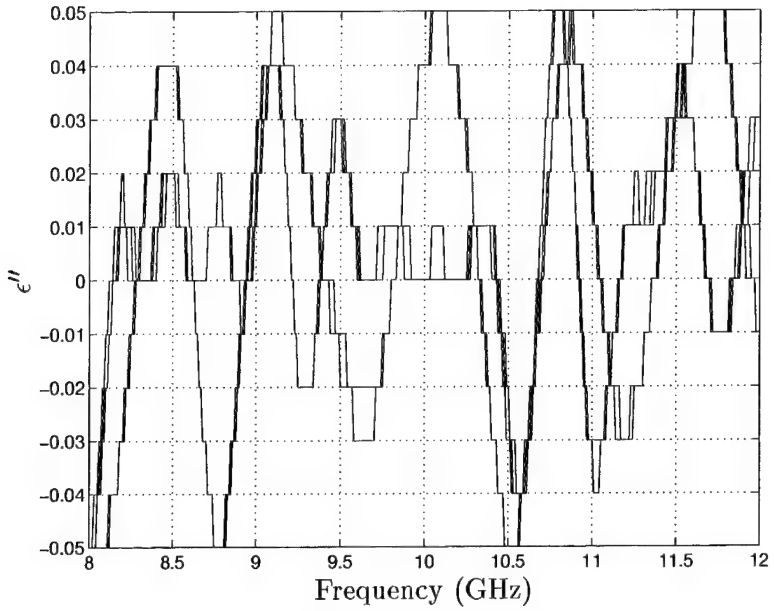

Figure A.29 Permittivity of the imaginary part (ϵ'') of Polyurethane Sample A.

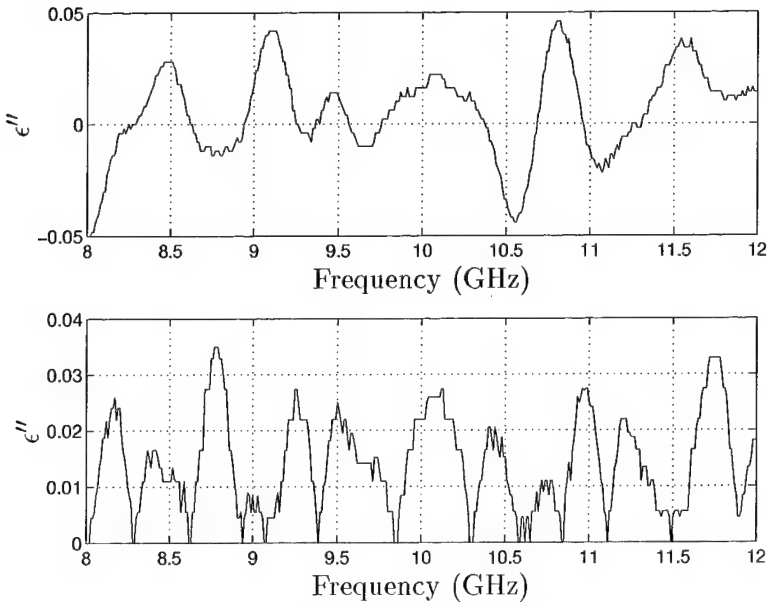

Figure A.30 The Average Permittivity and Standard Deviation of the imaginary part (ϵ'') of Polyurethane Sample A.

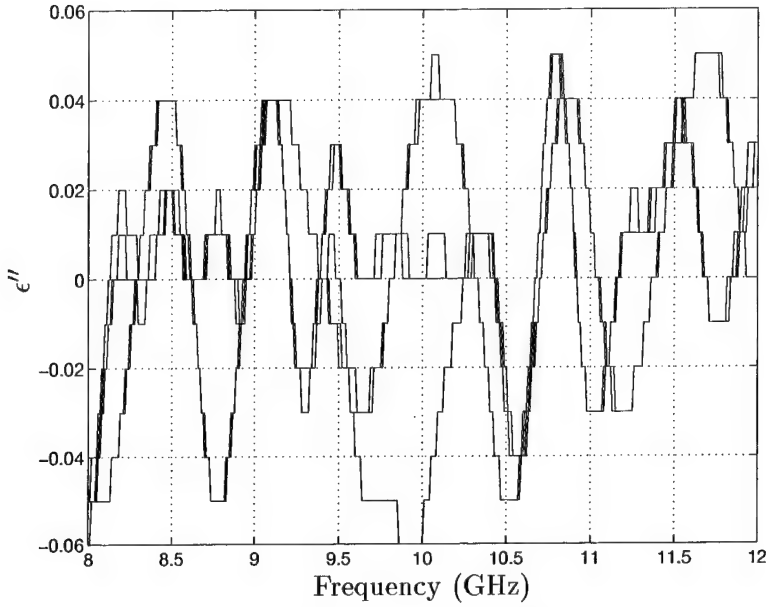

Figure A.31 Permittivity of the imaginary part (ϵ'') of Polyurethane Sample B.

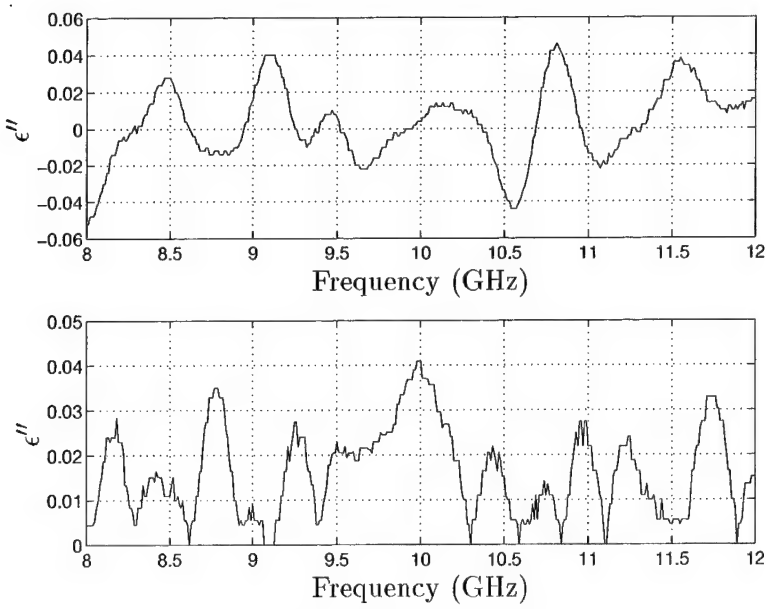

Figure A.32 The Average Permittivity and Standard Deviation of the imaginary part (ϵ'') of Polyurethane Sample B.

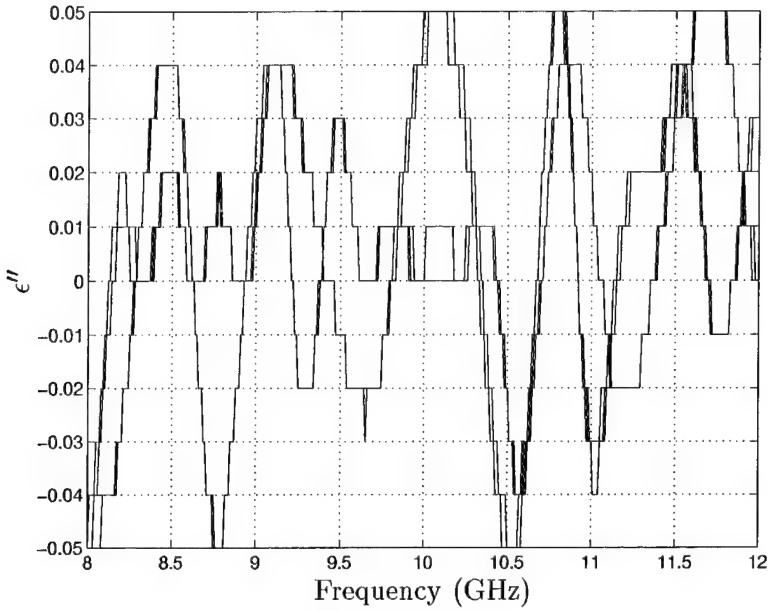

Figure A.33 Permittivity of the imaginary part (ϵ'') of Polyurethane Sample C.

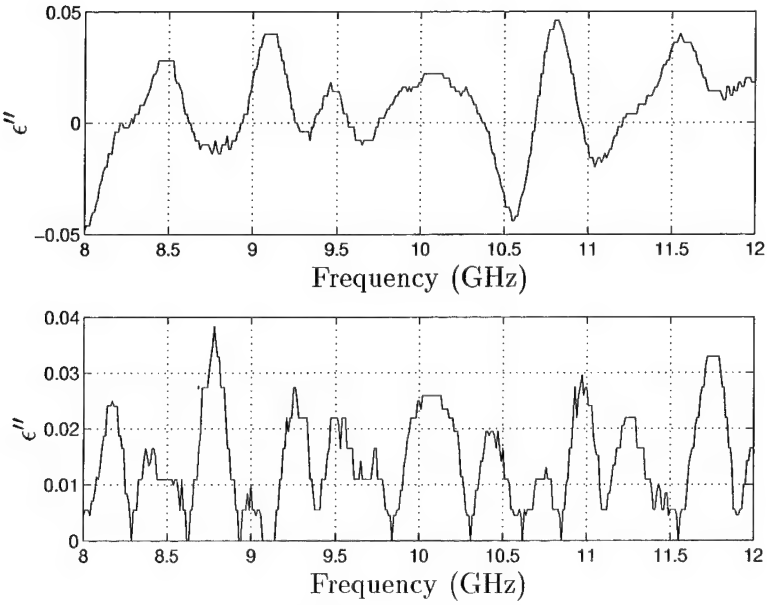

Figure A.34 The Average Permittivity and Standard Deviation of the imaginary part (ϵ'') of Polyurethane Sample C.

Permeability - Real Part (μ')

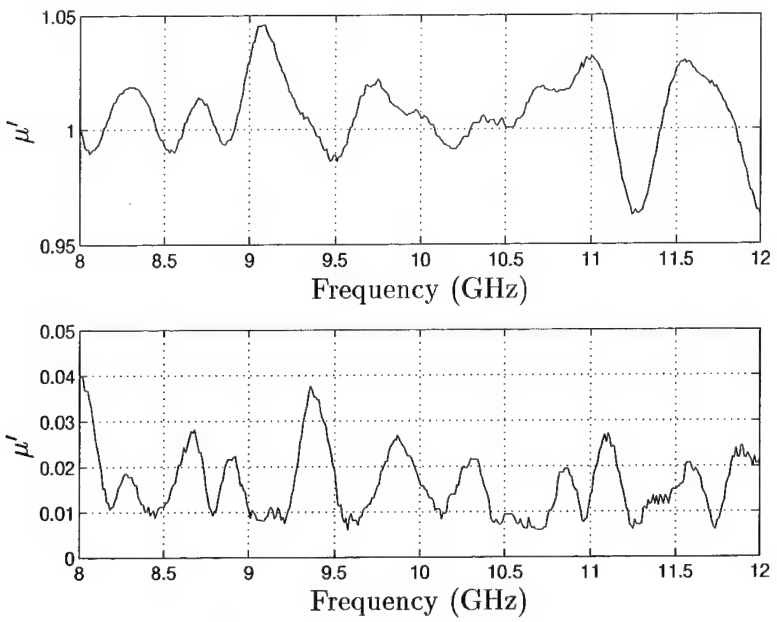

Figure A.35 The Average Permeability and Standard Deviation of the real part (μ') of the Polyurethane Samples.

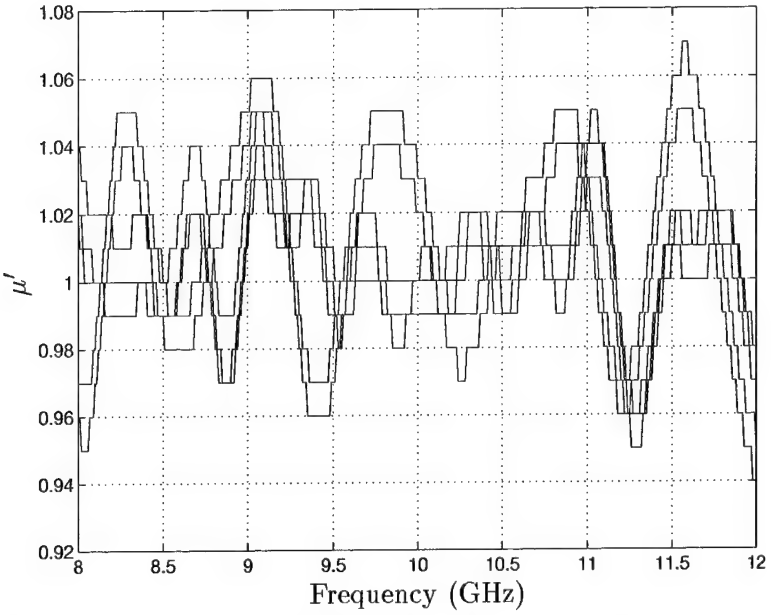

Figure A.36 Permeability of the real part (μ') of Polyurethane Sample A.

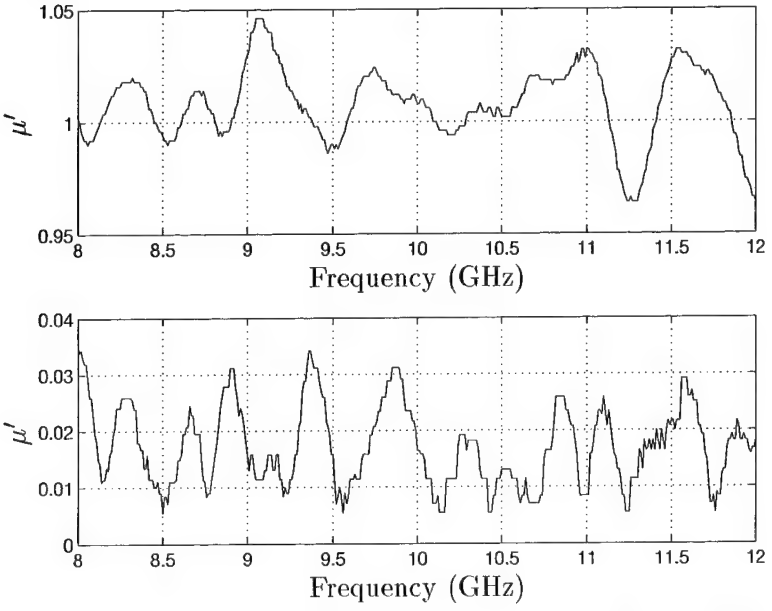

Figure A.37 The Average Permeability and Standard Deviation of the real part (μ') of Polyurethane Sample A.

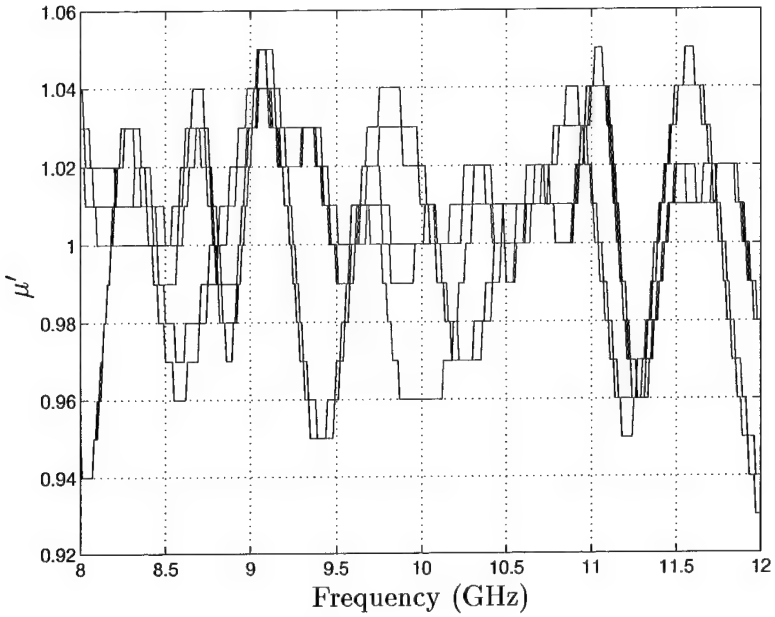

Figure A.38 Permeability of the real part (μ') of Polyurethane Sample B.

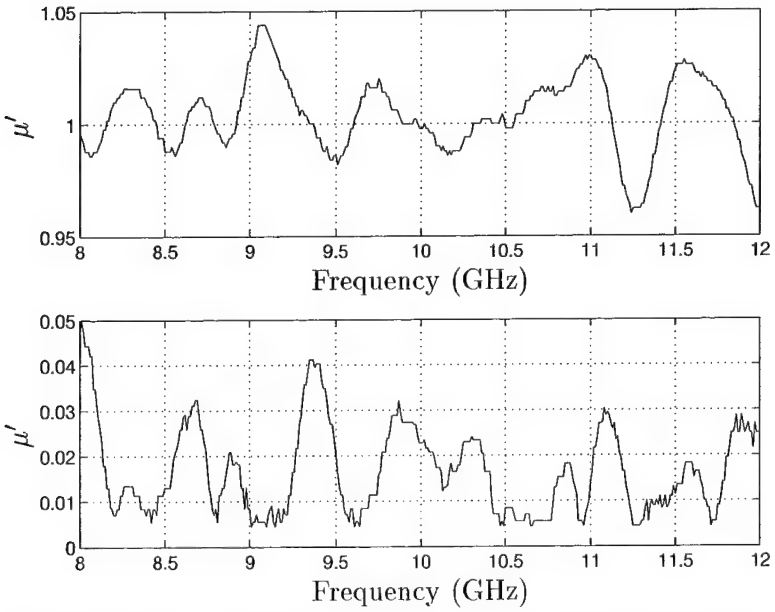

Figure A.39 The Average Permeability and Standard Deviation of the real part (μ') of Polyurethane Sample B.

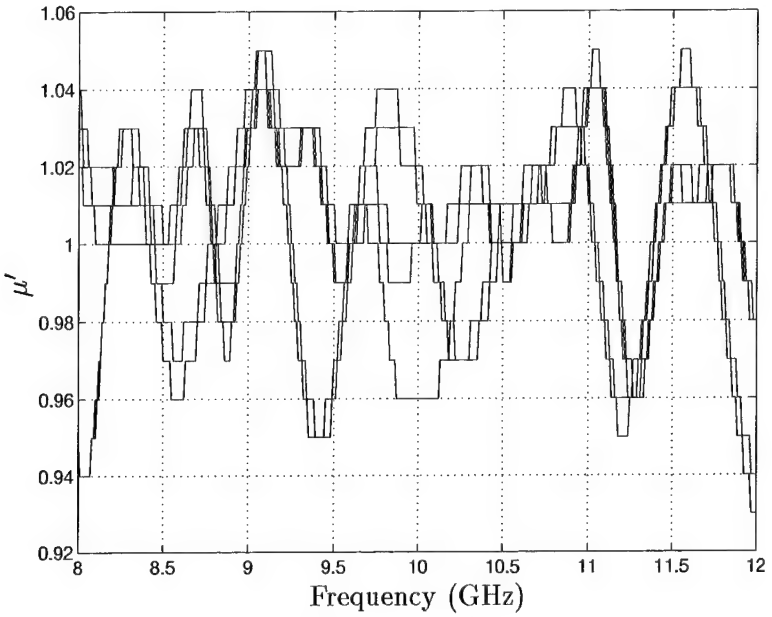

Figure A.40 Permeability of the real part (μ') of Polyurethane Sample C.

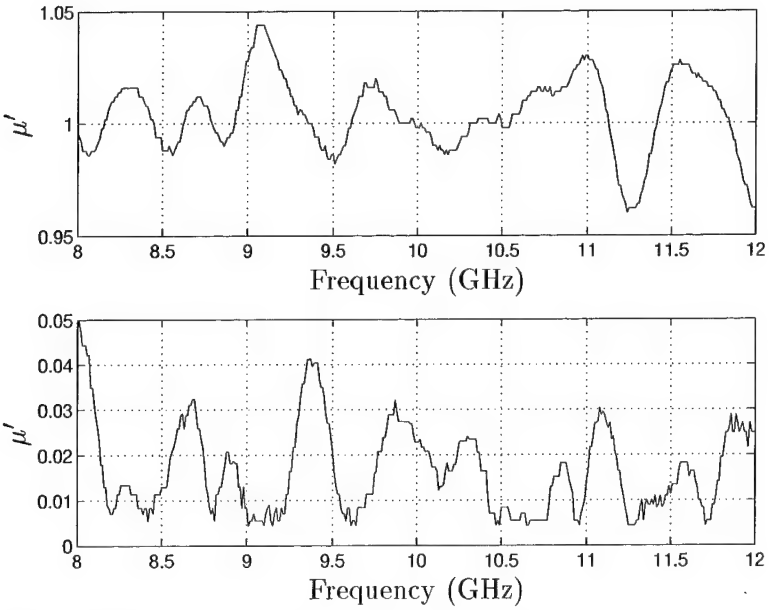

Figure A.41 The Average Permeability and Standard Deviation of the real part (μ') of Polyurethane Sample C.

Permeability - Imaginary Part (μ'')

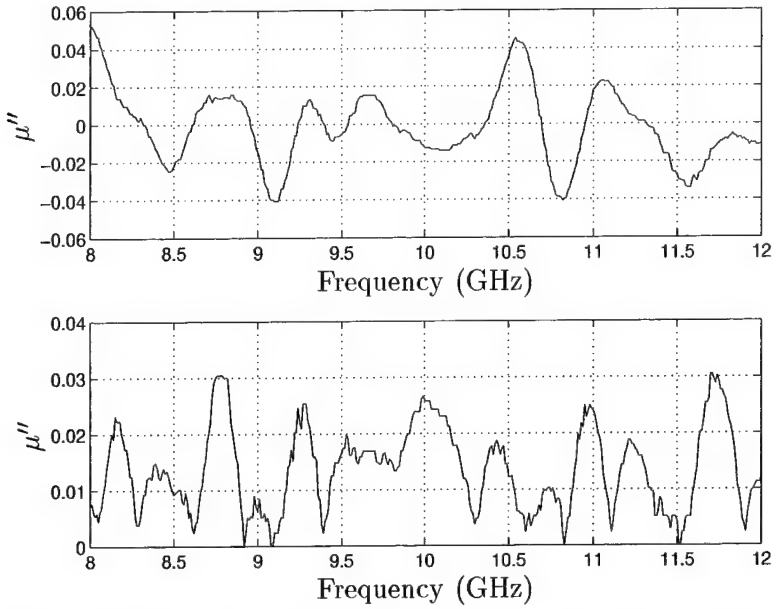

Figure A.42 The Average Permeability and Standard Deviation of the imaginary part (μ'') of the Polyurethane Samples.

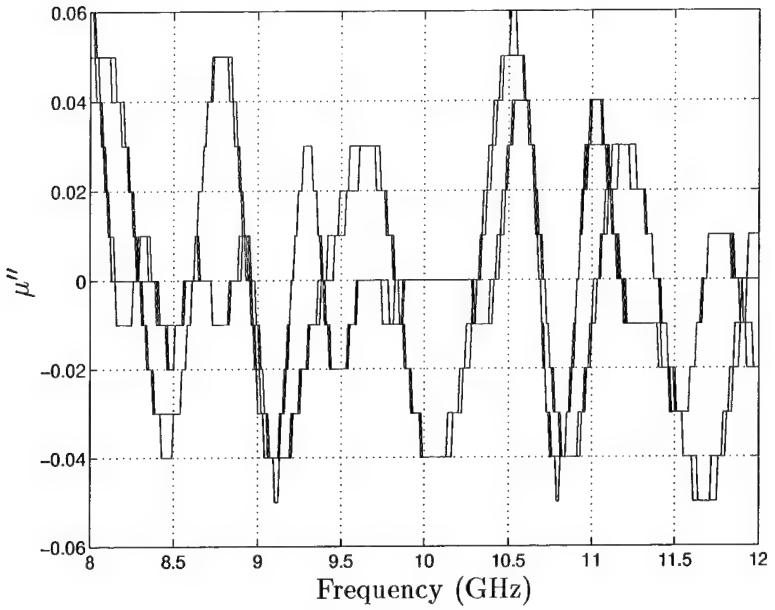

Figure A.43 Permeability of the imaginary part (μ'') of Polyurethane Sample A.

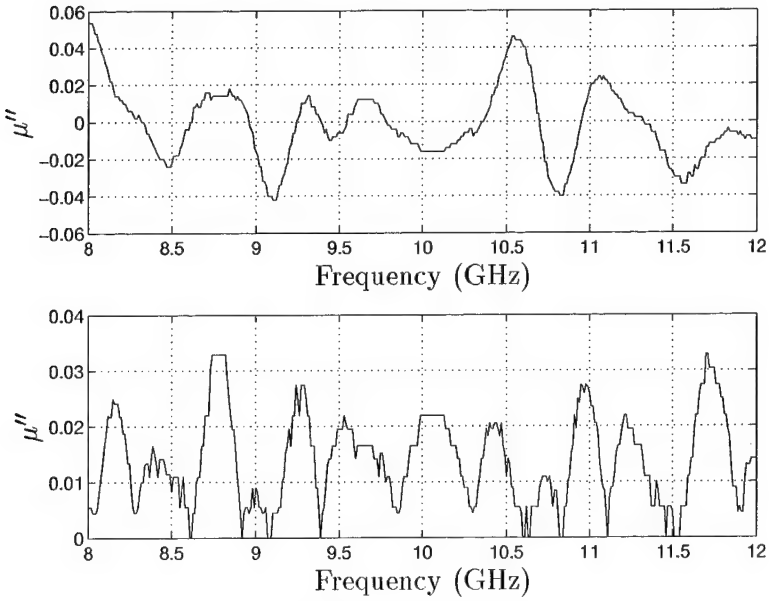

Figure A.44 The Average Permeability and Standard Deviation of the imaginary part (μ'') of Polyurethane Sample A.

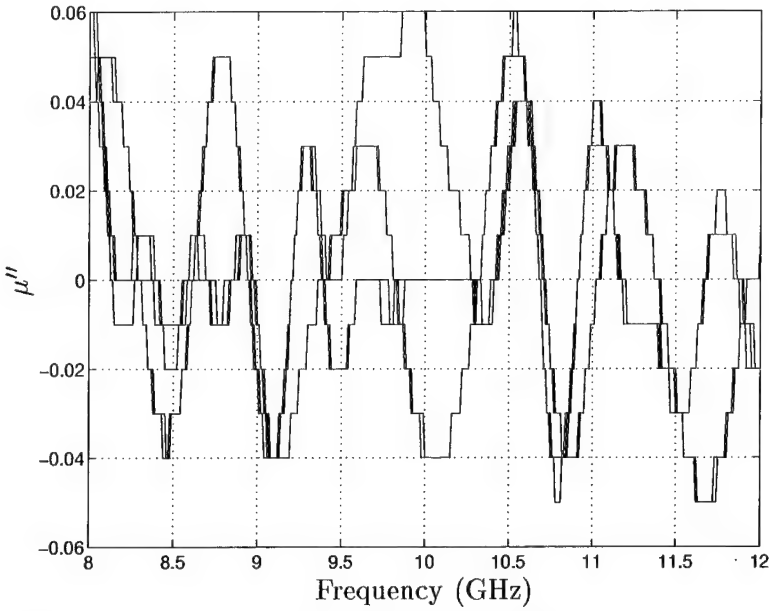

Figure A.45 Permeability of the imaginary part (μ'') of Polyurethane Sample B.

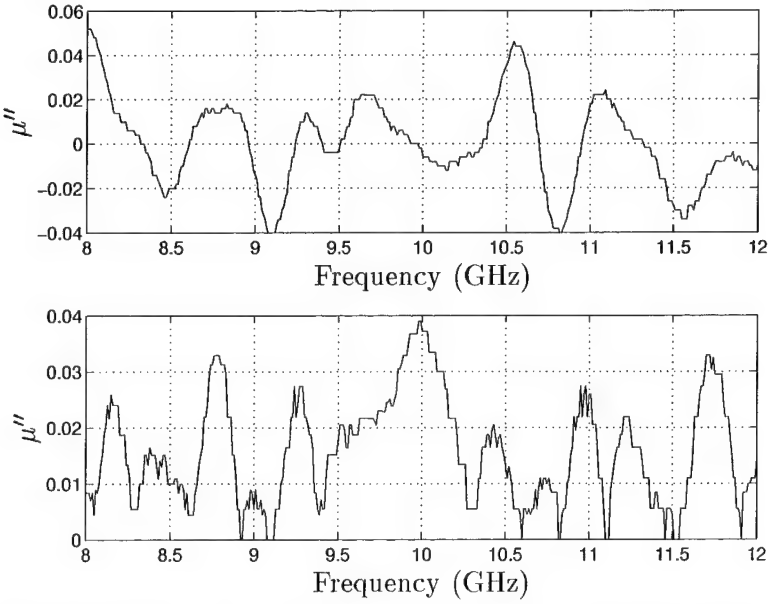

Figure A.46 The Average Permeability and Standard Deviation of the imaginary part (μ'') of Polyurethane Sample B.

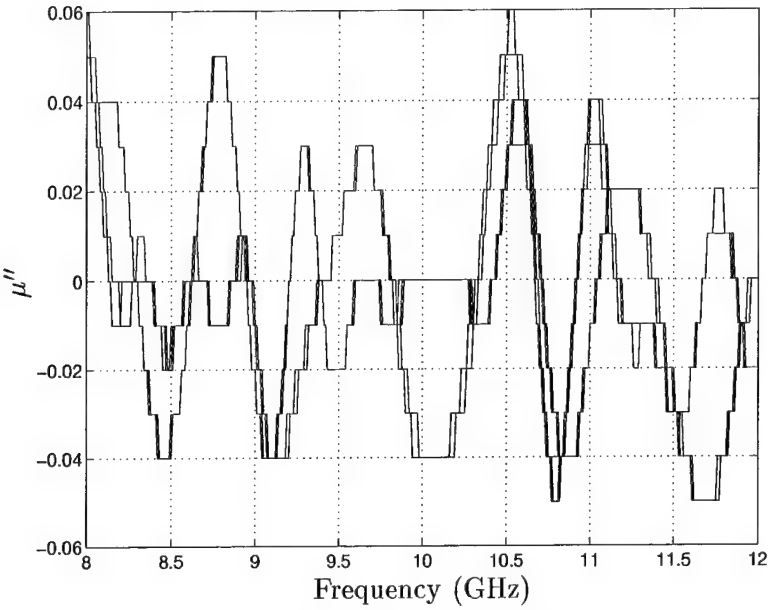

Figure A.47 Permeability of the imaginary part (μ'') of Polyurethane Sample C.

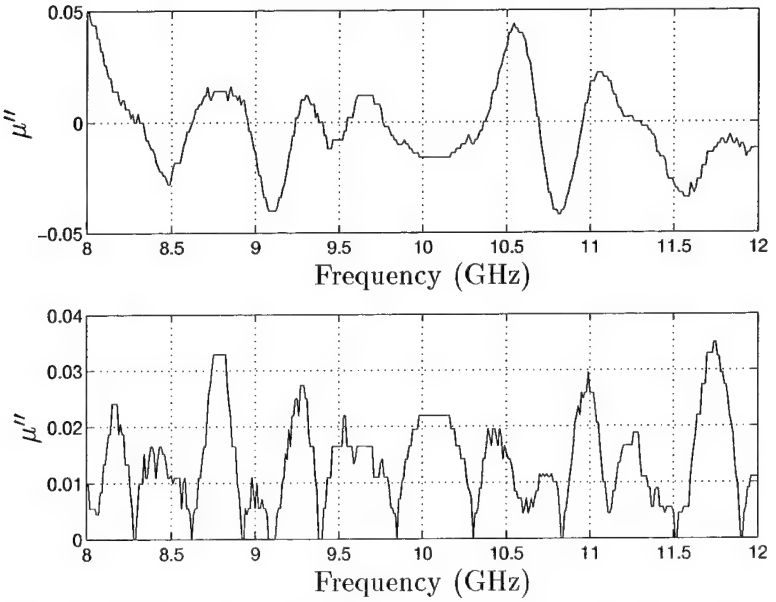

Figure A.48 The Average Permeability and Standard Deviation of the imaginary part (μ'') of Polyurethane Sample C.

Appendix B. RCS Plots

This appendix is a compilation of the monostatic RCS data for each target. The RCS measurements for this research were accomplished at Wright Laboratory's Multispectral Measurement Facility (WL/XPN), Wright-Patterson AFB, OH. Each of the targets were measured for both polarizations from 2 to 18 GHz, in 20 MHz increments, and from 0 to 360 degrees, in 0.5 degree increments, in azimuth.

Target	RCS Plot Type	Polarization	Figure
Small Polyethylene Cube	Frequency vs Azimuth	HH	B.1
Small Polyethylene Cube	Frequency vs Azimuth	VV	B.2
Small Polyethylene Cube with R-card	Frequency vs Azimuth	HH	B.3
Small Polyethylene Cube with R-card	Frequency vs Azimuth	VV	B.4
Small Polyurethane Cube	Frequency vs Azimuth	HH	B.5
Small Polyurethane Cube	Frequency vs Azimuth	VV	B.6
Small Polyurethane Cube with R-card	Frequency vs Azimuth	HH	B.7
Small Polyurethane Cube with R-card	Frequency vs Azimuth	VV	B.8
Large Polyethylene Cube	Frequency vs Azimuth	HH	B.9
Large Polyethylene Cube	Frequency vs Azimuth	VV	B.10
Large Polyurethane Cube	Frequency vs Azimuth	HH	B.11
Large Polyurethane Cube	Frequency vs Azimuth	VV	B.12
Large Polyurethane Cube	Range vs Azimuth	VV	B.13
Polyethylene Mini-Arrow	Frequency vs Azimuth	HH	B.14
Polyethylene Mini-Arrow	Frequency vs Azimuth	VV	B.15
Polyethylene Mini-Arrow with R-card	Frequency vs Azimuth	HH	B.16
Polyethylene Mini-Arrow with R-card	Frequency vs Azimuth	VV	B.17
Polyethylene Ogive	Frequency vs Azimuth	HH	B.18
Polyethylene Ogive	Frequency vs Azimuth	VV	B.19
Polyethylene Sphere	Frequency vs Azimuth	HH	B.20
Polyethylene Sphere	Frequency vs Azimuth	VV	B.21
Polyethylene Conesphere	Frequency vs Azimuth	HH	B.23
Polyethylene Conesphere	Frequency vs Azimuth	VV	B.23
Polyethylene Conesphere	Range vs Azimuth	HH	B.24
Polyethylene Conesphere with a Gap	Frequency vs Azimuth	HH	B.26
Polyethylene Conesphere with a Gap	Frequency vs Azimuth	VV	B.26

Table B.1 Listing of the RCS Plots.

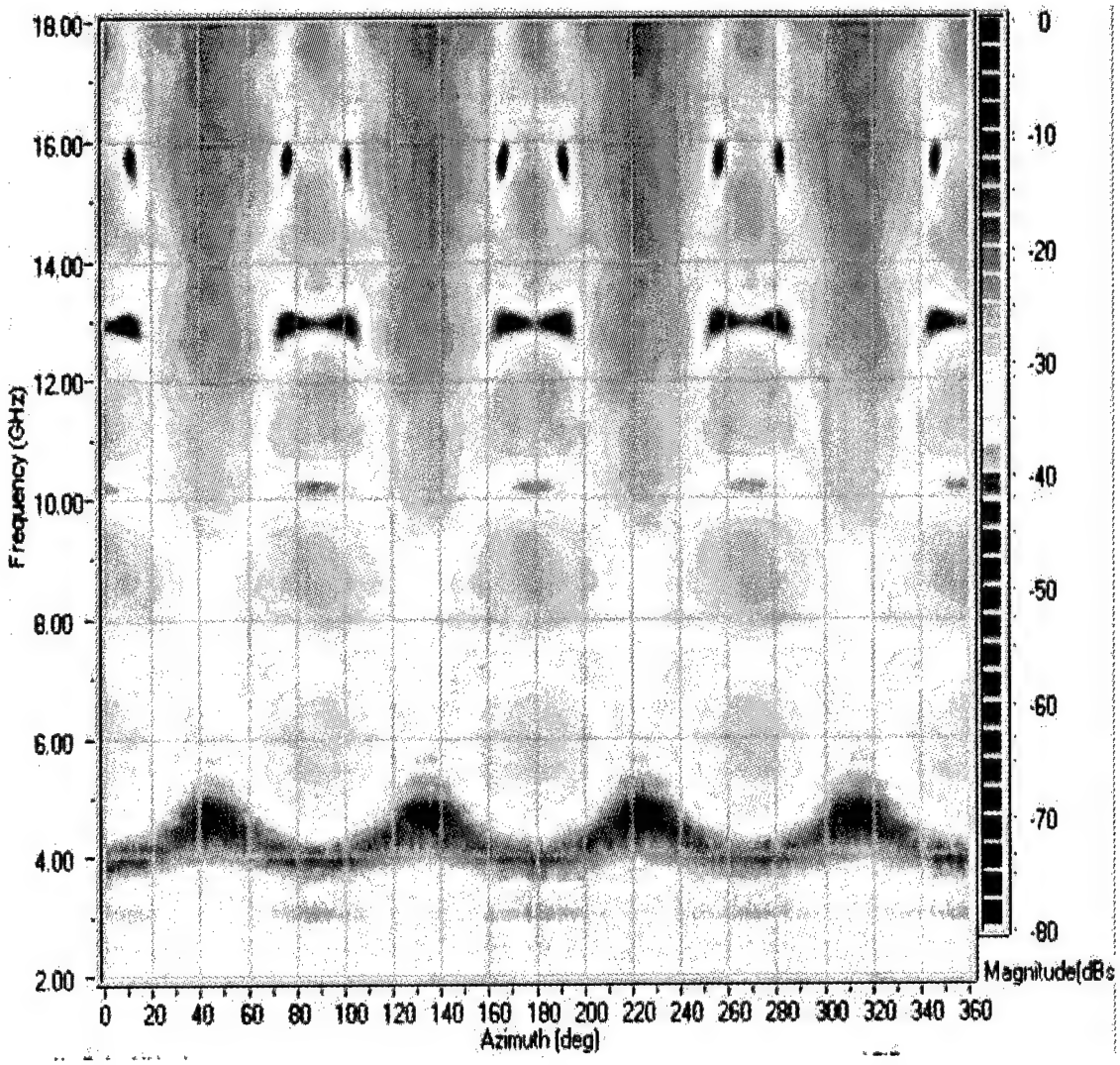

Figure B.1 RCS of the Small Polyethylene Cube for Horizontal Polarization.

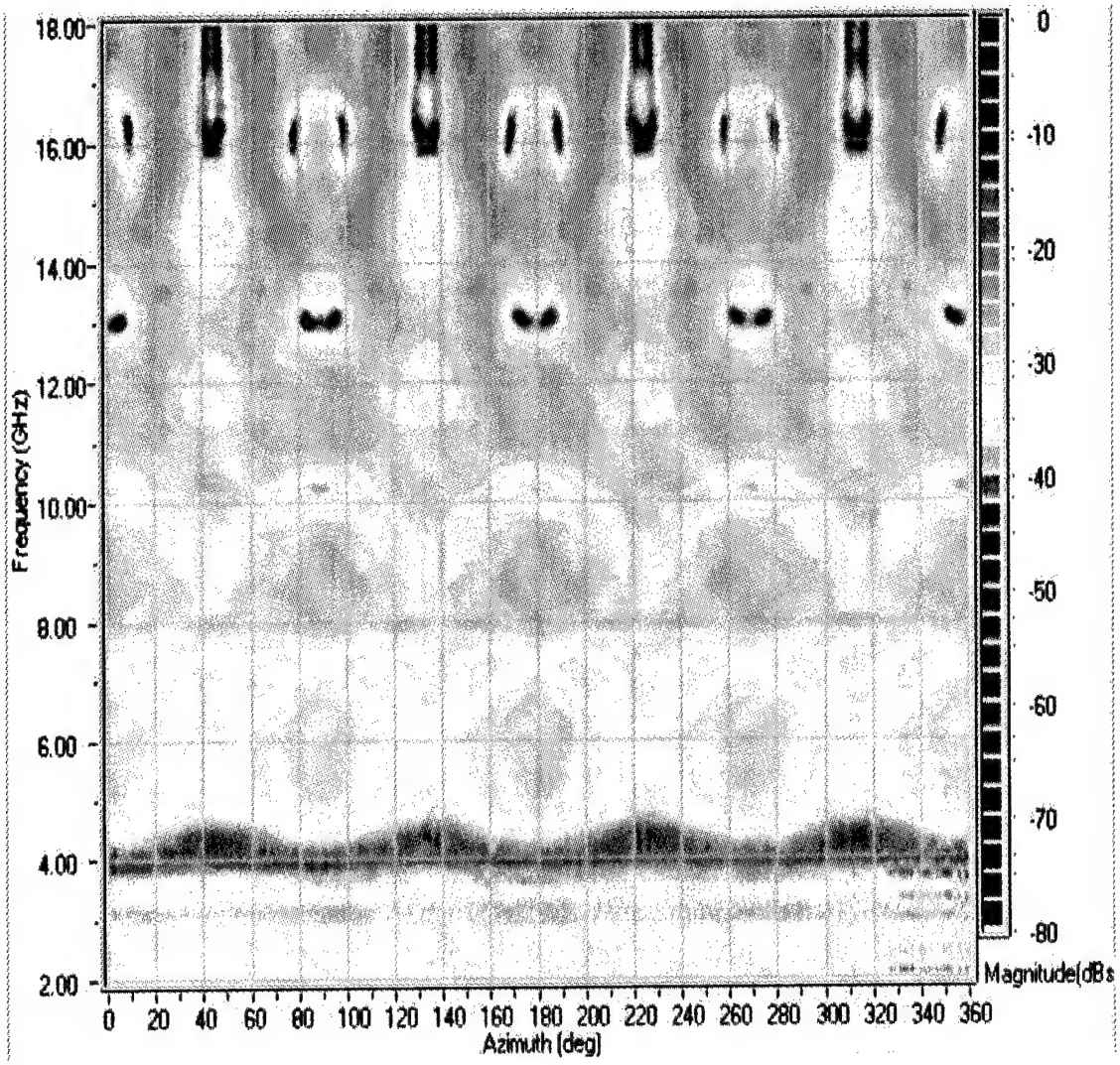

Figure B.2 RCS of the Small Polyethylene Cube for Vertical Polarization.

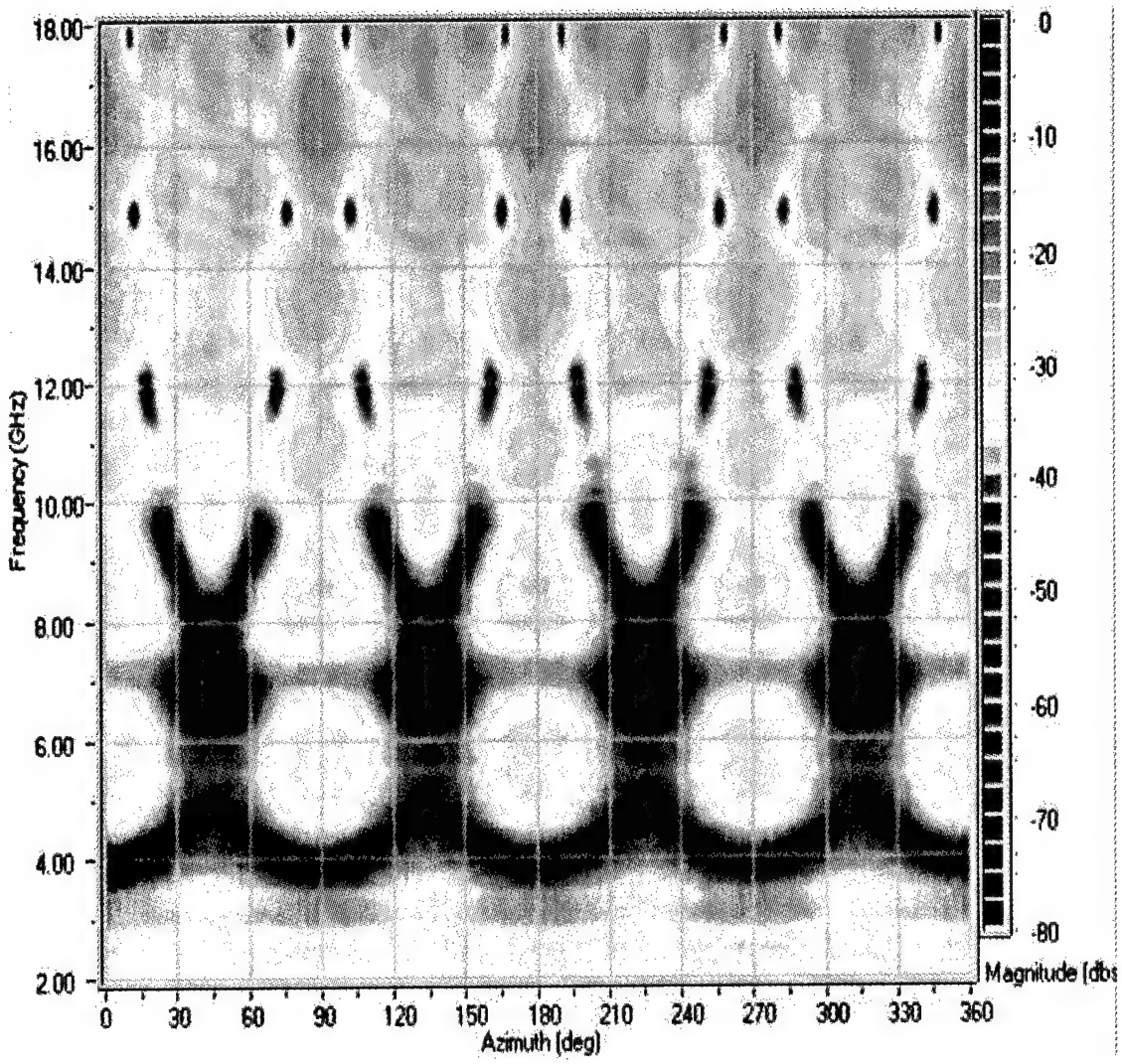

Figure B.3 RCS of the Small Polyethylene Cube with R-card for Horizontal Polarization.

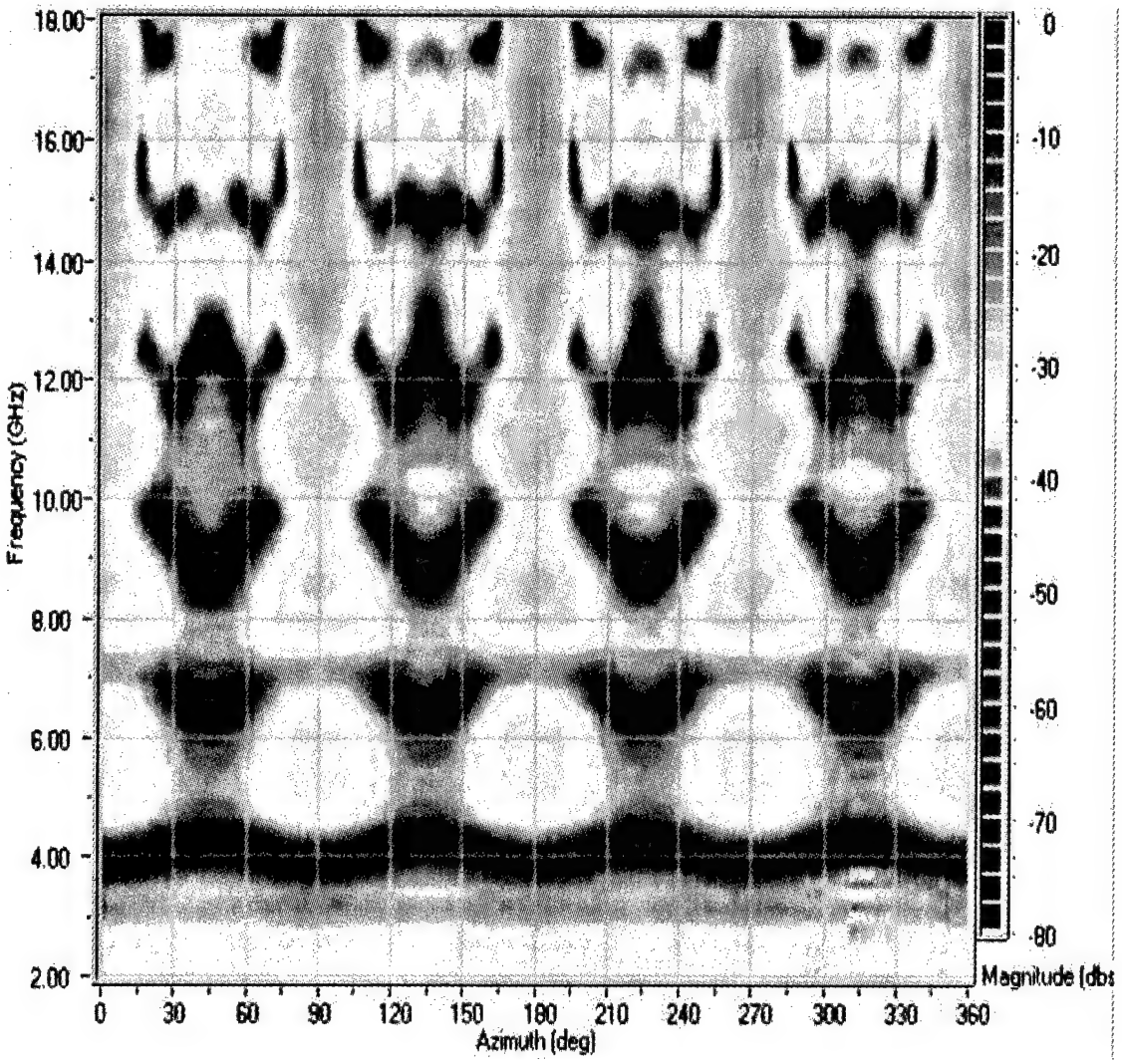

Figure B.4 RCS of the Small Polyethylene Cube with R-card for Vertical Polarization.

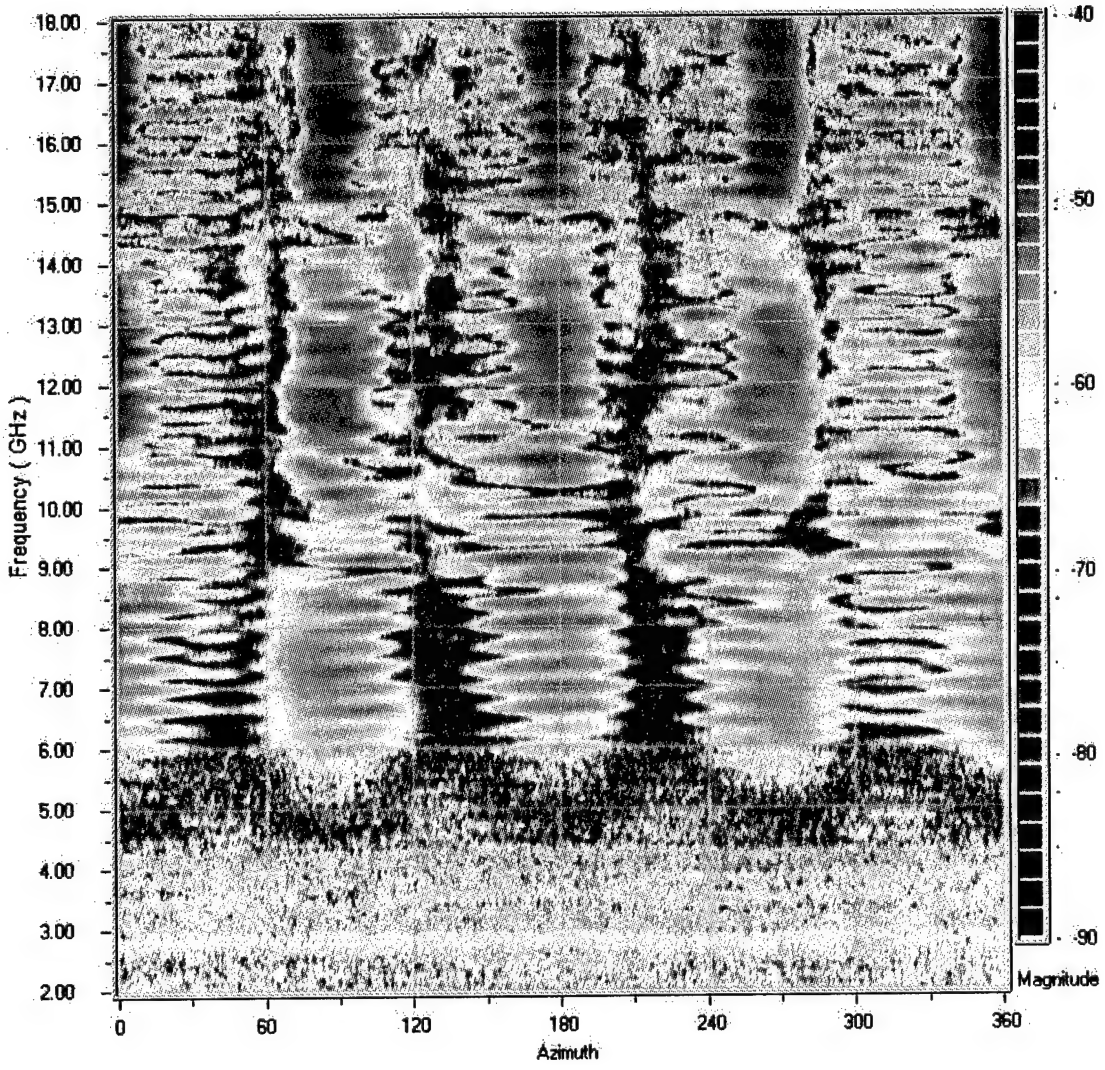

Figure B.5 RCS of the Small Polyurethane Cube for Horizontal Polarization.

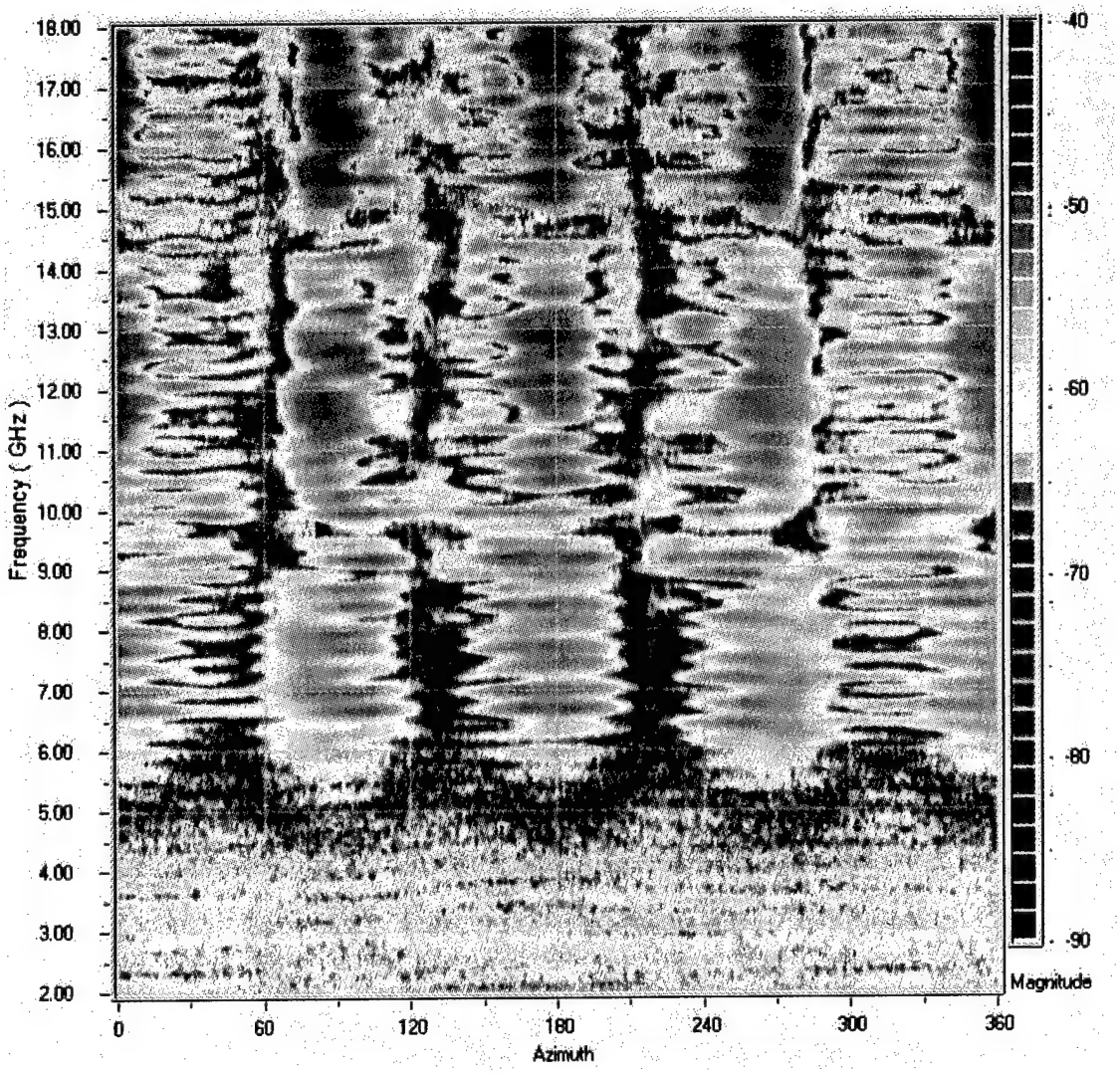

Figure B.6 RCS of the Small Polyurethane Cube for Vertical Polarization.

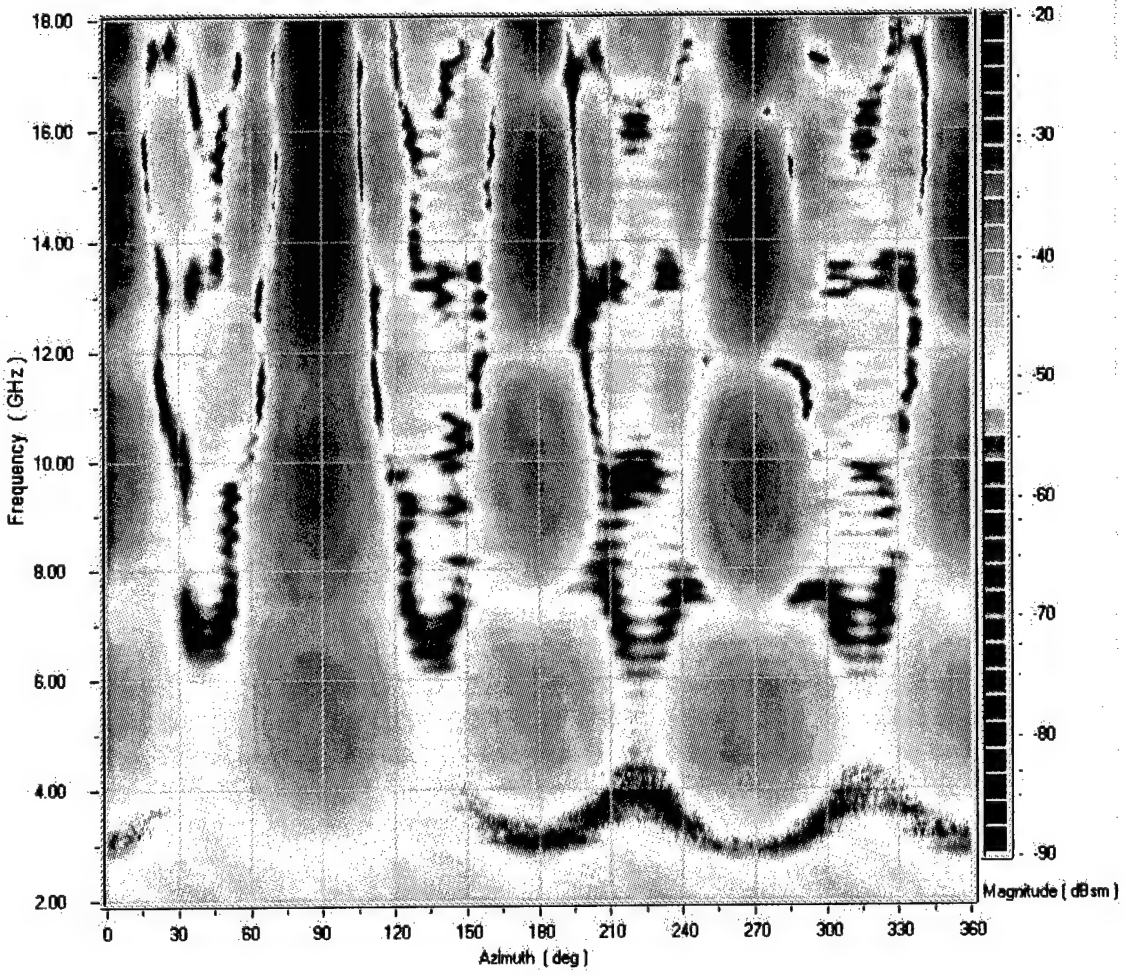

Figure B.7 RCS of the Small Polyurethane Cube with R-card for Horizontal Polarization.

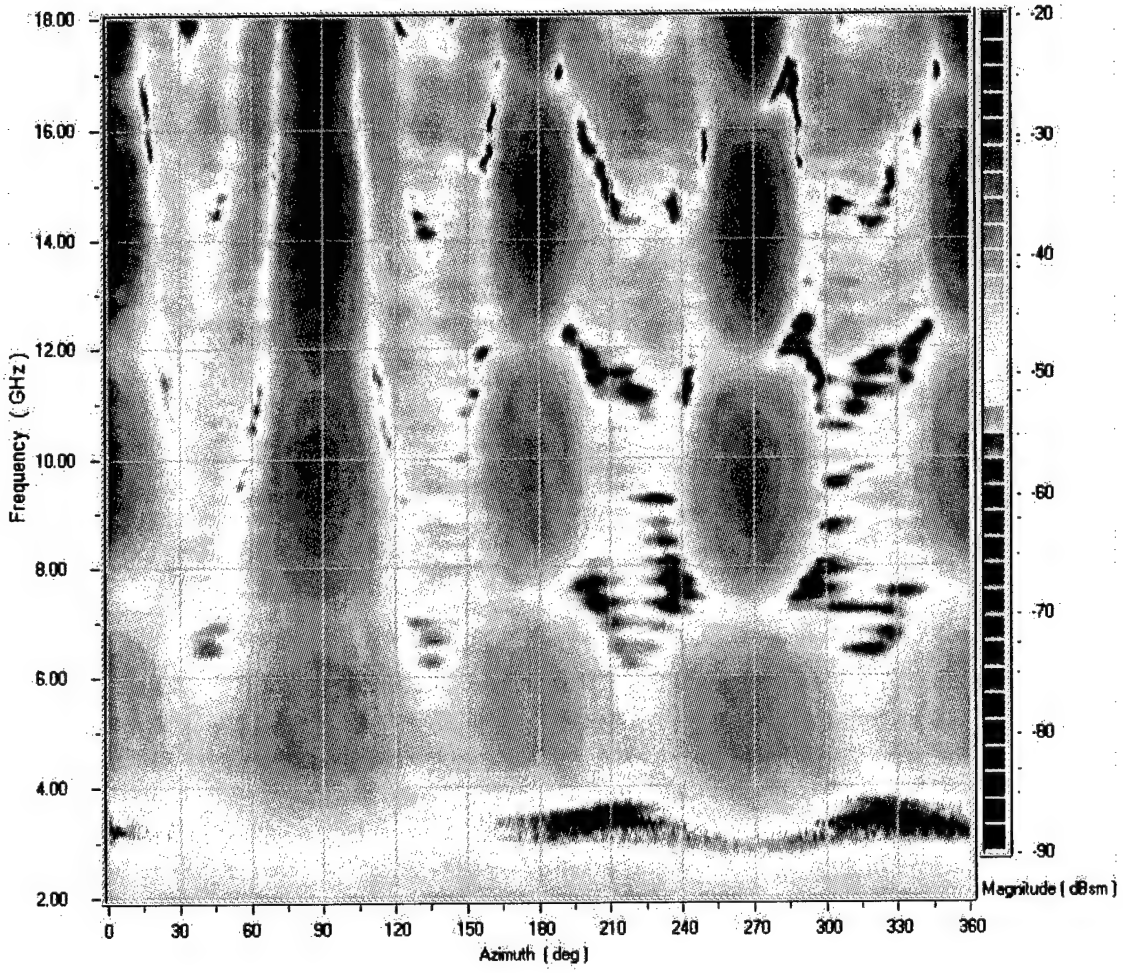

Figure B.8 RCS of the Small Polyurethane Cube with R-card for Vertical Polarization.

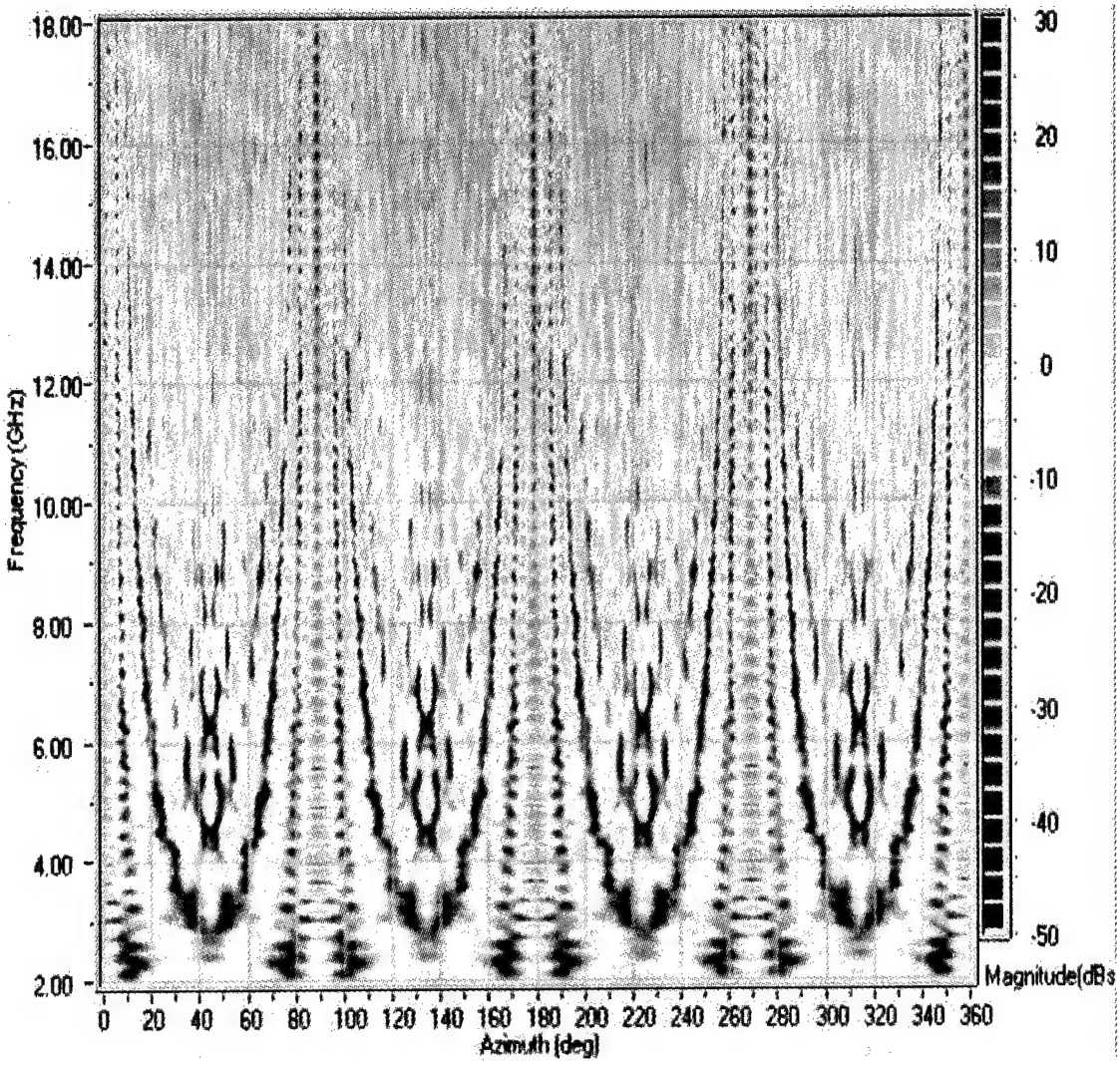

Figure B.9 RCS of the Large Polyethylene Cube for Horizontal Polarization.

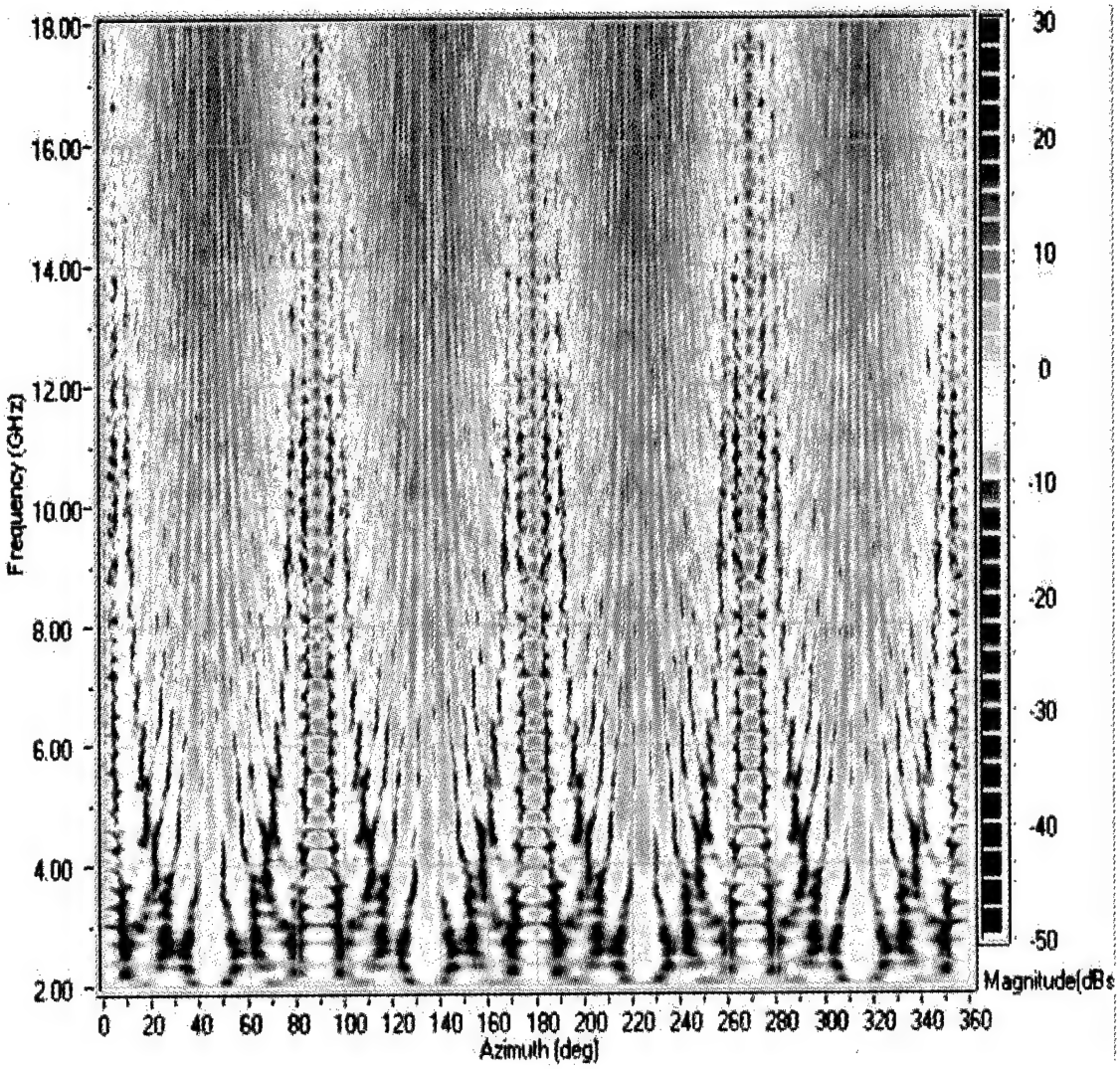

Figure B.10 RCS of the Large Polyethylene Cube for Vertical Polarization.

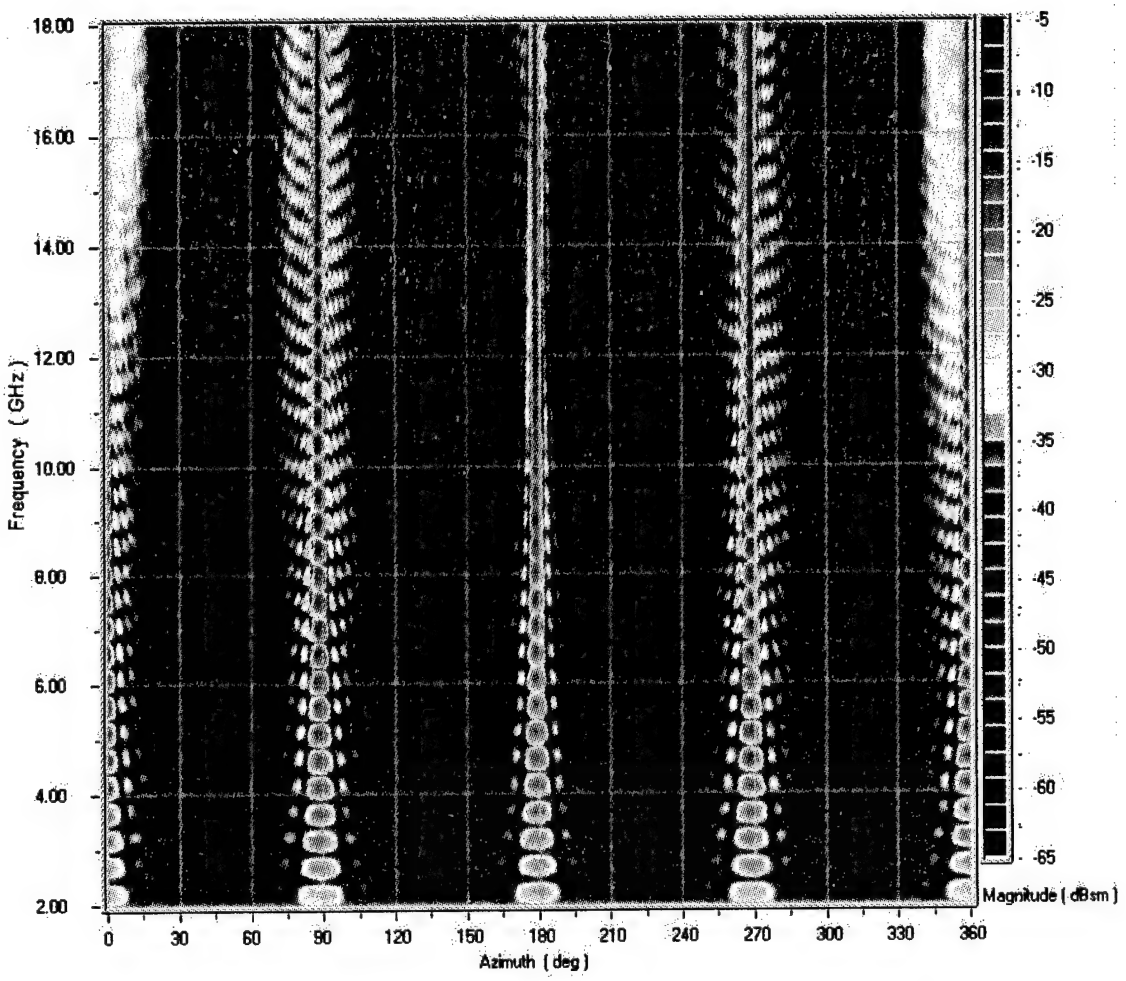

Figure B.11 RCS of the Large Polyurethane Cube for Horizontal Polarization.

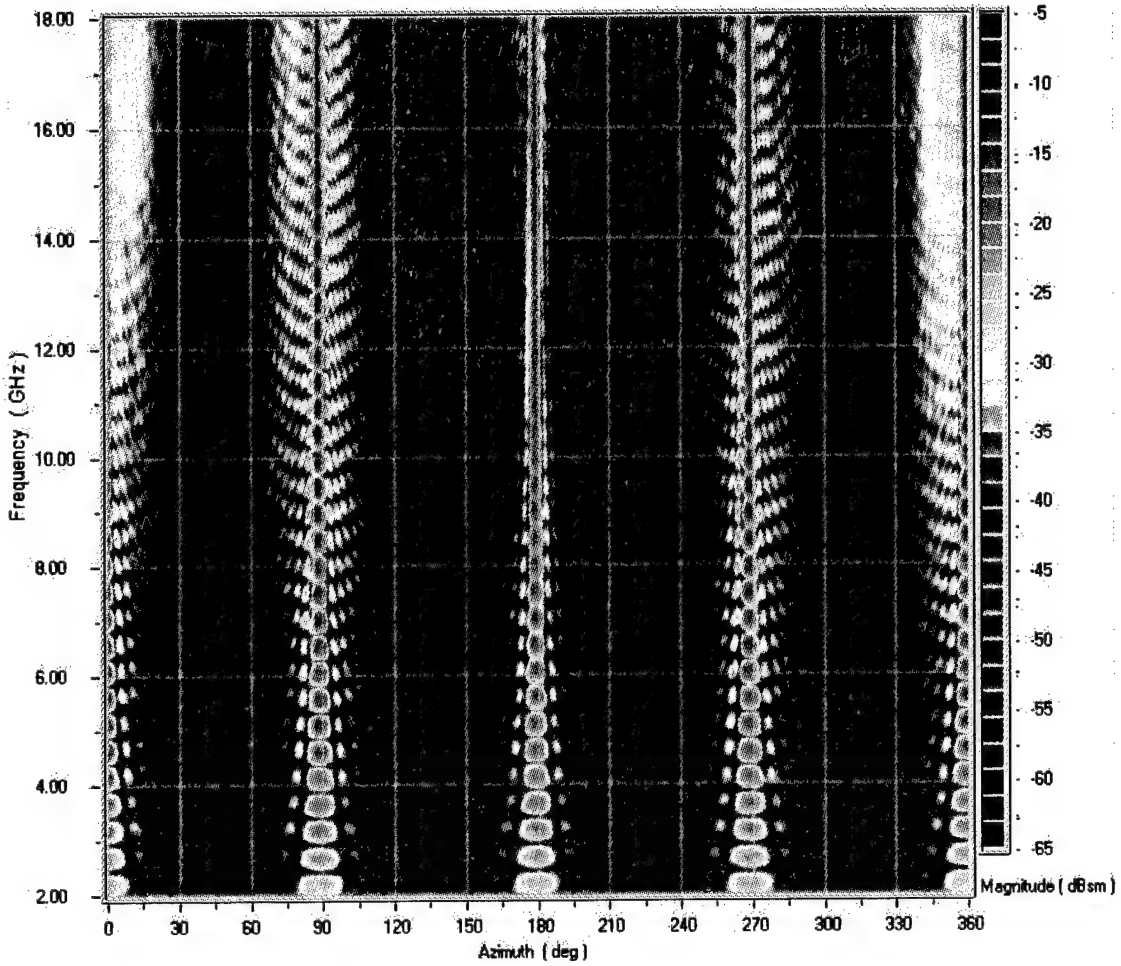

Figure B.12 RCS of the Large Polyurethane Cube for Vertical Polarization.

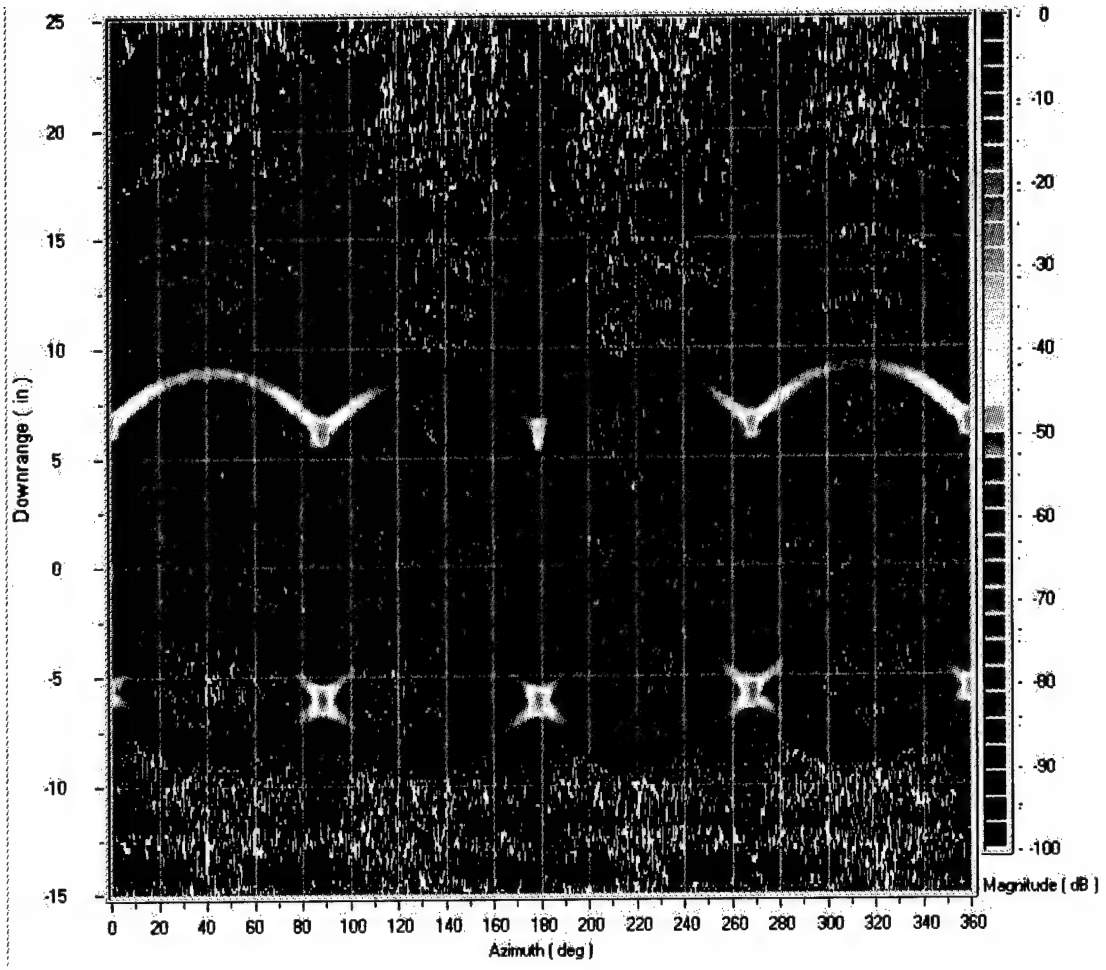

Figure B.13 Range vs. Azimuth Time Domain Plot of the Large Polyurethane Cube for Vertical Polarization.

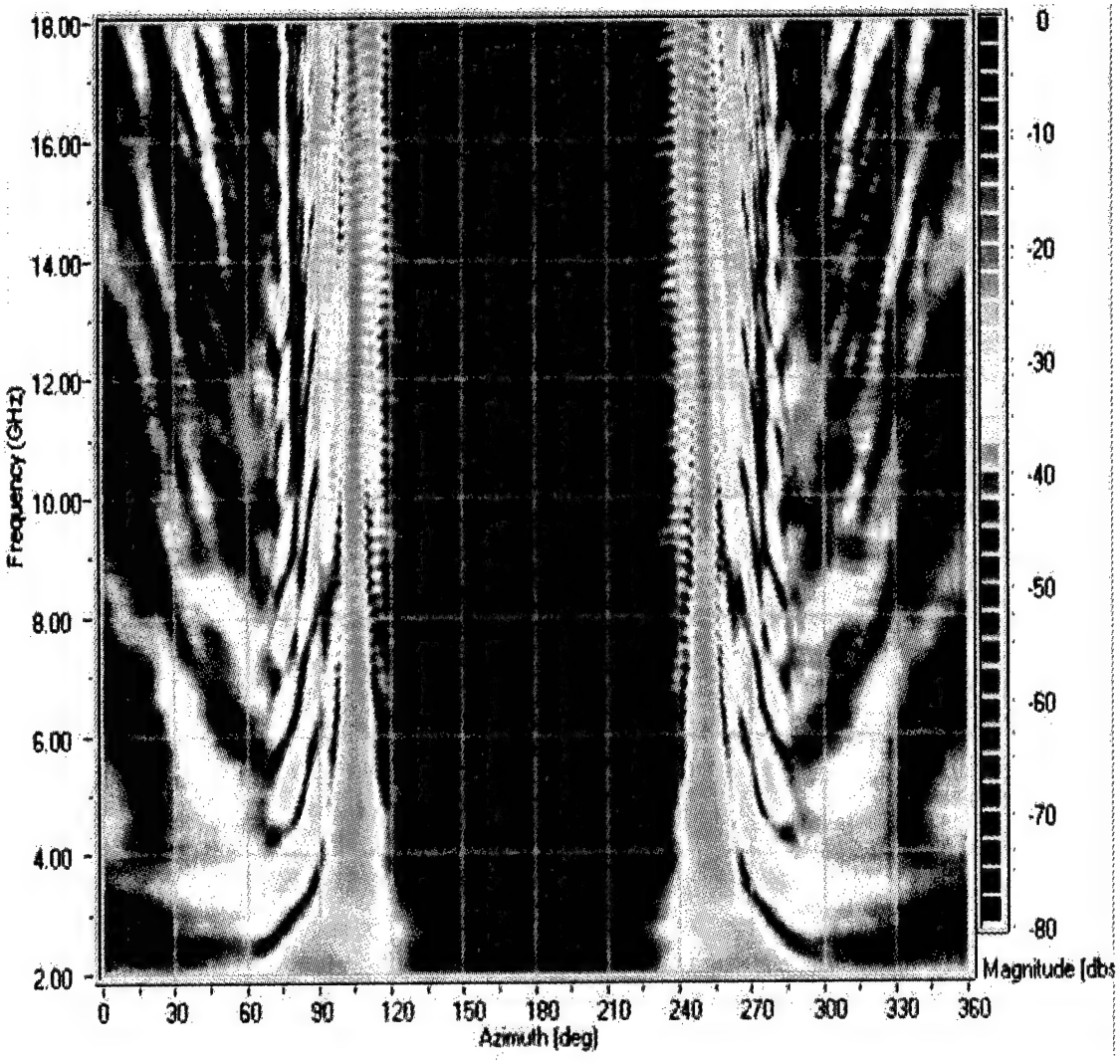

Figure B.14 RCS of the Polyethylene Mini-Arrow for Horizontal Polarization.

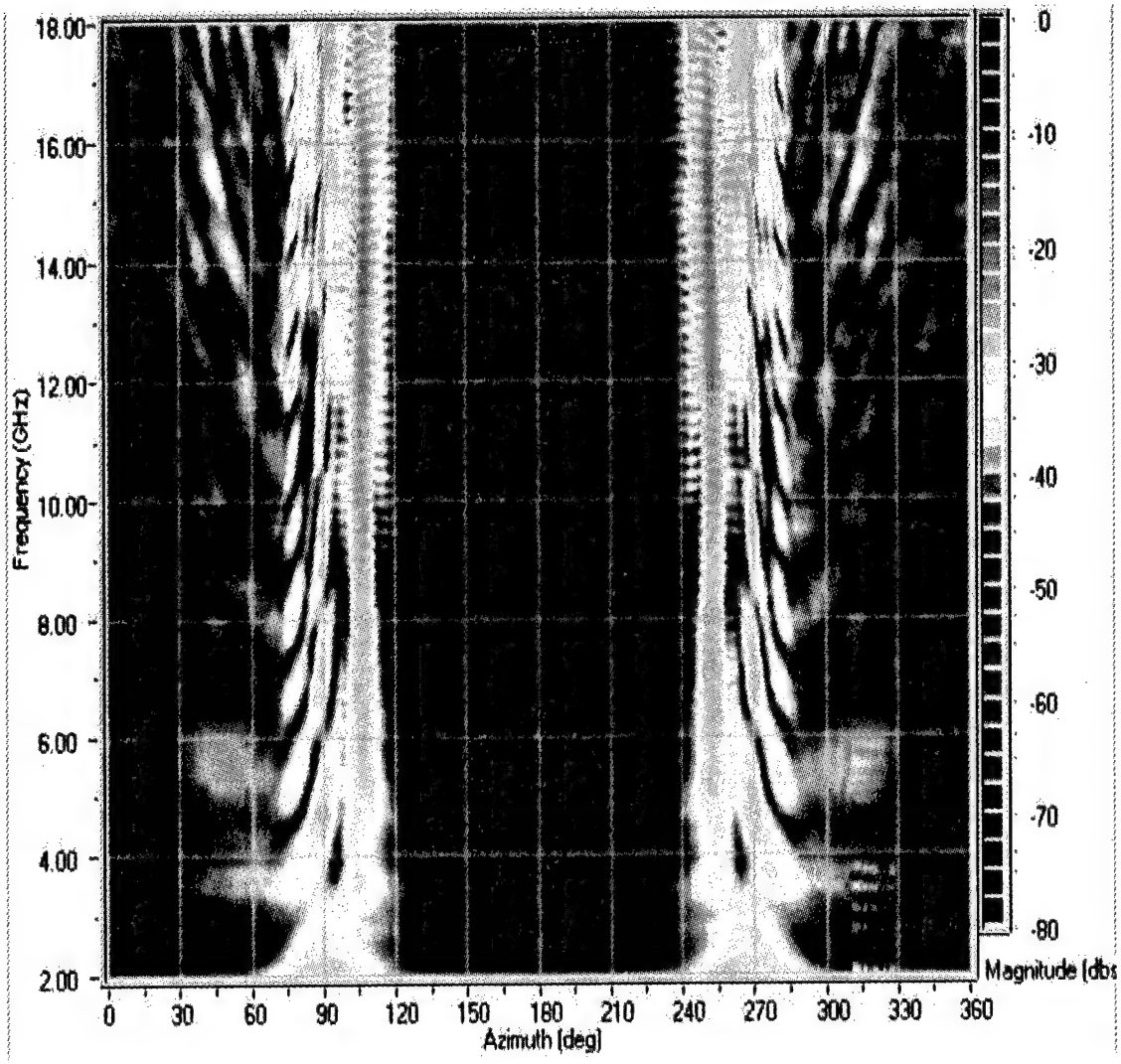

Figure B.15 RCS of the Polyethylene Mini-Arrow for Vertical Polarization.

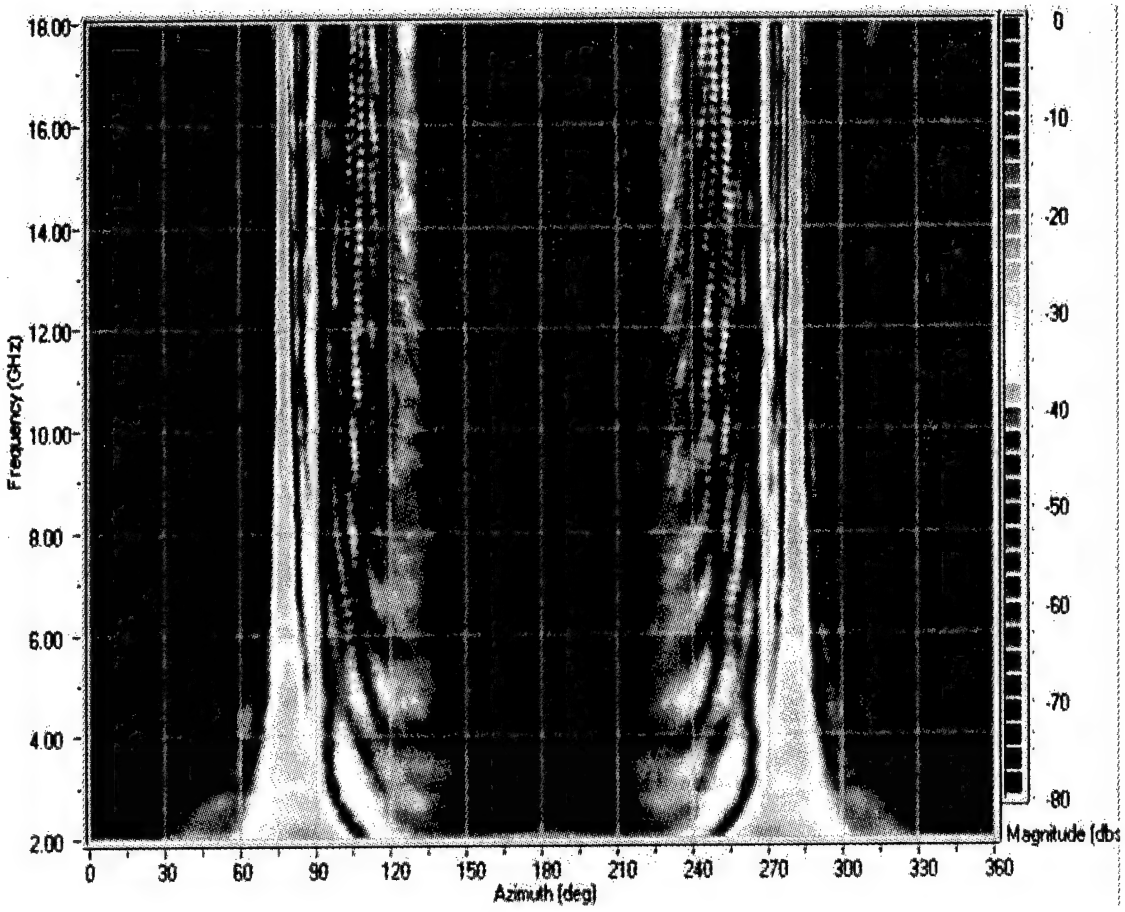

Figure B.16 RCS of the Polyethylene Mini-Arrow with R-card for Horizontal Polarization.

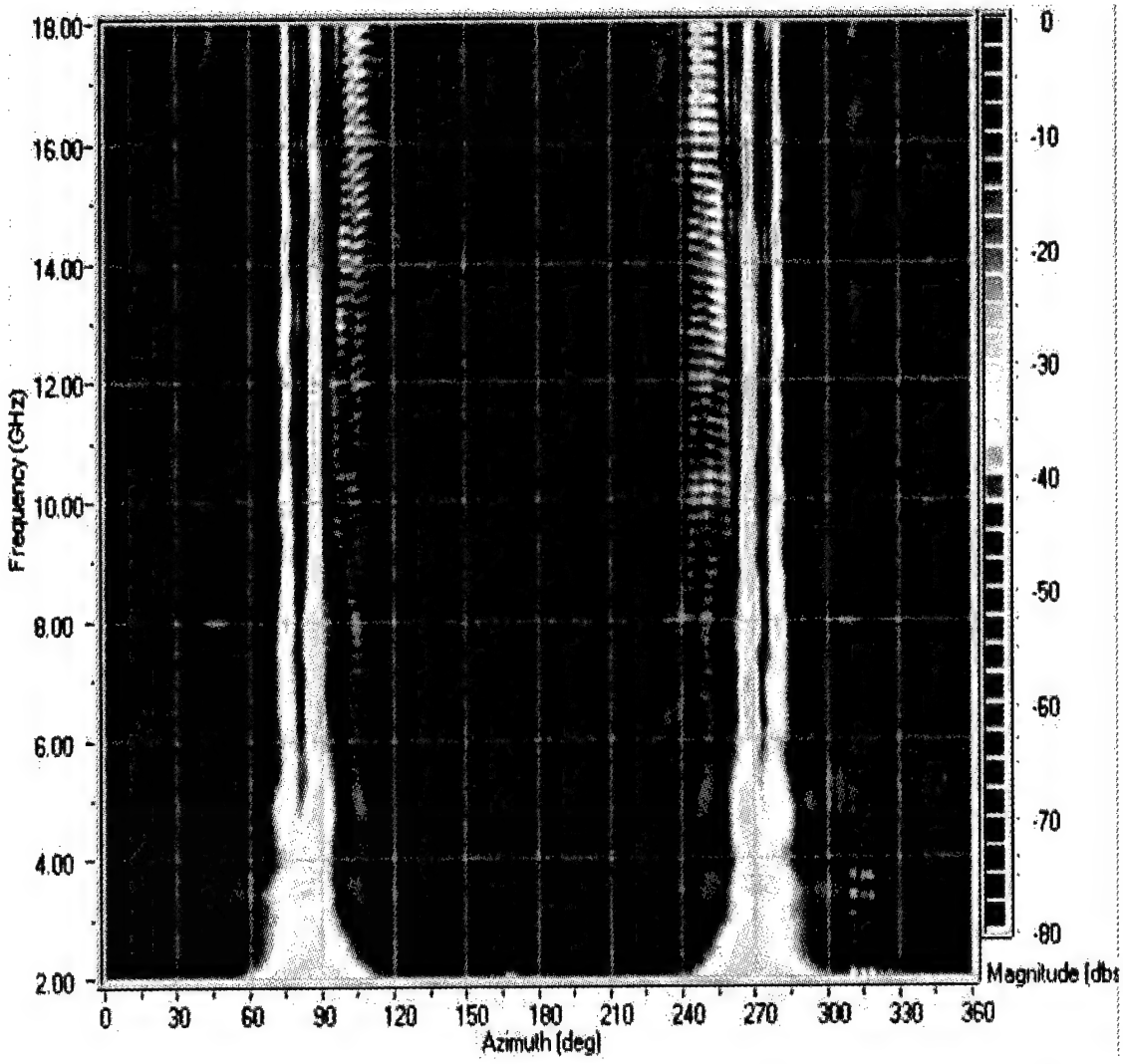

Figure B.17 RCS of the Polyethylene Mini-Arrow with R-card for Vertical Polarization.

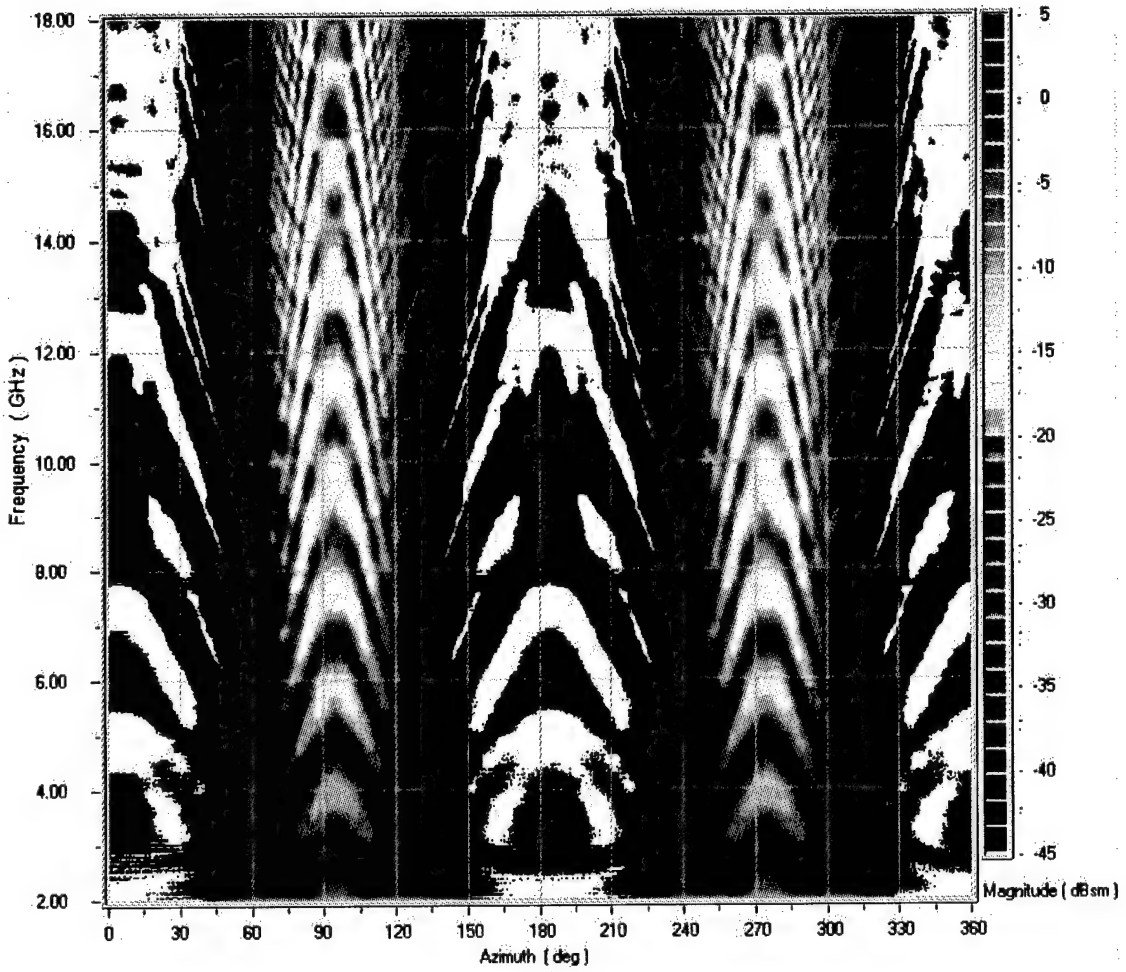

Figure B.18 RCS of the Polyethylene Ogive for Horizontal Polarization.

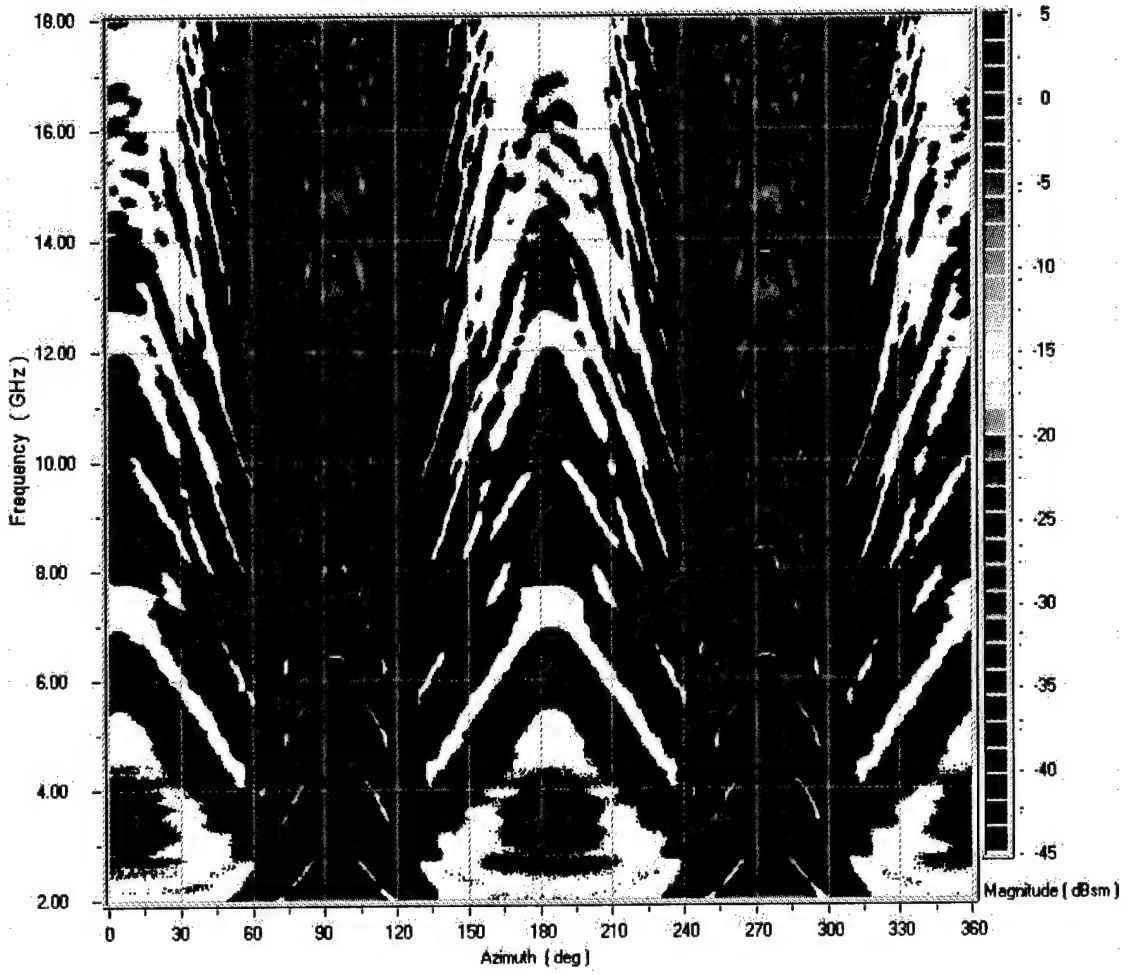

Figure B.19 RCS of the Polyethylene Ogive for Vertical Polarization.

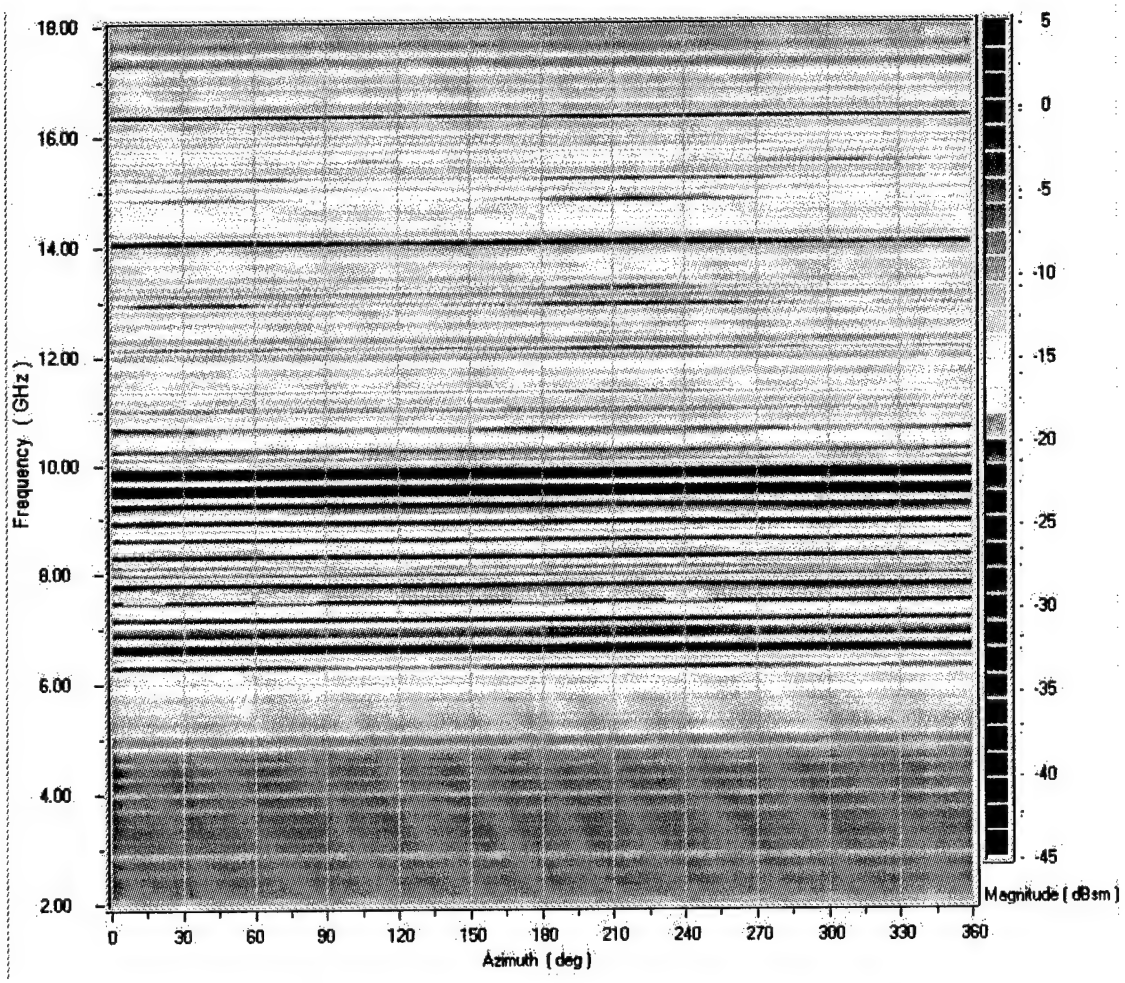

Figure B.20 RCS of the Polyethylene Sphere for Horizontal Polarization.

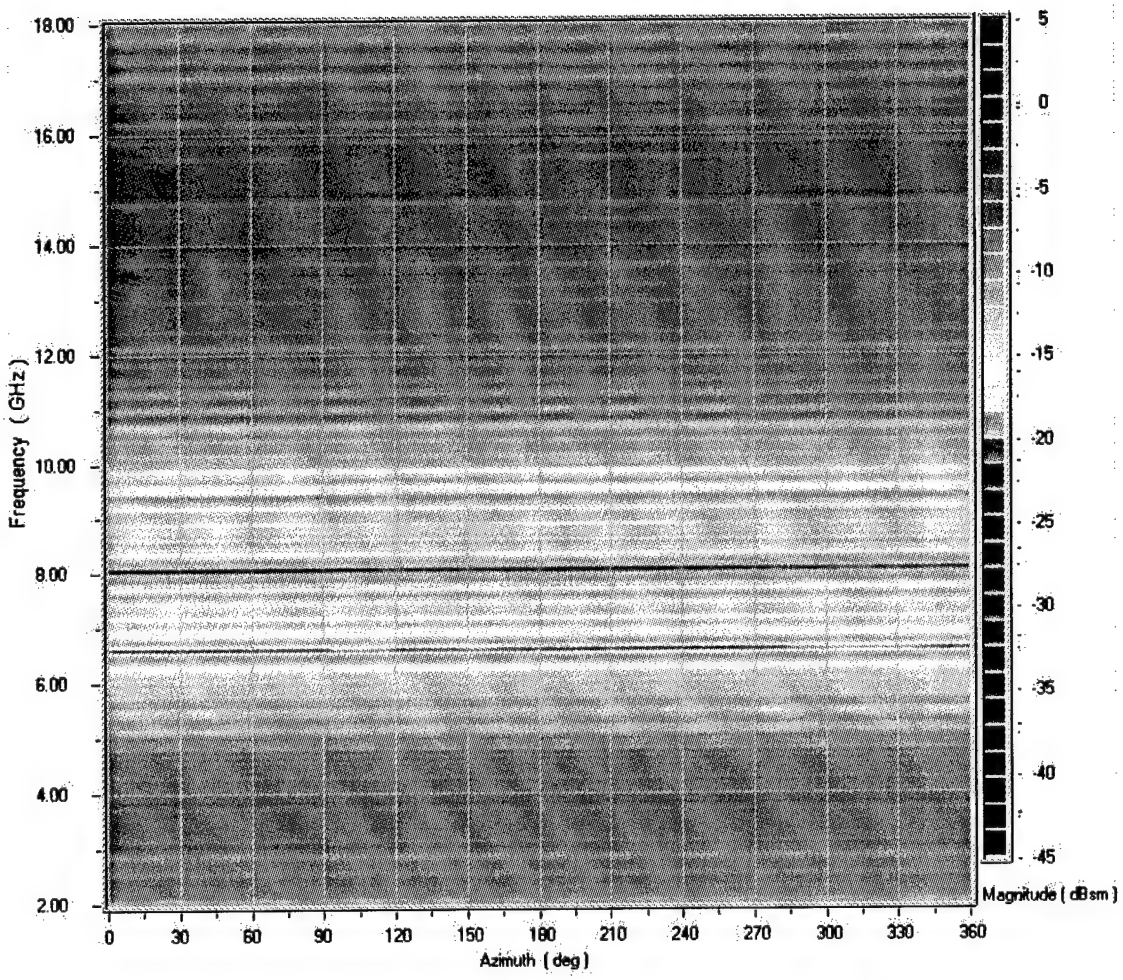

Figure B.21 RCS of the Polyethylene Sphere for Vertical Polarization.

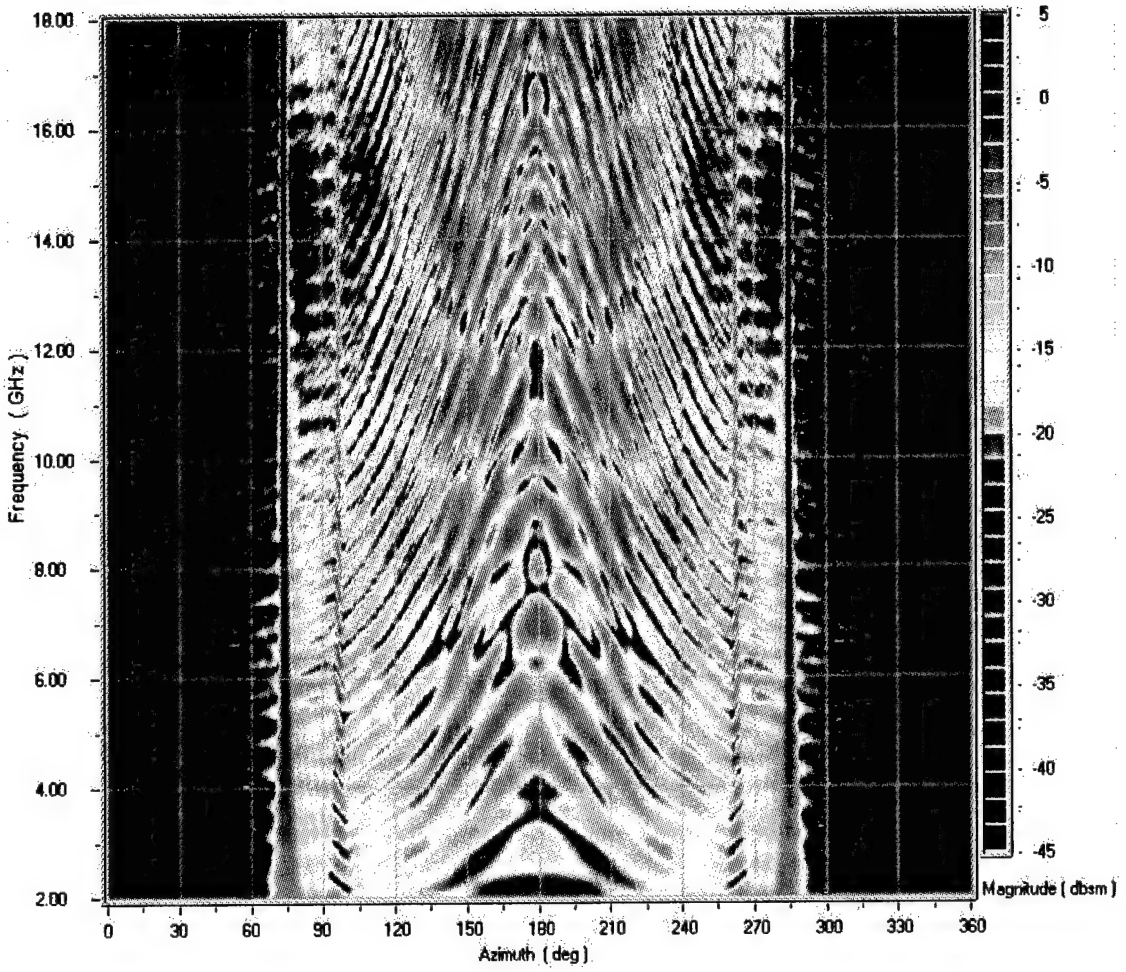

Figure B.22 RCS of the Polyethylene Conesphere for Horizontal Polarization.

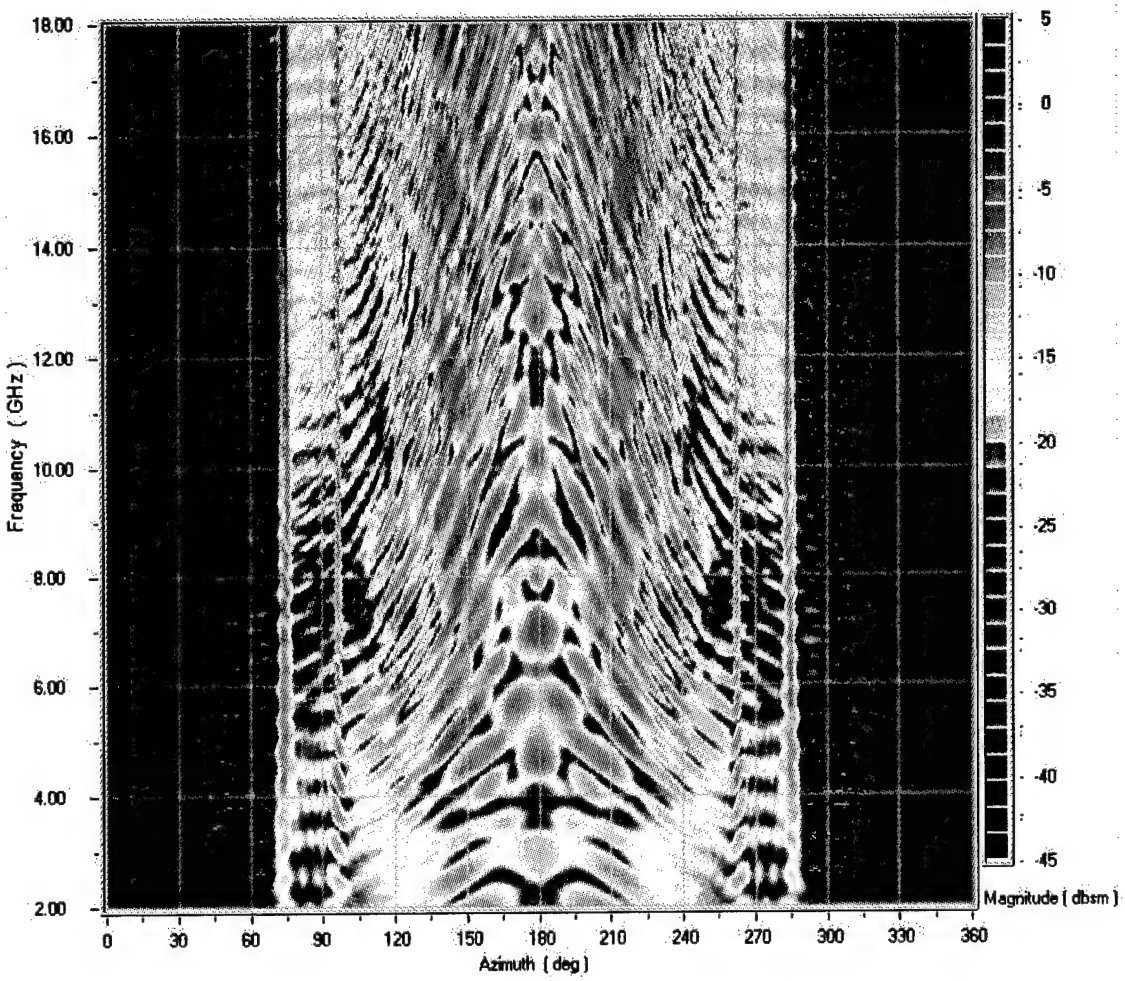

Figure B.23 RCS of the Polyethylene Conesphere for Vertical Polarization.

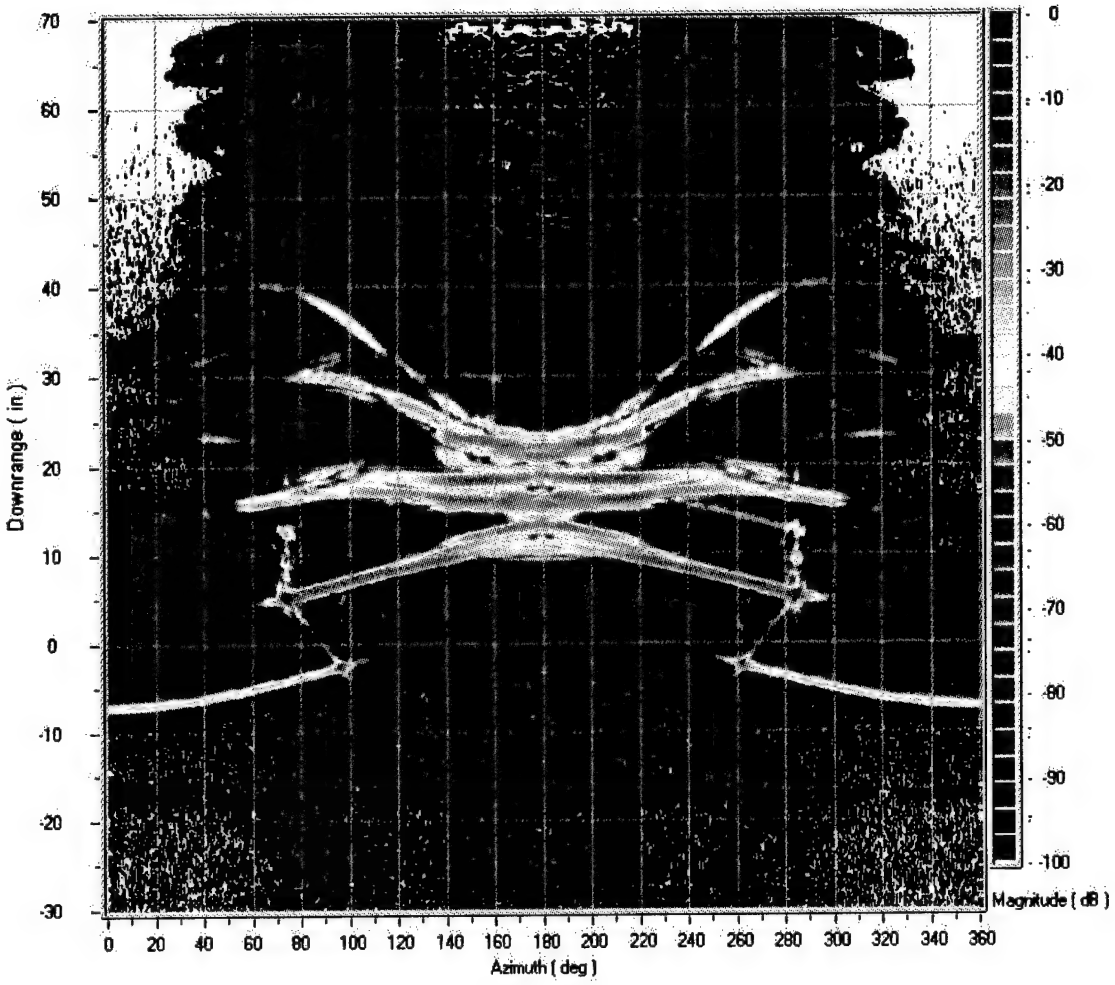

Figure B.24 Range vs. Aximuth Time Domain Plot of the Polyethylene conesphere for Horizontal Polarization.

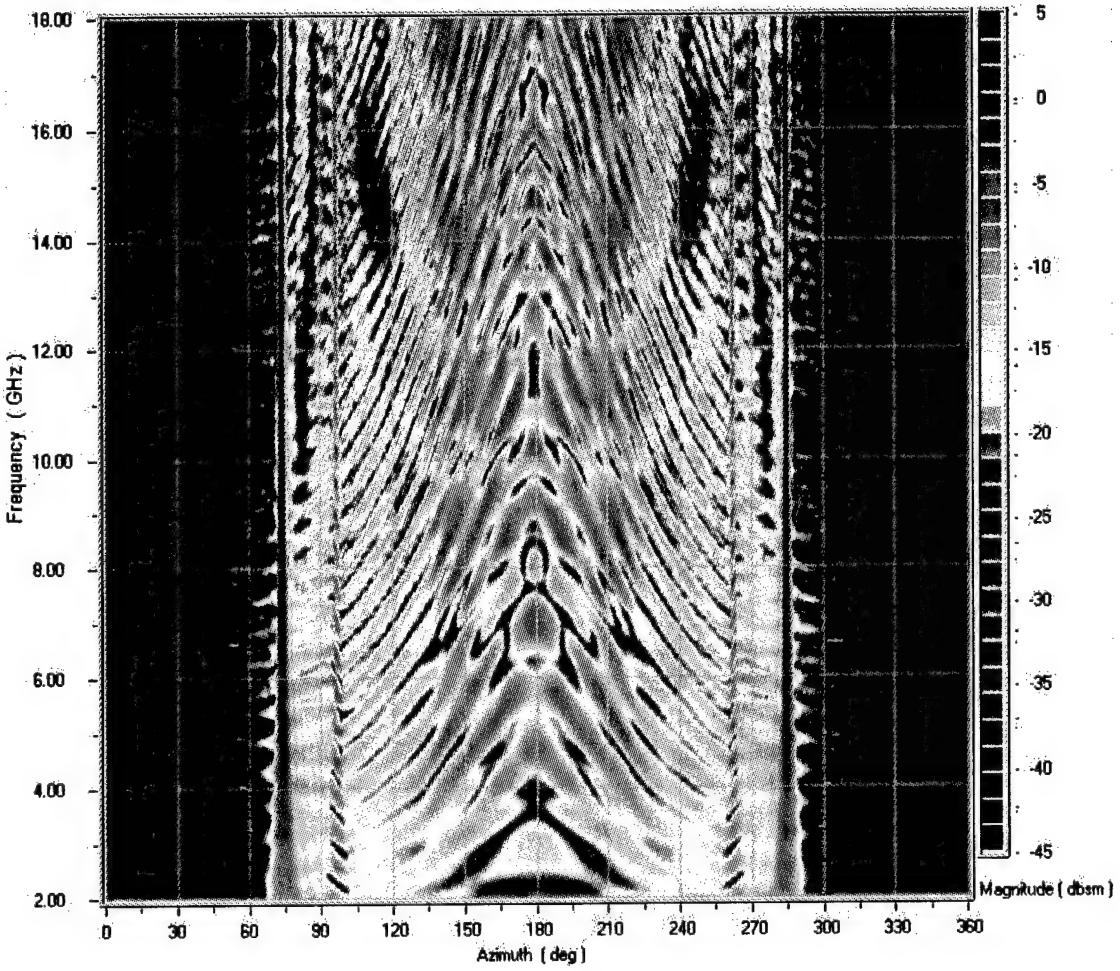

Figure B.25 RCS of the Polyethylene Conesphere with a Gap for Horizontal Polarization.

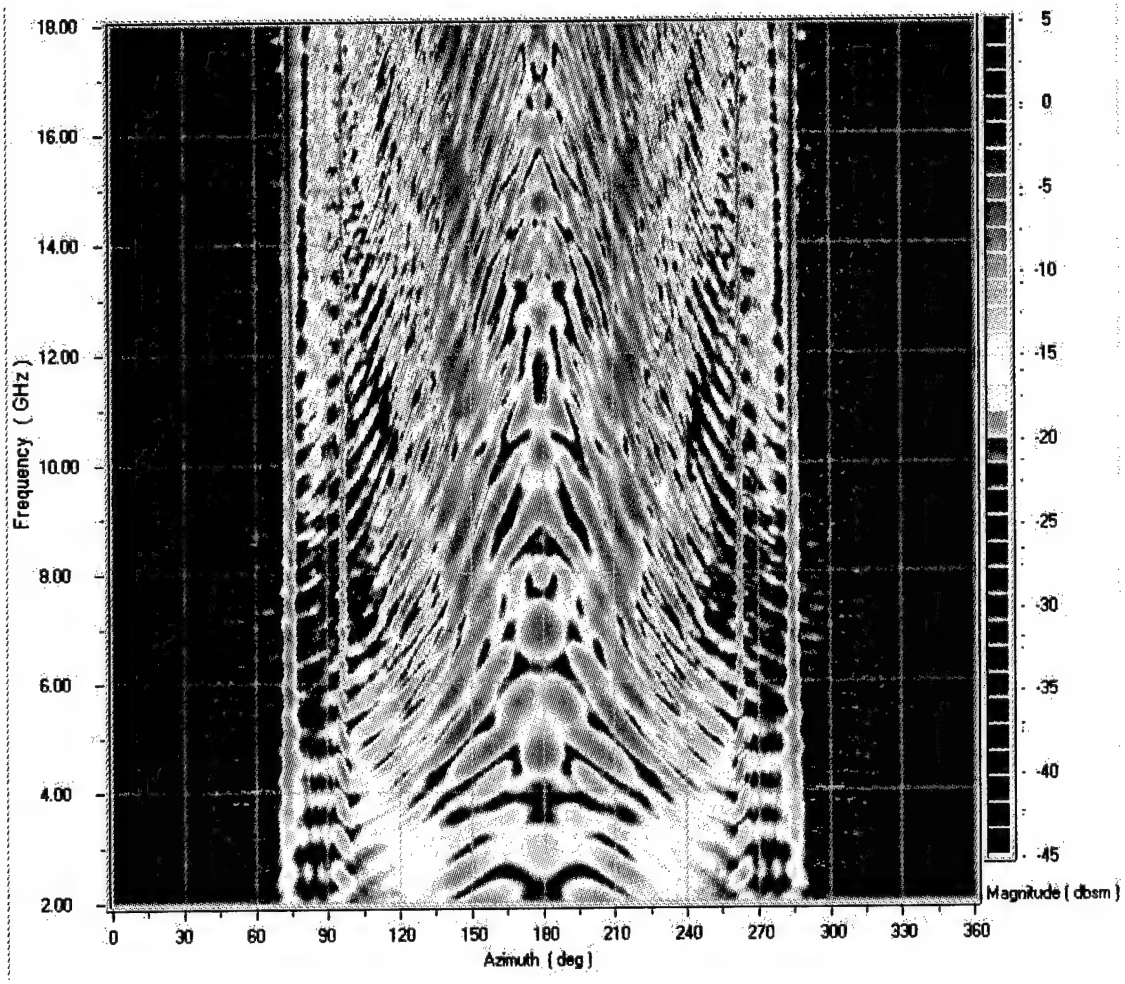

Figure B.26 RCS of the Polyethylene Conesphere with a Gap for Vertical Polarization.

Appendix C. Uncertainty Plots

This appendix presents data associated with the measured RCS uncertainty. The first section includes three plots of noise background, the average of three data sets, and the "smoothed" average. The next section contains the calibration data for the small and large polyethylene cubes, the mini-arrow, and the conespheres. The final section presents RCS plots of the overall uncertainty for selected targets and frequencies.

C.1 Noise-Background Uncertainty

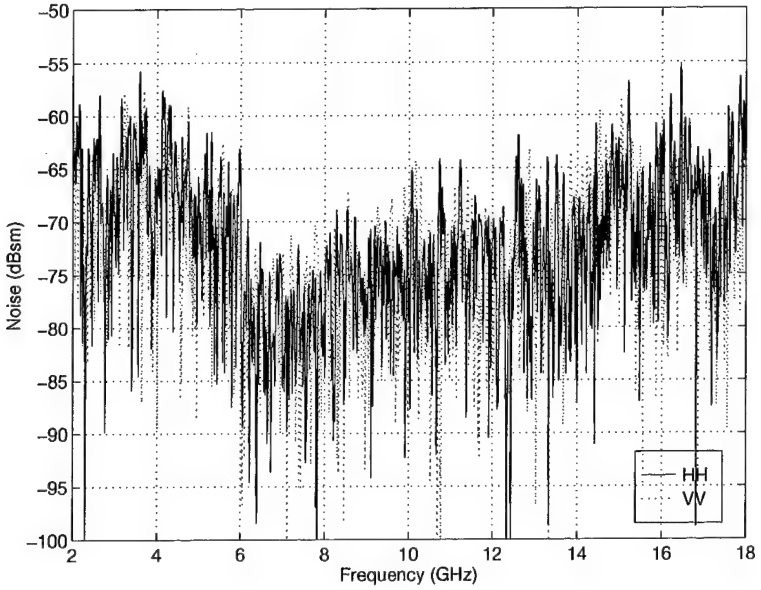

Figure C.1 The noise background measurement associated with the RCS measurement of the small polyethylene cube.

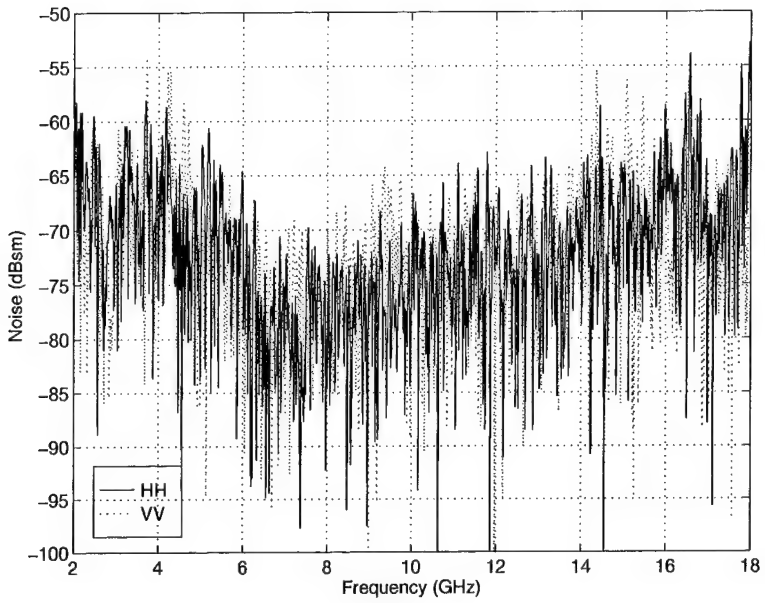

Figure C.2 The noise background measurement associated with the RCS measurement of the polyethylene mini-arrow.

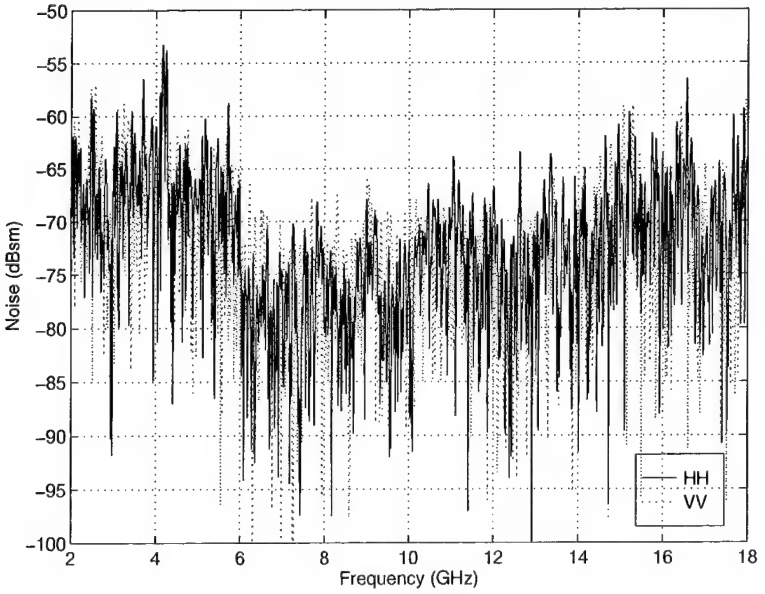

Figure C.3 The noise background measurement associated with the RCS measurement of the polyethylene ogive.

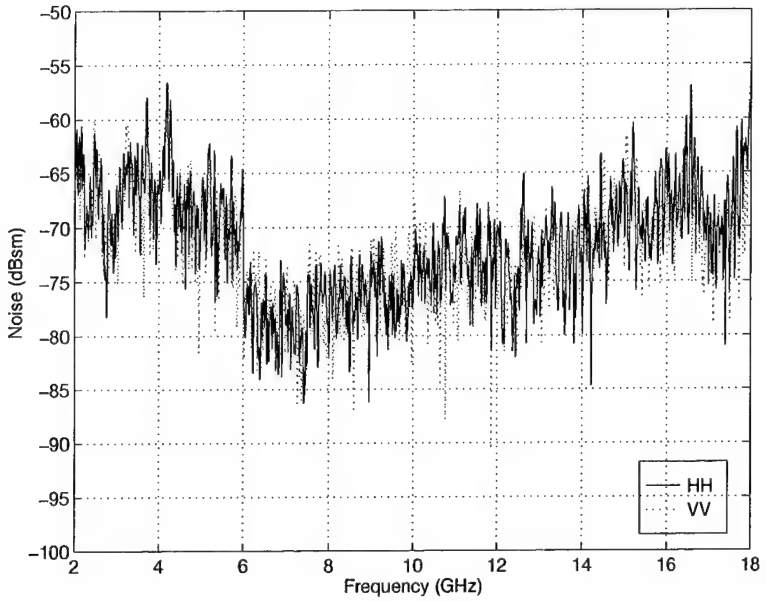

Figure C.4 The averaged noise background of Figures C.1, C.2, and C.3.

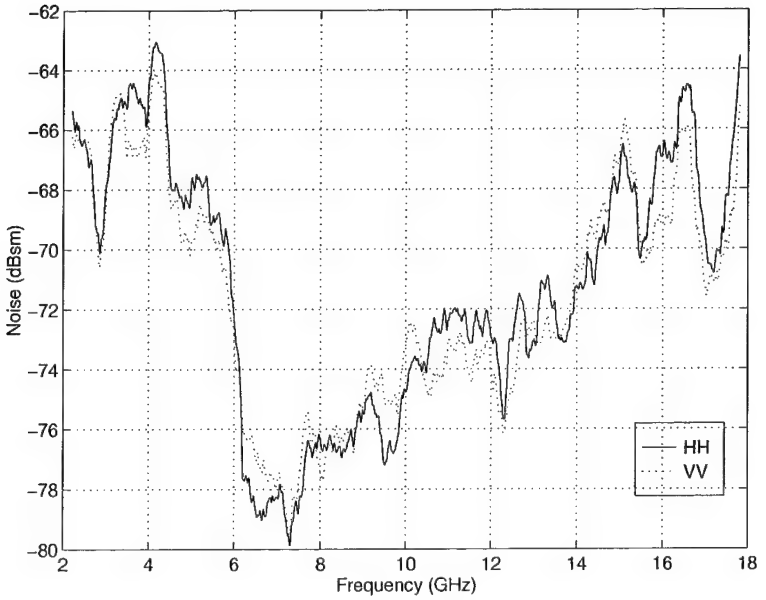

Figure C.5 The smoothed noise background from Figure C.4. The data was smoothed using an 41 point window.

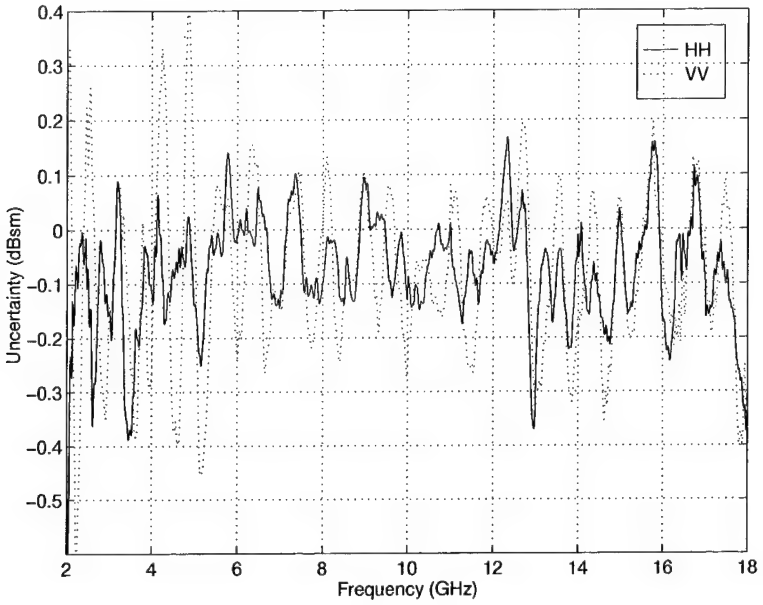

Figure C.6 The calibration data for the small polyethylene cube.

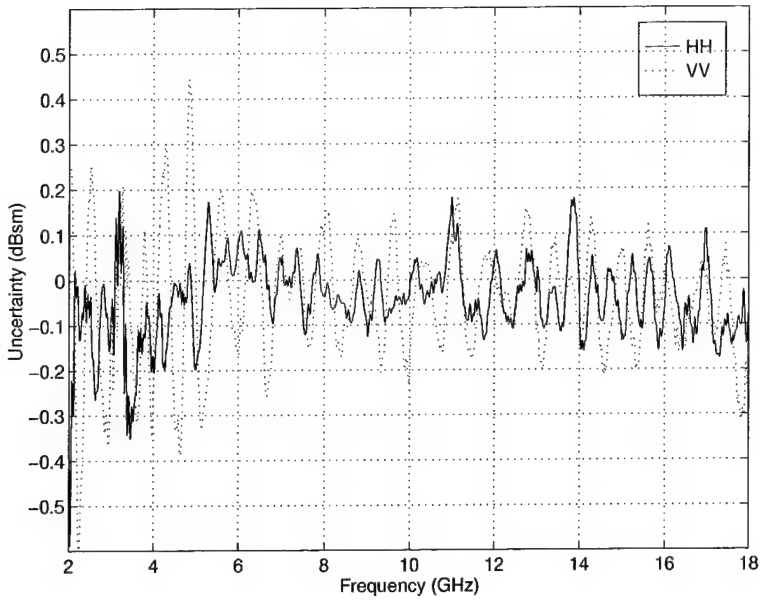

Figure C.7 The calibration data for the large polyethylene cube and the mini-arrow.

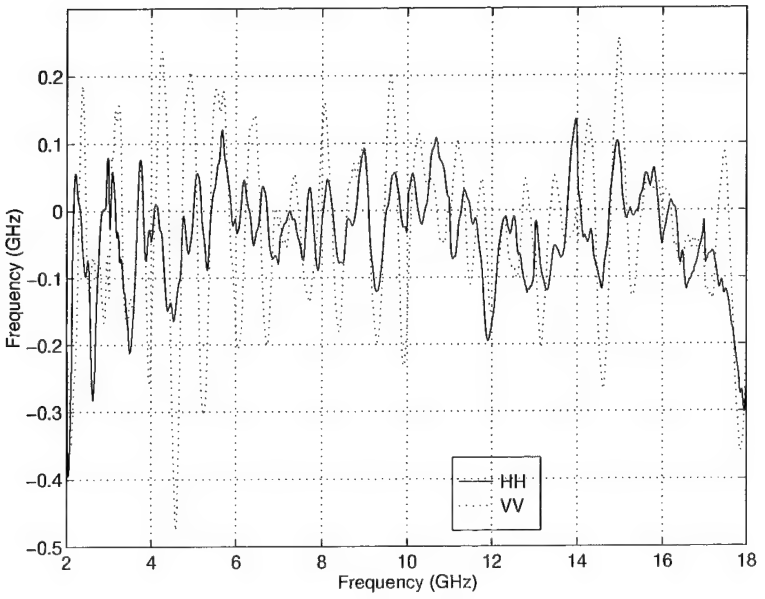

Figure C.8 The calibration data for both of the polyethylene conespheres.

C.3 Overall Uncertainty

Frequency	Target	Type of Plot	Figure
10	Small Polyethylene Cube	Overall Uncertainty	C.9
10	Small Polyethylene Cube	RCS with Error bounds	C.10
2	Large Polyethylene Cube	Overall Uncertainty	C.11
2	Large Polyethylene Cube	RCS with Error bounds	C.12
6	Polyethylene Mini-Arrow	Overall Uncertainty	C.13
6	Polyethylene Mini-Arrow	RCS with Error Bounds	C.14
10	Polyethylene Ogive	Overall Uncertainty	C.15
10	Polyethylene Ogive	RCS with Error Bounds	C.16
2	Polyethylene Conesphere	Overall Uncertainty	C.17
2	Polyethylene Conesphere	RCS with Error Bounds	C.18
2	Polyethylene Conesphere with a Gap	Overall Uncertainty	C.19
2	Polyethylene Conesphere with a Gap	RCS with Error Bounds	C.20

Table C.1 Measured RCS plots with uncertainty.

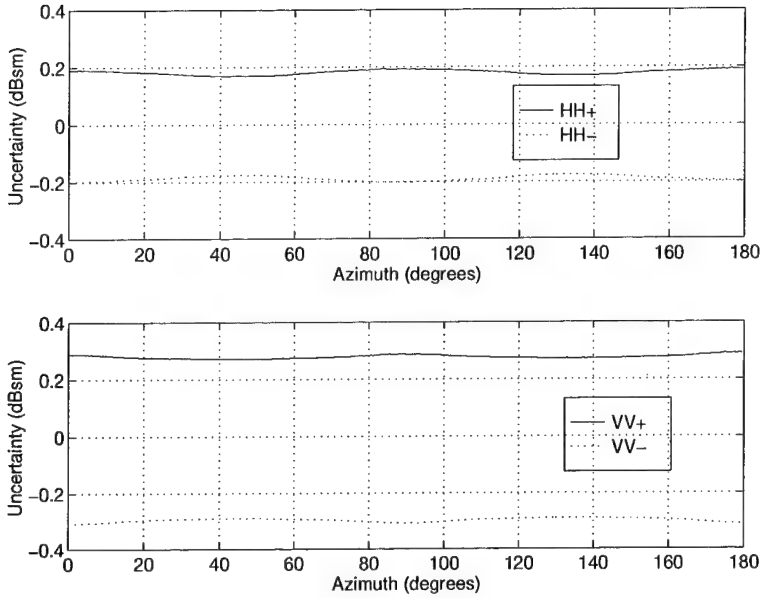

Figure C.9 The overall uncertainty for the small polyethylene cube at 10 GHz.

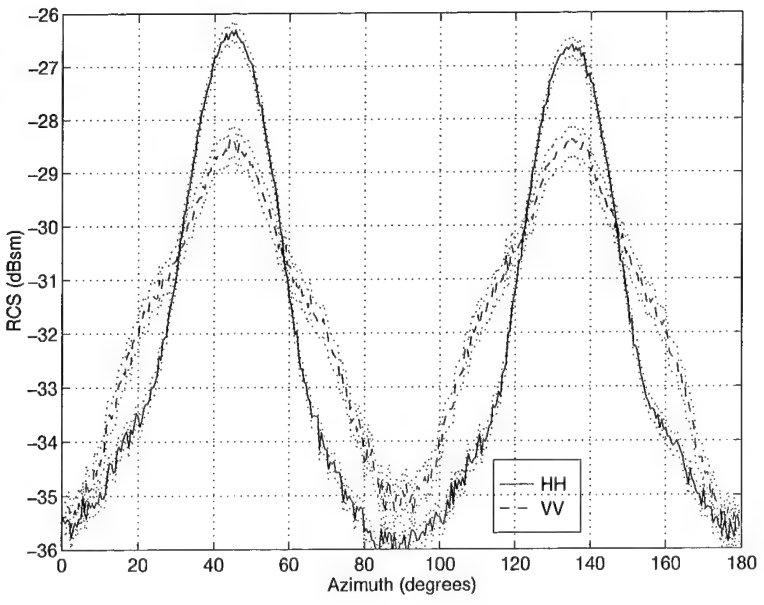

Figure C.10 The measured RCS of the small polyethylene cube at 10 GHz with error bounds.

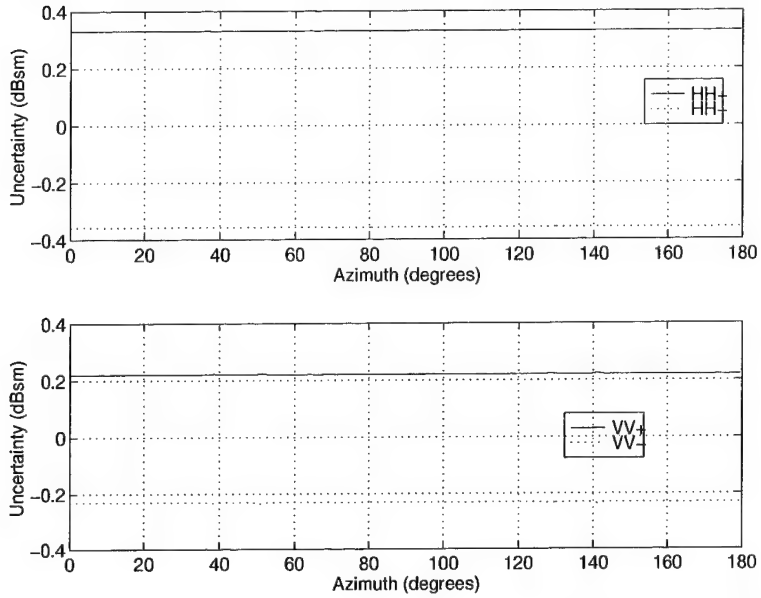

Figure C.11 The overall uncertainty for the large polyethylene cube at 2 GHz.

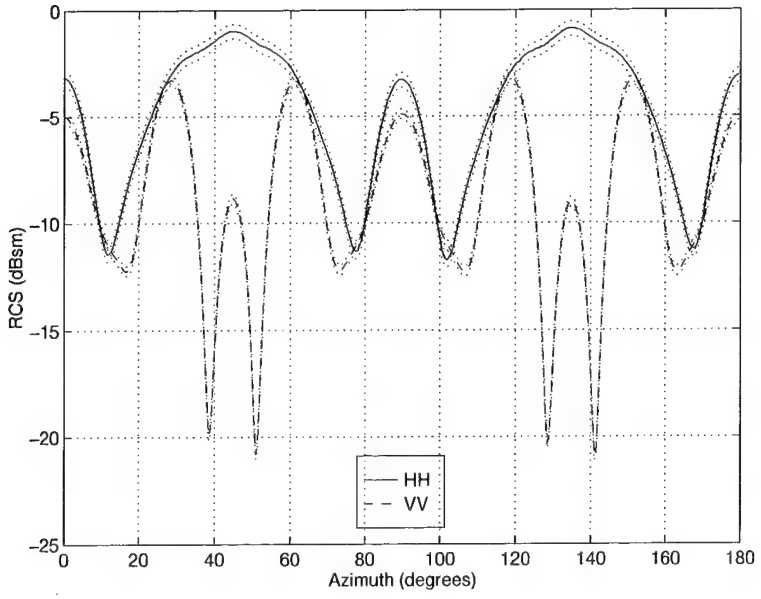

Figure C.12 The measured RCS of the large polyethylene cube at 2 GHz with error bounds.

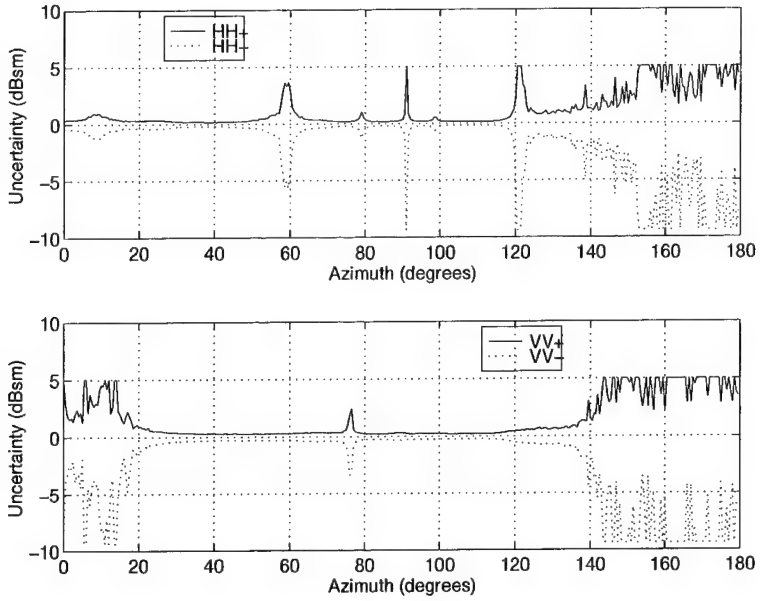

Figure C.13 The overall uncertainty for the polyethylene mini-arrow at 6 GHz.

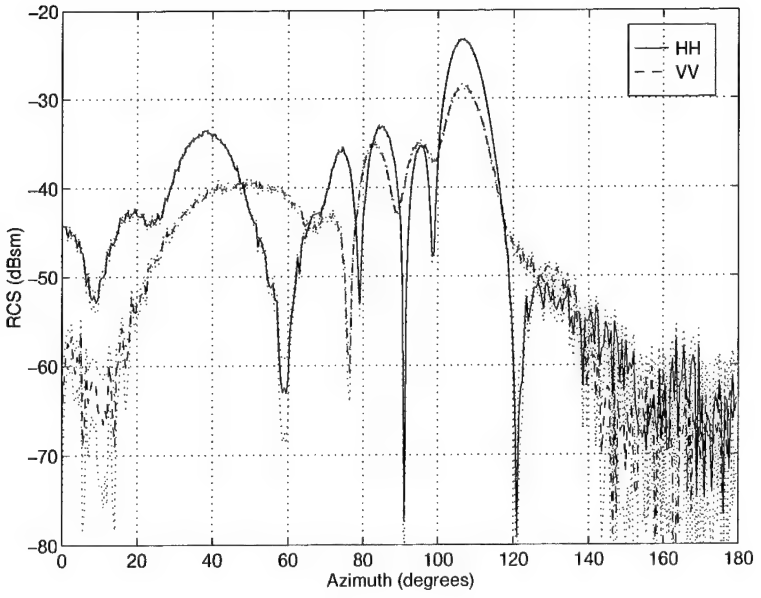

Figure C.14 The measured RCS of the polyethylene mini-arrow at 6 GHz with error bounds.

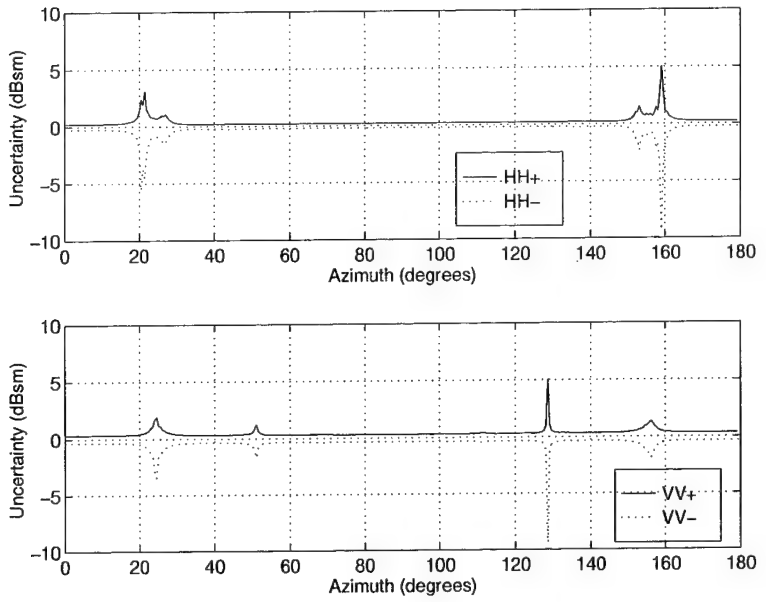

Figure C.15 The overall uncertainty for the polyethylene ogive at 10 GHz.

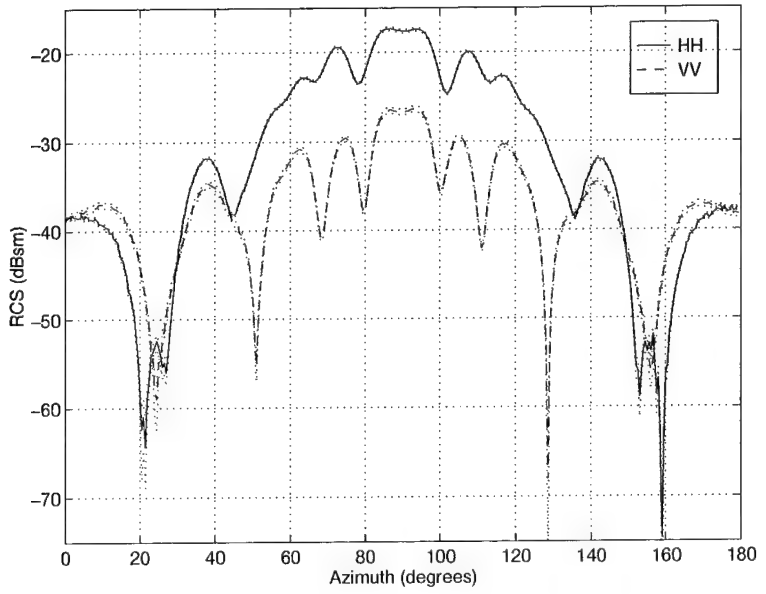

Figure C.16 The measured RCS of the polyethylene ogive at 10 GHz with error bounds.

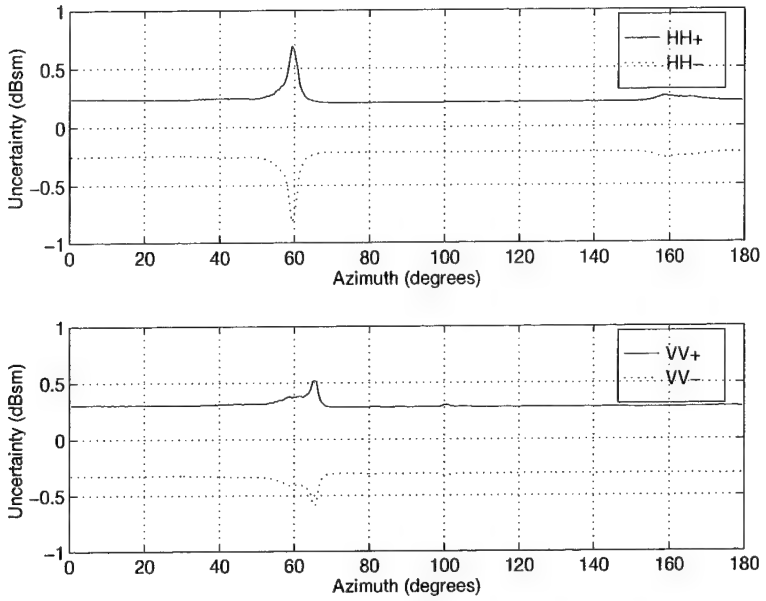

Figure C.17 The overall uncertainty for the polyethylene conesphere at 2 GHz.

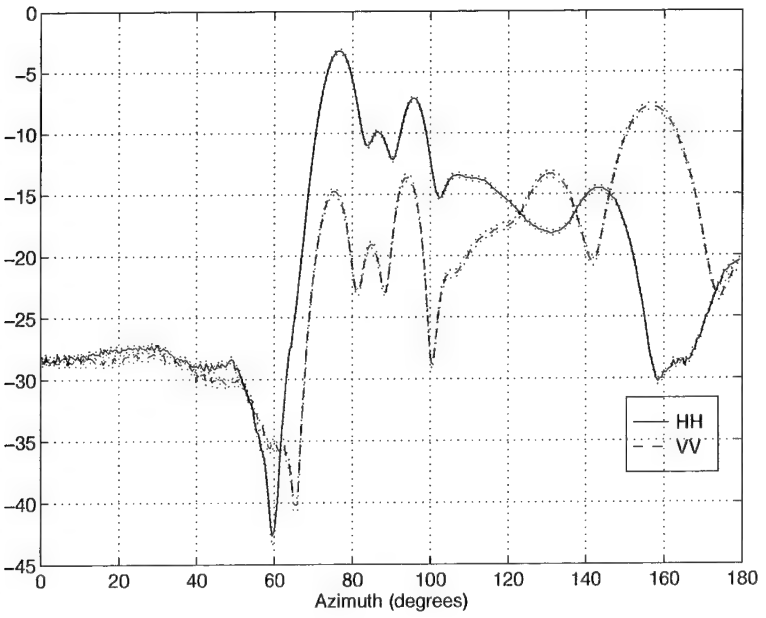

Figure C.18 The measured RCS of the polyethylene conesphere at 2 GHz with error bounds.

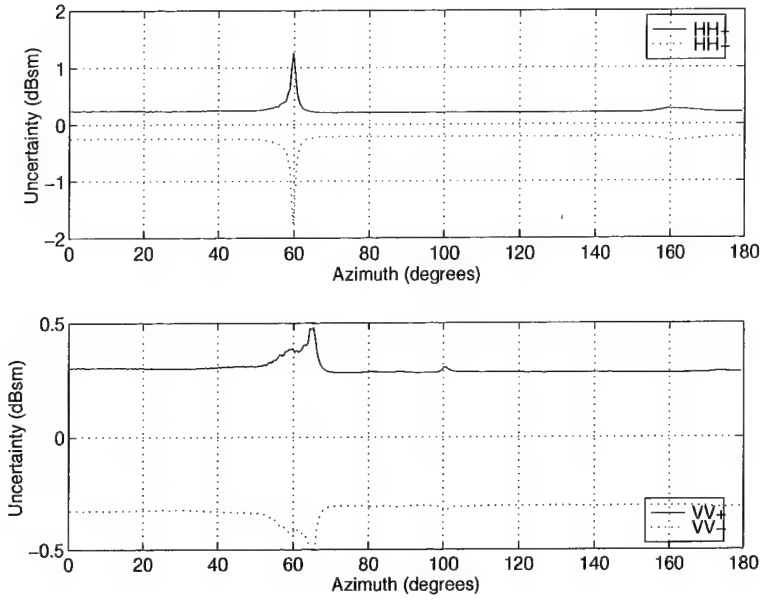

Figure C.19 The overall uncertainty for the polyethylene conesphere with a gap at 2 GHz.

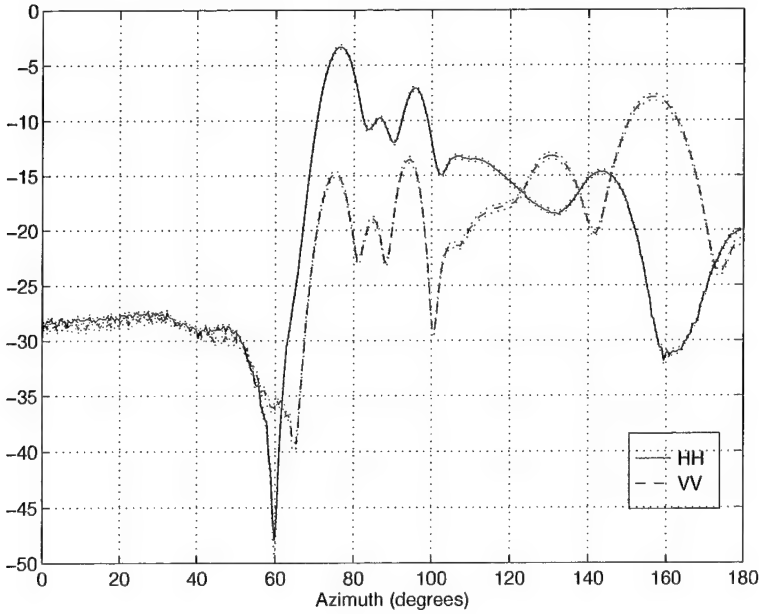

Figure C.20 The measured RCS of the polyethylene conesphere with a gap at 2 GHz with error bounds.

Appendix D. Code Validation Plots

This appendix is a compilation of the comparison between the 3D-RCIE predicted RCS and the measured RCS for each target. Additionally, comparisons of predicted RCS with altered mesh sizes, altered target dimensions, altered dielectric constants, and different matrix solving routines are presented.

D.1 Small Cube - Polyethylene

Description	Figure
RCS Comparison of the Small Polyethylene Cube at 2 GHz	D.1
RCS Comparison of the Small Polyethylene Cube at 4 GHz	D.2
RCS Comparison of the Small Polyethylene Cube at 6 GHz	D.3
RCS Comparison of the Small Polyethylene Cube at 7 GHz	D.4
RCS Comparison of the Small Polyethylene Cube at 8 GHz	D.5
RCS Comparison of the Small Polyethylene Cube at 10 GHz	D.6
RCS Comparison of the Small Polyethylene Cube at 12 GHz	D.7
RCS Comparison of the Small Polyethylene Cube at 13 GHz	D.8
RCS Comparison of the Small Polyethylene Cube at 14 GHz	D.9
RCS Comparison of the Small Polyethylene Cube at 16 GHz	D.10
RCS Comparison of the Small Polyethylene Cube at 18 GHz	D.11
Small Polyethylene Cube RCS with varied mesh sizes at 6 GHz	D.12
Small Polyethylene Cube RCS with varied mesh sizes at 8 GHz	D.13
Small Polyethylene Cube HH RCS with varied dielectric constants at 10 GHz	D.14
Small Polyethylene Cube VV RCS with varied dielectric constants at 10 GHz	D.15
Small Polyethylene Cube RCS with varied dimensions at 10 GHz	D.16
3D-RCIE (BLG vs. LU) RCS of the Small Polyethylene Cube at 2 GHz	D.17
3D-RCIE (BLG vs. LU) RCS of the Small Polyethylene Cube at 4 GHz	D.18
3D-RCIE (BLG vs. LU) RCS of the Small Polyethylene Cube at 6 GHz	D.19
3D-RCIE (BLG vs. LU) RCS of the Small Polyethylene Cube at 8 GHz	D.20
3D-RCIE (BLG vs. LU) RCS of the Small Polyethylene Cube at 10 GHz	D.21
3D-RCIE (BLG vs. LU) RCS of the Small Polyethylene Cube at 12 GHz	D.22
3D-RCIE (BLG vs. LU) RCS of the Small Polyethylene Cube at 14 GHz	D.23
3D-RCIE (BLG vs. LU) RCS of the Small Polyethylene Cube at 16 GHz	D.24
3D-RCIE (BLG vs. LU) RCS of the Small Polyethylene Cube at 18 GHz	D.25

Table D.1 List of plots for the RCS of the small polyethylene cube.

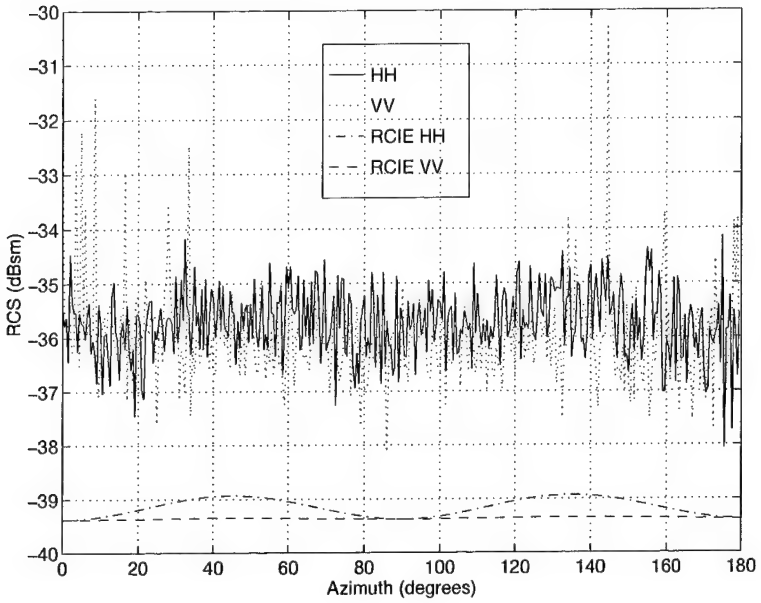

Figure D.1 The monostatic RCS of the small polyethylene cube using 3D-RCIE and measured data obtained at 2 GHz. The mesh size is $50/\lambda$ and BLGMRP was used to solve the matrix.

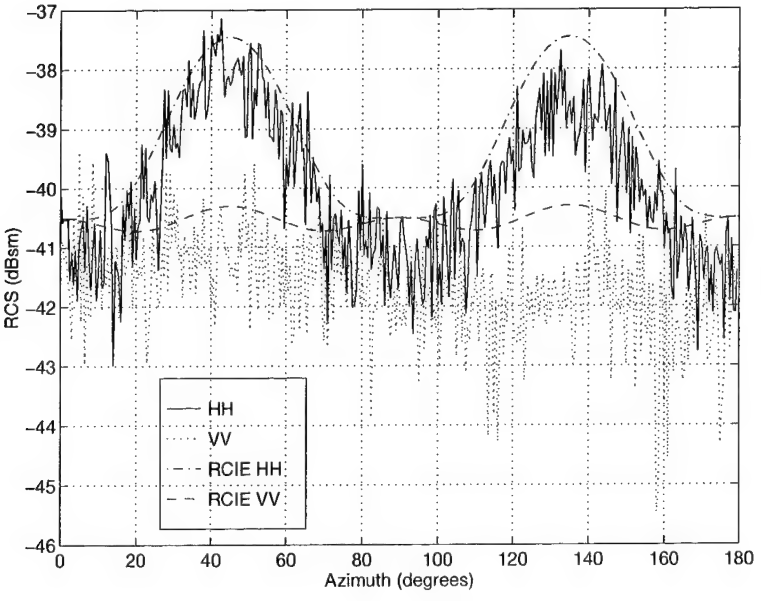

Figure D.2 The monostatic RCS of the small polyethylene cube using 3D-RCIE and measured data obtained at 4 GHz. The mesh size is $25/\lambda$ and BLGMRP was used to solve the matrix.

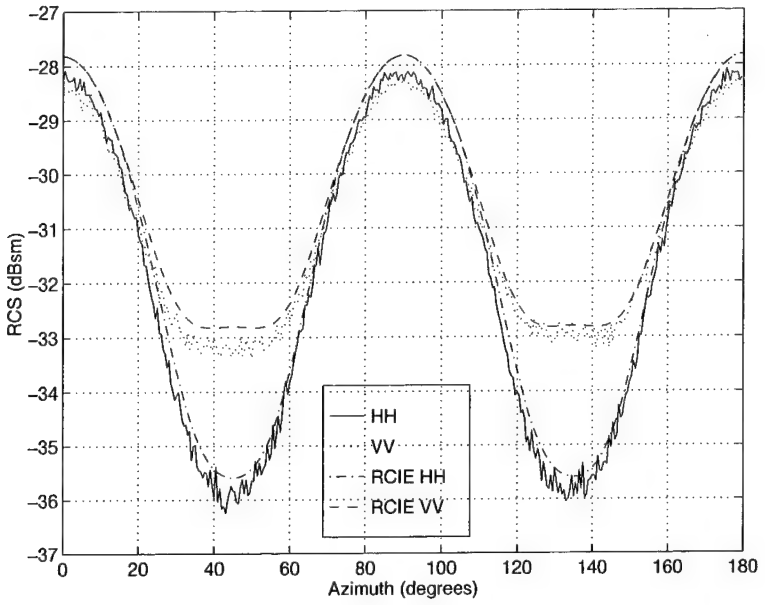

Figure D.3 The monostatic RCS of the small polyethylene cube using 3D-RCIE and measured data obtained at 6 GHz. The mesh size is $16.7/\lambda$ and BLGMRP was used to solve the matrix.

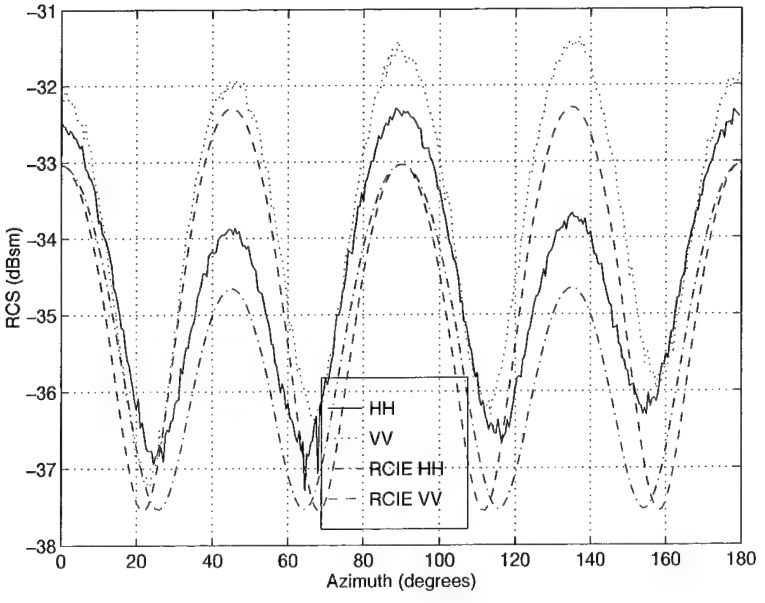

Figure D.4 The monostatic RCS of the small polyethylene cube using 3D-RCIE and measured data obtained at 7 GHz. The mesh size is $14.3/\lambda$ and BLGMRP was used to solve the matrix.

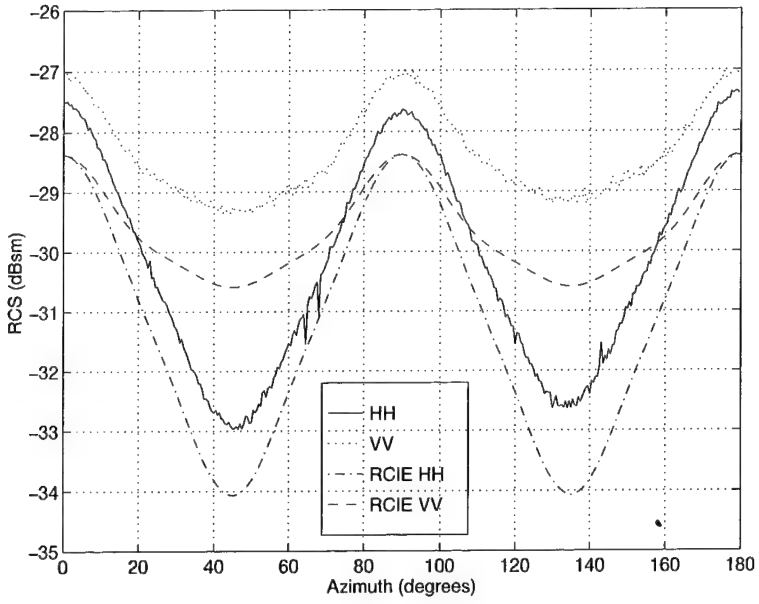

Figure D.5 The monostatic RCS of the small polyethylene cube using 3D-RCIE and measured data obtained at 8 GHz. The mesh size is $18.75/\lambda$ and BLGMRP was used to solve the matrix.

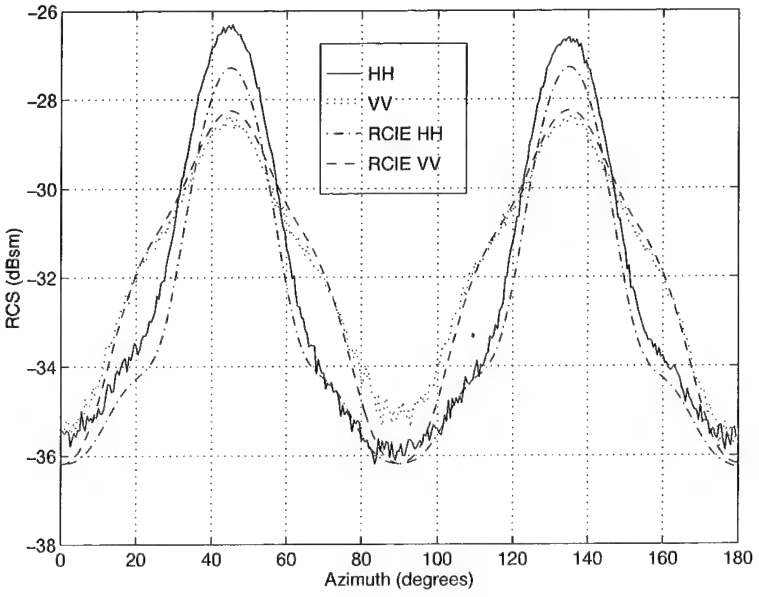

Figure D.6 The monostatic RCS of the small polyethylene cube using 3D-RCIE and measured data obtained at 10 GHz. The mesh size is $15/\lambda$ and BLGMRP was used to solve the matrix.

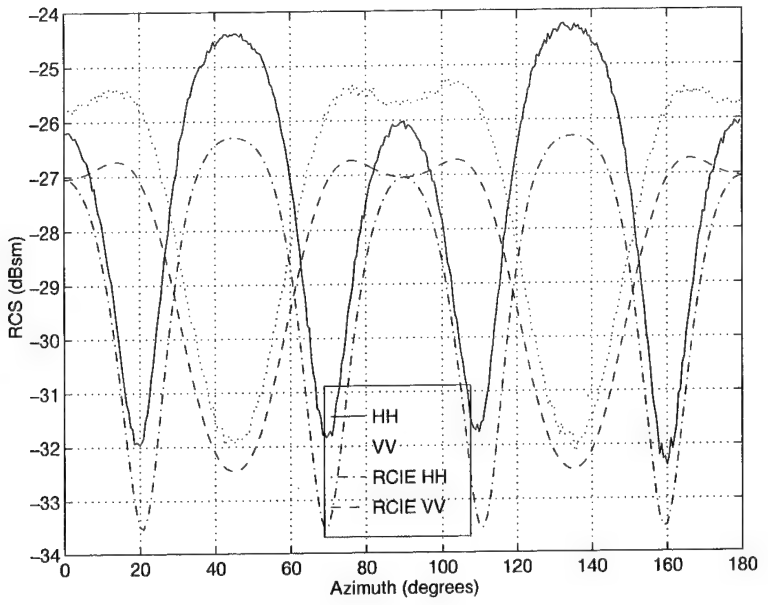

Figure D.7 The monostatic RCS of the small polyethylene cube using 3D-RCIE and measured data obtained at 12 GHz. The mesh size is $12.5/\lambda$ and BLGMRP was used to solve the matrix.

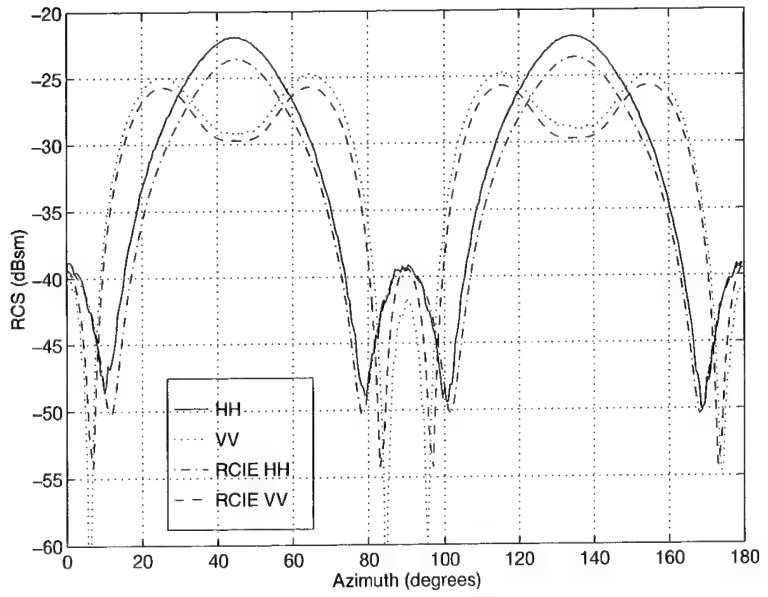

Figure D.8 The monostatic RCS of the small polyethylene cube using 3D-RCIE and measured data obtained at 13 GHz. The mesh size is $11.5/\lambda$ and BLGMRP was used to solve the matrix.

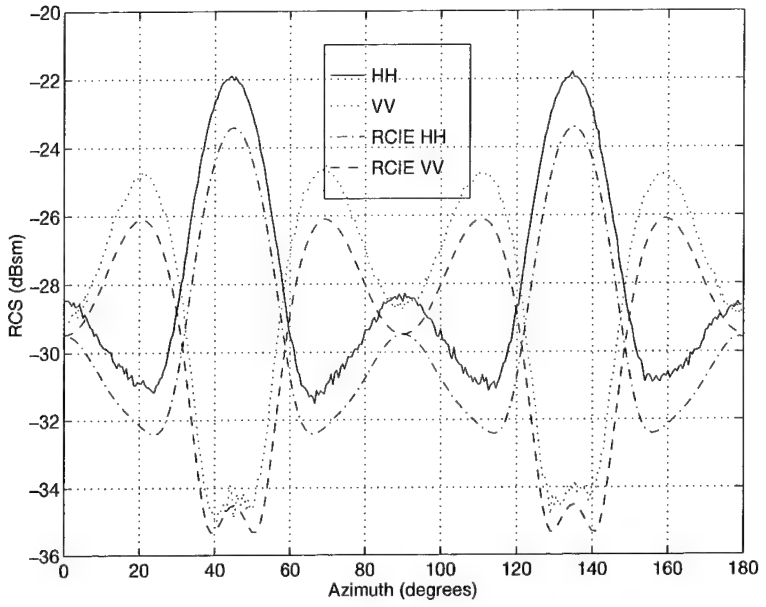

Figure D.9 The monostatic RCS of the small polyethylene cube using 3D-RCIE and measured data obtained at 14 GHz. The mesh size is $14.3/\lambda$ and BLGMRP was used to solve the matrix.

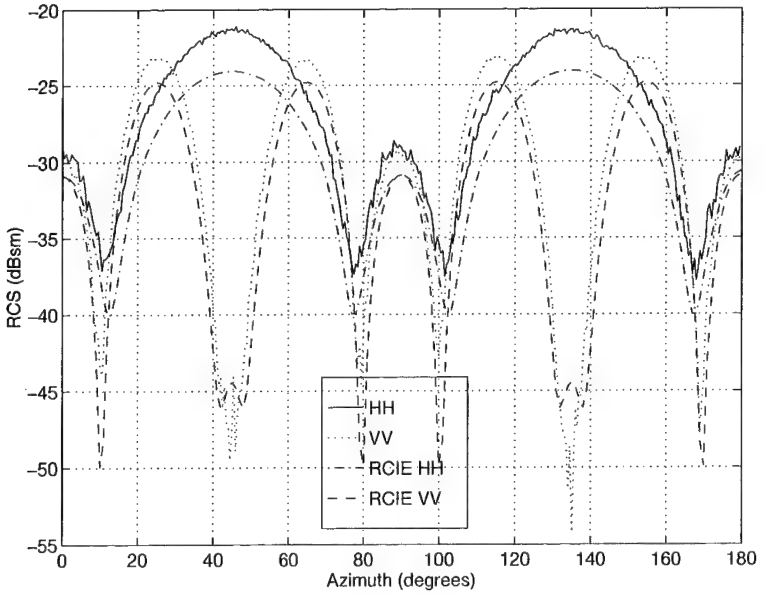

Figure D.10 The monostatic RCS of the small polyethylene cube using 3D-RCIE and measured data obtained at 16 GHz. The mesh size is $12.5/\lambda$ and BLGMRP was used to solve the matrix.

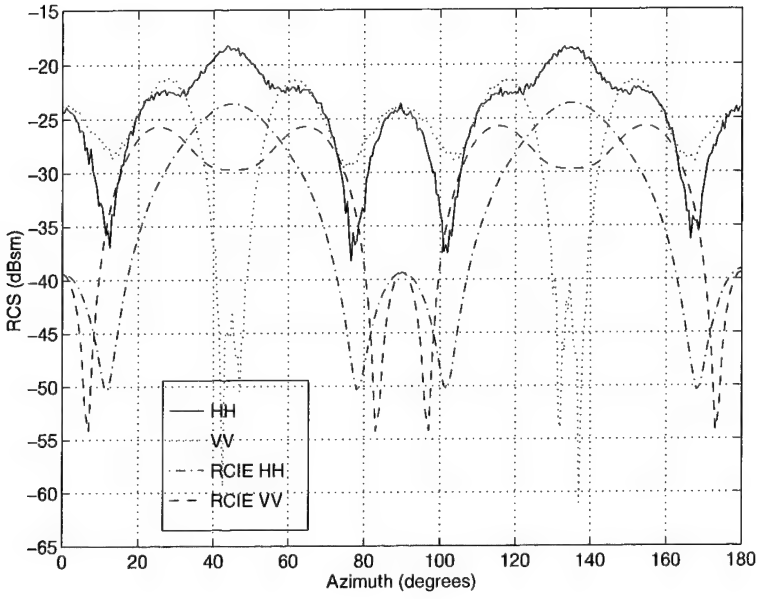

Figure D.11 The monostatic RCS of the small polyethylene cube using 3D-RCIE and measured data obtained at 18 GHz. The mesh size is $11.1/\lambda$ and BLGMRP was used to solve the matrix.

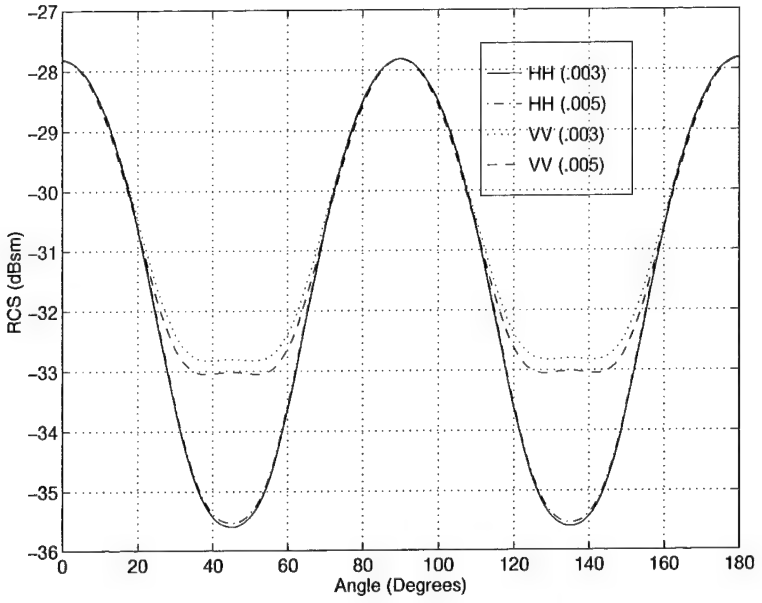

Figure D.12 The monostatic RCS of the small polyethylene cube using 3D-RCIE and varied mesh sizes obtained at 6 GHz. The mesh sizes are $16.7/\lambda$ (.003) and $10/\lambda$ (.005). BLGMRP was used to solve the matrix.

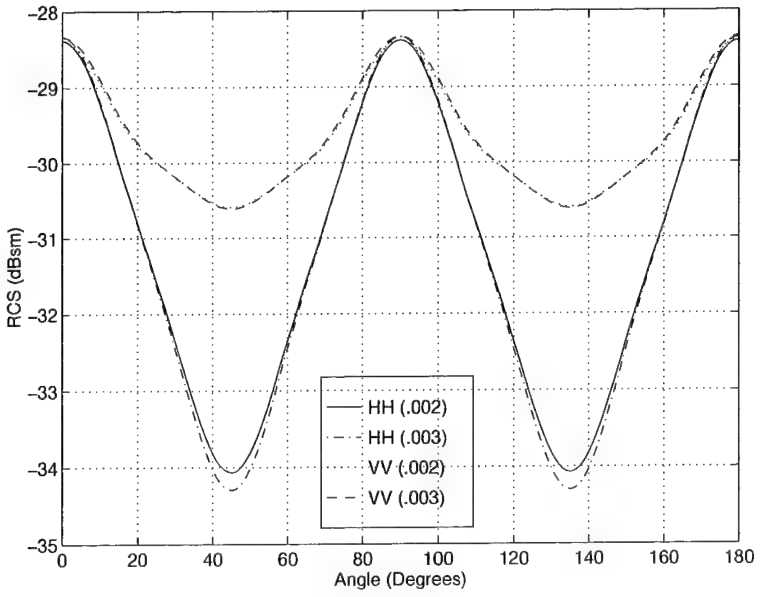

Figure D.13 The monostatic RCS of the small polyethylene cube using 3D-RCIE and varied mesh sizes obtained at 8 GHz. The mesh sizes are $18.75/\lambda$ (.002) and $12.5/\lambda$ (.003). BLGMRP was used to solve the matrix.

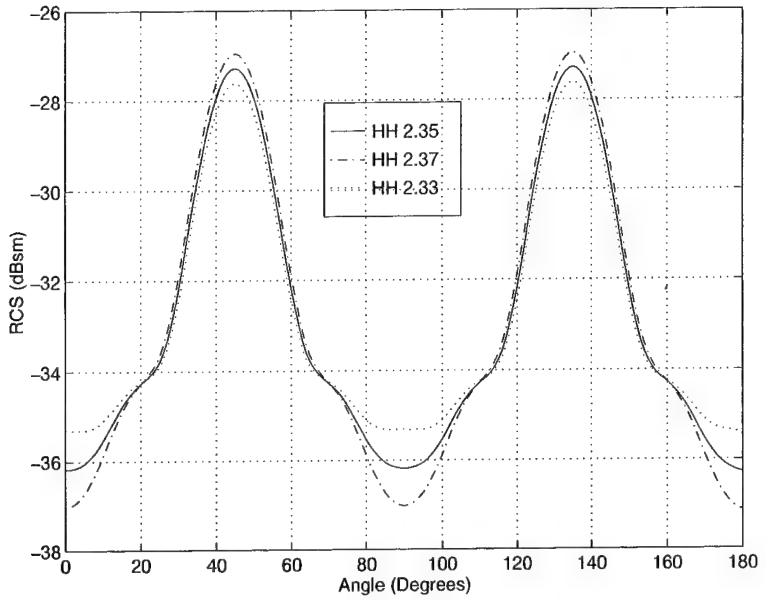

Figure D.14 The HH monostatic RCS of the small polyethylene cube using 3D-RCIE and varied dielectric constants obtained at 10 GHz. The dielectric constants are 2.33, 2.35, and 2.37. BLGMRP was used to solve the matrix.

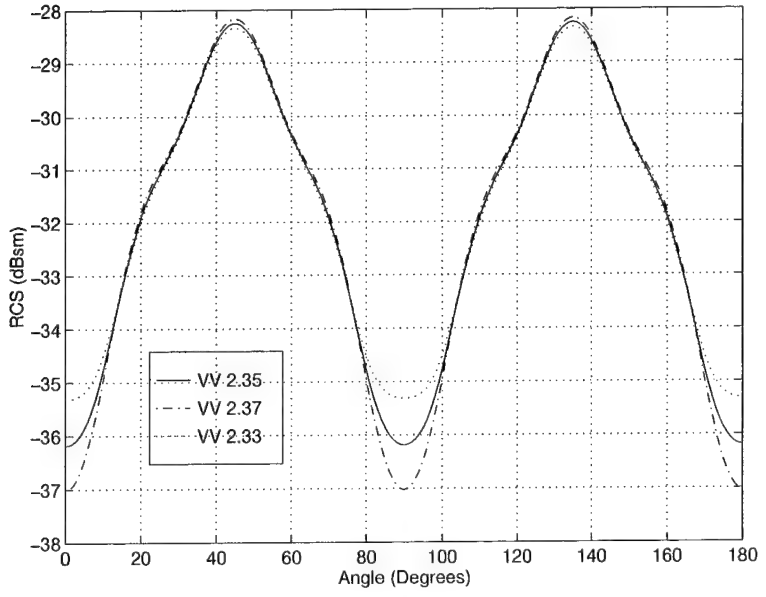

Figure D.15 The VV monostatic RCS of the small polyethylene cube using 3D-RCIE and varied dielectric constants obtained at 10 GHz. The dielectric constants are 2.33, 2.35, and 2.37. BLGMRP was used to solve the matrix.

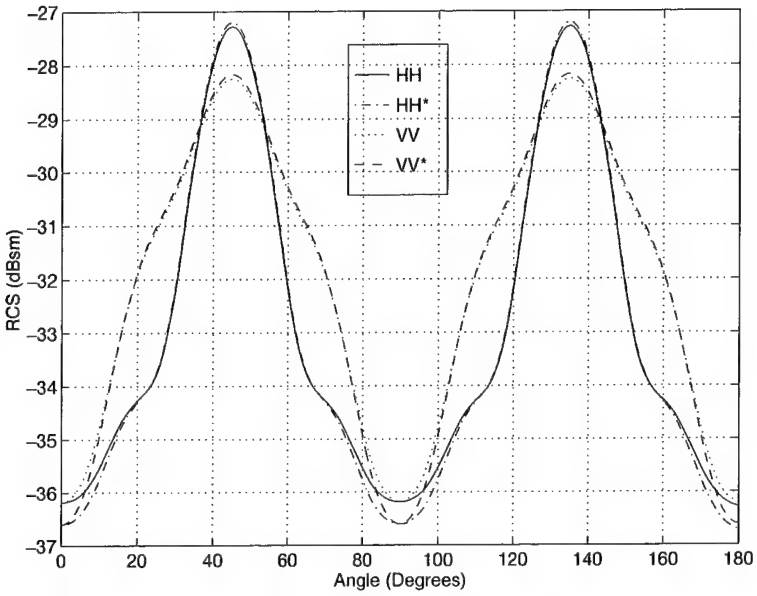

Figure D.16 The monostatic RCS of the small polyethylene cube using 3D-RCIE with varied dimensions obtained at 10 GHz. The length of each side was increased by 0.002 inches. BLGMRP was used to solve the matrix.

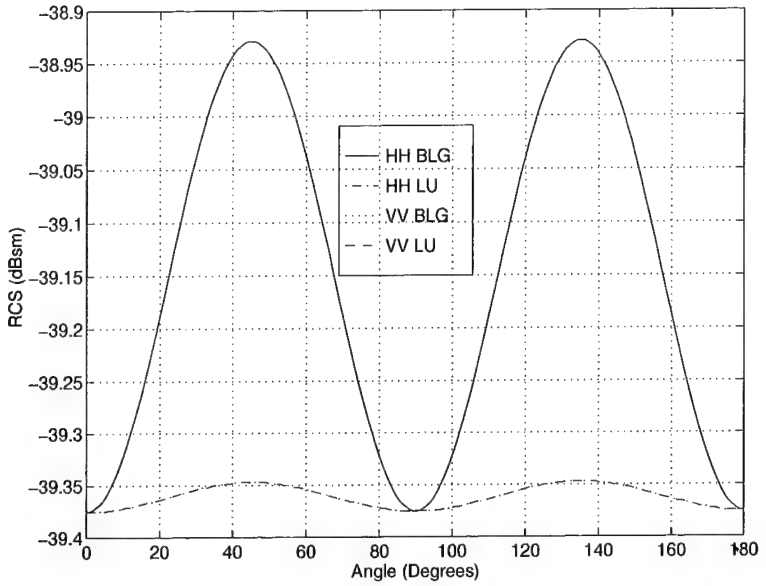

Figure D.17 The monostatic RCS of the small polyethylene cube using 3D-RCIE with BLGMRP and LUFACTOR obtained at 2 GHz. The mesh size is $50/\lambda$.

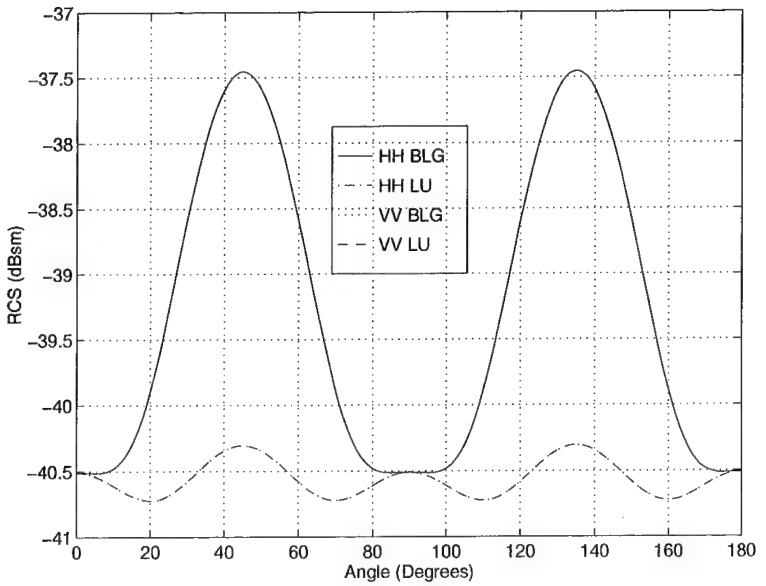

Figure D.18 The monostatic RCS of the small polyethylene cube using 3D-RCIE with BLGMRP and LUFACTOR obtained at 4 GHz. The mesh size is $25/\lambda$.

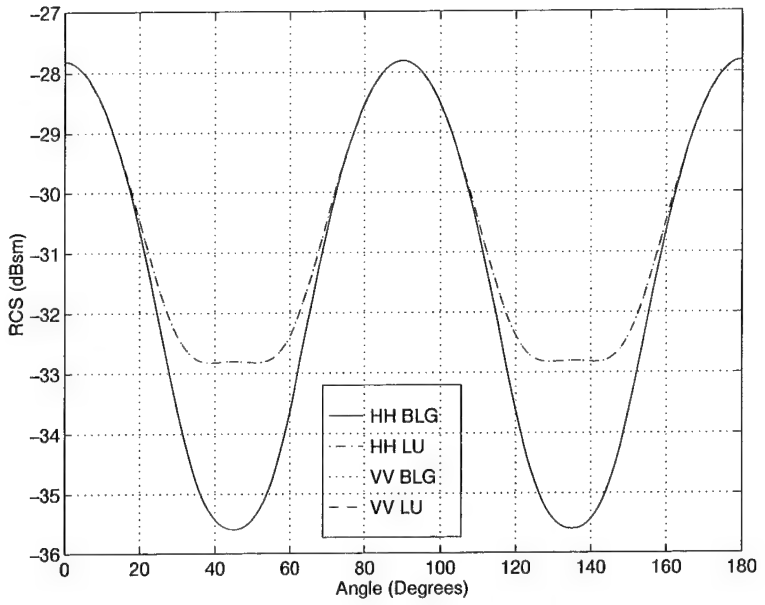

Figure D.19 The monostatic RCS of the small polyethylene cube using 3D-RCIE with BLGMRP and LUFACTOR obtained at 6 GHz. The mesh size is $16.7/\lambda$.

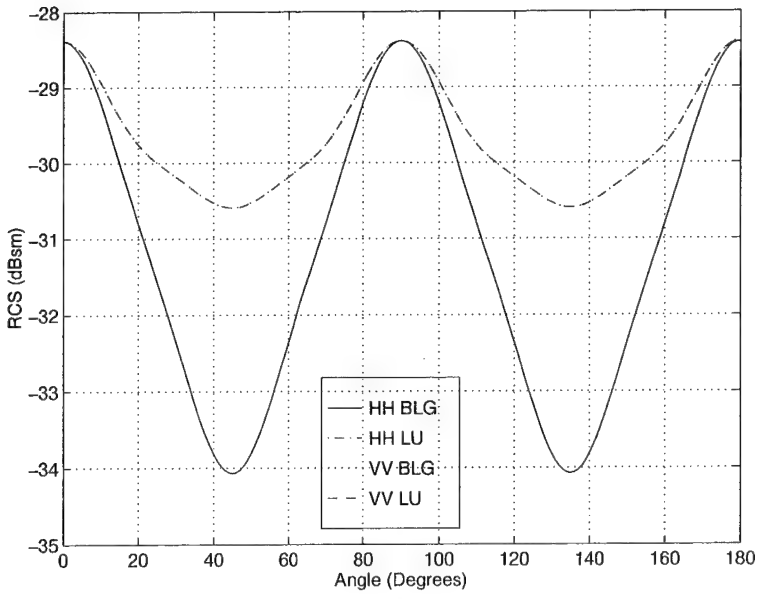

Figure D.20 The monostatic RCS of the small polyethylene cube using 3D-RCIE with BLGMRP and LUFACTOR obtained at 8 GHz. The mesh size is $18.75/\lambda$.

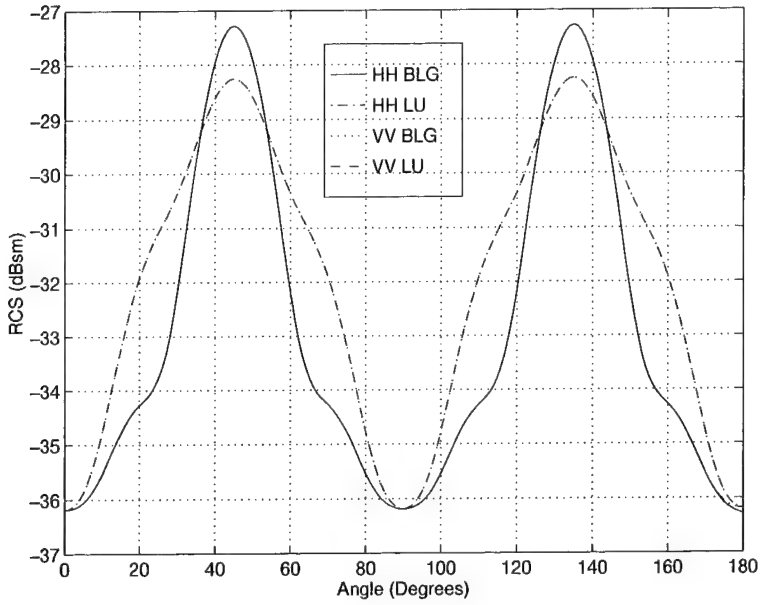

Figure D.21 The monostatic RCS of the small polyethylene cube using 3D-RCIE with BLGMRP and LUFACTOR obtained at 10 GHz. The mesh size is $15/\lambda$.

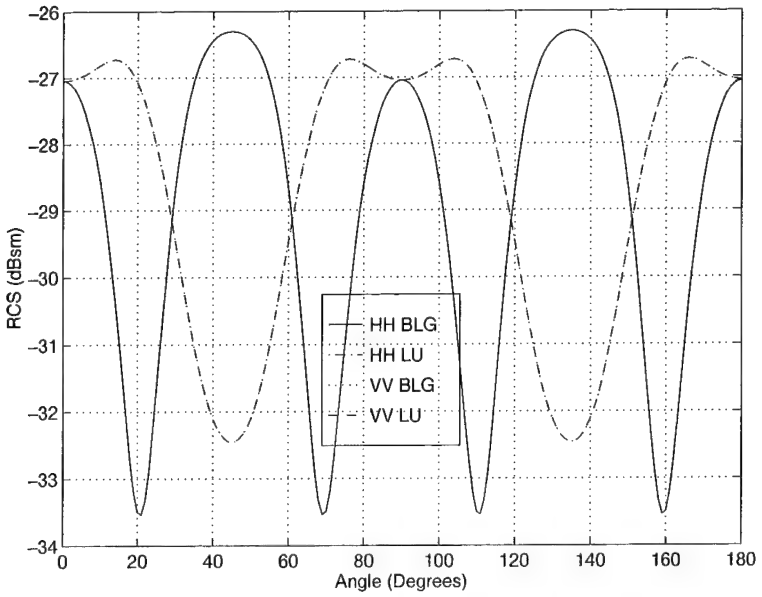

Figure D.22 The monostatic RCS of the small polyethylene cube using 3D-RCIE with BLGMRP and LUFACTOR obtained at 12 GHz. The mesh size is $12.5/\lambda$.

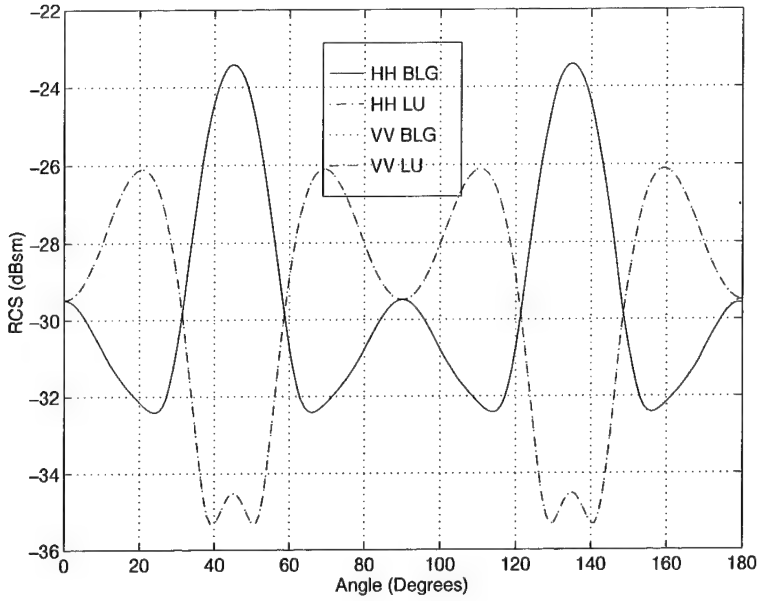

Figure D.23 The monostatic RCS of the small polyethylene cube using 3D-RCIE with BLGMRP and LUFACTOR obtained at 14 GHz. The mesh size is $14.3/\lambda$.

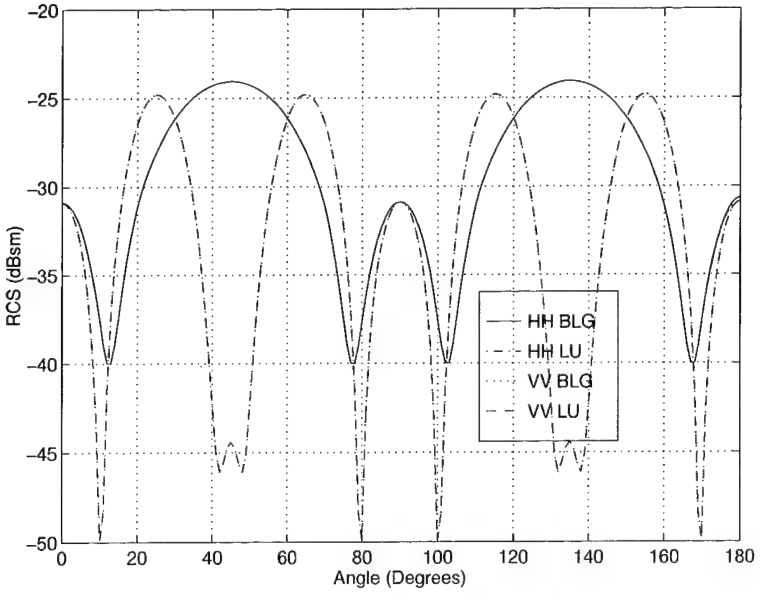

Figure D.24 The monostatic RCS of the small polyethylene cube using 3D-RCIE with BLGMRP and LUFACTOR obtained at 16 GHz. The mesh size is $12.5/\lambda$.

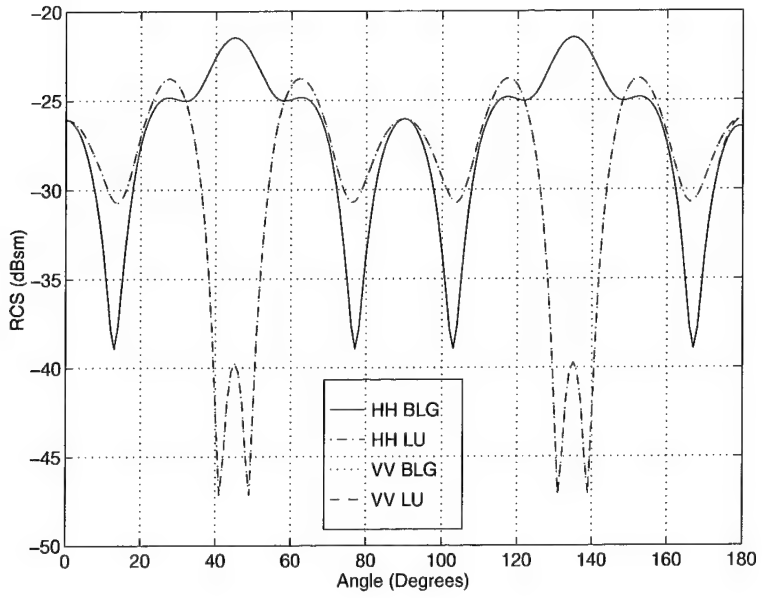

Figure D.25 The monostatic RCS of the small polyethylene cube using 3D-RCIE with BLGMRP and LUFACTOR obtained at 18 GHz. The mesh size is $11.1/\lambda$.

D.2 Small Cube with r-card - Polyethylene

Description	Figure
RCS Comparison of the Small Polyethylene Cube w/r-card at 2 GHz	D.26
RCS Comparison of the Small Polyethylene Cube w/r-card at 4 GHz	D.27
RCS Comparison of the Small Polyethylene Cube w/r-card at 6 GHz	D.28
RCS Comparison of the Small Polyethylene Cube w/r-card at 7 GHz	D.29
RCS Comparison of the Small Polyethylene Cube w/r-card at 8 GHz	D.30
RCS Comparison of the Small Polyethylene Cube w/r-card at 10 GHz	D.31
RCS Comparison of the Small Polyethylene Cube w/r-card at 12 GHz	D.32
RCS Comparison of the Small Polyethylene Cube w/r-card at 13 GHz	D.33
RCS Comparison of the Small Polyethylene Cube w/r-card at 14 GHz	D.34
RCS Comparison of the Small Polyethylene Cube w/r-card at 16 GHz	D.35
RCS Comparison of the Small Polyethylene Cube w/r-card at 18 GHz	D.36
Small Polyethylene Cube w/r-card RCS with varied mesh sizes at 6 GHz	D.37
Small Polyethylene Cube w/r-card RCS with varied mesh sizes at 8 GHz	D.38
Small Polyethylene Cube w/r-card HH RCS with varied dielectric constants at 10 GHz	D.39
Small Polyethylene Cube w/r-card VV RCS with varied dielectric constants at 10 GHz	D.40
Small Polyethylene Cube w/r-card RCS with varied dimensions at 10 GHz	D.41
3D-RCIE (BLG vs. LU) RCS of the Small Polyethylene Cube w/r-card at 2 GHz	D.42
3D-RCIE (BLG vs. LU) RCS of the Small Polyethylene Cube w/r-card at 4 GHz	D.43
3D-RCIE (BLG vs. LU) RCS of the Small Polyethylene Cube w/r-card at 6 GHz	D.44
3D-RCIE (BLG vs. LU) RCS of the Small Polyethylene Cube w/r-card at 8 GHz	D.45
3D-RCIE (BLG vs. LU) RCS of the Small Polyethylene Cube w/r-card at 10 GHz	D.46
3D-RCIE (BLG vs. LU) RCS of the Small Polyethylene Cube w/r-card at 12 GHz	D.47
3D-RCIE (BLG vs. LU) RCS of the Small Polyethylene Cube w/r-card at 14 GHz	D.48
3D-RCIE (BLG vs. LU) RCS of the Small Polyethylene Cube w/r-card at 16 GHz	D.49
3D-RCIE (BLG vs. LU) RCS of the Small Polyethylene Cube w/r-card at 18 GHz	D.50

Table D.2 List of plots for the RCS of the small polyethylene cube with r-card.

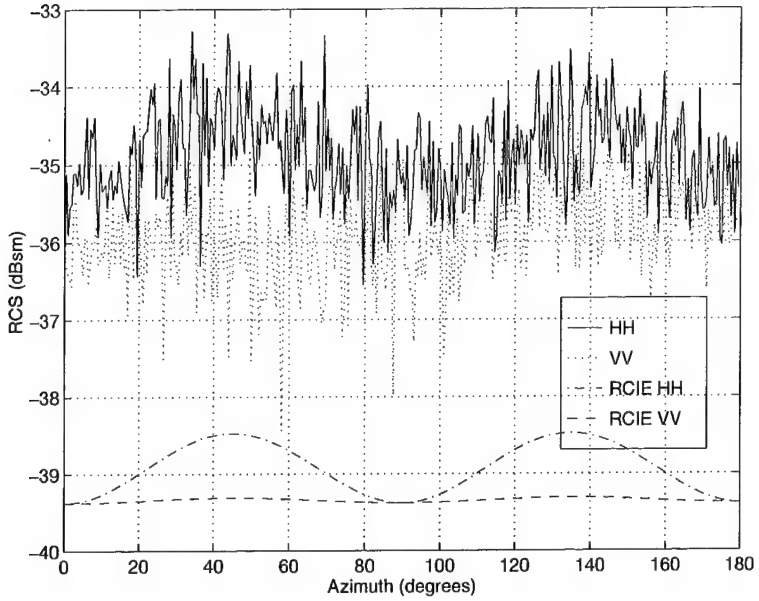

Figure D.26 The monostatic RCS of the small polyethylene cube with r-card using 3D-RCIE and measured data obtained at 2 GHz. The mesh size is $50/\lambda$ and BLGMRP was used to solve the matrix.

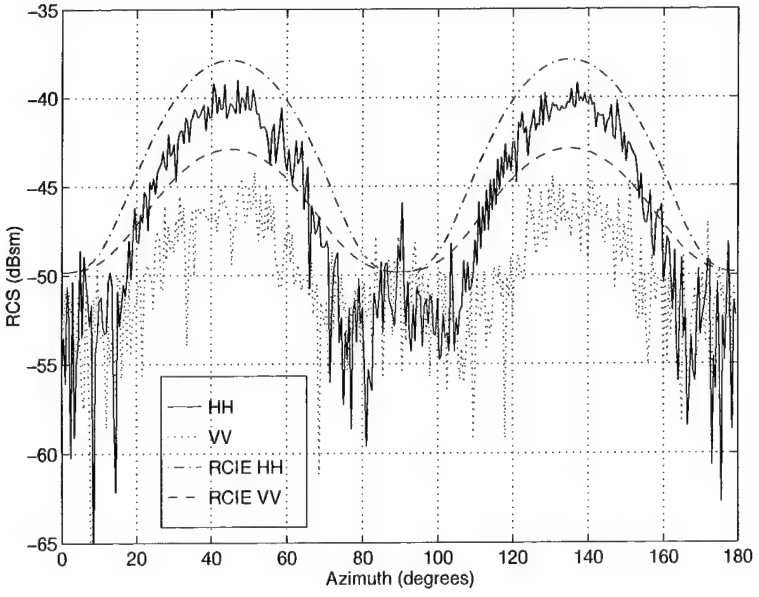

Figure D.27 The monostatic RCS of the small polyethylene cube with r-card using 3D-RCIE and measured data obtained at 4 GHz. The mesh size is $25/\lambda$ and BLGMRP was used to solve the matrix.

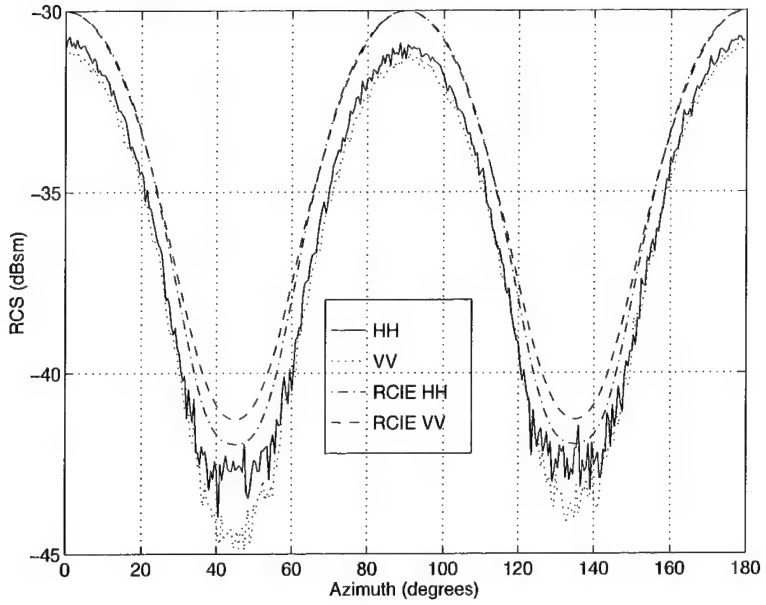

Figure D.28 The monostatic RCS of the small polyethylene cube with r-card using 3D-RCIE and measured data obtained at 6 GHz. The mesh size is $16.7/\lambda$ and BLGMRP was used to solve the matrix.

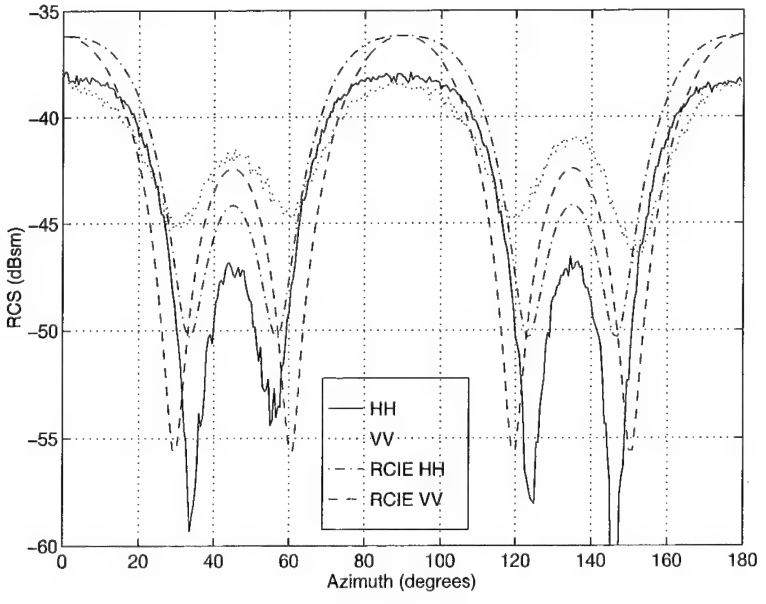

Figure D.29 The monostatic RCS of the small polyethylene cube with r-card using 3D-RCIE and measured data obtained at 7 GHz. The mesh size is $14.3/\lambda$ and BLGMRP was used to solve the matrix.

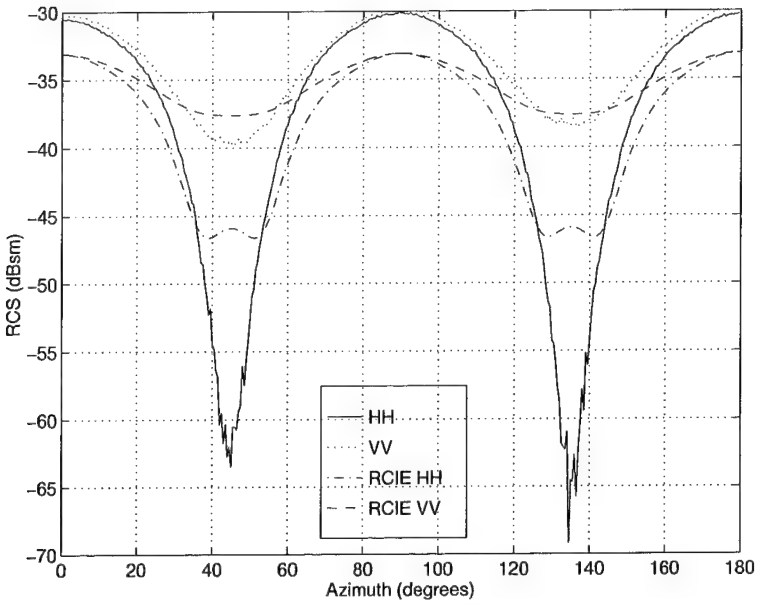

Figure D.30 The monostatic RCS of the small polyethylene cube with r-card using 3D-RCIE and measured data obtained at 8 GHz. The mesh size is $18.75/\lambda$ and BLGMRP was used to solve the matrix.

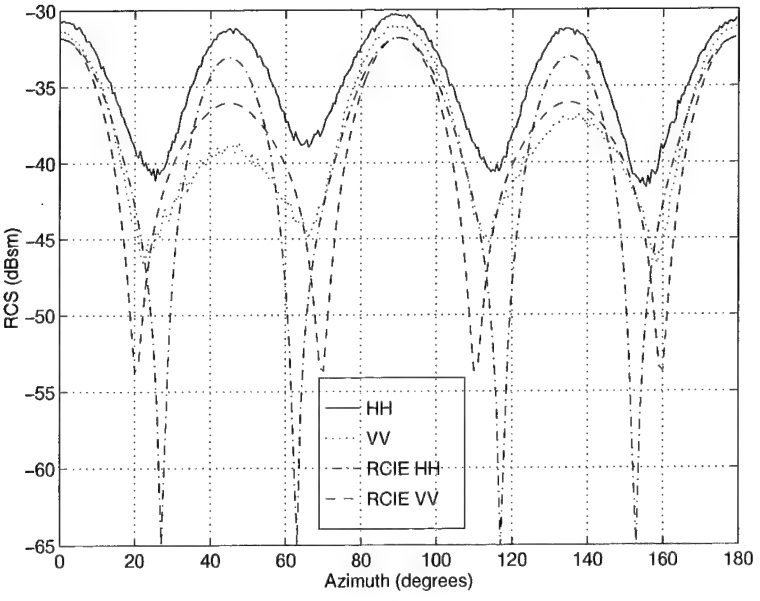

Figure D.31 The monostatic RCS of the small polyethylene cube with r-card using 3D-RCIE and measured data obtained at 10 GHz. The mesh size is $15/\lambda$ and BLGMRP was used to solve the matrix.

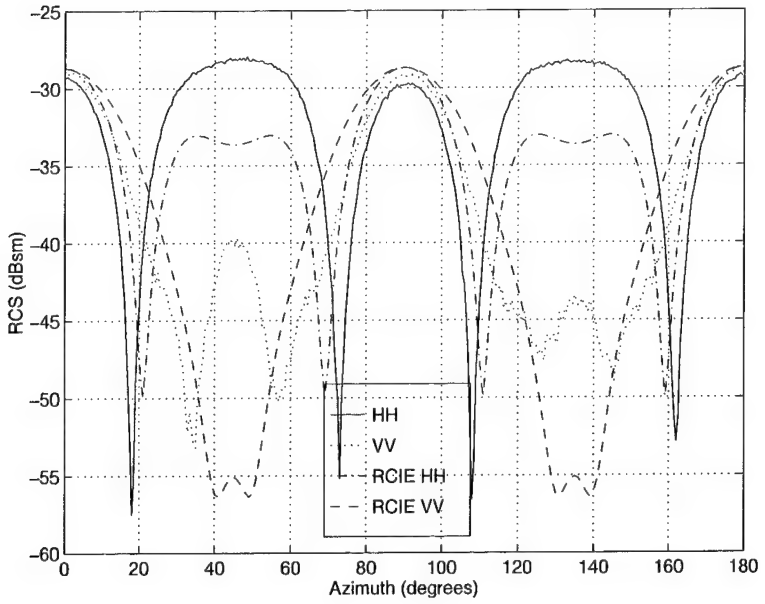

Figure D.32 The monostatic RCS of the small polyethylene cube with r-card using 3D-RCIE and measured data obtained at 12 GHz. The mesh size is $12.5/\lambda$ and BLGMRP was used to solve the matrix.

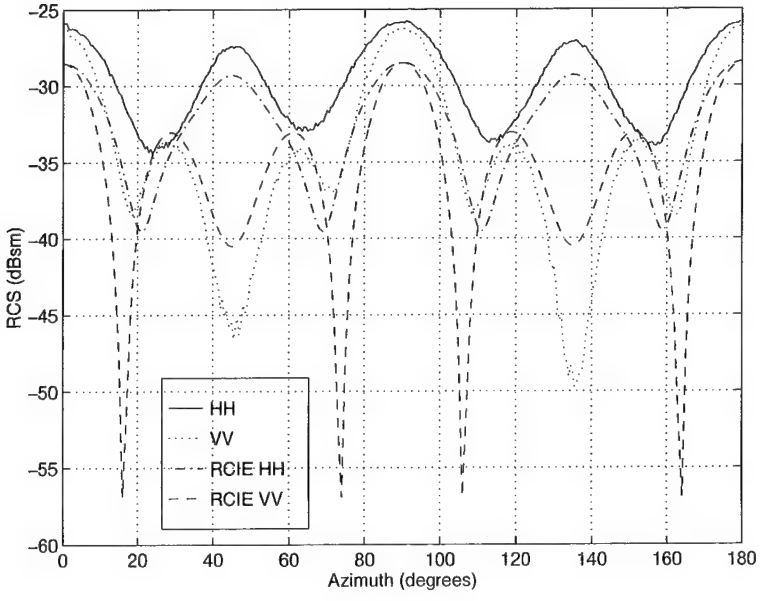

Figure D.33 The monostatic RCS of the small polyethylene cube with r-card using 3D-RCIE and measured data obtained at 13 GHz. The mesh size is $11.5/\lambda$ and BLGMRP was used to solve the matrix.

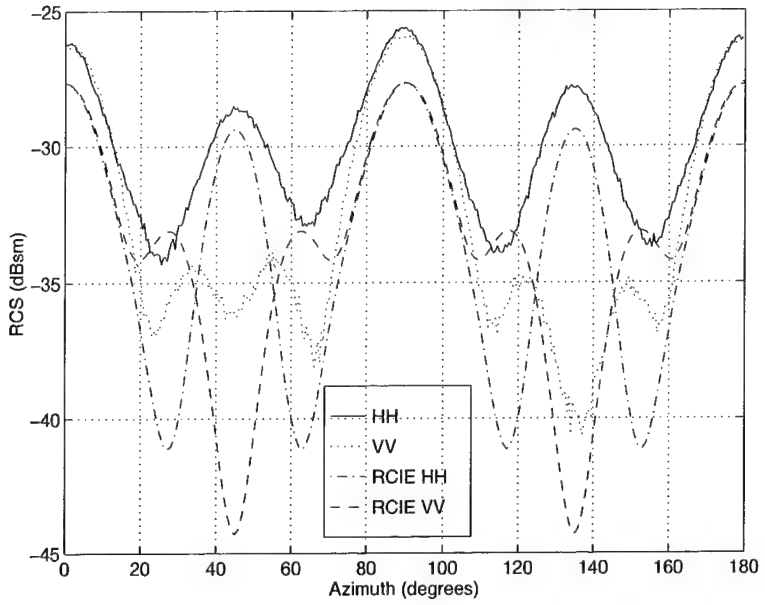

Figure D.34 The monostatic RCS of the small polyethylene cube with r-card using 3D-RCIE and measured data obtained at 14 GHz. The mesh size is $14.3/\lambda$ and BLGMRP was used to solve the matrix.

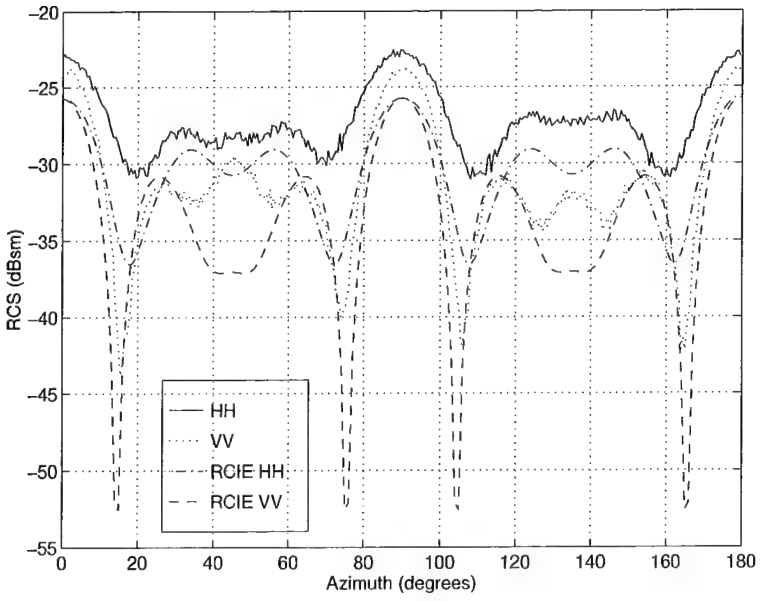

Figure D.35 The monostatic RCS of the small polyethylene cube with r-card using 3D-RCIE and measured data obtained at 16 GHz. The mesh size is $12.5/\lambda$ and BLGMRP was used to solve the matrix.

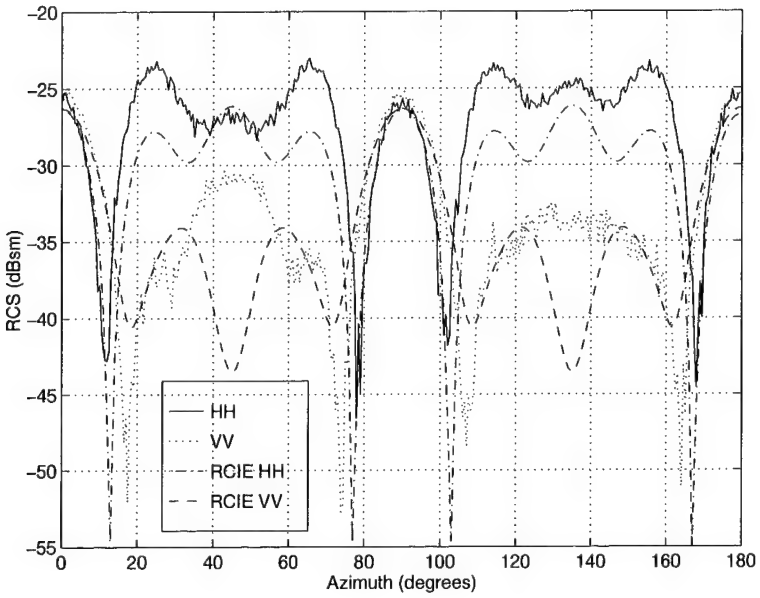

Figure D.36 The monostatic RCS of the small polyethylene cube with r-card using 3D-RCIE and measured data obtained at 18 GHz. The mesh size is $11.1/\lambda$ and BLGMRP was used to solve the matrix.

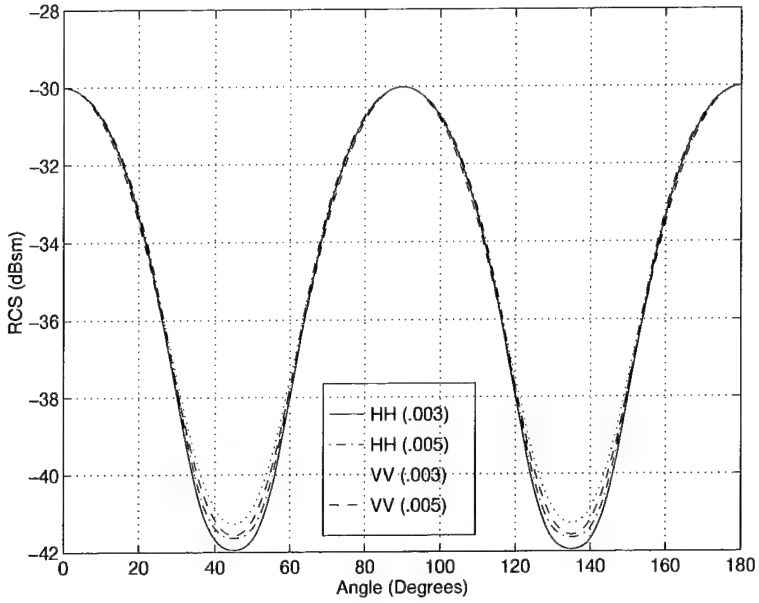

Figure D.37 The monostatic RCS of the small polyethylene cube with r-card using 3D-RCIE and varied mesh sizes obtained at 6 GHz. The mesh sizes are $16.7/\lambda$ (.003) and $10/\lambda$ (.005). BLGMRP was used to solve the matrix.

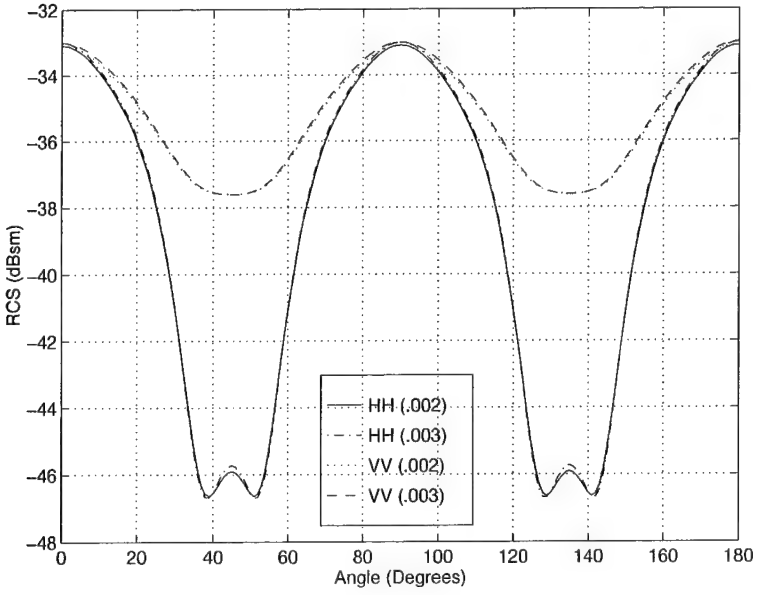

Figure D.38 The monostatic RCS of the small polyethylene cube with r-card using 3D-RCIE and varied mesh sizes obtained at 8 GHz. The mesh sizes are $18.75/\lambda$ (.002) and $12.5/\lambda$ (.003). BLGMRP was used to solve the matrix.

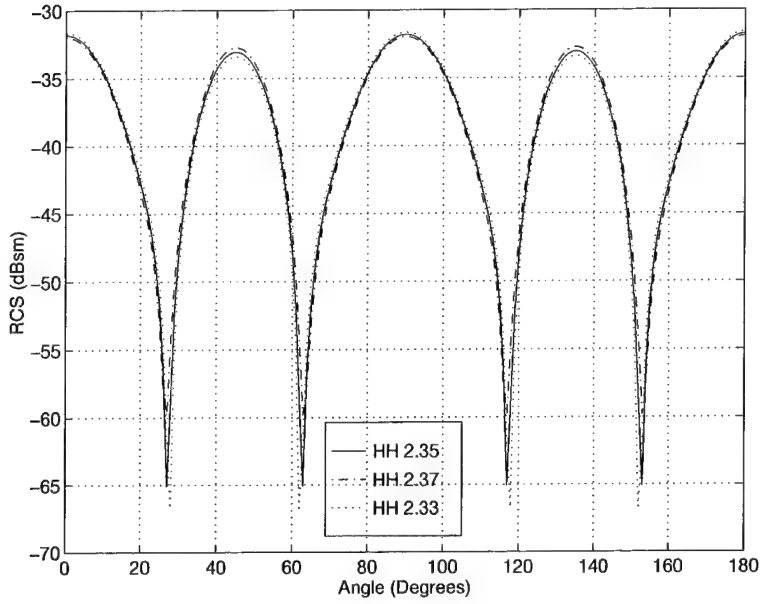

Figure D.39 The HH monostatic RCS of the small polyethylene cube with r-card using 3D-RCIE and varied dielectric constants obtained at 10 GHz. The dielectric constants are 2.33, 2.35, and 2.37. LUFACTOR was used to solve the matrix.

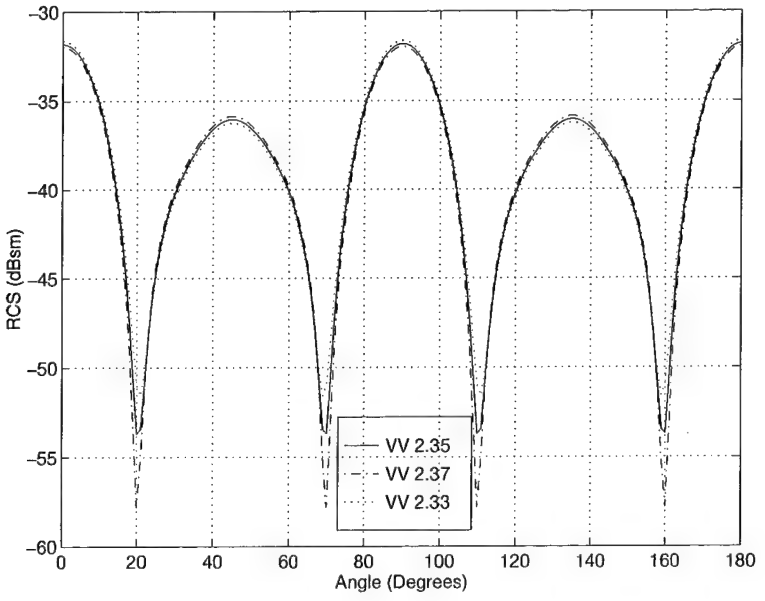

Figure D.40 The VV monostatic RCS of the small polyethylene cube with r-card using 3D-RCIE and varied dielectric constants obtained at 10 GHz. The dielectric constants are 2.33, 2.35, and 2.37. LUFACTOR was used to solve the matrix.

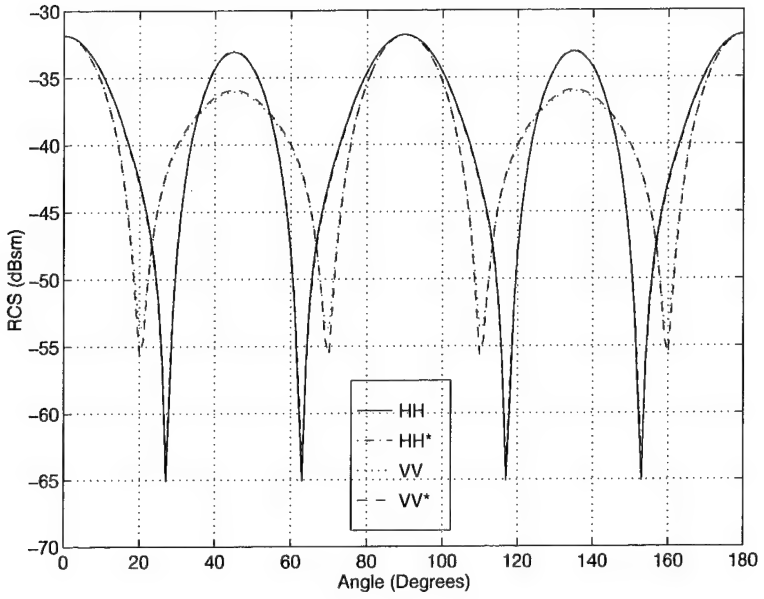

Figure D.41 The monostatic RCS of the small polyethylene cube with r-card using 3D-RCIE with varied dimensions obtained at 10 GHz. The length of each side was increased by 0.002 inches. LUFACTOR was used to solve the matrix.

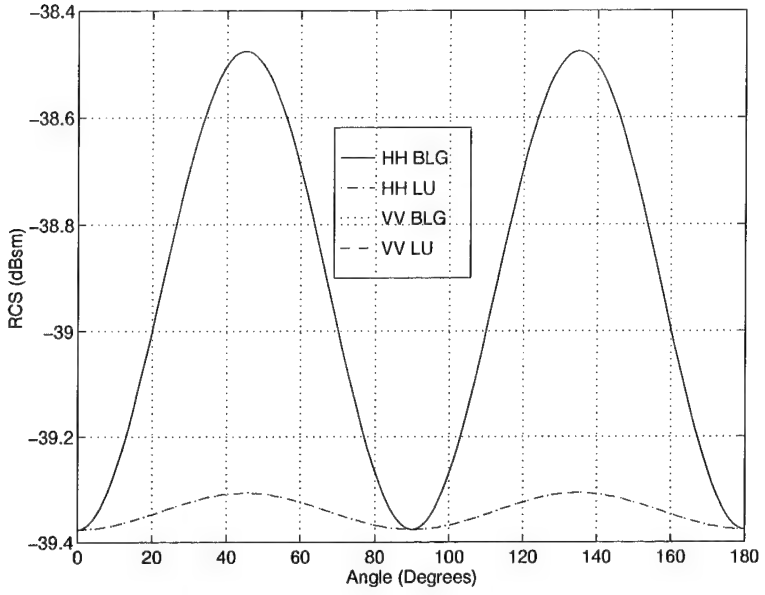

Figure D.42 The monostatic RCS of the small polyethylene cube with r-card using 3D-RCIE with BLGMRP and LUFACTOR obtained at 2 GHz. The mesh size is $50/\lambda$.

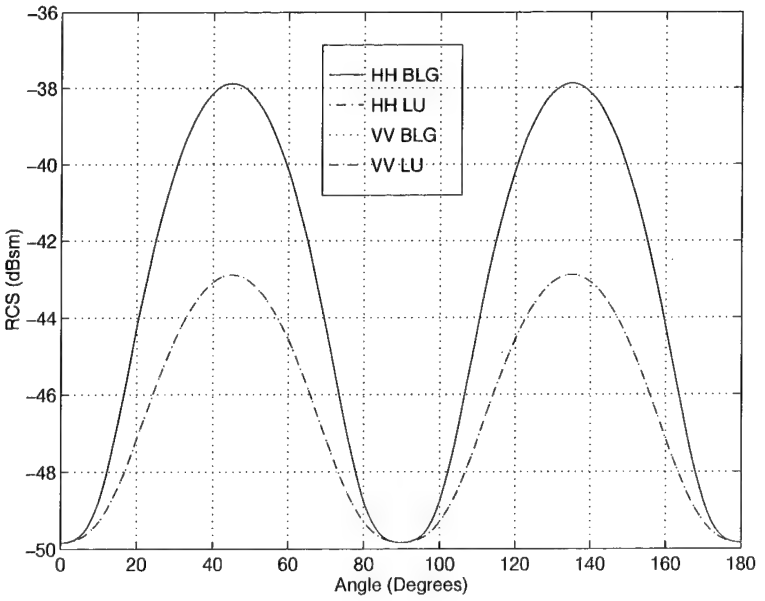

Figure D.43 The monostatic RCS of the small polyethylene cube with r-card using 3D-RCIE with BLGMRP and LUFACTOR obtained at 4 GHz. The mesh size is $25/\lambda$.

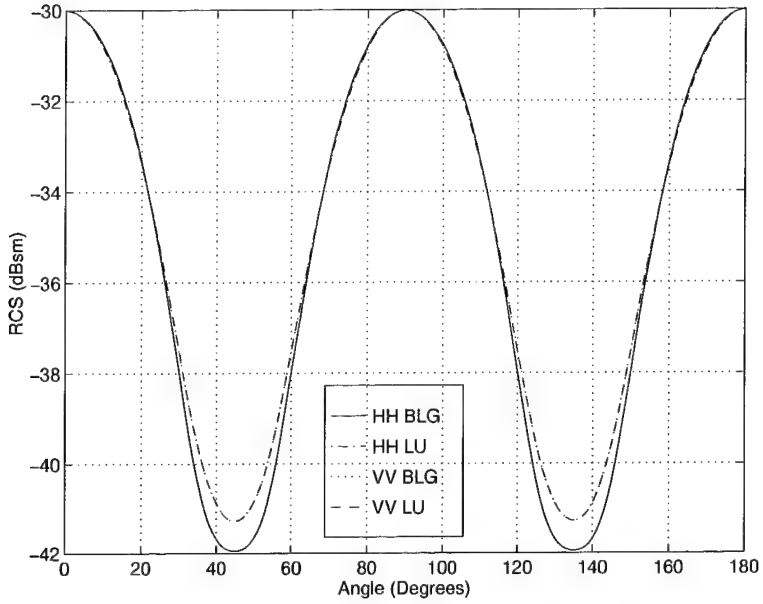

Figure D.44 The monostatic RCS of the small polyethylene cube with r-card using 3D-RCIE with BLGMRP and LUFACTOR obtained at 6 GHz. The mesh size is $16.7/\lambda$.

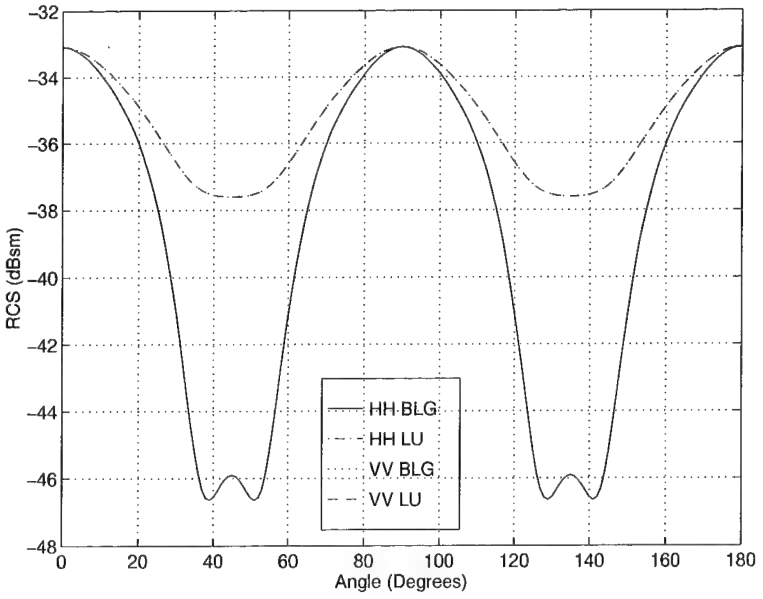

Figure D.45 The monostatic RCS of the small polyethylene cube with r-card using 3D-RCIE with BLGMRP and LUFACTOR obtained at 8 GHz. The mesh size is $18.75/\lambda$.

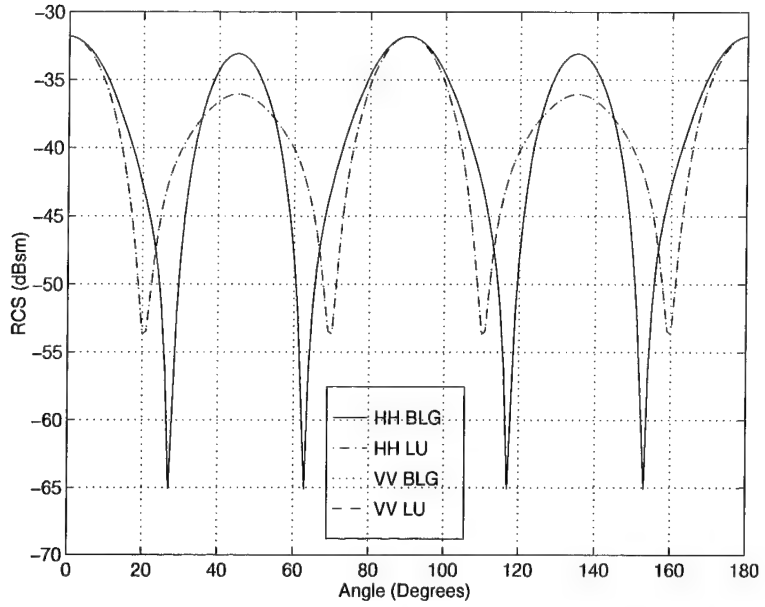

Figure D.46 The monostatic RCS of the small polyethylene cube with r-card using 3D-RCIE with BLGMRP and LUFACTOR obtained at 10 GHz. The mesh size is $15/\lambda$.

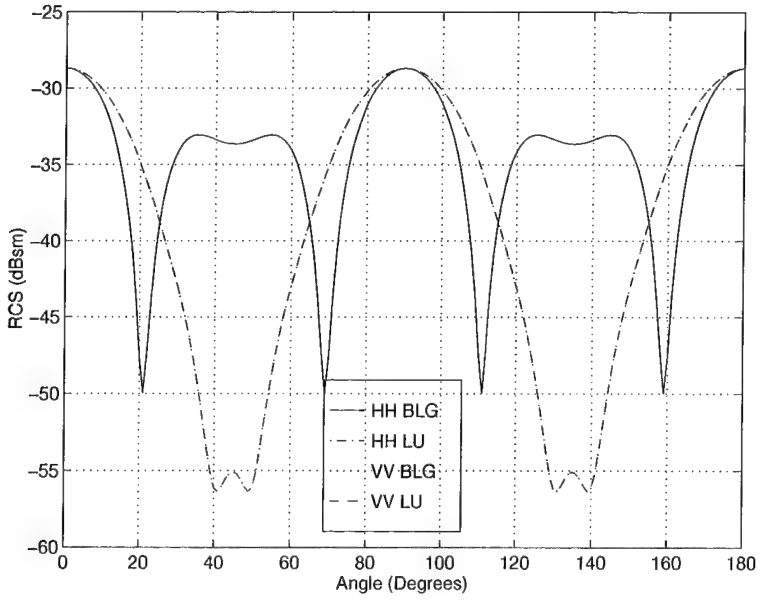

Figure D.47 The monostatic RCS of the small polyethylene cube with r-card using 3D-RCIE with BLGMRP and LUFACTOR obtained at 12 GHz. The mesh size is $12.5/\lambda$.

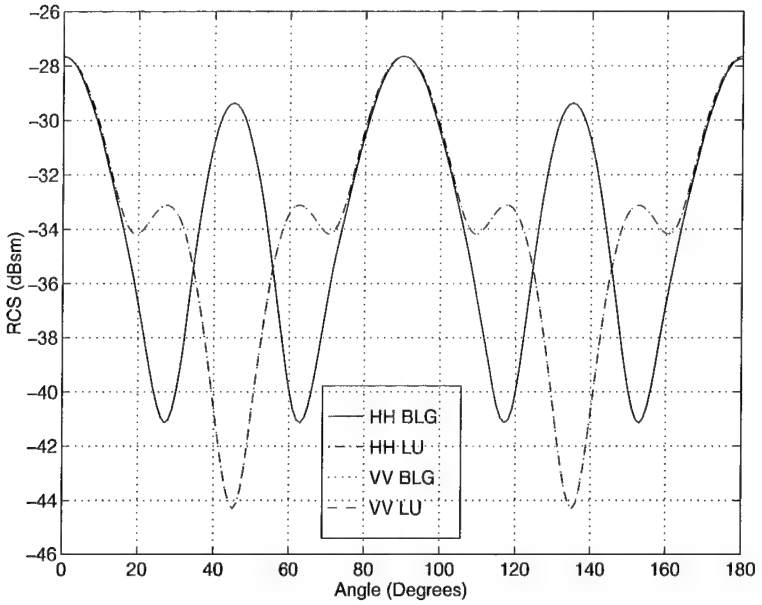

Figure D.48 The monostatic RCS of the small polyethylene cube with r-card using 3D-RCIE with BLGMRP and LUFACTOR obtained at 14 GHz. The mesh size is $14.3/\lambda$.

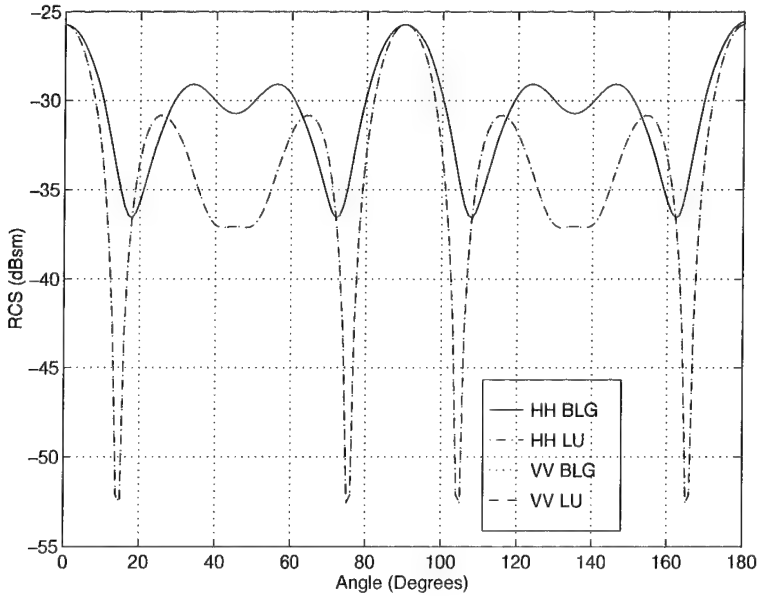

Figure D.49 The monostatic RCS of the small polyethylene cube with r-card using 3D-RCIE with BLGMRP and LUFACTOR obtained at 16 GHz. The mesh size is $12.5/\lambda$.

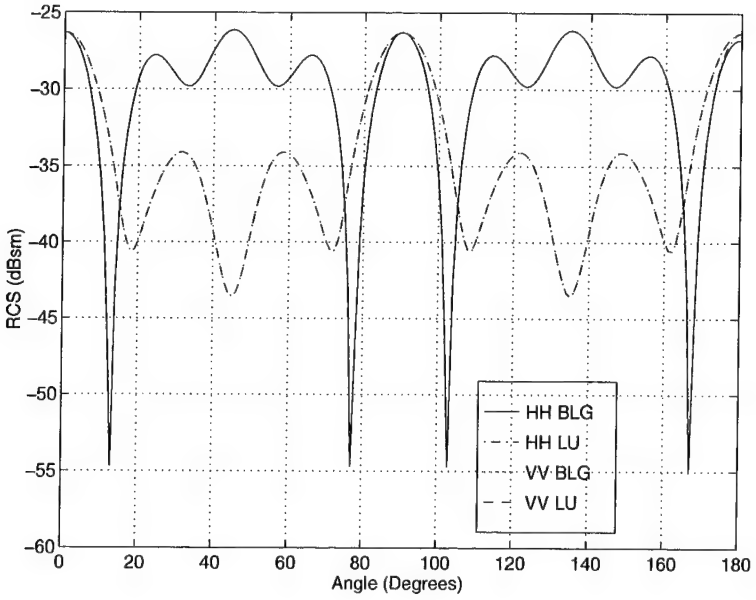

Figure D.50 The monostatic RCS of the small polyethylene cube with r-card using 3D-RCIE with BLGMRP and LUFACTOR obtained at 18 GHz. The mesh size is $11.1/\lambda$.

D.3 Small Cube - Polyurethane

Description	Figure
RCS Comparison of the Small Polyurethane Cube at 2 GHz	D.51
RCS Comparison of the Small Polyurethane Cube at 4 GHz	D.52
RCS Comparison of the Small Polyurethane Cube at 6 GHz	D.53
RCS Comparison of the Small Polyurethane Cube at 8 GHz	D.54
RCS Comparison of the Small Polyurethane Cube at 10 GHz	D.55
RCS Comparison of the Small Polyurethane Cube at 12 GHz	D.56
RCS Comparison of the Small Polyurethane Cube at 14 GHz	D.57
RCS Comparison of the Small Polyurethane Cube at 16 GHz	D.58
RCS Comparison of the Small Polyurethane Cube at 18 GHz	D.59
Small Polyurethane Cube RCS with varied dimensions at 10 GHz	D.60

Table D.3 List of plots for the RCS of the small polyurethane cube.

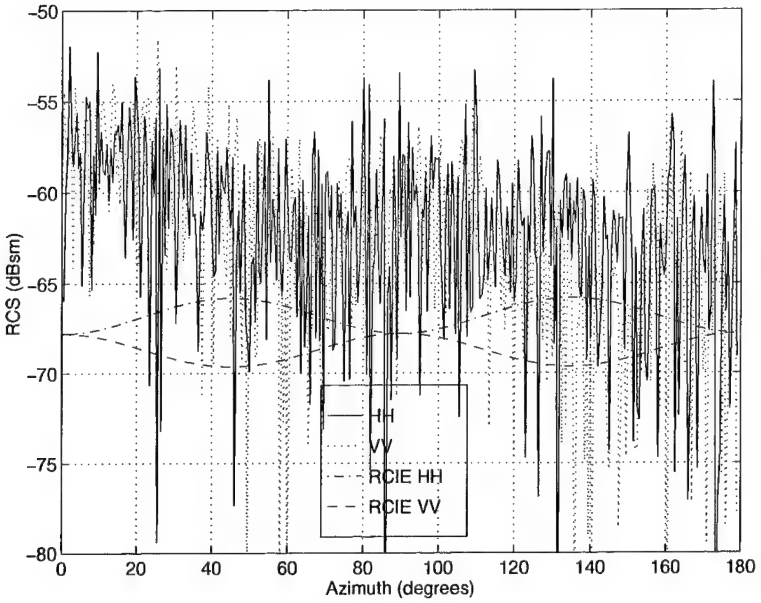

Figure D.51 The monostatic RCS of the small polyurethane cube using 3D-RCIE and measured data obtained at 2 GHz. The mesh size is $50/\lambda$ and BLGMRP was used to solve the matrix.

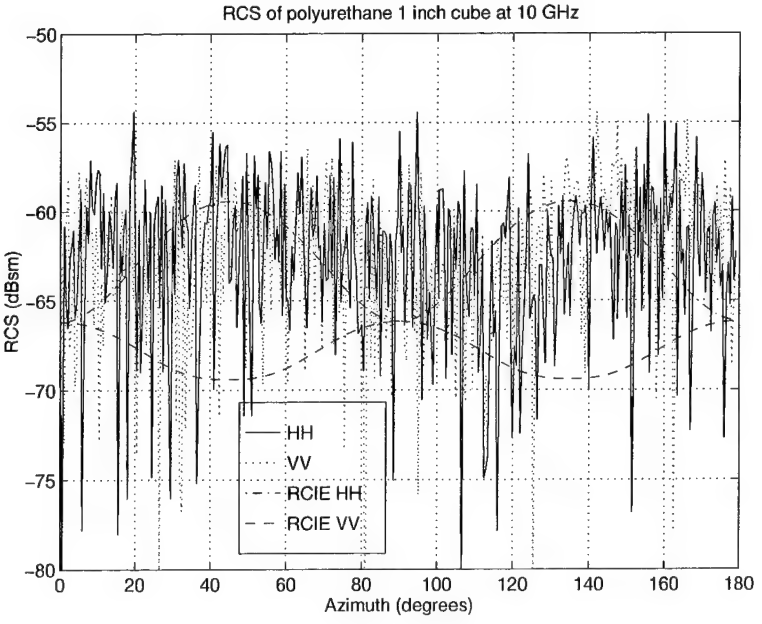

Figure D.52 The monostatic RCS of the small polyurethane cube using 3D-RCIE and measured data obtained at 4 GHz. The mesh size is $25/\lambda$ and BLGMRP was used to solve the matrix.

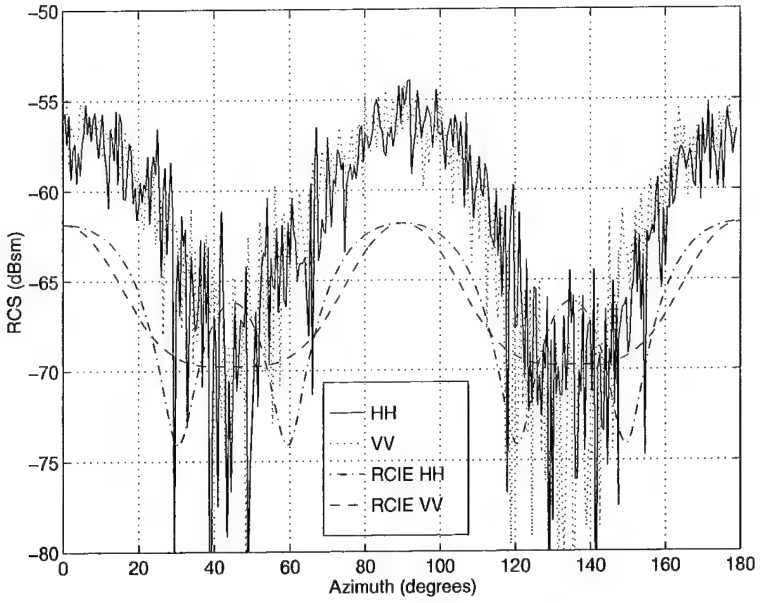

Figure D.53 The monostatic RCS of the small polyurethane cube using 3D-RCIE and measured data obtained at 6 GHz. The mesh size is $16.7/\lambda$ and BLGMRP was used to solve the matrix.

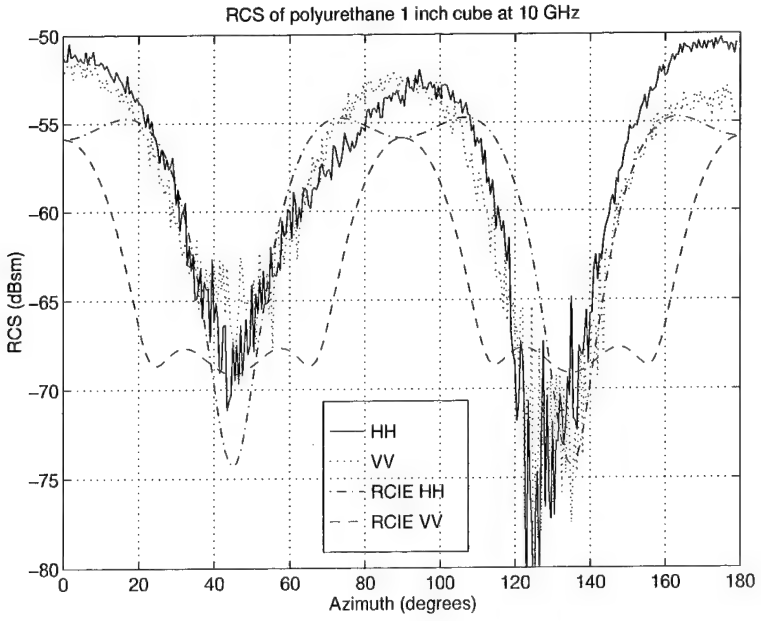

Figure D.54 The monostatic RCS of the small polyurethane cube using 3D-RCIE and measured data obtained at 8 GHz. The mesh size is $12.5/\lambda$ and BLGMRP was used to solve the matrix.

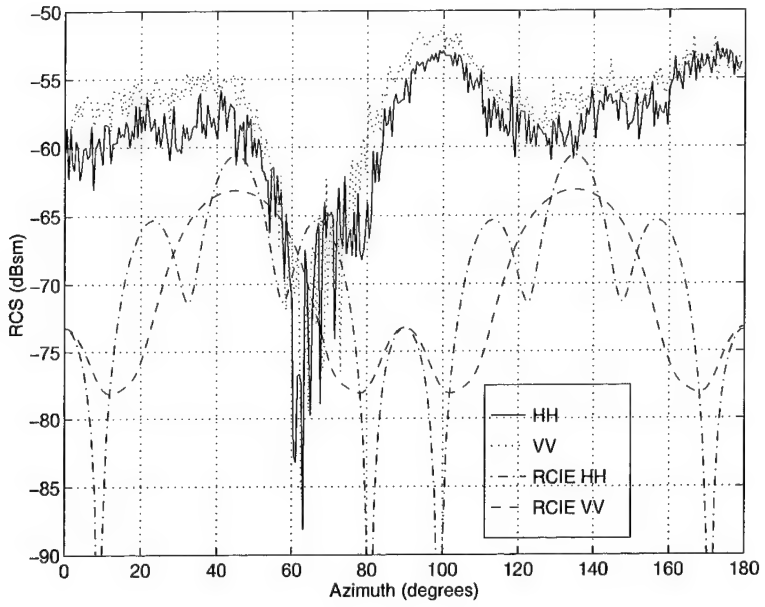

Figure D.55 The monostatic RCS of the small polyurethane cube using 3D-RCIE and measured data obtained at 10 GHz. The mesh size is $15/\lambda$ and BLGMRP was used to solve the matrix.

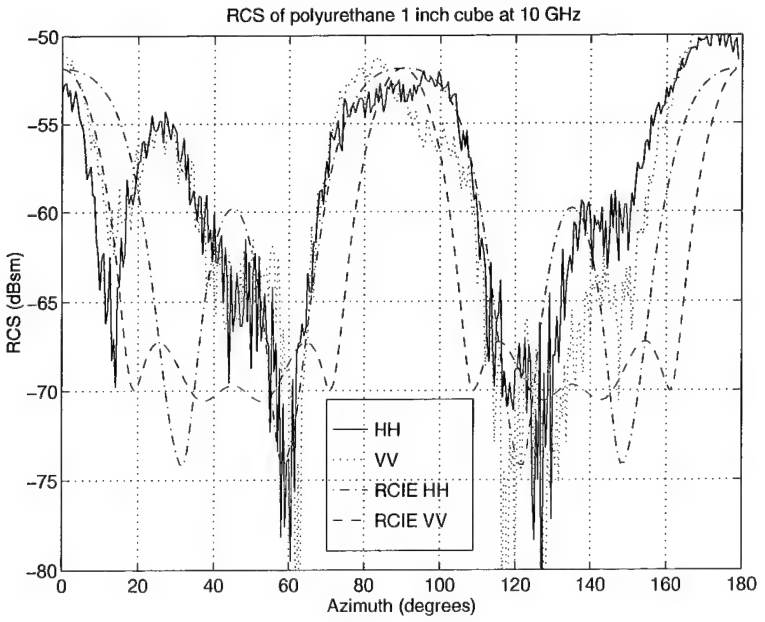

Figure D.56 The monostatic RCS of the small polyurethane cube using 3D-RCIE and measured data obtained at 12 GHz. The mesh size is $12.5/\lambda$ and BLGMRP was used to solve the matrix.

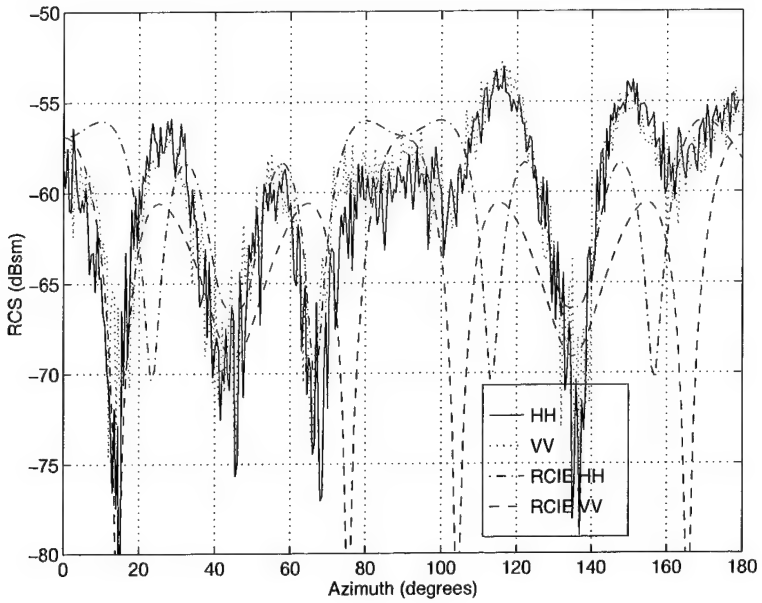

Figure D.57 The monostatic RCS of the small polyurethane cube using 3D-RCIE and measured data obtained at 14 GHz. The mesh size is $10.7/\lambda$ and BLGMRP was used to solve the matrix.

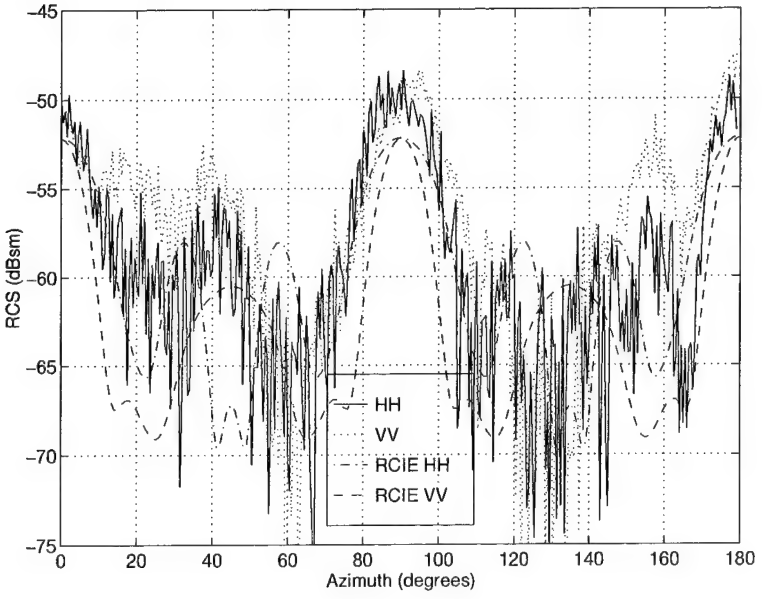

Figure D.58 The monostatic RCS of the small polyurethane cube using 3D-RCIE and measured data obtained at 16 GHz. The mesh size is $9.4/\lambda$ and BLGMRP was used to solve the matrix.

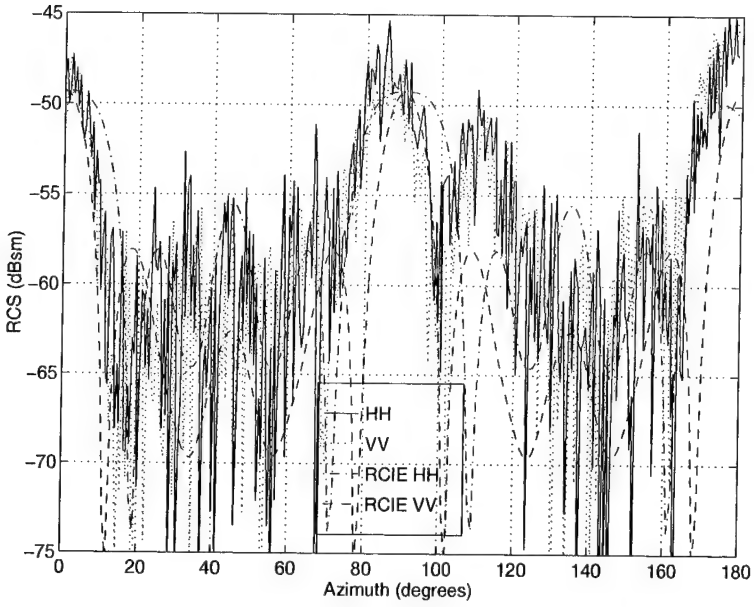

Figure D.59 The monostatic RCS of the small polyurethane cube using 3D-RCIE and measured data obtained at 18 GHz. The mesh size is $8.3/\lambda$ and BLGMRP was used to solve the matrix.

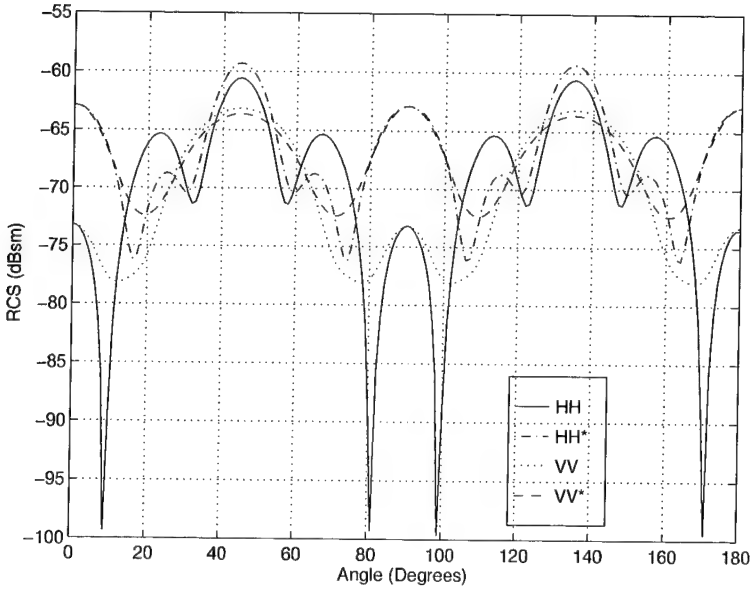

Figure D.60 The monostatic RCS of the small polyurethane cube using 3D-RCIE with varied dimensions obtained at 10 GHz. The length of each side was increased by 0.04 inches. BLGMRP was used to solve the matrix.

D.4 Small Cube - Polyurethane with R-card

Description	Figure
RCS Comparison of the Small Polyurethane Cube with R-card at 2 GHz	D.61
RCS Comparison of the Small Polyurethane Cube with R-card at 4 GHz	D.62
RCS Comparison of the Small Polyurethane Cube with R-card at 6 GHz	D.63
RCS Comparison of the Small Polyurethane Cube with R-card at 8 GHz	D.64
RCS Comparison of the Small Polyurethane Cube with R-card at 10 GHz	D.65
RCS Comparison of the Small Polyurethane Cube with R-card at 12 GHz	D.66
RCS Comparison of the Small Polyurethane Cube with R-card at 16 GHz	D.67
RCS Comparison of the Small Polyurethane Cube with R-card at 18 GHz	D.68
Small Polyurethane Cube w/r-card RCS with varied dimensions at 10 GHz	D.69

Table D.4 List of plots for the RCS of the small polyurethane cube with r-card.

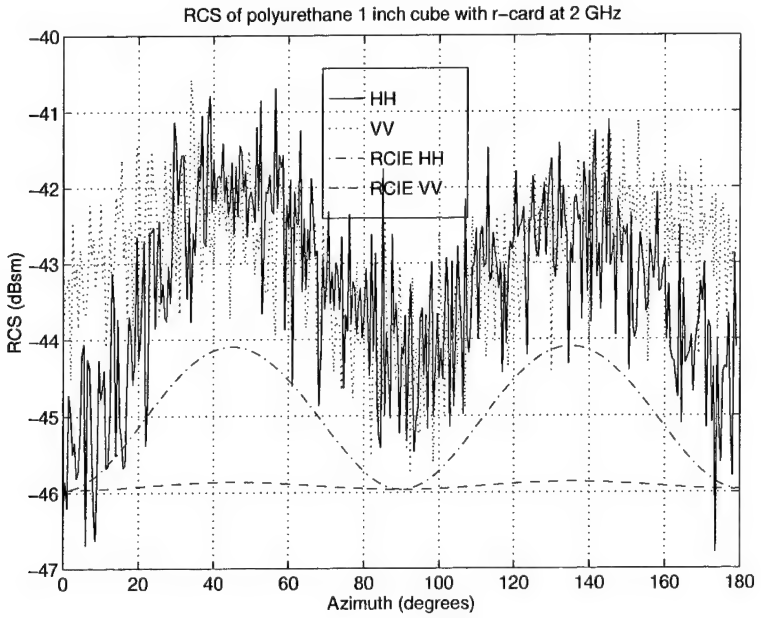

Figure D.61 The monostatic RCS of the small polyurethane cube with r-card using 3D-RCIE and measured data obtained at 2 GHz. The mesh size is $50/\lambda$ and BLGMRP was used to solve the matrix.

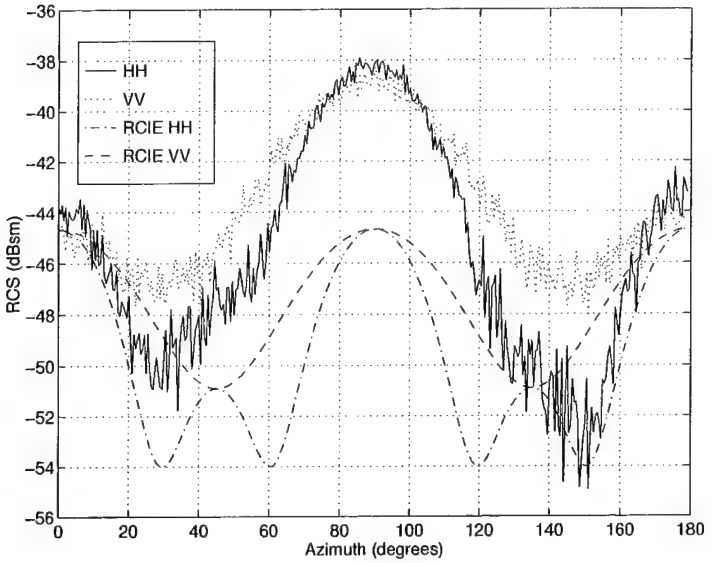

Figure D.62 The monostatic RCS of the small polyurethane cube with r-card using 3D-RCIE and measured data obtained at 4 GHz. The mesh size is $25/\lambda$ and BLGMRP was used to solve the matrix.

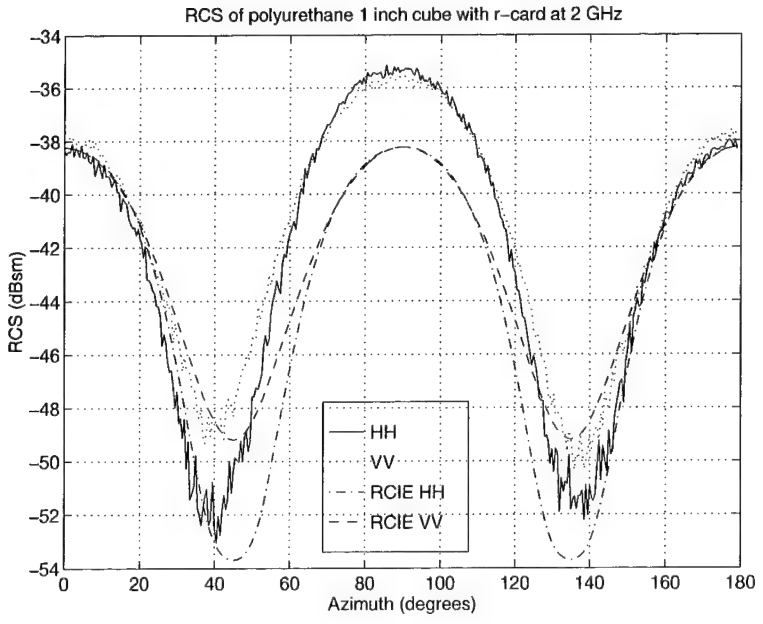

Figure D.63 The monostatic RCS of the small polyurethane cube with r-card using 3D-RCIE and measured data obtained at 6 GHz. The mesh size is $16.7/\lambda$ and BLGMRP was used to solve the matrix.

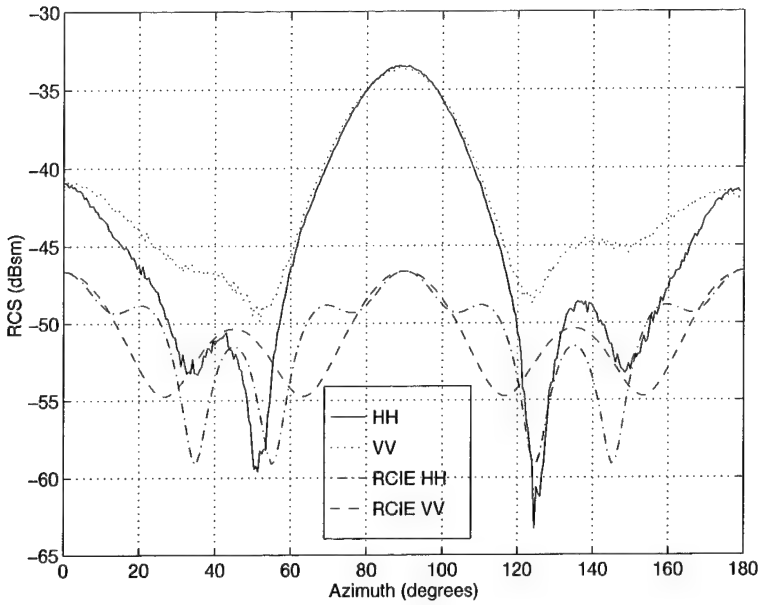

Figure D.64 The monostatic RCS of the small polyurethane cube with r-card using 3D-RCIE and measured data obtained at 8 GHz. The mesh size is $12.5/\lambda$ and BLGMRP was used to solve the matrix.

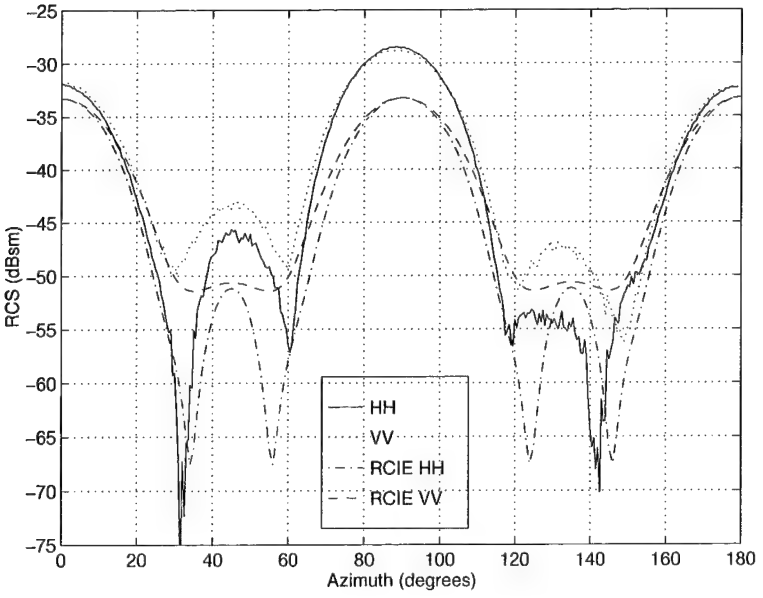

Figure D.65 The monostatic RCS of the small polyurethane cube with r-card using 3D-RCIE and measured data obtained at 10 GHz. The mesh size is $15/\lambda$ and BLGMRP was used to solve the matrix.

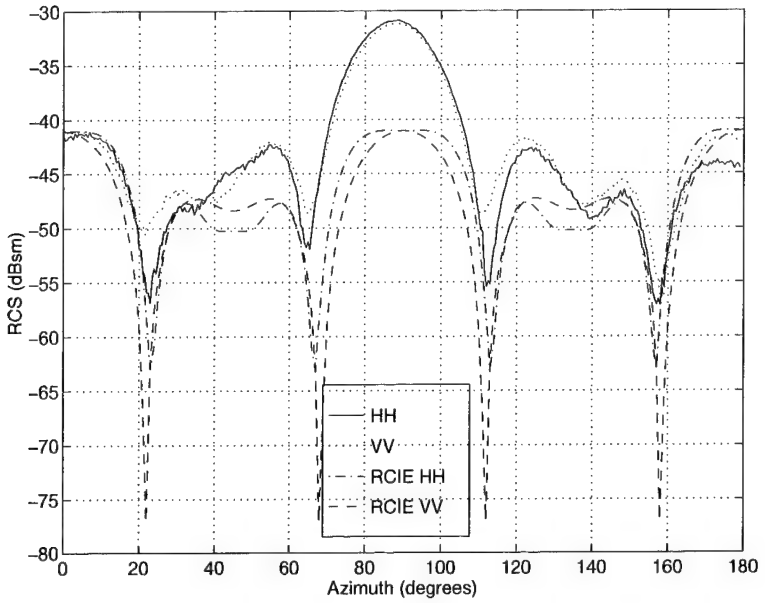

Figure D.66 The monostatic RCS of the small polyurethane cube with r-card using 3D-RCIE and measured data obtained at 12 GHz. The mesh size is $12.5/\lambda$ and BLGMRP was used to solve the matrix.

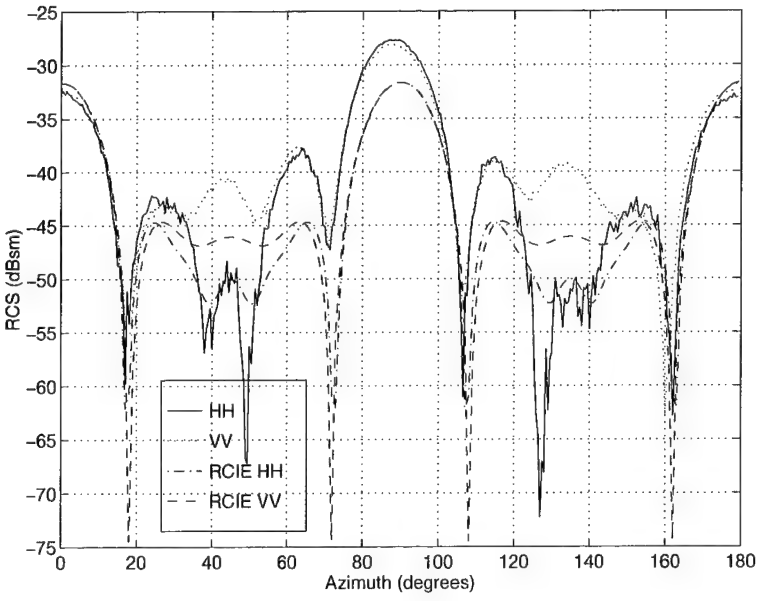

Figure D.67 The monostatic RCS of the small polyurethane cube with r-card using 3D-RCIE and measured data obtained at 16 GHz. The mesh size is $9.4/\lambda$ and BLGMRP was used to solve the matrix.

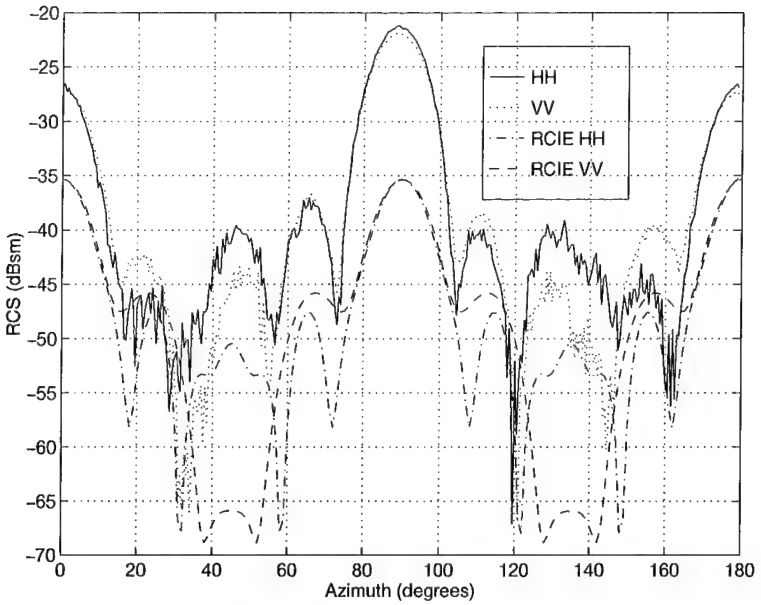

Figure D.68 The monostatic RCS of the small polyurethane cube with r-card using 3D-RCIE and measured data obtained at 18 GHz. The mesh size is $8.3/\lambda$ and BLGMRP was used to solve the matrix.

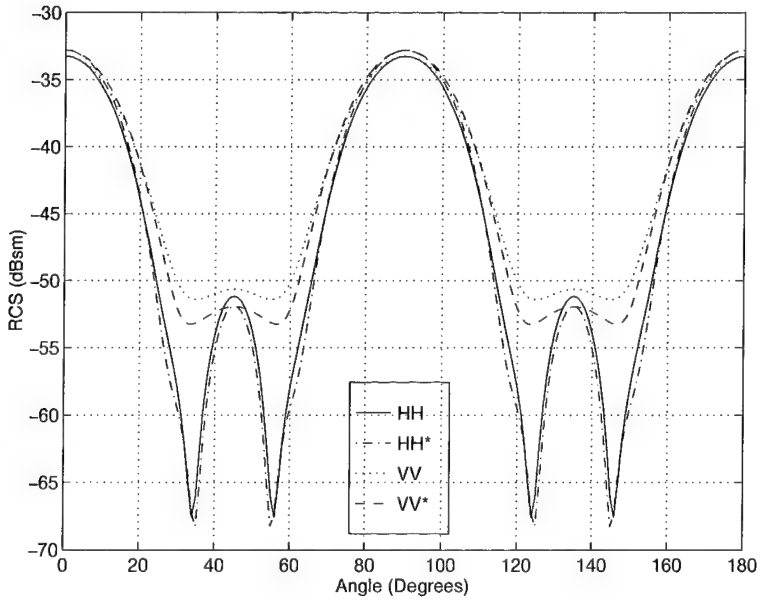

Figure D.69 The monostatic RCS of the small polyurethane cube with r-card using 3D-RCIE with varied dimensions obtained at 10 GHz. The length of each side was increased by 0.04 inches. BLGMRP was used to solve the matrix.

Description	Figure
RCS Comparison of the Large Polyethylene Cube at 2 GHz	D.70
RCS Comparison of the Large Polyethylene Cube at 4 GHz	D.71
Large Polyethylene Cube with varied mesh sizes at 2 GHz	D.72
Large Polyethylene Cube RCS with varied dimensions at 2 GHz	D.73
Large Polyethylene Cube HH RCS with varied dielectric constants at 2 GHz	D.74
Large Polyethylene Cube VV RCS with varied dielectric constants at 2 GHz	D.75

Table D.5 List of plots for the RCS of the large polyethylene cube.

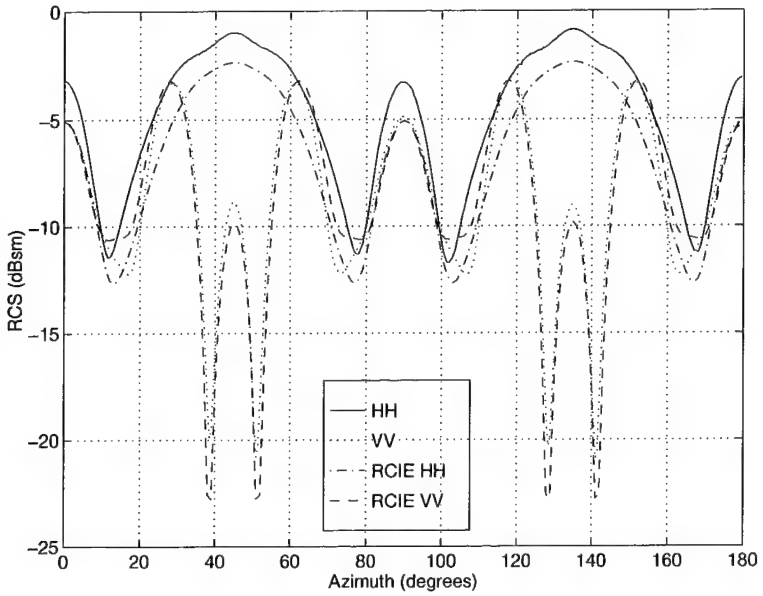

Figure D.70 The monostatic RCS of the large polyethylene cube using 3D-RCIE and measured data obtained at 2 GHz. The mesh size is $10/\lambda$ and BLGMRP was used to solve the matrix.

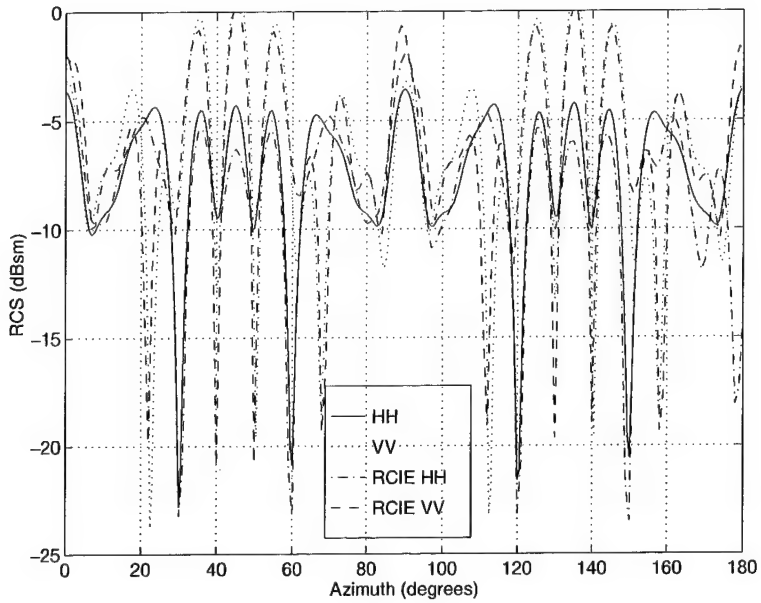

Figure D.71 The monostatic RCS of the large polyethylene cube using 3D-RCIE and measured data obtained at 4 GHz. The mesh size is $5/\lambda$ and BLGMRP was used to solve the matrix.

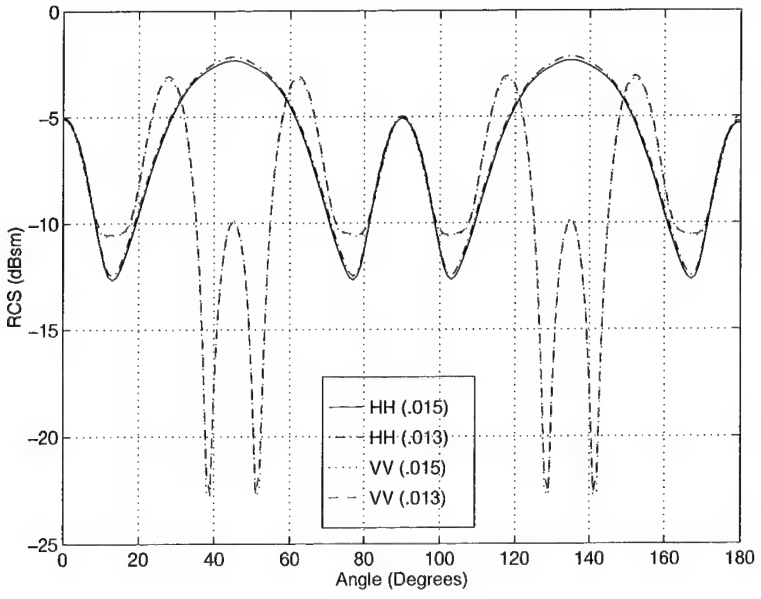

Figure D.72 The monostatic RCS of the large polyethylene cube using 3D-RCIE and varied mesh sizes obtained at 2 GHz. The mesh sizes are $11.5/\lambda$ (.013) and $10/\lambda$ (.015). BLGMRP was used to solve the matrix.

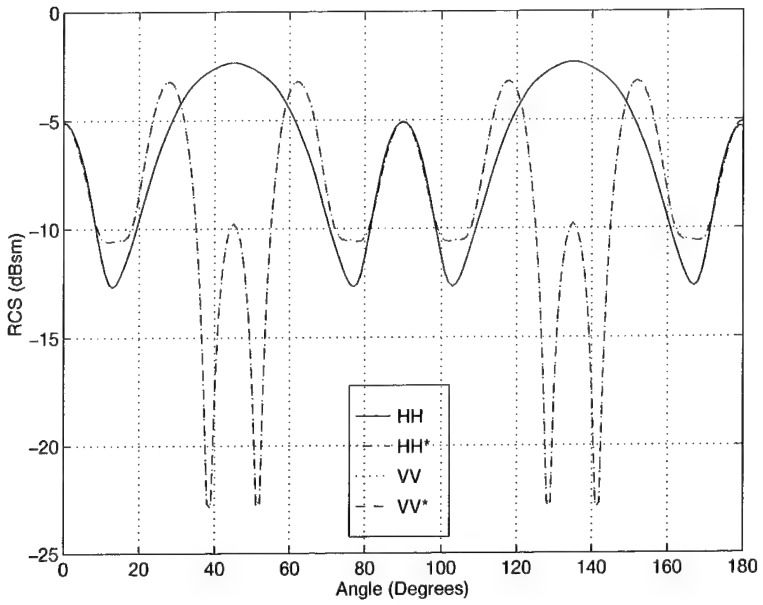

Figure D.73 The monostatic RCS of the large polyethylene cube using 3D-RCIE with varied dimensions obtained at 2 GHz. The length of each side was increased by 0.005 inches. BLGMRP was used to solve the matrix.

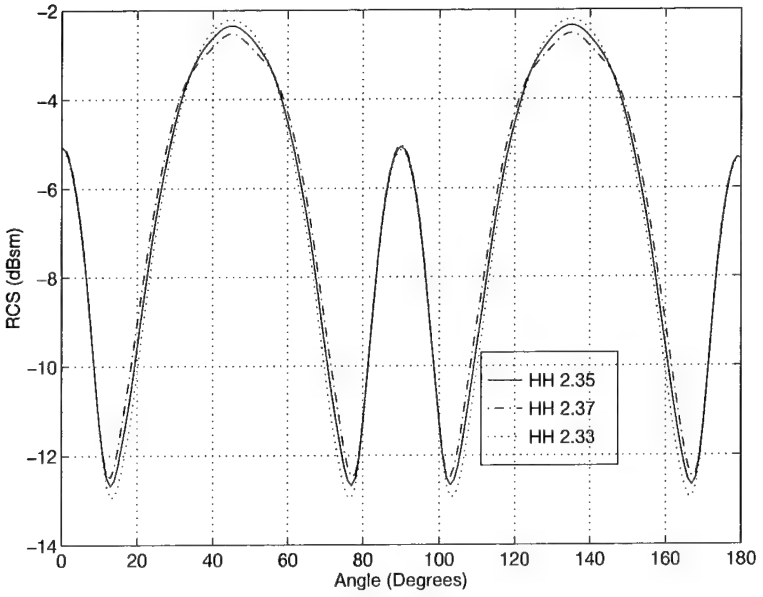

Figure D.74 The HH monostatic RCS of the large polyethylene cube using 3D-RCIE and varied dielectric constants obtained at 2 GHz. The dielectric constants are 2.33, 2.35, and 2.37. BLGMRP was used to solve the matrix.

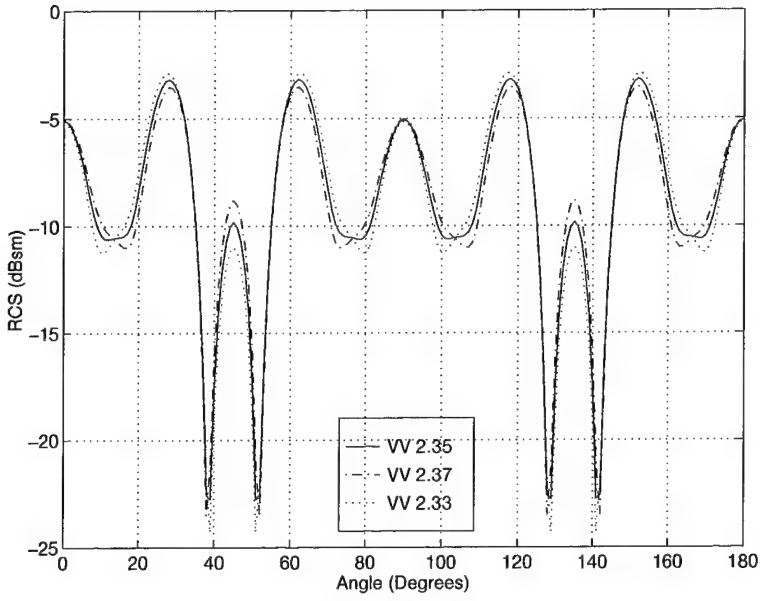

Figure D.75 The VV monostatic RCS of the large polyethylene cube using 3D-RCIE and varied dielectric constants obtained at 2 GHz. The dielectric constants are 2.33, 2.35, and 2.37. BLGMRP was used to solve the matrix.

D.6 Large Cube - Polyurethane

Description	Figure
RCS Comparison of the Large Polyurethane Cube at 2 GHz	D.76
RCS Comparison of the Large Polyurethane Cube at 4 GHz	D.77
Large Polyurethane Cube RCS with varied dimensions at 2 GHz	D.78
3D-RCIE (BLG vs. LU) RCS of the Large Polyurethane Cube at 2 GHz	D.79

Table D.6 List of plots for the RCS of the large polyurethane cube.

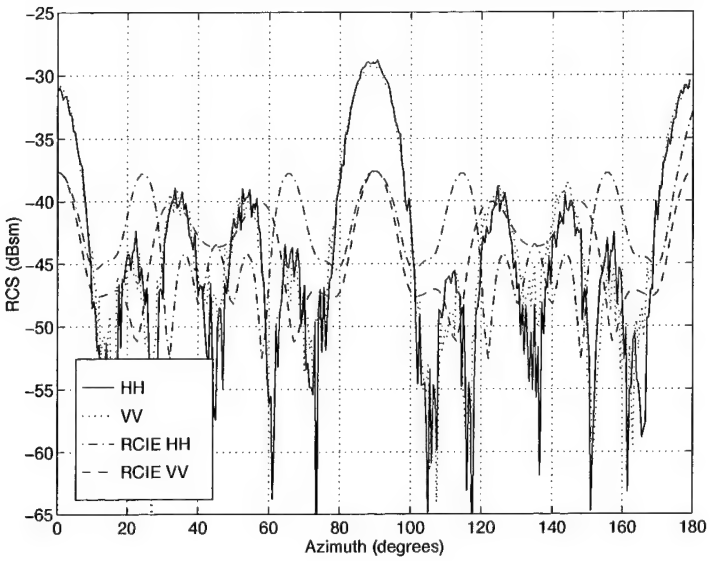

Figure D.76 The monostatic RCS of the large polyurethane cube using 3D-RCIE and measured data obtained at 2 GHz. The mesh size is $10/\lambda$ and BLGMRP was used to solve the matrix.

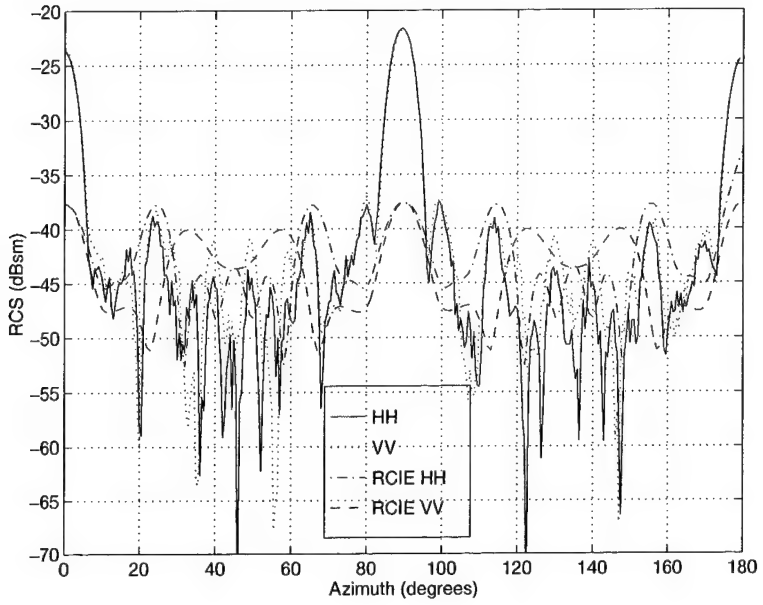

Figure D.77 The monostatic RCS of the large polyurethane cube using 3D-RCIE and measured data obtained at 4 GHz. The mesh size is $5/\lambda$ and BLGMRP was used to solve the matrix.

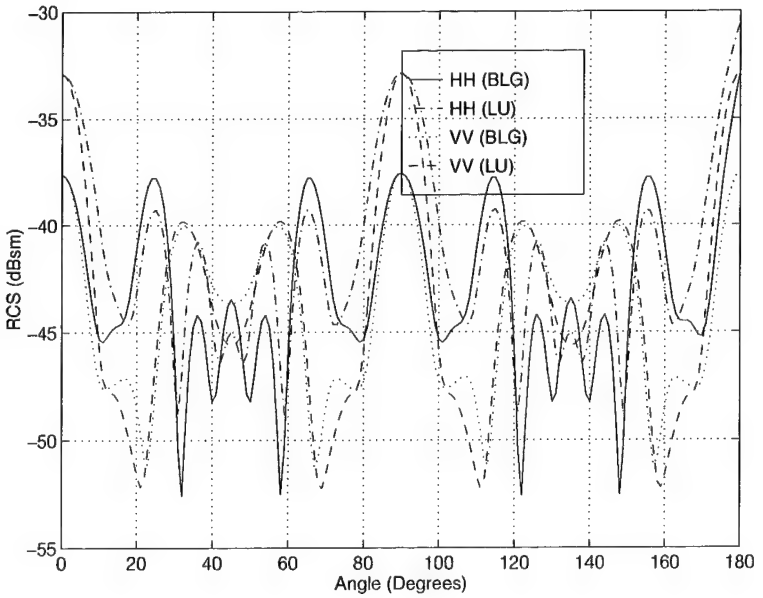

Figure D.78 The monostatic RCS of the large polyurethane cube using 3D-RCIE with varied dimensions obtained at 2 GHz. The length of each side was increased by 0.2 inches. BLGMRP was used to solve the matrix.

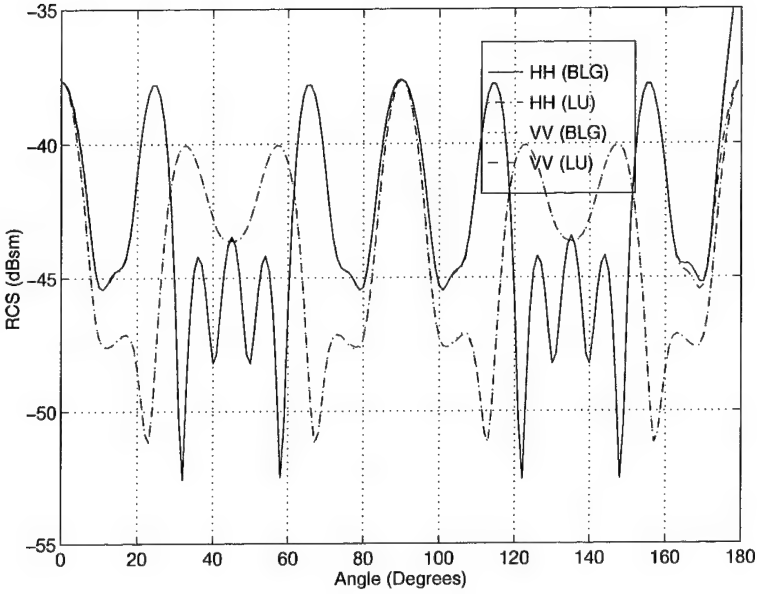

Figure D.79 The monostatic RCS of the large polyurethane cube using 3D-RCIE with BLGMRP and LUFACTOR obtained at 2 GHz. The mesh size is $10/\lambda$.

D.7 Sphere - Polyethylene

Description	Figure
RCS Comparison of the Polyethylene Sphere at 2 GHz	D.80
Polyethylene Sphere with varied mesh sizes at 2 GHz	D.81
Polyethylene Sphere RCS with varied dimensions at 2 GHz	D.82
3D-RCIE (BLG vs. LU) RCS of the Polyethylene Sphere at 2 GHz	D.83

Table D.7 List of plots for the RCS of the polyethylene sphere.

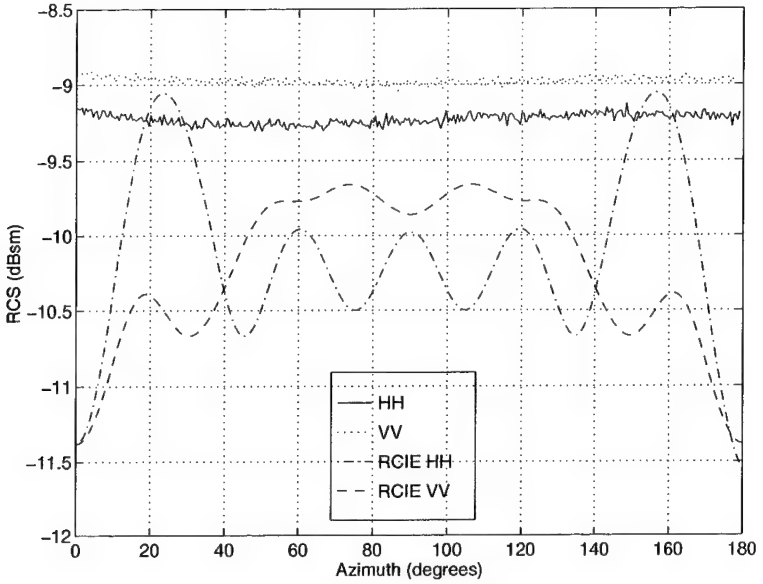

Figure D.80 The monostatic RCS of the polyethylene sphere using 3D-RCIE and measured data obtained at 2 GHz. The mesh size is $10/\lambda$ and BLGMRP was used to solve the matrix.

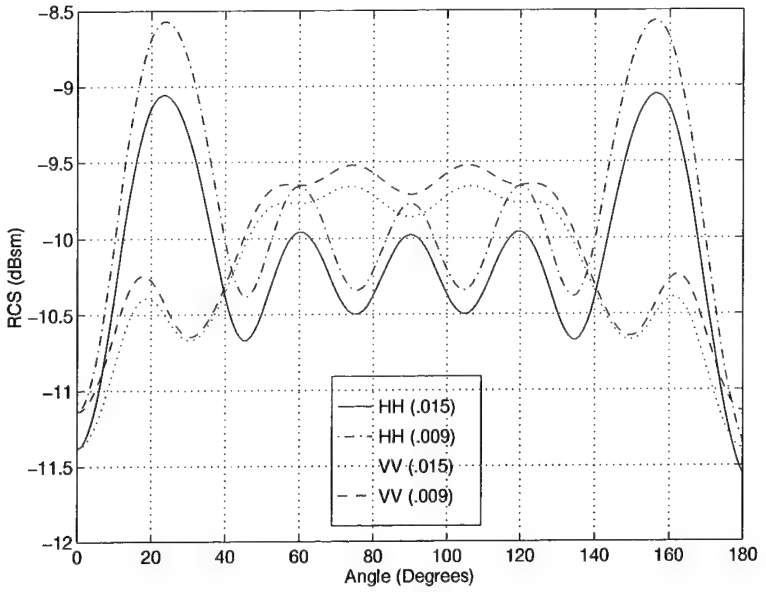

Figure D.81 The monostatic RCS of the polyethylene sphere using 3D-RCIE and varied mesh sizes obtained at 2 GHz. The mesh sizes are $16.7/\lambda$ (.009) and $10/\lambda$ (.015). BLGMRP was used to solve the matrix.

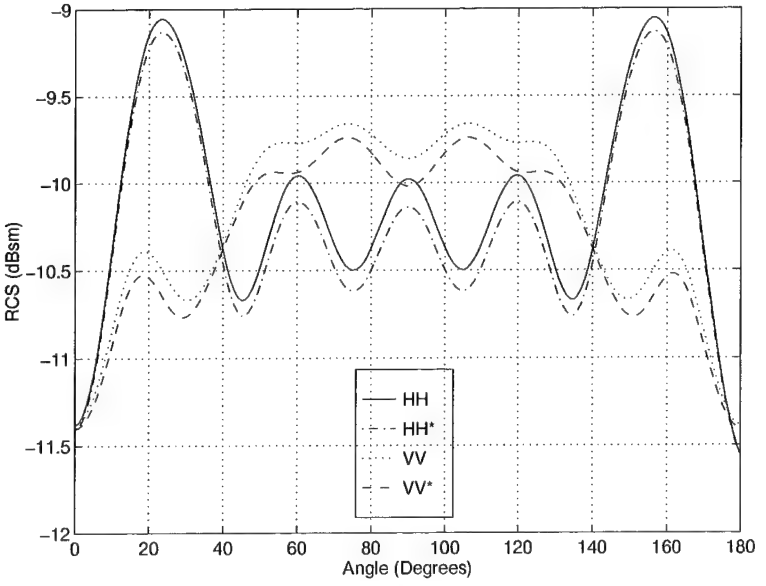

Figure D.82 The monostatic RCS of the polyethylene sphere using 3D-RCIE with varied dimensions obtained at 2 GHz. The length of the diameter was increased by 0.1 inches. BLGMRP was used to solve the matrix.

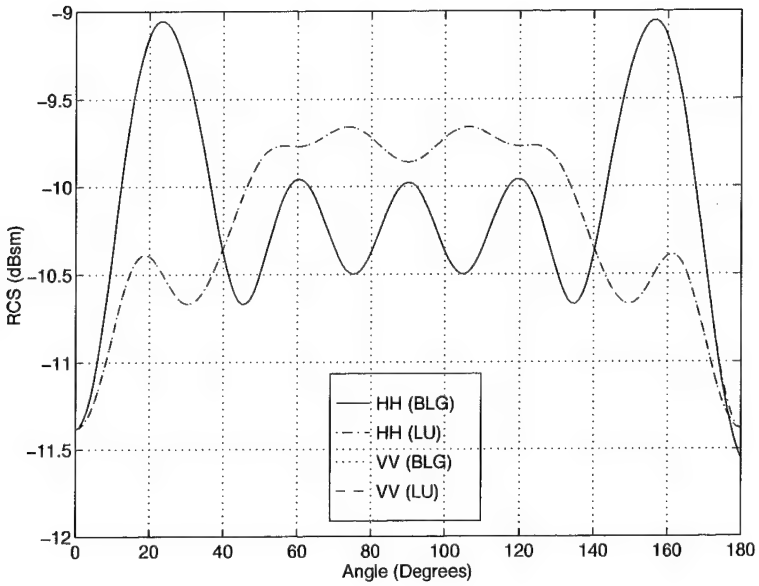

Figure D.83 The monostatic RCS of the polyethylene sphere using 3D-RCIE with BLGMRP and LUFACTOR obtained at 2 GHz. The mesh size is $10/\lambda$.

D.8 Mini-Arrow - Polyethylene

Description	Figure
RCS Comparison of the Mini-Arrow at 2 GHz	D.84
RCS Comparison of the Mini-Arrow at 4 GHz	D.85
RCS Comparison of the Mini-Arrow at 6 GHz	D.86
RCS Comparison of the Mini-Arrow at 8 GHz	D.87
RCS Comparison of the Mini-Arrow at 10 GHz	D.88
3D-RCIE (BLG vs. LU) RCS of the Polyethylene Mini-Arrow at 6 GHz	D.89
Polyethylene Mini-Arrow RCS with varied mesh sizes at 6 GHz	D.90
Polyethylene Mini-Arrow RCS with varied dimensions at 6 GHz	D.91
Polyethylene Mini-Arrow HH RCS with varied dielectric constants at 6 GHz	D.92
Polyethylene Mini-Arrow VV RCS with varied dielectric constants at 6 GHz	D.93

Table D.8 List of plots for the RCS of the polyethylene mini-arrow.

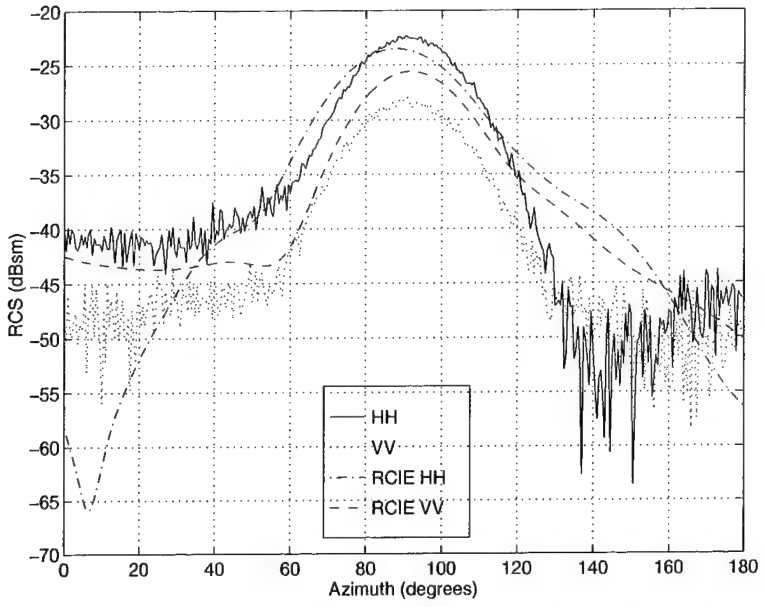

Figure D.84 The monostatic RCS of the polyethylene mini-arrow using 3D-RCIE and measured data obtained at 2 GHz. The mesh size is $30/\lambda$ and BLGMRP was used to solve the matrix.

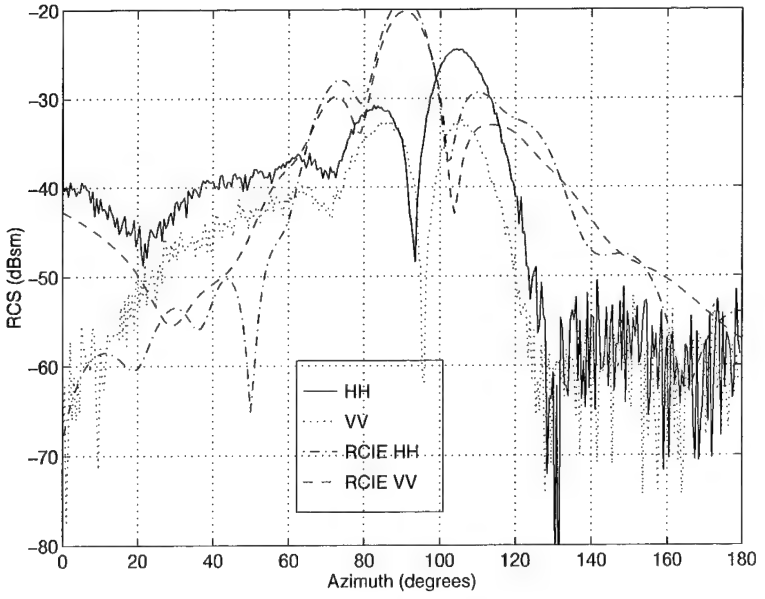

Figure D.85 The monostatic RCS of the polyethylene mini-arrow using 3D-RCIE and measured data obtained at 4 GHz. The mesh size is $15/\lambda$ and BLGMRP was used to solve the matrix.

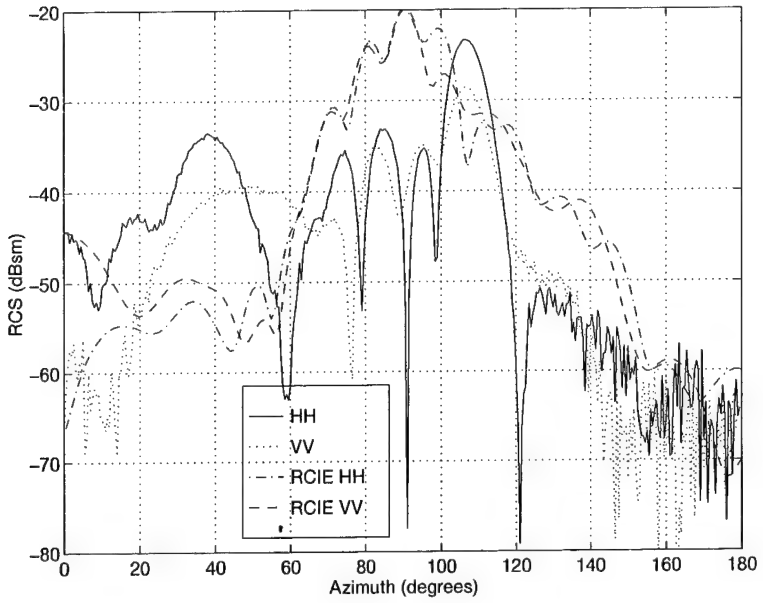

Figure D.86 The monostatic RCS of the polyethylene mini-arrow using 3D-RCIE and measured data obtained at 6 GHz. The mesh size is $10/\lambda$ and BLGMRP was used to solve the matrix.

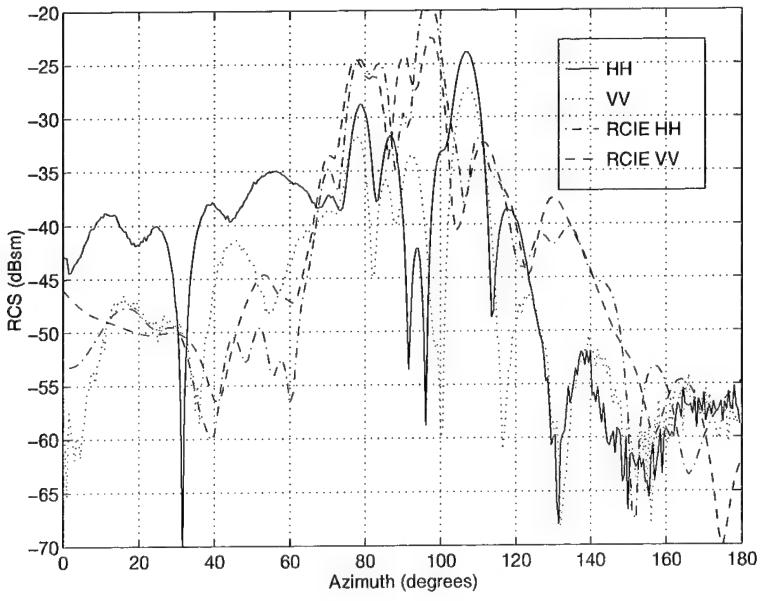

Figure D.87 The monostatic RCS of the polyethylene mini-arrow using 3D-RCIE and measured data obtained at 8 GHz. The mesh size is $7.5/\lambda$ and BLGMRP was used to solve the matrix.

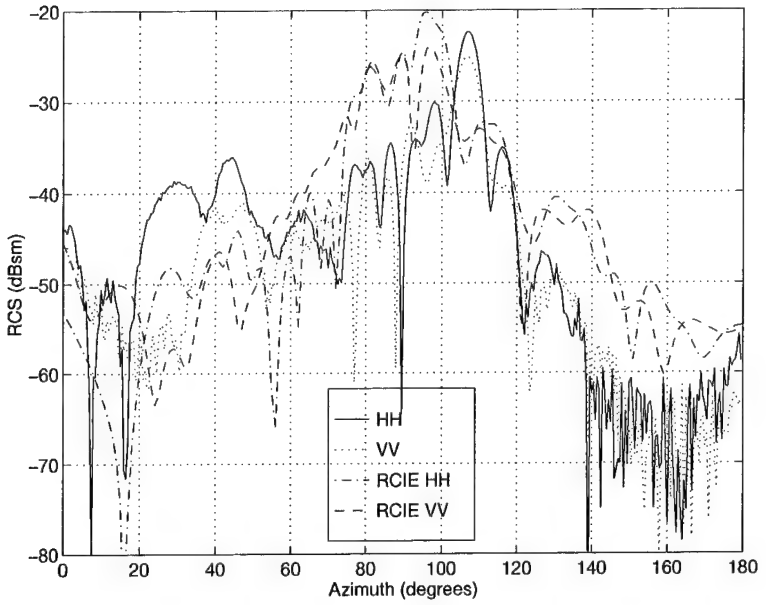

Figure D.88 The monostatic RCS of the polyethylene mini-arrow using 3D-RCIE and measured data obtained at 10 GHz. The mesh size is $6/\lambda$ and BLGMRP was used to solve the matrix.

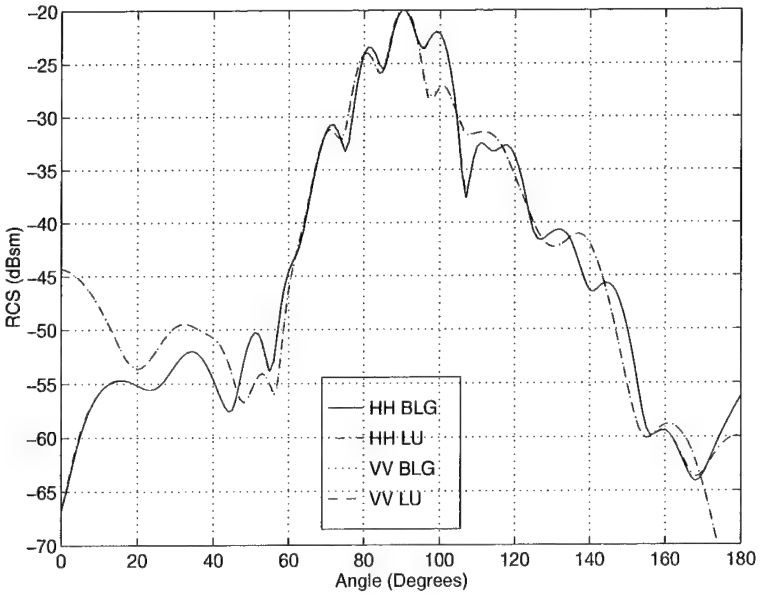

Figure D.89 The monostatic RCS of the polyethylene mini-arrow using 3D-RCIE with BLGMRP and LUFACTOR obtained at 6 GHz. The mesh size is $10/\lambda$.

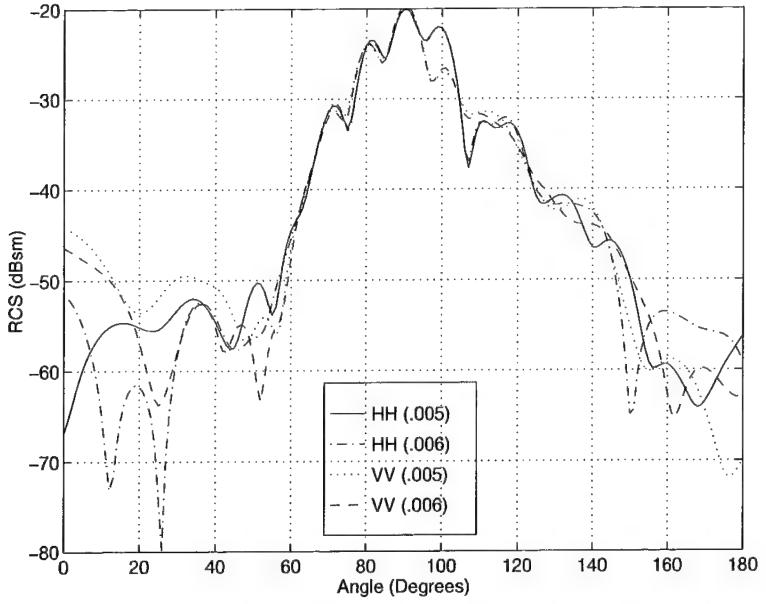

Figure D.90 The monostatic RCS of the polyethylene mini-arrow using 3D-RCIE and varied mesh sizes obtained at 6 GHz. The mesh sizes are $10/\lambda$ (.005) and $8.3/\lambda$ (.006). BLGMRP was used to solve the matrix.

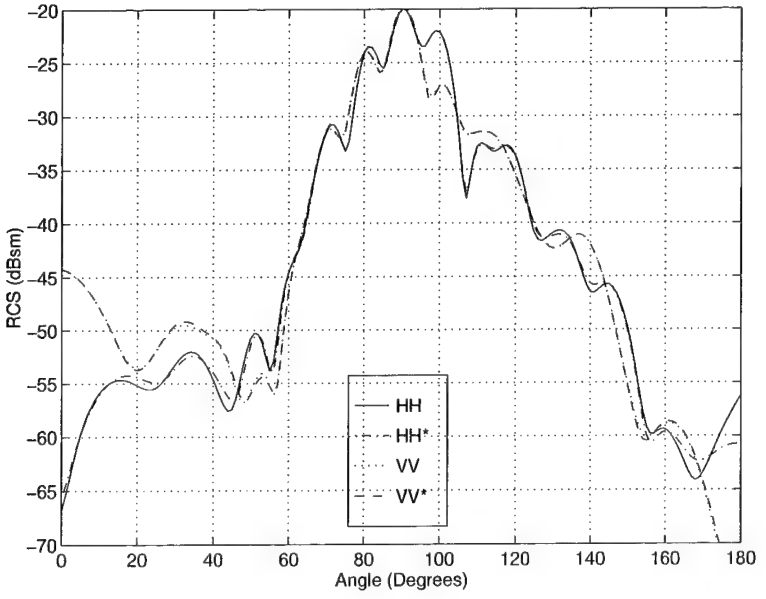

Figure D.91 The monostatic RCS of the polyethylene mini-arrow using 3D-RCIE with varied dimensions obtained at 6 GHz. The length of each dimension was increased by 0.0025 inches. BLGMRP was used to solve the matrix.

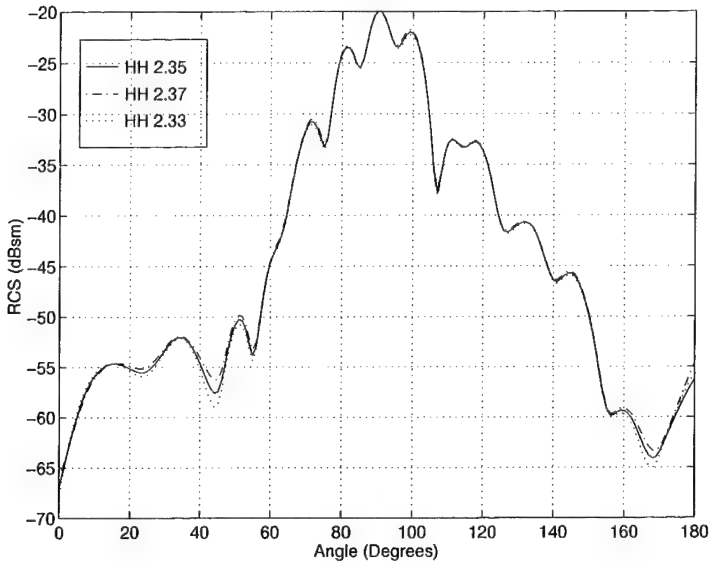

Figure D.92 The HH monostatic RCS of the polyethylene mini-arrow using 3D-RCIE and varied dielectric constants obtained at 6 GHz. The dielectric constants are 2.33, 2.35, and 2.37. BLGMRP was used to solve the matrix.

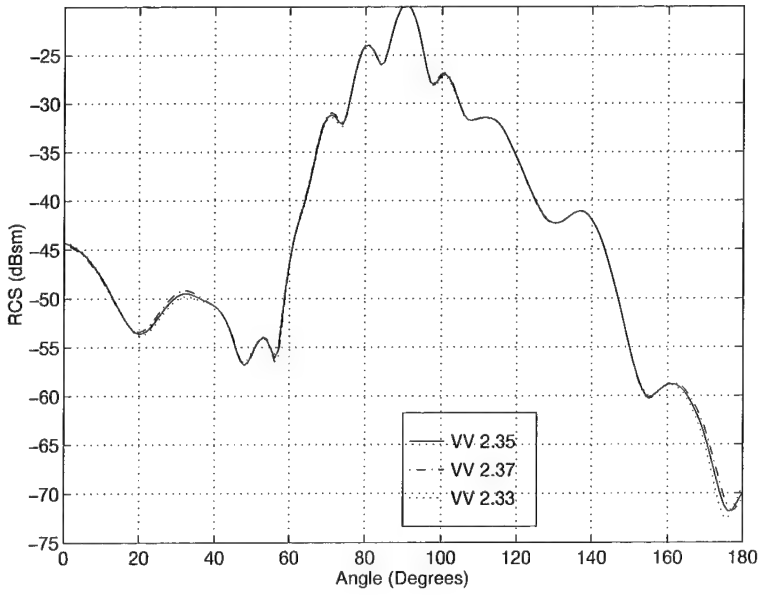

Figure D.93 The VV monostatic RCS of the polyethylene mini-arrow using 3D-RCIE and varied dielectric constants obtained at 6 GHz. The dielectric constants are 2.33, 2.35, and 2.37. BLGMRP was used to solve the matrix.

D.9 Mini-Arrow with R-Card - Polyethylene

Description	Figure
RCS Comparison of the Mini-Arrow with R-Card at 2 GHz	D.94
RCS Comparison of the Mini-Arrow with R-Card at 4 GHz	D.95
RCS Comparison of the Mini-Arrow with R-Card at 6 GHz	D.96
RCS Comparison of the Mini-Arrow with R-Card at 8 GHz	D.97
RCS Comparison of the Mini-Arrow with R-Card at 10 GHz	D.98
Polyethylene Mini-Arrow with R-Card RCS with varied mesh sizes at 6 GHz	D.99
Polyethylene Mini-Arrow with R-Card RCS with varied dimensions at 6 GHz	D.100
Polyethylene Mini-Arrow W/R-card HH RCS with varied dielectric constants at 6 GHz	D.101
Polyethylene Mini-Arrow W/R-card VV RCS with varied dielectric constants at 6 GHz	D.102

Table D.9 List of plots for the RCS of the polyethylene mini-arrow with r-card.

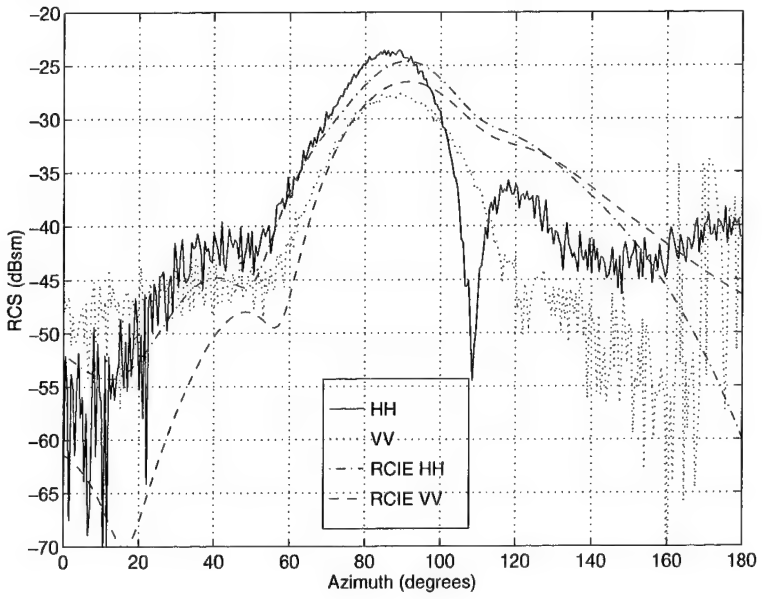

Figure D.94 The monostatic RCS of the polyethylene mini-arrow with r-card using 3D-RCIE and measured data obtained at 2 GHz. The mesh size is $30/\lambda$ and LUFACTOR was used to solve the matrix.

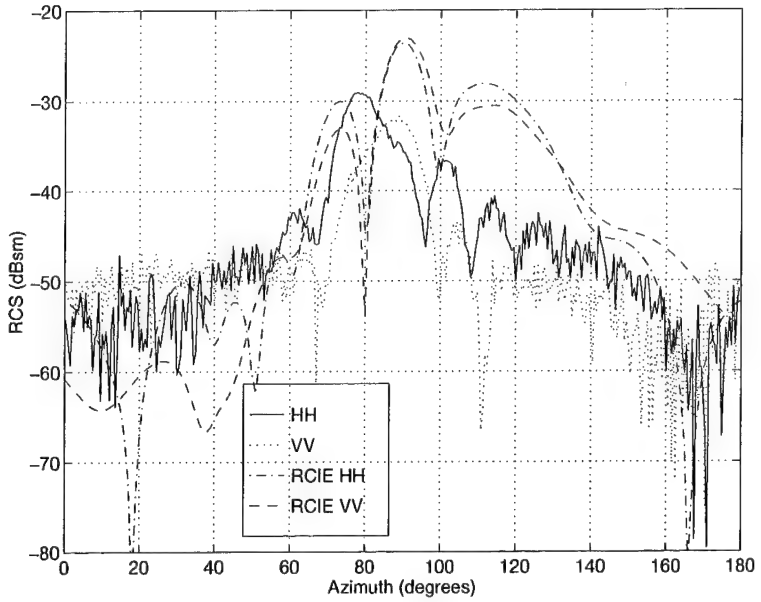

Figure D.95 The monostatic RCS of the polyethylene mini-arrow with r-card using 3D-RCIE and measured data obtained at 4 GHz. The mesh size is $15/\lambda$ and LUFACTOR was used to solve the matrix.

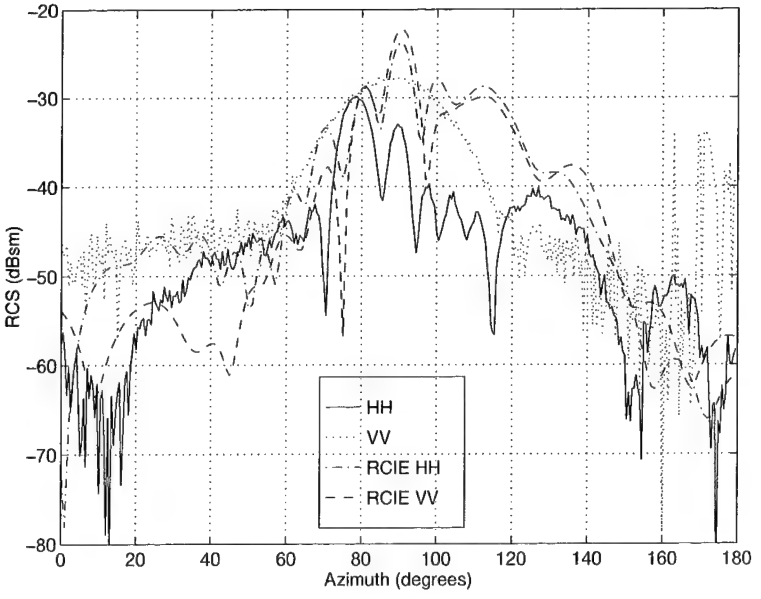

Figure D.96 The monostatic RCS of the polyethylene mini-arrow with r-card using 3D-RCIE and measured data obtained at 6 GHz. The mesh size is $10/\lambda$ and LUFACTOR was used to solve the matrix.

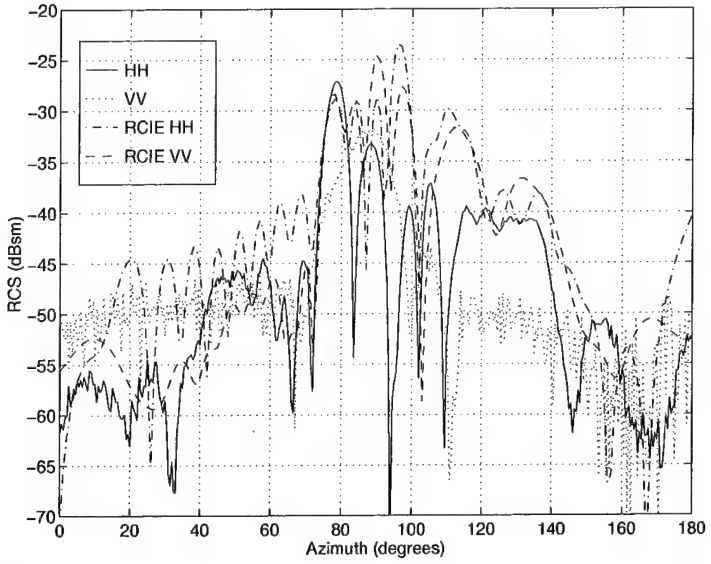

Figure D.97 The monostatic RCS of the polyethylene mini-arrow with r-card using 3D-RCIE and measured data obtained at 8 GHz. The mesh size is $7.5/\lambda$ and LUFACTOR was used to solve the matrix.

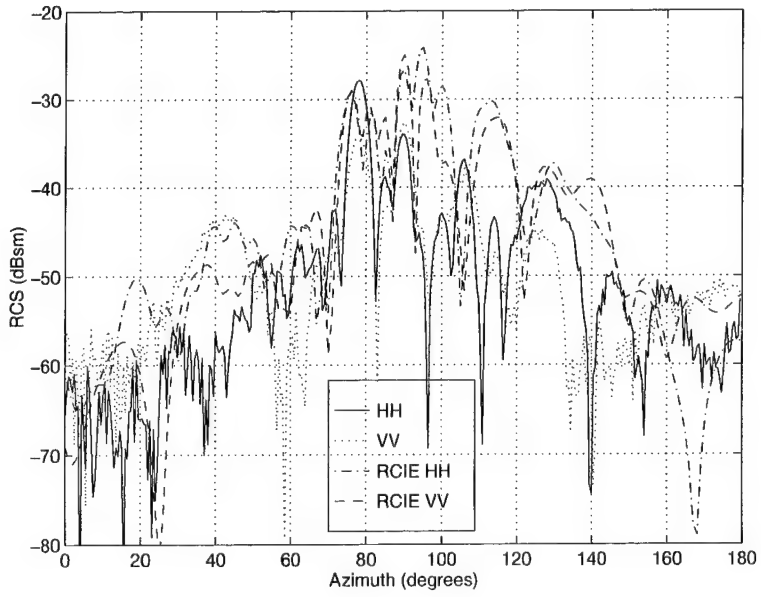

Figure D.98 The monostatic RCS of the polyethylene mini-arrow with r-card using 3D-RCIE and measured data obtained at 10 GHz. The mesh size is $6/\lambda$ and LUFACTOR was used to solve the matrix.

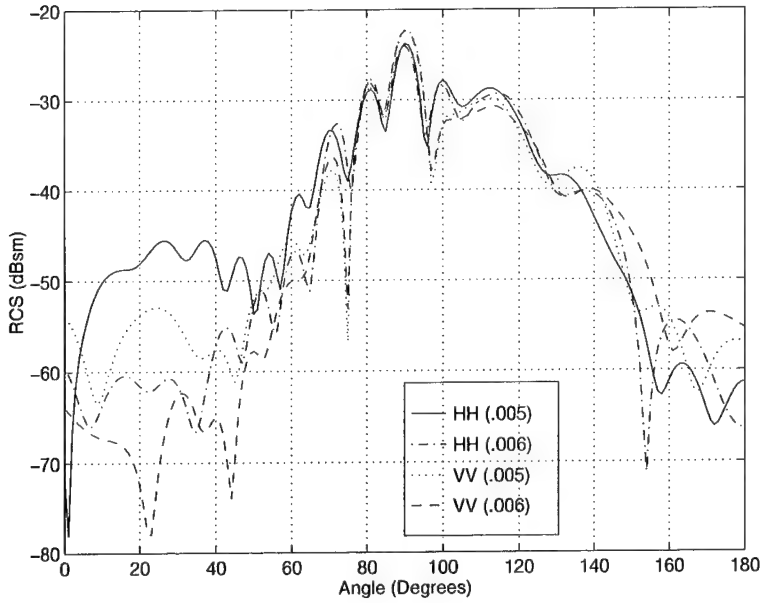

Figure D.99 The monostatic RCS of the polyethylene mini-arrow with r-card using 3D-RCIE and varied mesh sizes obtained at 6 GHz. The mesh sizes are $10/\lambda$ (.005) and $8.3/\lambda$ (.006). LUFACTOR was used to solve the matrix.

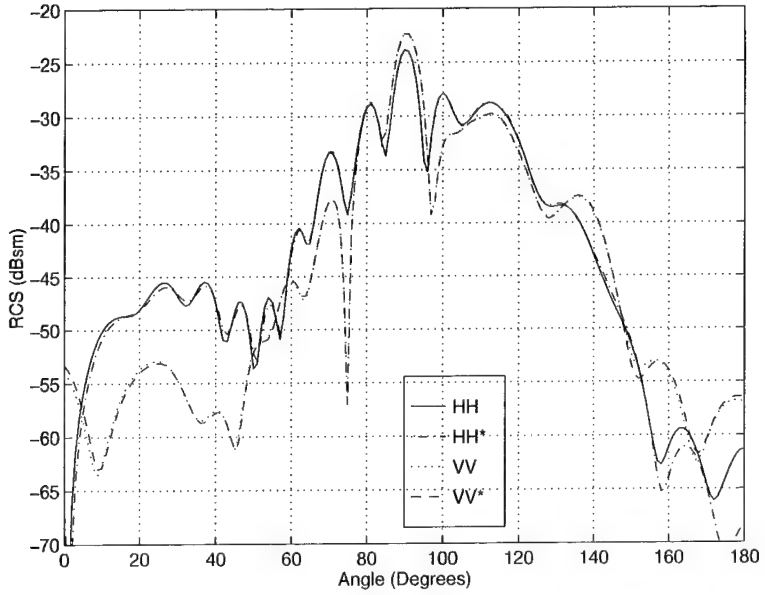

Figure D.100 The monostatic RCS of the polyethylene mini-arrow with r-card using 3D-RCIE with varied dimensions obtained at 6 GHz. The length of each dimension was increased by 0.0025 inches. LUFACTOR was used to solve the matrix.

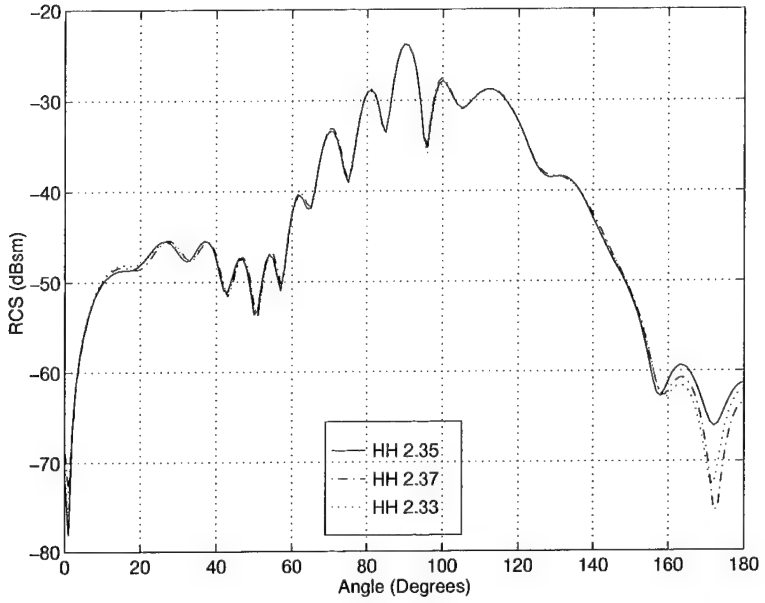

Figure D.101 The HH monostatic RCS of the polyethylene mini-arrow with r-card using 3D-RCIE and varied dielectric constants obtained at 6 GHz. The dielectric constants are 2.33, 2.35, and 2.37. LUFACTOR was used to solve the matrix.

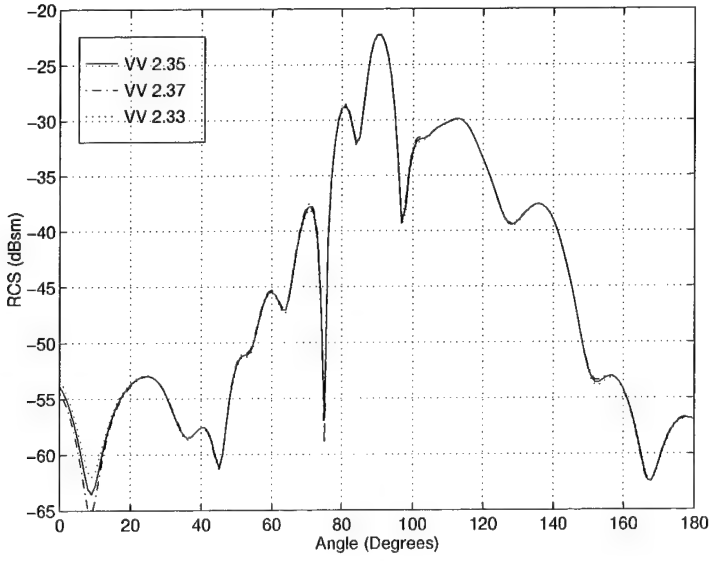

Figure D.102 The VV monostatic RCS of the polyethylene mini-arrow with r-card using 3D-RCIE and varied dielectric constants obtained at 6 GHz. The dielectric constants are 2.33, 2.35, and 2.37. LUFACTOR was used to solve the matrix.

D.10 Ogive

Description	Figure
RCS Comparison of the Ogive at 2 GHz	D.103
RCS Comparison of the Ogive at 4 GHz	D.104
RCS Comparison of the Ogive at 6 GHz	D.105
RCS Comparison of the Ogive at 8 GHz	D.106
RCS Comparison of the Ogive at 10 GHz	D.107
RCS Comparison of the Ogive at 12 GHz	D.108
RCS Comparison of the Ogive at 14 GHz	D.109
RCS Comparison of the Ogive at 16 GHz	D.110
RCS Comparison of the Ogive at 18 GHz	D.111
Ogive RCS with varied mesh sizes at 6 GHz	D.112
Ogive RCS with varied dimensions at 10 GHz	D.113
Ogive HH RCS with varied dielectric constants at 10 GHz	D.114
Ogive VV RCS with varied dielectric constants at 10 GHz	D.113
3D-RCIE (BLG vs. LU) RCS of the Polyethylene Ogive at 6 GHz	D.116

Table D.10 List of plots for the RCS of the ogive.

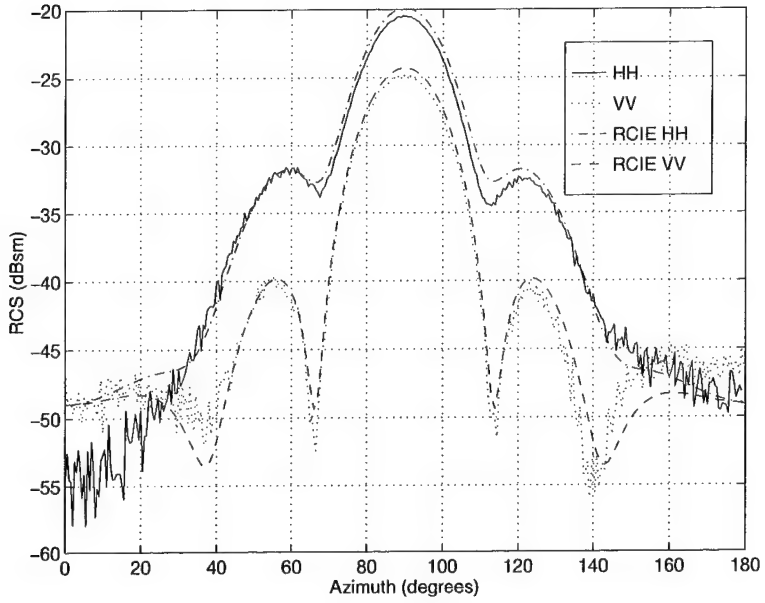

Figure D.103 The monostatic RCS of the ogive using 3D-RCIE and measured data obtained at 2 GHz. The mesh size is $50/\lambda$ and BLGMRP was used to solve the matrix.

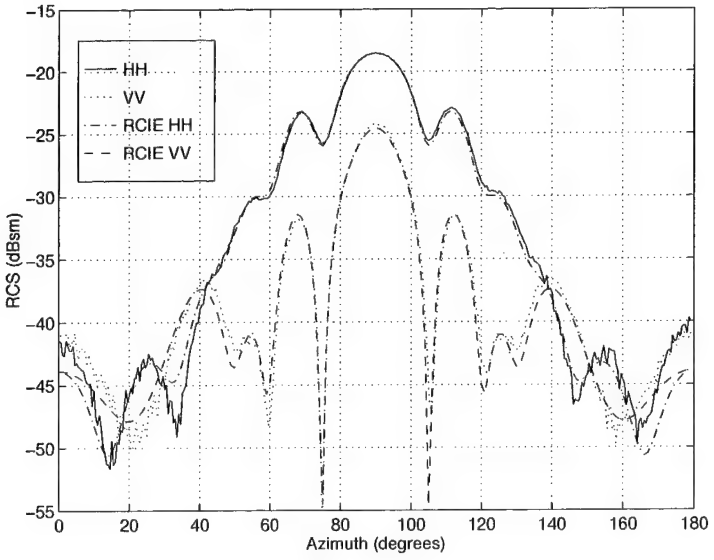

Figure D.104 The monostatic RCS of the ogive using 3D-RCIE and measured data obtained at 4 GHz. The mesh size is $25/\lambda$ and BLGMRP was used to solve the matrix.

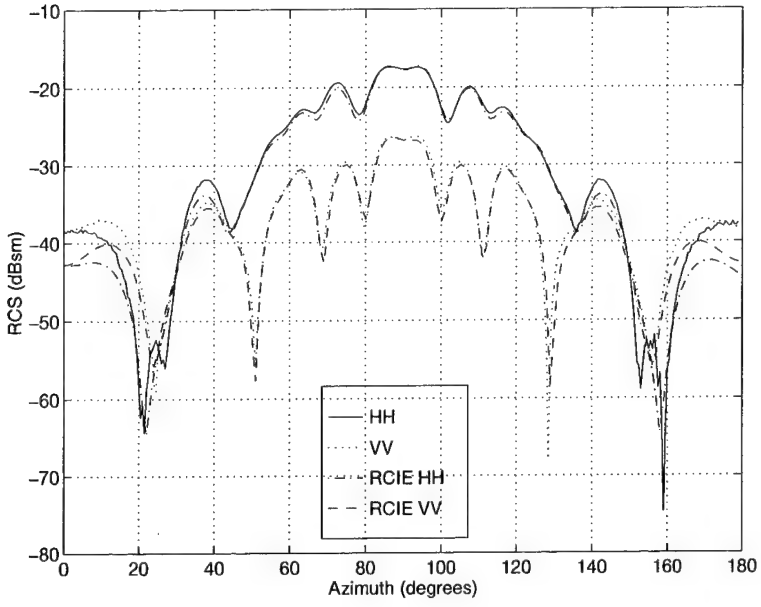

Figure D.105 The monostatic RCS of the ogive using 3D-RCIE and measured data obtained at 6 GHz. The mesh size is $16.7/\lambda$ and BLGMRP was used to solve the matrix.

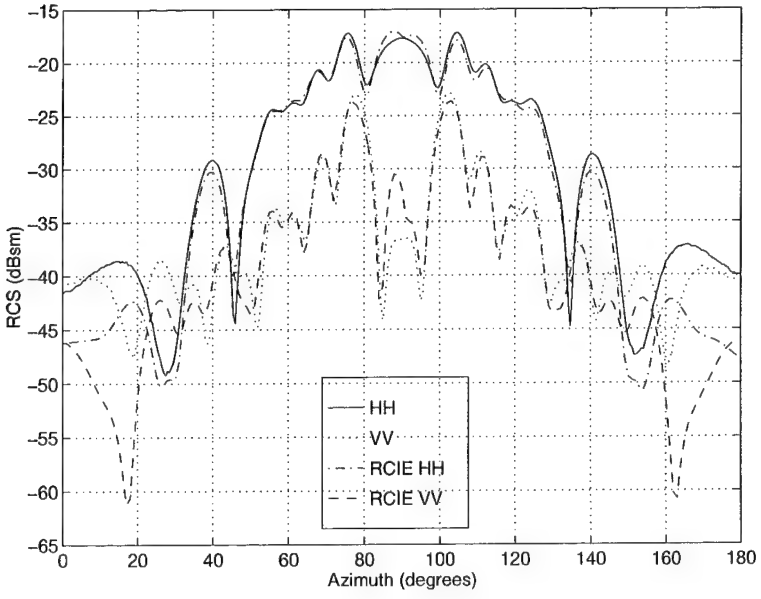

Figure D.106 The monostatic RCS of the ogive using 3D-RCIE and measured data obtained at 8 GHz. The mesh size is $12.5/\lambda$ and BLGMRP was used to solve the matrix.

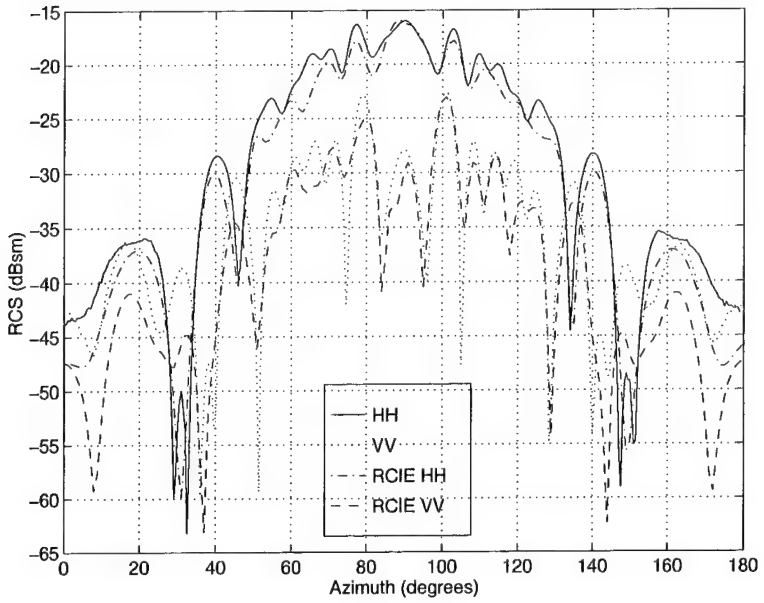

Figure D.107 The monostatic RCS of the ogive using 3D-RCIE and measured data obtained at 10 GHz. The mesh size is $10/\lambda$ and BLGMRP was used to solve the matrix.

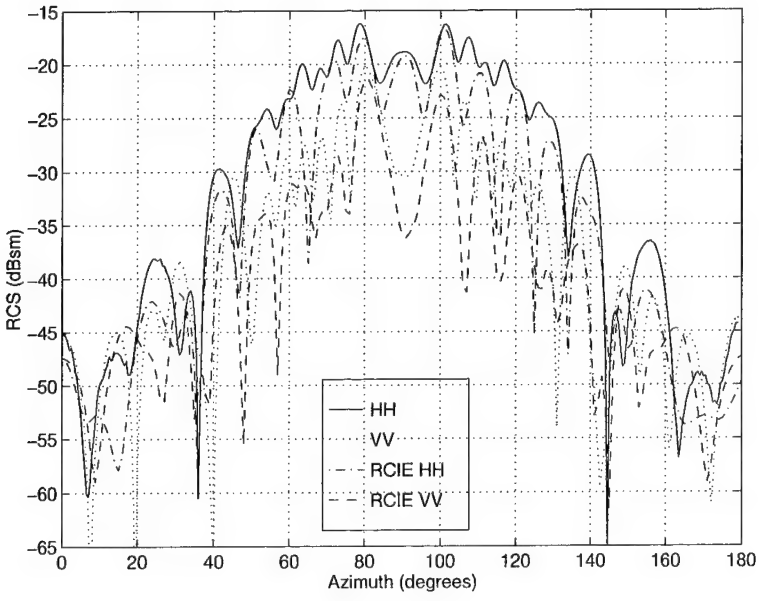

Figure D.108 The monostatic RCS of the ogive using 3D-RCIE and measured data obtained at 12 GHz. The mesh size is $8.3/\lambda$ and BLGMRP was used to solve the matrix.

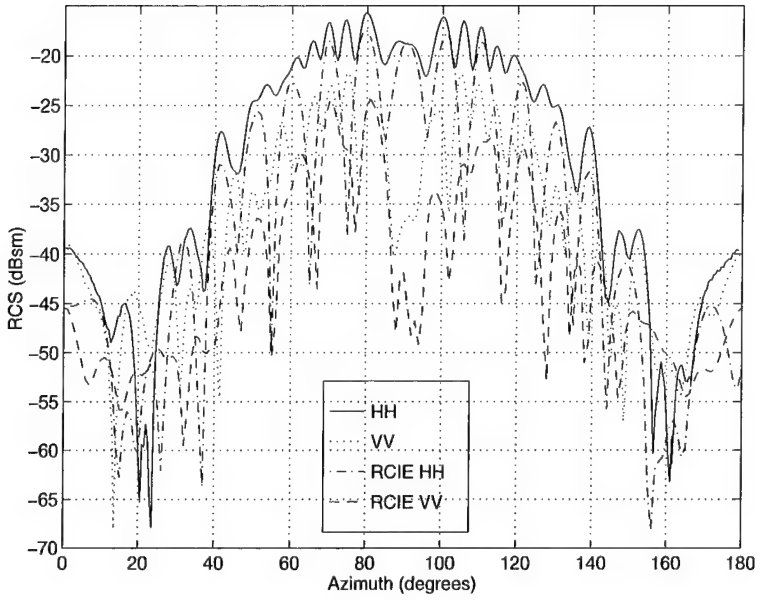

Figure D.109 The monostatic RCS of the ogive using 3D-RCIE and measured data obtained at 14 GHz. The mesh size is $7.1/\lambda$ and BLGMRP was used to solve the matrix.

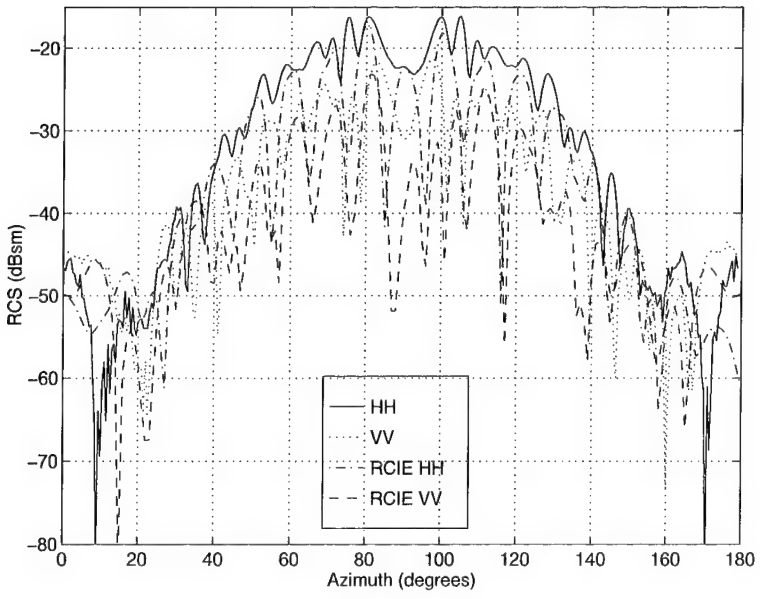

Figure D.110 The monostatic RCS of the ogive using 3D-RCIE and measured data obtained at 16 GHz. The mesh size is $6.25/\lambda$ and BLGMRP was used to solve the matrix.

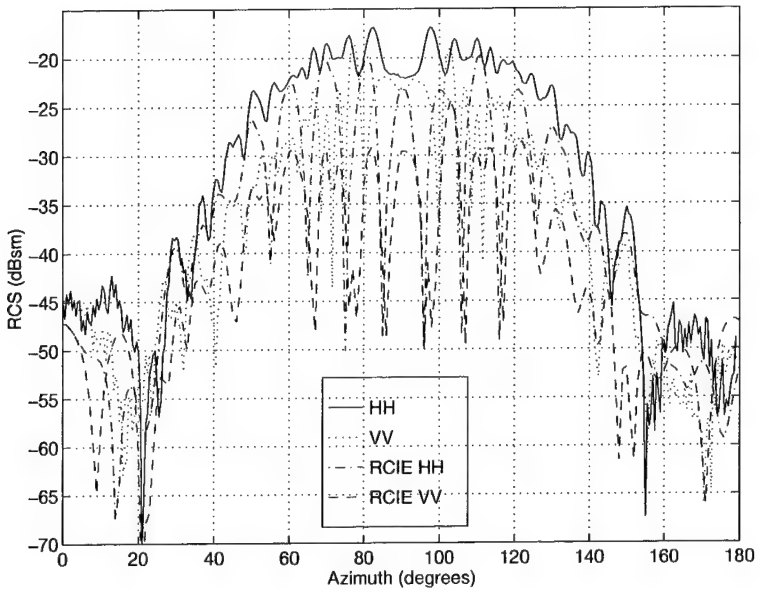

Figure D.111 The monostatic RCS of the ogive using 3D-RCIE and measured data obtained at 18 GHz. The mesh size is $5.6/\lambda$ and BLGMRP was used to solve the matrix.

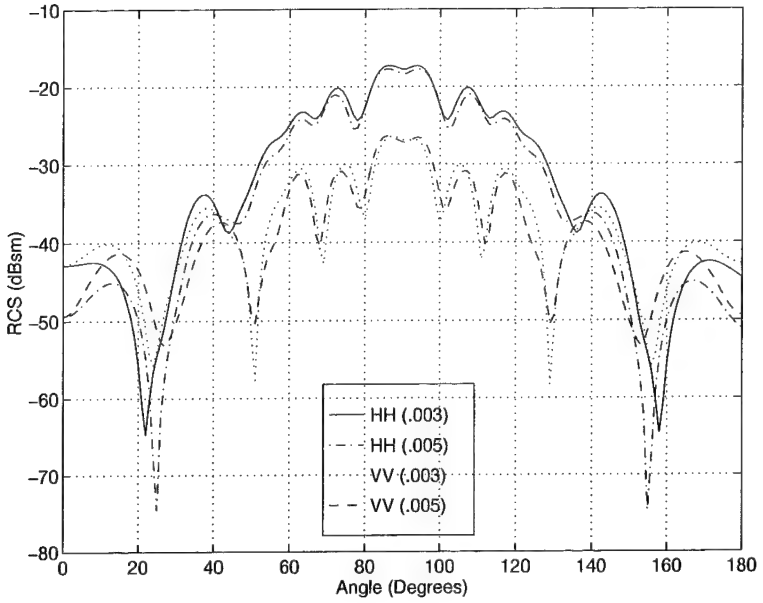

Figure D.112 The monostatic RCS of the ogive using 3D-RCIE and varied mesh sizes obtained at 6 GHz. The mesh sizes are $16.7/\lambda$ (.003) and $10/\lambda$ (.005). BLGMRP was used to solve the matrix.

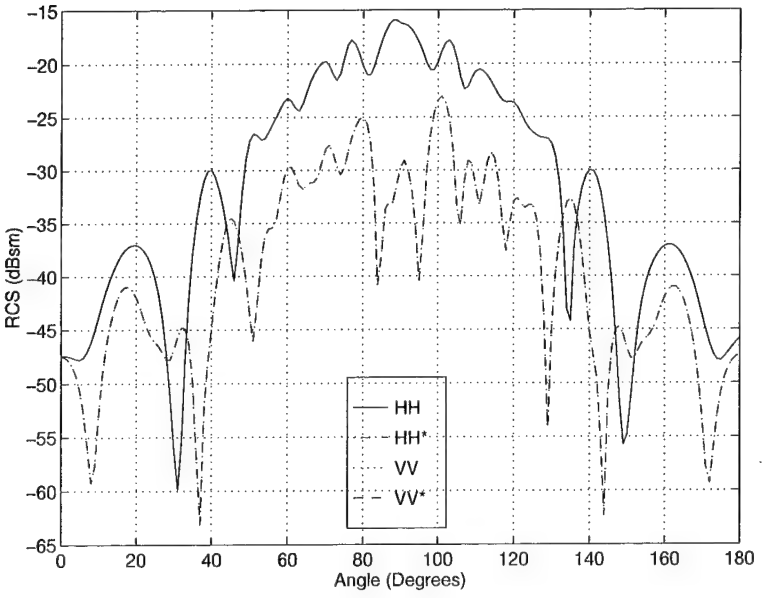

Figure D.113 The monostatic RCS of the polyethylene ogive using 3D-RCIE with varied dimensions obtained at 10 GHz. The length of each dimension was increased by 0.005 inches. BLGMRP was used to solve the matrix.

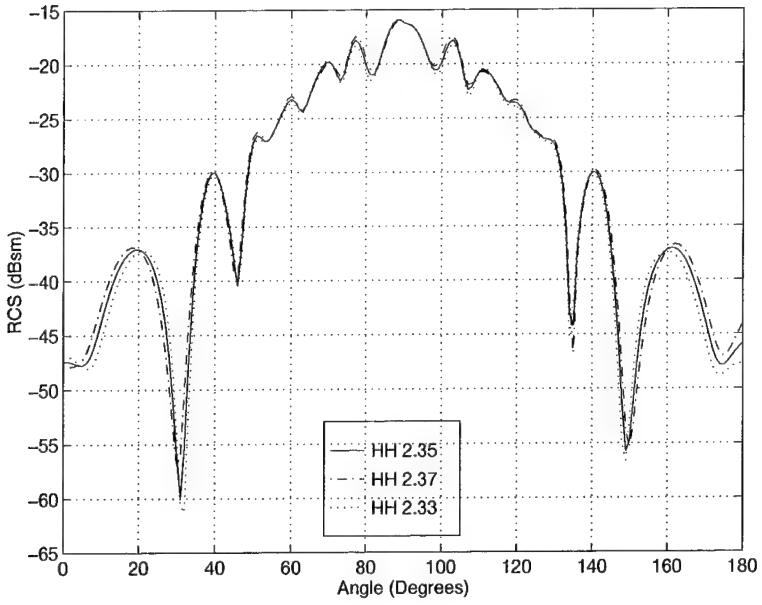

Figure D.114 The HH monostatic RCS of the polyethylene ogive using 3D-RCIE and varied dielectric constants obtained at 10 GHz. The dielectric constants are 2.33, 2.35, and 2.37. BLGMRP was used to solve the matrix.

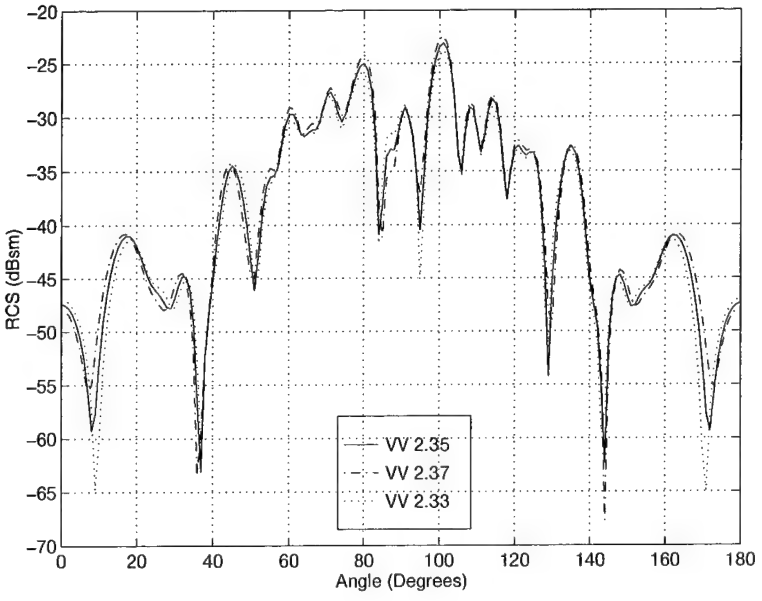

Figure D.115 The VV monostatic RCS of the polyethylene ogive using 3D-RCIE and varied dielectric constants obtained at 10 GHz. The dielectric constants are 2.33, 2.35, and 2.37. BLGMRP was used to solve the matrix.

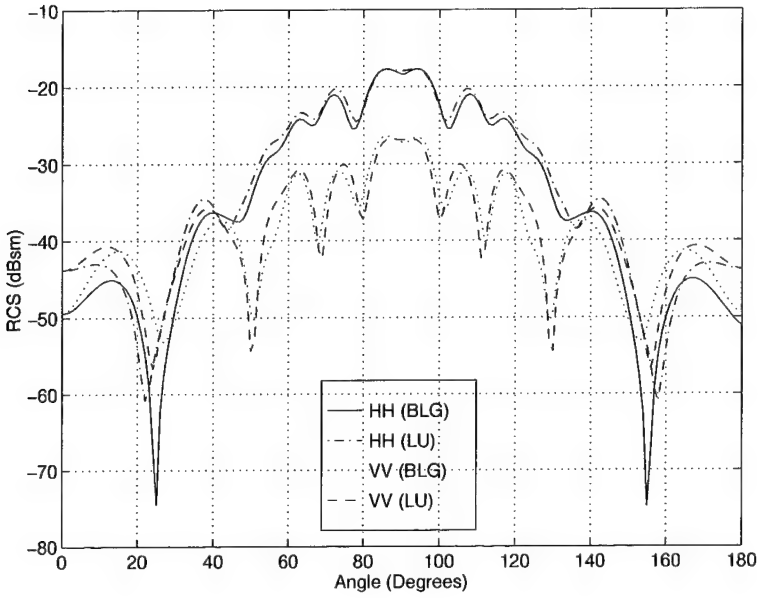

Figure D.116 The monostatic RCS of the polyethylene ogive using 3D-RCIE with BLGMRP and LUFACTOR obtained at 6 GHz. The mesh size is $10/\lambda$.

D.11 Conesphere

Description	Figure
RCS Comparison of the Conesphere at 2 GHz	D.117
RCS Comparison of the Conesphere at 4 GHz	D.118
RCS Comparison of the Conesphere at 6 GHz	D.119
RCS Comparison of the Conesphere at 8 GHz	D.120
RCS Comparison of the Conesphere at 10 GHz	D.121
RCS Comparison of the Conesphere at 12 GHz	D.122
RCS Comparison of the Conesphere at 14 GHz	D.123
RCS Comparison of the Conesphere at 16 GHz	D.124
RCS Comparison of the Conesphere at 18 GHz	D.125
Conesphere RCS with varied mesh sizes at 2 GHz	D.126
Conesphere RCS with varied dimensions at 2 GHz	D.127
Conesphere HH RCS with varied dielectric constants at 2 GHz	D.128
Conesphere VV RCS with varied dielectric constants at 2 GHz	D.129
3D-RCIE (BLG vs. LU) RCS of the Polyethylene Conesphere at 2 GHz	D.130

Table D.11 List of plots for the RCS of the conesphere.

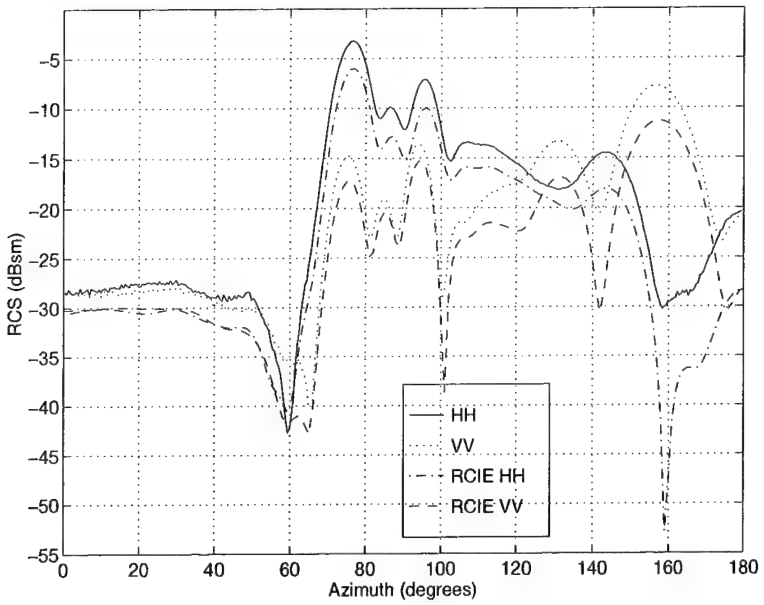

Figure D.117 The monostatic RCS of the conesphere using 3D-RCIE and measured data obtained at 2 GHz. The mesh size is $15/\lambda$ and BLGMRP was used to solve the matrix.

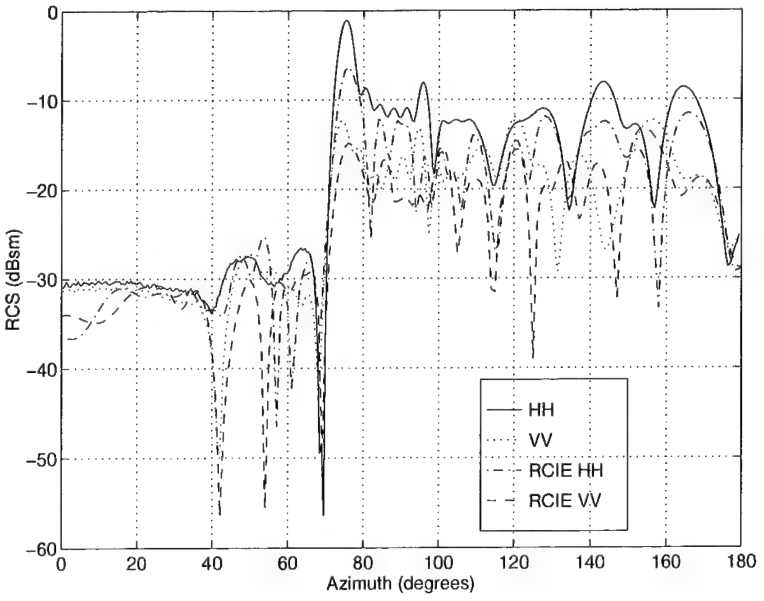

Figure D.118 The monostatic RCS of the conesphere using 3D-RCIE and measured data obtained at 4 GHz. The mesh size is $7.5/\lambda$ and BLGMRP was used to solve the matrix.

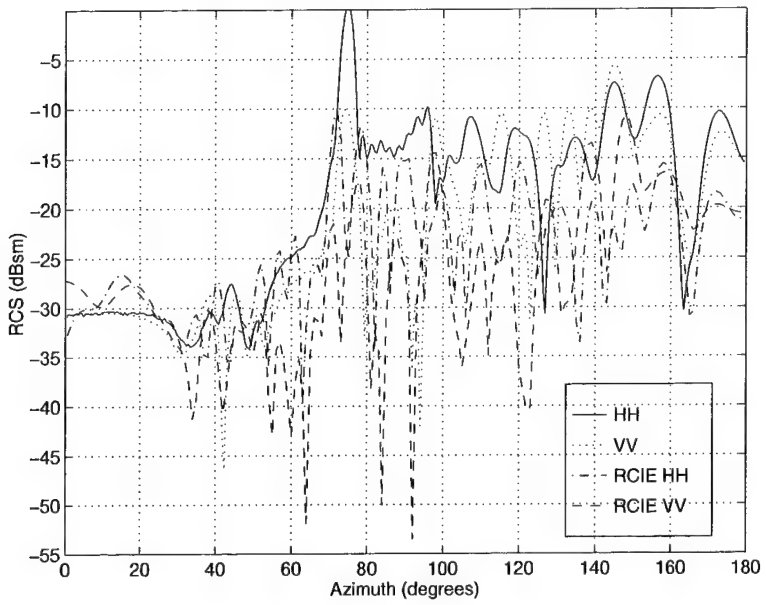

Figure D.119 The monostatic RCS of the conesphere using 3D-RCIE and measured data obtained at 6 GHz. The mesh size is $5/\lambda$ and BLGMRP was used to solve the matrix.

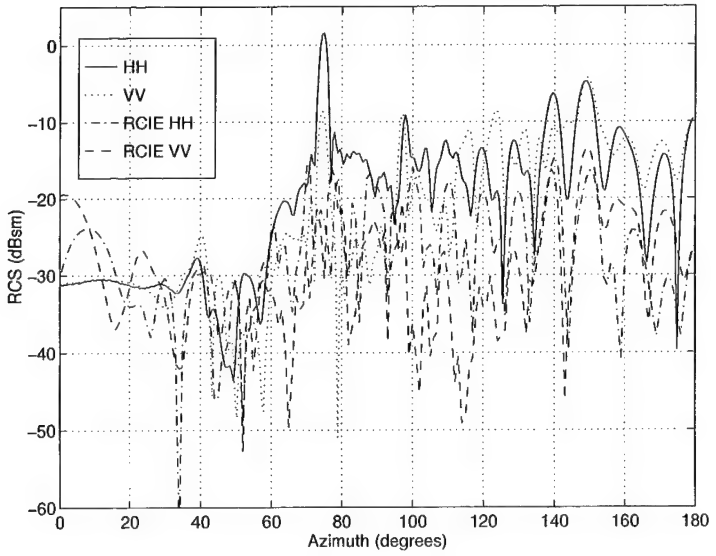

Figure D.120 The monostatic RCS of the conesphere using 3D-RCIE and measured data obtained at 8 GHz. The mesh size is $3.75/\lambda$ and BLGMRP was used to solve the matrix.

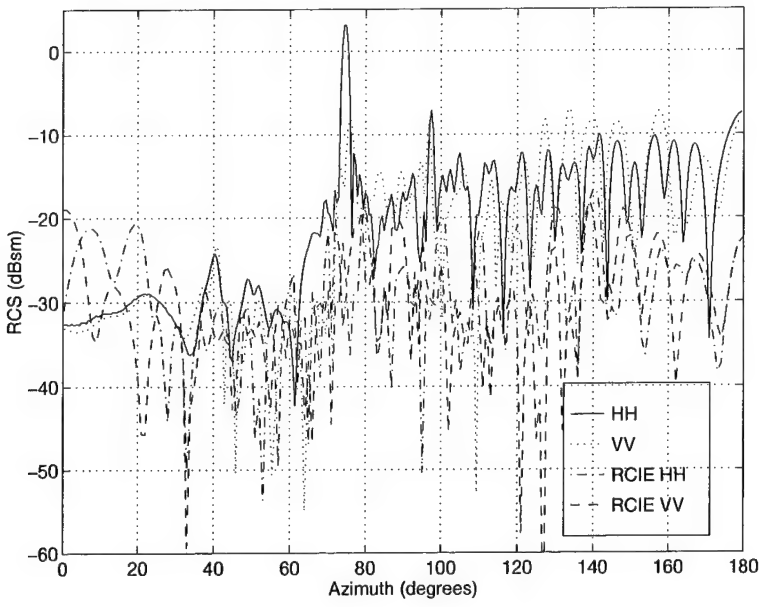

Figure D.121 The monostatic RCS of the conesphere using 3D-RCIE and measured data obtained at 10 GHz. The mesh size is $3/\lambda$ and BLGMRP was used to solve the matrix.

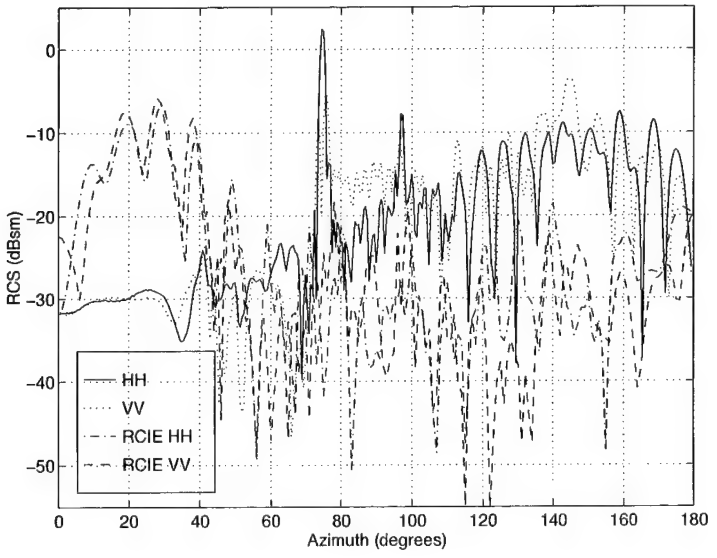

Figure D.122 The monostatic RCS of the conesphere using 3D-RCIE and measured data obtained at 12 GHz. The mesh size is $2.5/\lambda$ and BLGMRP was used to solve the matrix.

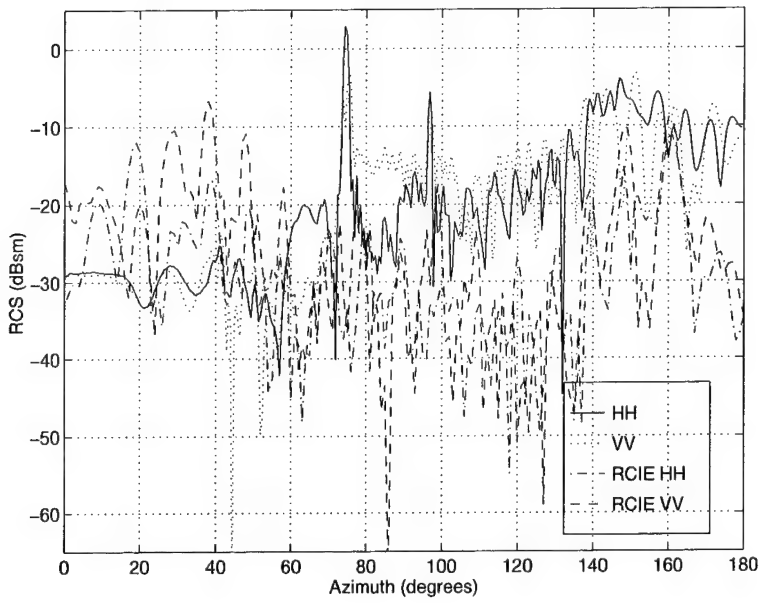

Figure D.123 The monostatic RCS of the conesphere using 3D-RCIE and measured data obtained at 14 GHz. The mesh size is $2.1/\lambda$ and BLGMRP was used to solve the matrix.

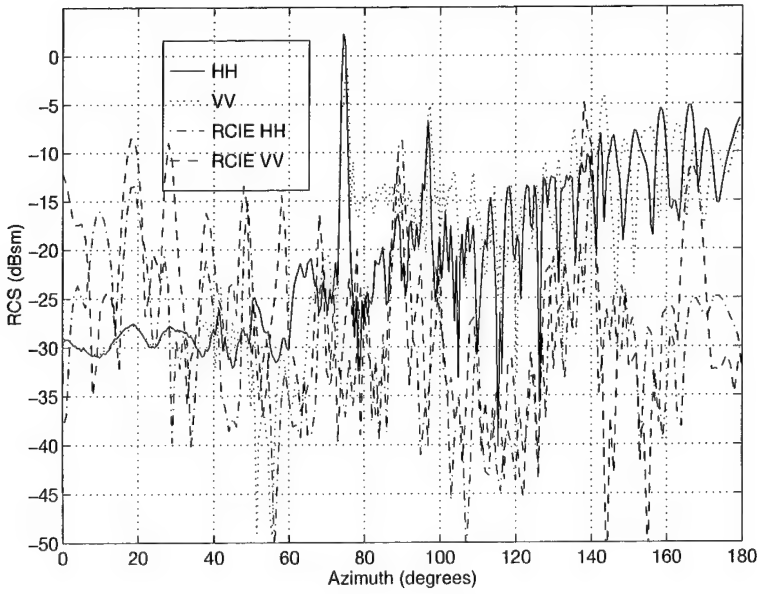

Figure D.124 The monostatic RCS of the conesphere using 3D-RCIE and measured data obtained at 16 GHz. The mesh size is $1.9/\lambda$ and BLGMRP was used to solve the matrix.

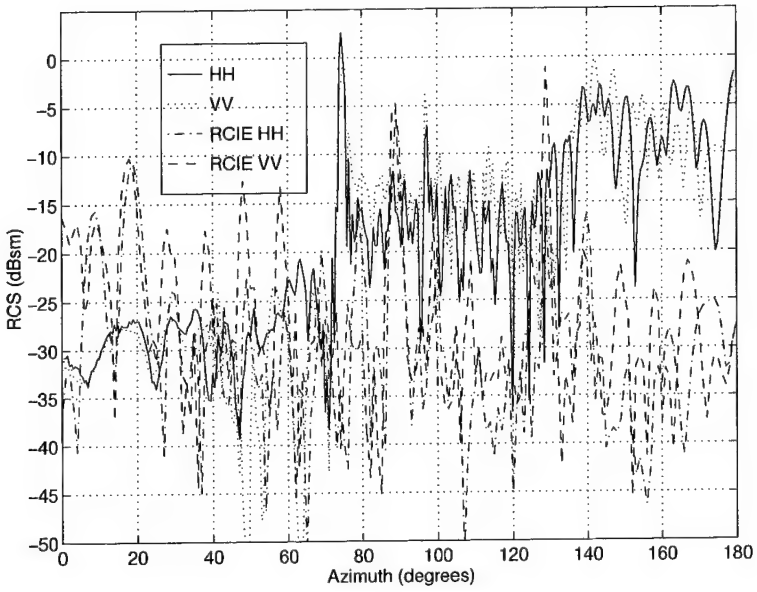

Figure D.125 The monostatic RCS of the conesphere using 3D-RCIE and measured data obtained at 18 GHz. The mesh size is $1.7/\lambda$ and BLGMRP was used to solve the matrix.

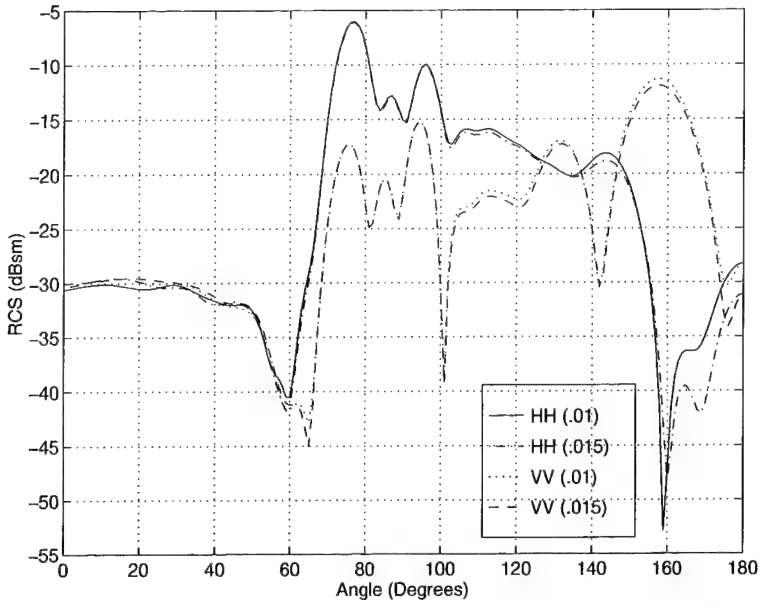

Figure D.126 The monostatic RCS of the conesphere using 3D-RCIE and varied mesh sizes obtained at 2 GHz. The mesh sizes are $15/\lambda$ (.01) and $10/\lambda$ (.015). BLGMRP was used to solve the matrix.

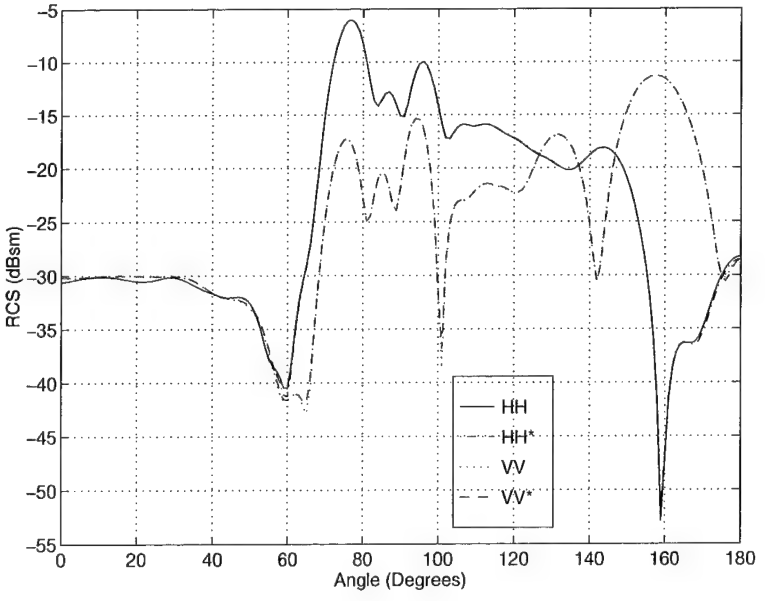

Figure D.127 The monostatic RCS of the polyethylene conesphere using 3D-RCIE with varied dimensions obtained at 2 GHz. The length of each dimension was increased by 0.005 inches. BLGMRP was used to solve the matrix.

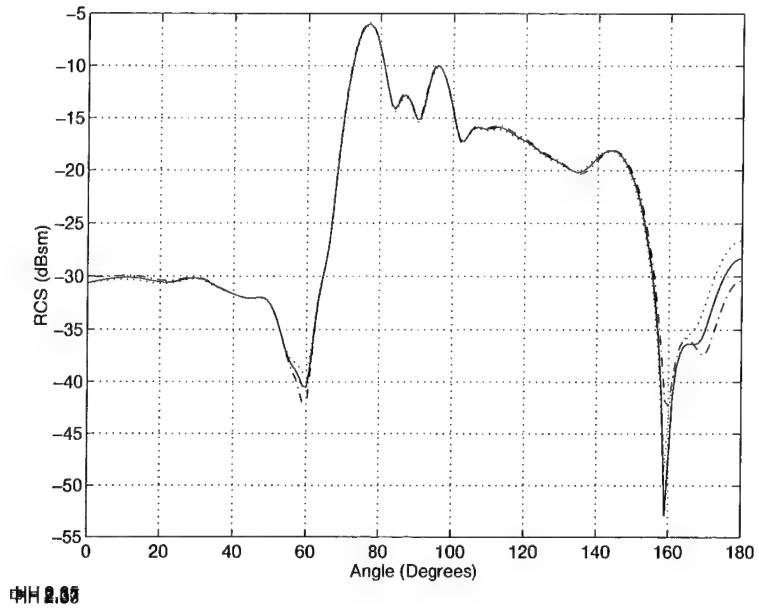

Figure D.128 The HH monostatic RCS of the polyethylene conesphere using 3D-RCIE and varied dielectric constants obtained at 2 GHz. The dielectric constants are 2.33, 2.35, and 2.37. BLGMRP was used to solve the matrix.

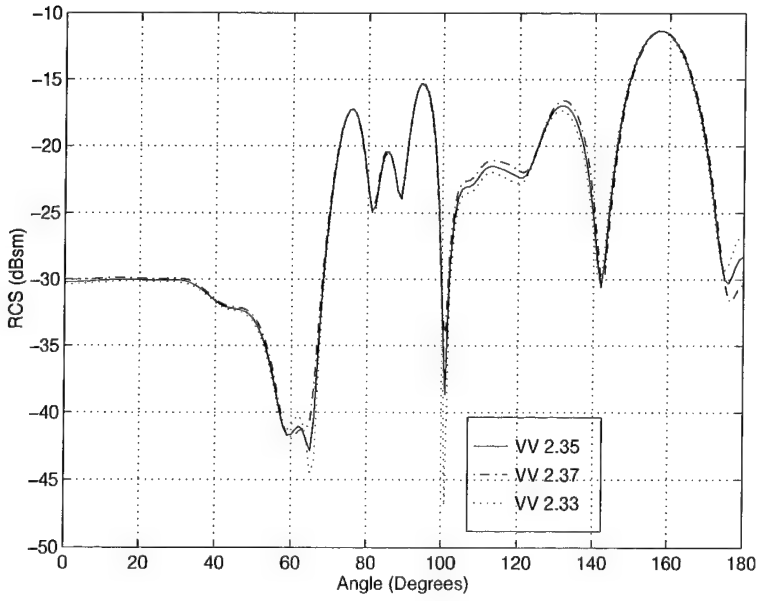

Figure D.129 The VV monostatic RCS of the polyethylene conesphere using 3D-RCIE and varied dielectric constants obtained at 2 GHz. The dielectric constants are 2.33, 2.35, and 2.37. BLGMRP was used to solve the matrix.

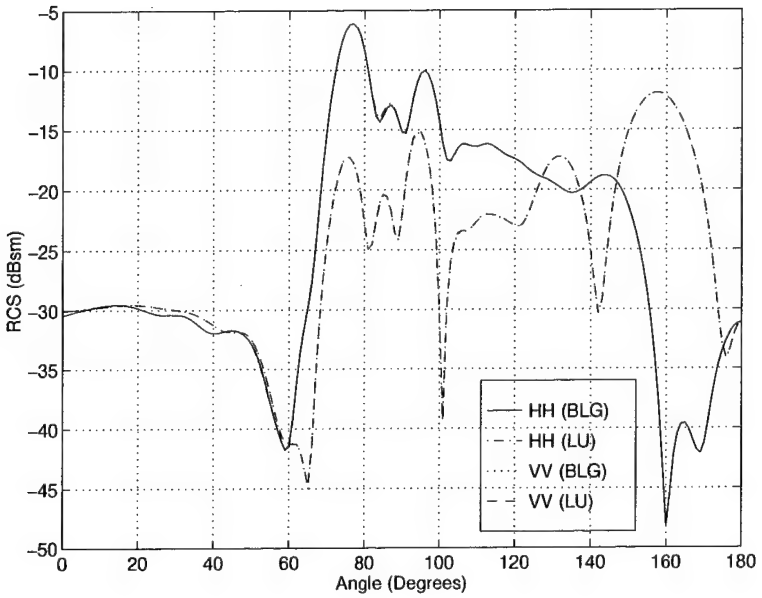

Figure D.130 The monostatic RCS of the polyethylene conesphere using 3D-RCIE with BLGMRP and LUFACTOR obtained at 2 GHz. The mesh size is $10/\lambda$.

D.12 Conesphere

Description	Figure
RCS Comparison of the Conesphere with a Gap at 2 GHz	D.131
RCS Comparison of the Conesphere with a Gap at 4 GHz	D.132
RCS Comparison of the Conesphere with a Gap at 6 GHz	D.133
RCS Comparison of the Conesphere with a Gap at 8 GHz	D.134
RCS Comparison of the Conesphere with a Gap at 10 GHz	D.135
RCS Comparison of the Conesphere with a Gap at 12 GHz	D.136
RCS Comparison of the Conesphere with a Gap at 14 GHz	D.137
RCS Comparison of the Conesphere with a Gap at 16 GHz	D.138
RCS Comparison of the Conesphere with a Gap at 18 GHz	D.139
Conesphere with a Gap RCS with varied mesh sizes at 2 GHz	D.140
Conesphere with a Gap RCS with varied dimensions at 2 GHz	D.141
Conesphere with a Gap HH RCS with varied dielectric constants at 2 GHz	D.142
Conesphere with a Gap VV RCS with varied dielectric constants at 2 GHz	D.143
3D-RCIE (BLG vs. LU) RCS of the Polyethylene Conesphere with a Gap at 2 GHz	D.144

Table D.12 List of plots for the RCS of the conesphere with a gap.

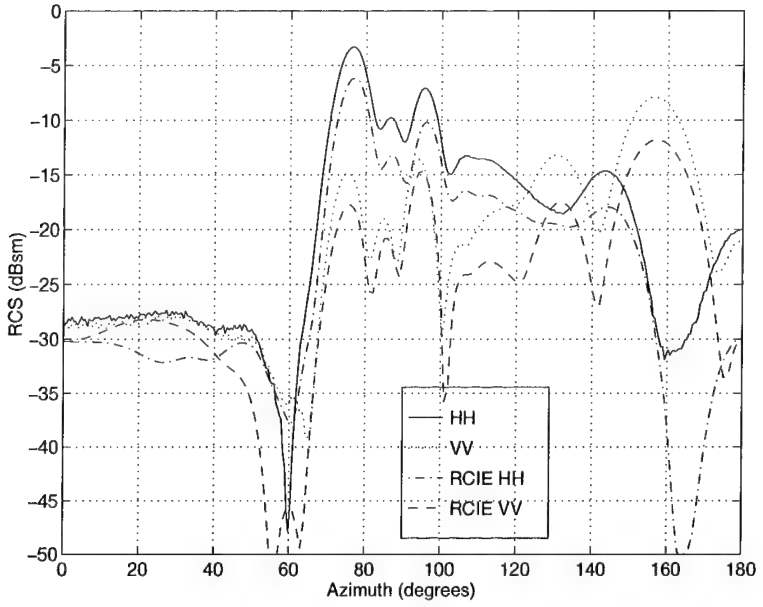

Figure D.131 The monostatic RCS of the conesphere with a gap using 3D-RCIE and measured data obtained at 2 GHz. The mesh size is $13.6/\lambda$ and BLGMRP was used to solve the matrix.

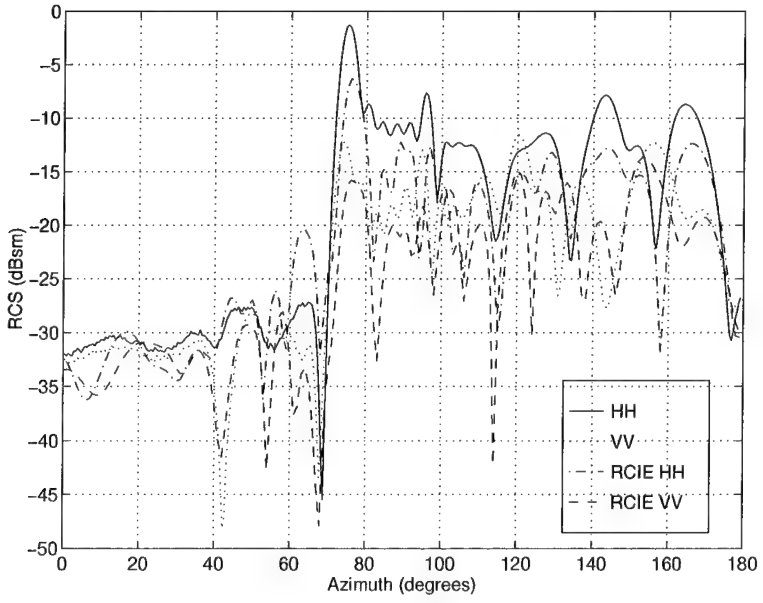

Figure D.132 The monostatic RCS of the conesphere with a gap using 3D-RCIE and measured data obtained at 4 GHz. The mesh size is $6.8/\lambda$ and BLGMRP was used to solve the matrix.

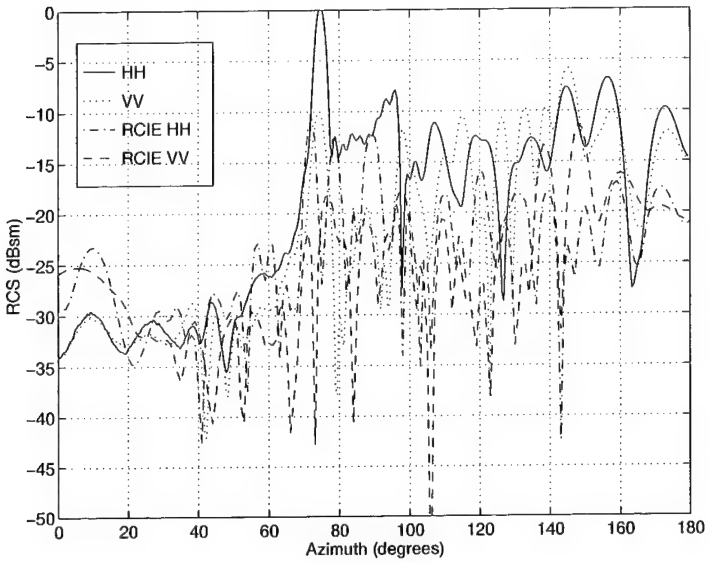

Figure D.133 The monostatic RCS of the conesphere with a gap using 3D-RCIE and measured data obtained at 6 GHz. The mesh size is $4.5/\lambda$ and BLGMRP was used to solve the matrix.

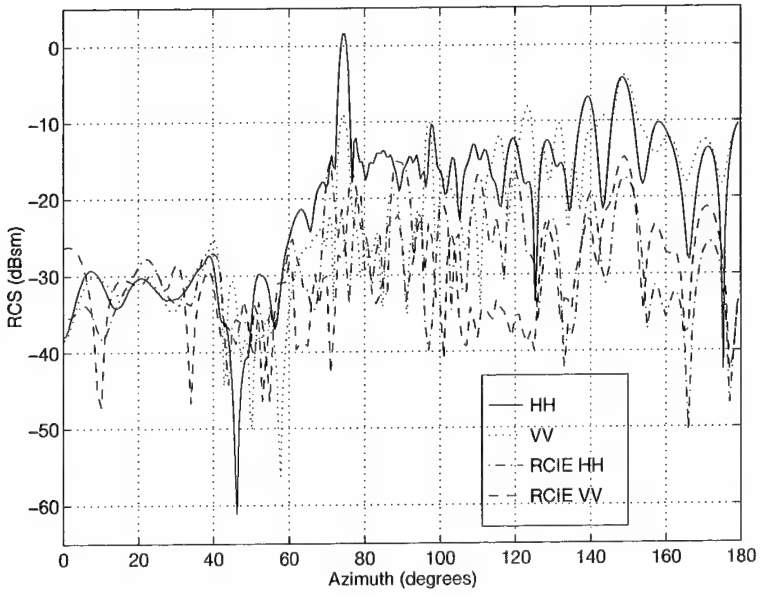

Figure D.134 The monostatic RCS of the conesphere with a gap using 3D-RCIE and measured data obtained at 8 GHz. The mesh size is $3.4/\lambda$ and BLGMRP was used to solve the matrix.

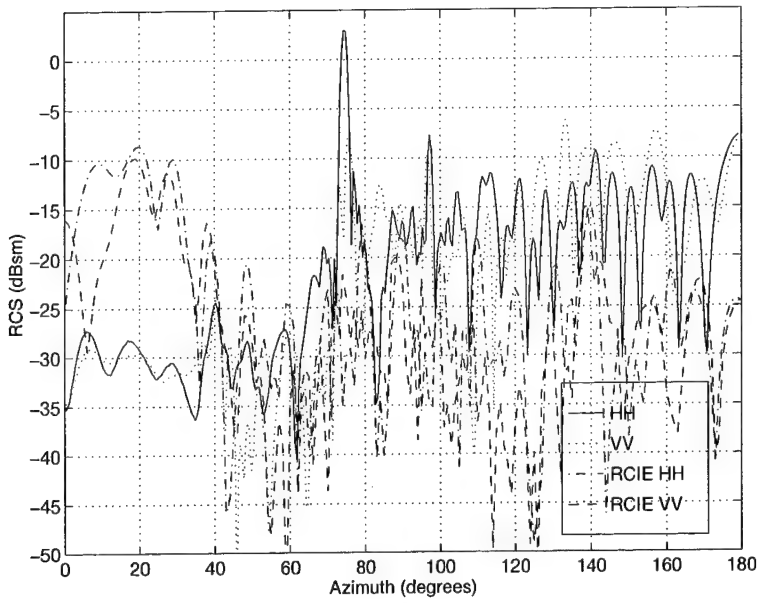

Figure D.135 The monostatic RCS of the conesphere with a gap using 3D-RCIE and measured data obtained at 10 GHz. The mesh size is $2.7/\lambda$ and BLGMRP was used to solve the matrix.

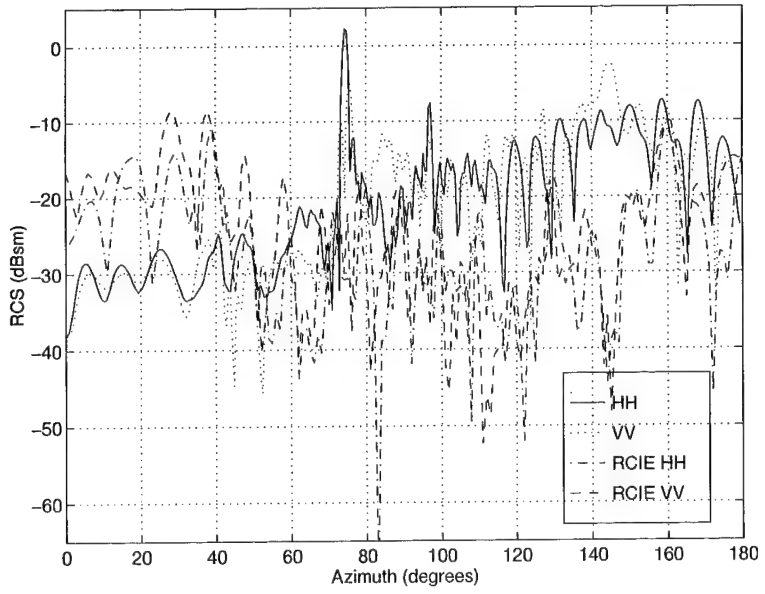

Figure D.136 The monostatic RCS of the conesphere with a gap using 3D-RCIE and measured data obtained at 12 GHz. The mesh size is $2.3/\lambda$ and BLGMRP was used to solve the matrix.

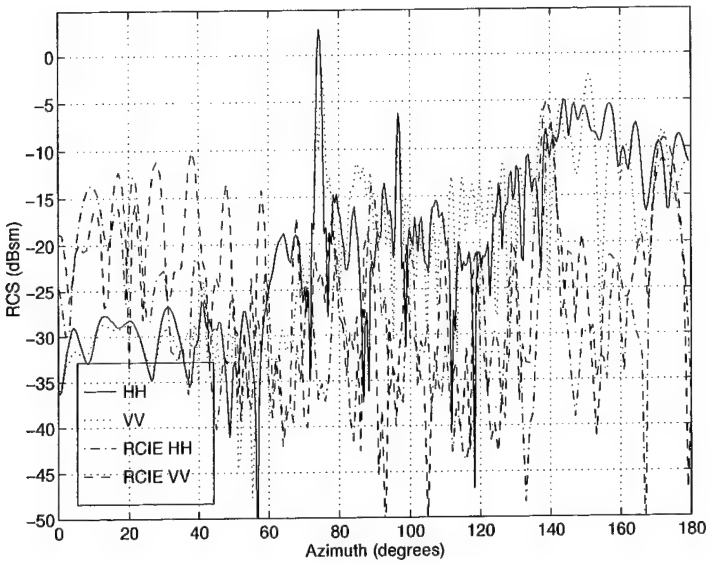

Figure D.137 The monostatic RCS of the conesphere with a gap using 3D-RCIE and measured data obtained at 14 GHz. The mesh size is $1.9/\lambda$ and BLGMRP was used to solve the matrix.

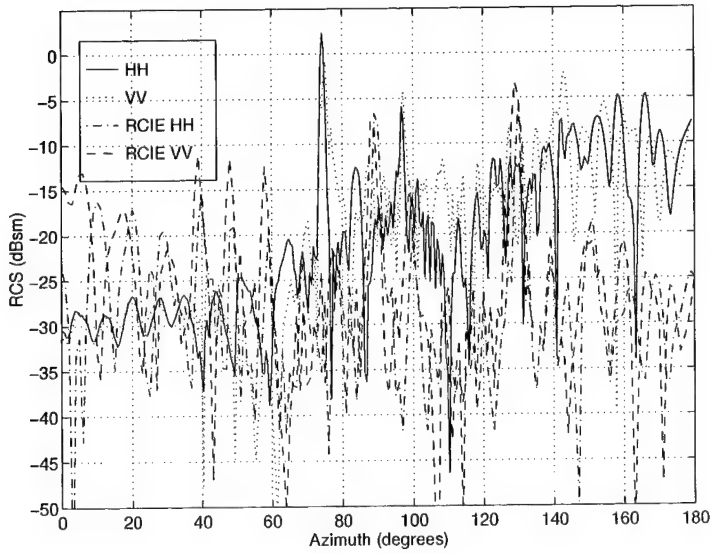

Figure D.138 The monostatic RCS of the conesphere with a gap using 3D-RCIE and measured data obtained at 16 GHz. The mesh size is $1.7/\lambda$ and BLGMRP was used to solve the matrix.

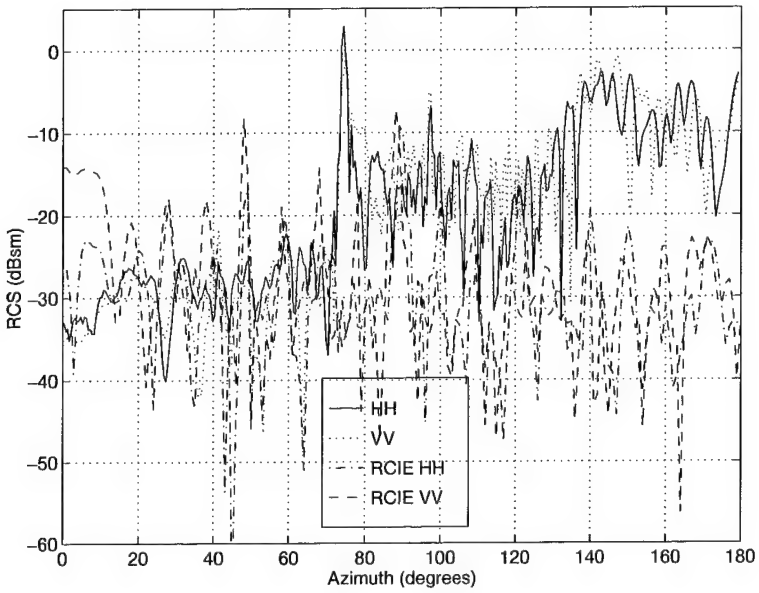

Figure D.139 The monostatic RCS of the conesphere with a gap using 3D-RCIE and measured data obtained at 18 GHz. The mesh size is $1.5/\lambda$ and BLGMRP was used to solve the matrix.

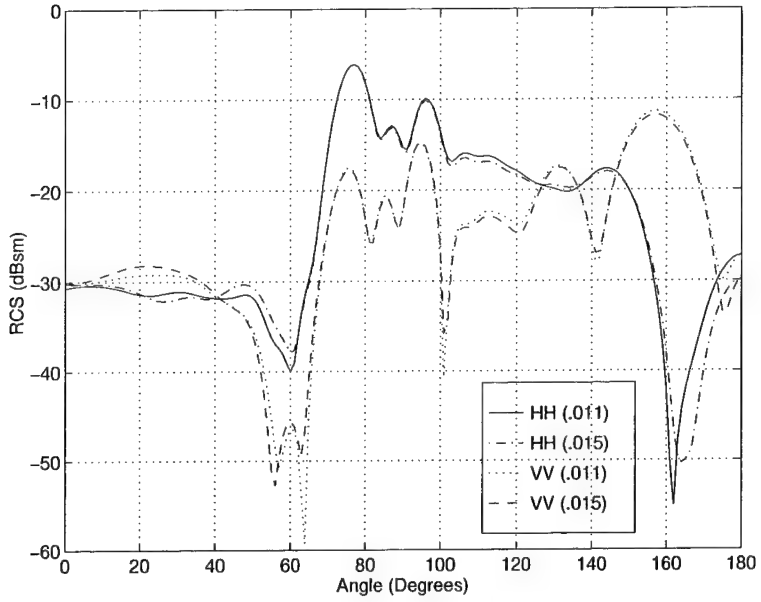

Figure D.140 The monostatic RCS of the conesphere with a gap using 3D-RCIE and varied mesh sizes obtained at 2 GHz. The mesh sizes are $13.6/\lambda$ (.011) and $10/\lambda$ (.015). BLGMRP was used to solve the matrix.

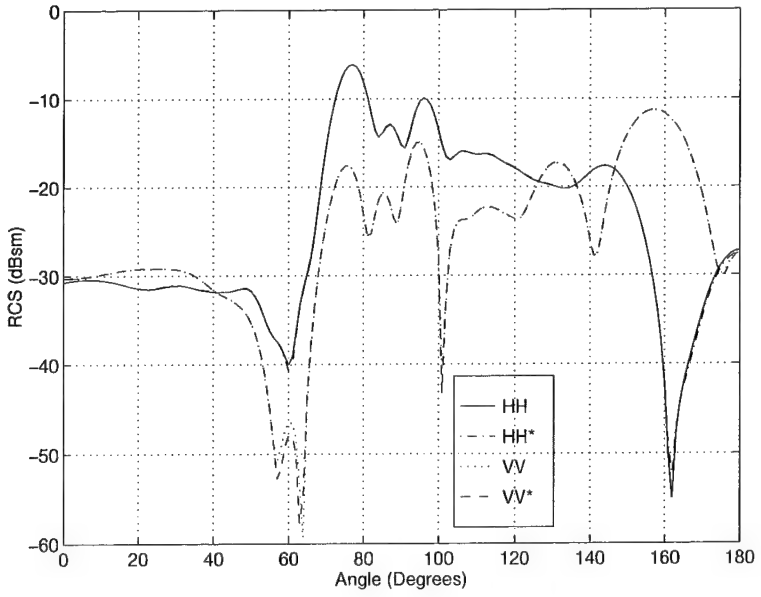

Figure D.141 The monostatic RCS of the polyethylene conesphere with a gap using 3D-RCIE with varied dimensions obtained at 2 GHz. The length of each dimension was increased by 0.005 inches. BLGMRP was used to solve the matrix.

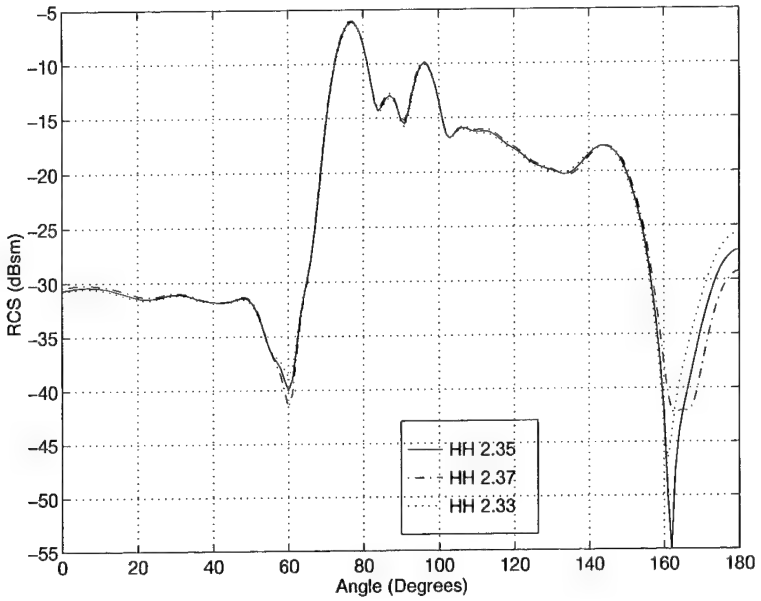

Figure D.142 The HH monostatic RCS of the polyethylene conesphere with a gap using 3D-RCIE and varied dielectric constants obtained at 2 GHz. The dielectric constants are 2.33, 2.35, and 2.37. BLGMRP was used to solve the matrix.

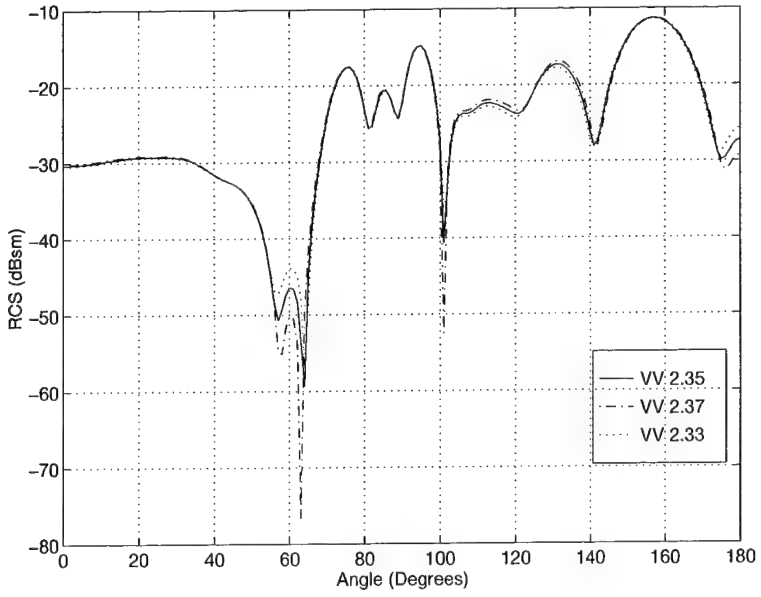

Figure D.143 The VV monostatic RCS of the polyethylene conesphere with a gap using 3D-RCIE and varied dielectric constants obtained at 2 GHz. The dielectric constants are 2.33, 2.35, and 2.37. BLGMRP was used to solve the matrix.

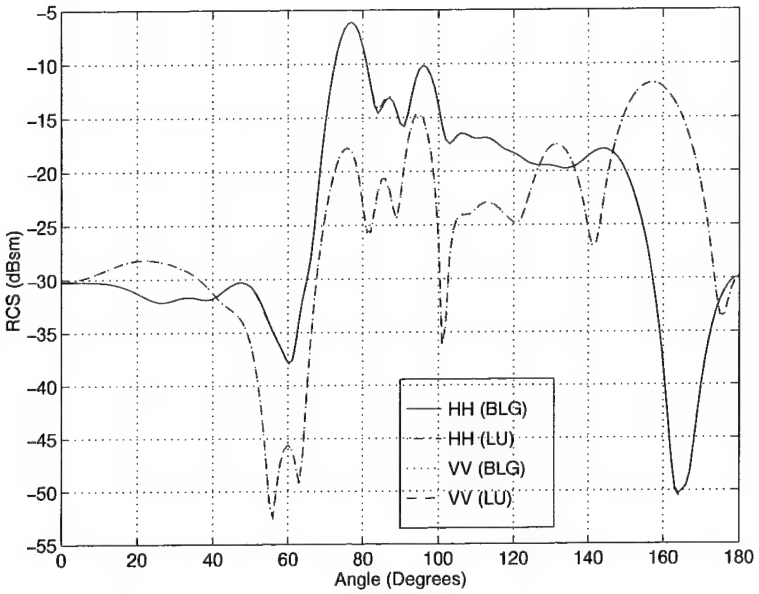

Figure D.144 The monostatic RCS of the polyethylene conesphere with a gap using 3D-RCIE with BLGMRP and LUFACTOR obtained at 2 GHz. The mesh size is $10/\lambda$.

Appendix E. Measured Data in Ascii Format

All the measured data in this research is available on the attached CD. The data is in ascii format and includes material property measurements, RCS measurements and the Mie series data. The RCS measurements include noise and calibration measurements.

E.1 Material Measurements

Two samples of polyethylene and three samples of polyurethane were measured five times each using an X-band waveguide. The HP 8510C network analyzer measured S_{11} and S_{21} for each sample from 8 to 12 GHz, in 10 MHz steps averaging 128 measurements per step. From the S-parameter data, an external computer calculated the permittivity and permeability using a Matlab routine.

The data, in ascii format, is presented for each measurement in five columns. The first column is the frequency. The second and third columns are the corresponding real and imaginary part of the permittivity. The final two columns are the permeability, real and imaginary. Table E.1 is a listing of the data files.

E.2 RCS Measurements

The RCS measurements for this research were accomplished at Wright Laboratory's Multispectral Measurement Facility (WL/XPN), Wright-Patterson AFB, OH. Each of the targets were measured for both polarizations from 2 to 18 GHz, in 20 MHz increments, and from 0 to 360 degrees, in 0.5 degree increments, in azimuth.

The data for each measurement was provided in three columns. The first column is the azimuth angle. The next two columns are the I (real part) and Q (imaginary part) channel data, respectively. The frequency is folded into the azimuth angle starting with 2 GHz and then incrementing by 20 MHz until 18 GHz is reached. Thus, there are 801 rows of I and Q channel data corresponding to a particular frequency for each angle. Overall, each data set has 576,720 rows of data. The RCS in dB per square meter (dBsm) can be calculated using the following equation:

Material	Sample	Measurement	File Name
Polyethylene	1	1	a1.m
Polyethylene	1	2	a2.m
Polyethylene	1	3	a3.m
Polyethylene	1	4	a4.m
Polyethylene	1	5	a5.m
Polyethylene	2	1	b1.m
Polyethylene	2	2	b2.m
Polyethylene	2	3	b3.m
Polyethylene	2	4	b4.m
Polyethylene	2	5	b5.m
Polyurethane	1	1	c1.m
Polyurethane	1	2	c2.m
Polyurethane	1	3	c3.m
Polyurethane	1	4	c4.m
Polyurethane	1	5	c5.m
Polyurethane	2	1	d1.m
Polyurethane	2	2	d2.m
Polyurethane	2	3	d3.m
Polyurethane	2	4	d4.m
Polyurethane	2	5	d5.m
Polyurethane	3	1	e1.m
Polyurethane	3	2	e2.m
Polyurethane	3	3	e3.m
Polyurethane	3	4	e4.m
Polyurethane	3	5	e5.m

Table E.1 List of material measurement data files.

$$\sigma = 10 \cdot log_{10}(I^2 + Q^2) \tag{E.1}$$

Table E.2 is a listing of the RCS data file names. For each target there are a total of four data files: HH and VV split from 0 to 180 and 180 to 360 degrees. Note that the ogive data was measured every 10 MHz, instead of 20 MHz, and is centered at approximately 5 degrees, not 0 degrees.

Target	Polarization	Azimuth Angle (Degrees)	File Name
Small Polyethylene Cube	HH	0-180	cube_1h.asc
Small Polyethylene Cube	HH	180-360	cube_1h_x.asc
Small Polyethylene Cube	VV	0-180	cube_1v.asc
Small Polyethylene Cube	VV	180-360	cube_1v_x.asc
Small Polyethylene Cube with R-card	HH	0-180	cb_1hrcd.asc
Small Polyethylene Cube with R-card	HH	180-360	cb_1hrcd_x.asc
Small Polyethylene Cube with R-card	VV	0-180	cb_1vrcd.asc
Small Polyethylene Cube with R-card	VV	180-360	cb_1vrcd_x.asc
Small Polyurethane Cube	HH	0-180	cbur_h.asc
Small Polyurethane Cube	HH	180-360	cbur_h_x.asc
Small Polyurethane Cube	VV	0-180	cbur_v.asc
Small Polyurethane Cube	VV	180-360	cbur_v_x.asc
Small Polyurethane Cube with R-card	HH	0-180	cburr_h.asc
Small Polyurethane Cube with R-card	HH	180-360	cburr_h_x.asc
Small Polyurethane Cube with R-card	VV	0-180	cburr_v.asc
Small Polyurethane Cube with R-card	VV	180-360	cburr_v_x.asc
Large Polyethylene Cube	HH	0-180	cube_12h.asc
Large Polyethylene Cube	HH	180-360	cube_12h_x.asc
Large Polyethylene Cube	VV	0-180	cube_12v.asc
Large Polyethylene Cube	VV	180-360	cube_12v_x.asc
Large Polyurethane Cube	HH	0-180	cbur_12h.asc
Large Polyurethane Cube	HH	180-360	cbur_12h_x.asc
Large Polyurethane Cube	VV	0-180	cbur_12v.asc
Large Polyurethane Cube	VV	180-360	cbur_12v_x.asc
Polyethylene Mini-Arrow	HH	0-180	m_arwh.asc
Polyethylene Mini-Arrow	HH	180-360	m_arrow_h_x.asc
Polyethylene Mini-Arrow	VV	0-180	m_arwv.asc
Polyethylene Mini-Arrow	VV	180-360	m_arrow_v_x.asc
Polyethylene Mini-Arrow with R-card	HH	0-180	m_arwh_r.asc
Polyethylene Mini-Arrow with R-card	HH	180-360	m_arwh_r_x.asc
Polyethylene Mini-Arrow with R-card	VV	0-180	m_arwv_r.asc
Polyethylene Mini-Arrow with R-card	VV	180-360	m_arwv_r_x.asc

Table E.2 List of RCS data files.

Target	Polarization	Azimuth Angle (Degrees)	File Name
Polyethylene Sphere	HH	0-180	sphere_h.asc
Polyethylene Sphere	HH	180-360	sphere_h_x.asc
Polyethylene Sphere	VV	0-180	sphere_v.asc
Polyethylene Sphere	VV	180-360	sphere_v_x.asc
Polyethylene Ogive	HH	0-180	ogive_h.asc
Polyethylene Ogive	HH	180-360	ogive_h_x.asc
Polyethylene Ogive	VV	0-180	ogive_v.asc
Polyethylene Ogive	VV	180-360	ogive_v_x.asc
Polyethylene Conesphere	HH	0-180	cone_h.asc
Polyethylene Conesphere	HH	180-360	cone_h_x.asc
Polyethylene Conesphere	VV	0-180	cone_v.asc
Polyethylene Conesphere	VV	180-360	cone_v_x.asc
Polyethylene Conesphere with a Gap	HH	0-180	conegp_h.asc
Polyethylene Conesphere with a Gap	HH	180-360	conegp_h_x.asc
Polyethylene Conesphere with a Gap	VV	0-180	conegp_v.asc
Polyethylene Conesphere with a Gap	VV	180-360	conegp_v_x.asc

Table E.2 List of RCS data files.

E.2.1 Noise. To determine the uncertainty due to noise-background, the background noise of the range is required. Three separate background noise measurements are provided. Each measurement consists of both polarizations from 2 to 18 GHz. The background noise measurements associated with the conespheres were measured in increments of 20 MHz while the others were measured in increments of 10 MHz. The data is provided in three columns. The first column is the frequency and the second and third columns are the I and Q channel data, respectively. The data is provided in Table E.3.

Target	Polarization	File Name
Polyethylene Mini-Arrow	HH	marwhh.asc
Polyethylene Mini-Arrow	VV	marwvv.asc
Polyethylene Ogive	HH	ogivehh.asc
Polyethylene Ogive	VV	ogivevv.asc
Polyethylene Conesphere	HH	conehh.asc
Polyethylene Conesphere	VV	conevv.asc

Table E.3 List of RCS background noise files.

E.2.2 Calibration. The calibration uncertainty is produced by comparing the "exact" calibration target solution to the measured results of the double calibration. Three separate calibration measurements are provided. Each measurement consists of both polarizations from 2 to 18 GHz. The calibration measurements c7152h.asc and c7152v.asc were measured in increments of 20 MHz while the others were measured in increments of 10 MHz. The data is provided in three columns. The first column is the frequency and the second and third columns are the I and Q channel data, respectively. The data is provided in Table E.4.

Target	Polarization	File Name
Small Polyethylene Cube	HH	c7192h.asc
Small Polyethylene Cube	VV	c7192v.asc
Large Polyethylene Cube	HH	c7191h.asc
Large Polyethylene Cube	VV	c7191v.asc
Polyethylene Mini-Arrow	HH	c7191h.asc
Polyethylene Mini-Arrow	VV	c7191v.asc
Polyethylene Conesphere	HH	7152h.asc
Polyethylene Conesphere	VV	7152v.asc
Polyethylene Conesphere with a Gap	HH	7152h.asc
Polyethylene Conesphere with a Gap	VV	7152v.asc

Table E.4 List of RCS calibration files.

E.3 Mie Series

The exact monostatic RCS for a 10 inch diameter sphere with a dielectric constant of 2.35 was calculated using the Mie Series. This data is in the file entitled "mie10.asc." The RCS was calculated for both polarizations from 2 to 18 GHz, in 10 MHz increments. The first column is the frequency. The second column, labeled "KOA", is the wave number multiplied by the radius. The next column is the bistatic angle, which is zero for this case. The last four columns are the theta and phi returns. Columns 4 and 5 are the theta return in square meters and dBsm, respectively. Columns 6 and 7 are the phi return in square meters and dBsm, respectively. Note that for a sphere, both theta and phi are equal.

Bibliography

1. Afsar, Mohammed Nurul, et al. "The Measurement of the Properties of Materials," *Proceedings of the IEEE*, *74*:183–195 (January 1996).

2. Balanis, Constantine A. *Advanced Engineering Electromagnetics*. New York, NY: John Wiley and Sons, 1989.

3. Barnhart, Greg A. *Evaluation of the Sensitivity of Radar Cross Section Predictions to Uncertainties in Material Characteristics*. MS thesis, AFIT/GE/ENG/95D-02, Air Force Institute of Technology, Wright-Patterson AFB, Ohio, 1995.

4. Chambers, Michael W. *Radar Scattering From Foamed Plastic Target Supports*. MS thesis, AFIT/GE/ENG/91D-10, Air Force Institute of Technology, Wright-Patterson AFB, Ohio, 1991.

5. Cheng, D.K. *Field and Wave Electromagnetics*. Reading, Massachusetts: Addison-Wesley Publishing Company, 1990.

6. Chizever, Hirsch M., et al. "On Reducing Primary Calibration Errors In Radar Cross Section Measurements." *Antenna Measurements Techniques Association Symposium Proceedings*. 383–388. 1996.

7. Colby, Paul C., et al. *Three Dinemsional Radiation Condition Integral Equations (3D-RCIE)*. Final Report CDRL A008, Palo Alto, CA: Lockheed Martin Missiles And Space Co., Inc., March 1997.

8. Colby, Paul C., et al. *Three Dinemsional Radiation Condition Integral Equations (3D-RCIE)*. Software User's Manual, Palo Alto, CA: Lockheed Martin Missiles And Space Co., Inc., January 1997.

9. Collins, Capt., Peter J. Class notes distributed in EENG 627: RCS Analysis, Measurement, and Reduction. Graduate School of Engineering, Air Force Institute of Technology, Wright-Patterson AFB OH, March 1997.

10. Friederich, Paul G., Senior Research Engineer for the Signature Technology Laboratory. Telephone interview. Georgia Tech Research Institute (GTRI), Atlanta, GA, 28 October 1997.

11. Gupta, Inder J., et al. "Scattering by Dielectric Straps with Potential Application as Target Support Structures," *IEEE Transactions on Antennas and Propagation*, *37*:1164–1171 (September 1989).

12. Hewlett Packard. *Measuring Dielectric Constant with the HP 8510 Network Analyzer*. Technical Report 8510-3. Santa Rose, CA, August 1985.

13. Jasik, Henry. *Antenna Engineering Handbook*. New York, NY: McGraw-Hill Book Company, 1961.

14. Kent, Brian M. NIST Briefings of Air Force Wright Laboratory Compact Range Review. Wright Laboratories, Signature Technology Directorate, Wright Laboratory (AFMC), Wright-Patterson AFB OH, May 1993.

15. Knott, E.F., et al. *Radar Cross Section*. Dedham, MA: Artech House, Inc., 1985.

16. Parker, Earl R. *Materials Data Book For Engineers And Scientists*. New York, NY: McGraw-Hill Book Company, 1967.

17. Pettofrezzo, Anthony J. *Elements of Linear Algebra*. Englewood Cliffs, NJ: Prentice-Hall, Inc., 1970.

18. Plonus, M.A. "Theoretical Investigations of Scattering from Plastic Foams," *IEEE Transactions on Antennas and Propagation*, *13*:88–93 (January 1965).

19. Pozar, David M. *Microwave Engineering*. Reading, MA: Addison-Wesley Publishing Company, 1990.

20. VonHippel, Arthur R. *Dielectric Materials and Applications*. New York, NY: John Wiley and Sons, Inc., 1954.

21. Wittmann, R.C., et al. "Proposed Analysis of RCS Measurement Uncertainty." *Antenna Measurements Techniques Association Symposium Proceedings*. 51–57. 1994.

22. Woo, Alex C., et al. "Benchmark Radar Targets for the Validation of Computational Electromagnetics Programs," *IEEE Antennas and Propagation Magazine*, *35*:84–89 (February 1993).

Vita

Captain Jeffery Michael Parks was born on December 29, 1968 at Wright-Patterson AFB, Ohio. He graduated from Mayfield High School in Las Cruces, New Mexico in 1987. Later that year he attended New Mexico State University on an AFROTC scholarship. In December of 1991 he graduated with a Bachelor of Science in Electrical Engineering. In September of 1992 he entered active duty as a Second Lieutenant at Vandenberg AFB, CA. While at Vandenberg, he served as a Titan Electrical Engineer for the 6595 Aerospace Test Group, AFMC. In the following years the 6595 ATG switched to the 4th Space Launch Squadron, AFSPC, and Captain Parks became a certified Booster Operations Controller, and held that position for the launch of the Titan IV K-15 booster on December 5, 1995. In May of 1996, Captain Parks entered the Air Force Institute of Technology at Wright-Patterson AFB, Ohio, to pursue a Master's Degree in Electrical Engineering. His follow-on assignment is with Wright Laboratory's Multispectral Measurement Facility (WL/XPN) at Wright-Patterson AFB, Ohio. Captain Parks is married to the former Ms. Katrina Dawn Hall of Farmington, NM.

Permanent address: 2420 Janet Ann Lane
Las Cruces, NM 88005

REPORT DOCUMENTATION PAGE

Form Approved
OMB No. 0704-0188

1. AGENCY USE ONLY *(Leave blank)*	2. REPORT DATE	3. REPORT TYPE AND DATES COVERED
	December 1997	Masters Thesis

4. TITLE AND SUBTITLE
Scattering From Dielectric Bodies

5. FUNDING NUMBERS

6. AUTHOR(S)
Jeffery M. Parks, Captain, USAF

7. PERFORMING ORGANIZATION NAME(S) AND ADDRESS(ES)
Air Force Institute of Technology, WPAFB, OH 45433-6583

8. PERFORMING ORGANIZATION REPORT NUMBER
AFIT/GE/ENG/97D-13

9. SPONSORING/MONITORING AGENCY NAME(S) AND ADDRESS(ES)
Major Paul Skinner, SAF/OR
14675 Lee Road
Chantilly, VA 20151-1715

10. SPONSORING/MONITORING AGENCY REPORT NUMBER

11. SUPPLEMENTARY NOTES

12a. DISTRIBUTION AVAILABILITY STATEMENT
Distribution Unlimited

12b. DISTRIBUTION CODE

13. ABSTRACT *(Maximum 200 words)*

The purpose of this study was to develop an RCS measured database of non-PEC targets and provide an example of its use to validate a code, 3D-RCIE. RCS prediction codes that handle penetrable materials require measured data to determine their accuracy. The materials used for this research include polyethylene and polyurethane with dielectric constants around 2.3 and 1.03, respectively. The polyethylene targets include a mini-arrow, ogive, conesphere, conesphere with a gap, sphere, and a large and small cube. The cubes were the only targets made from the polyurethane foam. Additionally, r-card was applied to the cubes and mini-arrow. The material properties of the two materials were measured using an X-band waveguide reflectometer. The RCS measurements were accomplished for each target at the Wright Laboratory Signature Technology Office's Multispectral Measurement Facility (WL/XPN). For each measurement, an uncertainty analysis was completed. RCS predictions of each target were accomplished using 3D-RCIE, a method of moments electromagnetic scattering code based on the radiation condition integral equations. The comparison of measured and predicted RCS data indicated that the linear mesh rate had a large impact on the results. Use of the appropriate mesh sizes generally produced good comparisons. For targets that were electrically large, mesh sizes were limited by the computer resources which in turn greatly deteriorated the predicted results. Furthermore, 3D-RCIE provided the most accurate predictions on the polyethylene targets, less the sphere and r-card application.

14. SUBJECT TERMS
Radar Cross Section, Material Characteristics, Three Dimensional Radiation Condition Integral Equation

15. NUMBER OF PAGES
296

16. PRICE CODE

17. SECURITY CLASSIFICATION OF REPORT	18. SECURITY CLASSIFICATION OF THIS PAGE	19. SECURITY CLASSIFICATION OF ABSTRACT	20. LIMITATION OF ABSTRACT
UNCLASSIFIED	UNCLASSIFIED	UNCLASSIFIED	UL